1-1-2013

X-Band Rapid-Scan EPR

Deborah Gale Mitchell
University of Denver

X-BAND RAPID-SCAN EPR

A Dissertation

Presented to

The Faculty of Natural Sciences and Mathematics

University of Denver

In Partial Fulfillment

of the Requirements for the Degree

Doctor of Philosophy

By

Deborah Gale Mitchell

August 2013

Advisor: Gareth R. Eaton

.

Author: Deborah Gale Mitchell
Title: X-band Rapid-scan EPR
Advisor: Gareth R. Eaton
Degree Date: August 2013

Abstract

The advantages of rapid-scan EPR relative to CW and pulse techniques for samples with long longitudinal relaxation time T_1 (N_s^0 defects in diamond, $N@C_{60}$, and amorphous hydrogenated silicon), heterogeneous samples (crystalline 1:1 α,γ-bisdiphenylene-β-phenylallyl (BDPA):benzene), lossy samples (aqueous nitroxyl radicals), and transient radicals (5-tert-butoxycarbonyl-5-methyl-1-pyrroline-N-oxide (BMPO)-superoxide adduct) were studied.

For samples with long relaxation times, CW (continuous wave) EPR is challenging due to power saturation and distortions from passage effects. In rapid-scan EPR, the field is swept through resonance in a time that is short relative to T_2. In rapid-scan EPR, the magnetic field is on resonance for a short time relative to CW EPR. Because of this, the energy absorbed by the spins, for the same microwave B_1, is less than in conventional CW spectra, and the signal does not saturate as readily. For samples with long electron relaxation times, pulse techniques can also be challenging, particularly if T_2 is long and T_2* is short. Rapid-scan EPR is a powerful alternative to CW and pulse EPR because it is a straight-forward technique that does not require the high power of pulse EPR. For the samples studied, improvements in signal-to-noise ranging from factors of 10 to 250 were observed.

Rapid-scan can also be used to extract relaxation information from a sample. The rapid-scan spectra for lithium phthalocyanine (LiPc) and ^{15}N-PDT (4-oxo-2,2,6,6-tetra-perdeuteromethyl-piperidinyl-^{15}N-oxyl-d_{16}) were simulated to determine T_2. The extraction of T_2 from the rapid-scan spectra of BDPA was also attempted. Through our difficulty in simulating the rapid-scan spectra of BDPA, we realized that commercial BDPA was not a homogeneous sample. The experiments studying BDPA demonstrated that rapid-scan experiments can give insight into the relaxation of a sample that might not otherwise be evident with conventional CW EPR.

Finally, rapid-scan EPR at X-band was applied to spin trapping experiments. Superoxide was generated by the reaction of xanthine oxidase and hypoxanthine and trapped with BMPO. Spin trapping with 5-tert-butoxycarbonyl-5-methyl-1-pyrroline N-oxide (BMPO) to form BMPO-OOH adduct converts the short-lived superoxide into a more stable spin adduct. The detection limit for spin-trapped superoxide was compared between CW and rapid-scan EPR. The signal-to-noise ratio was more than 40 times greater for rapid-scan than for CW EPR. We also demonstrated detection of superoxide produced by *Enterococcus faecalis* at rates that are too low for detection by CW EPR.

Acknowledgements

I would like to thank Drs. Sandra and Gareth Eaton for their mentorship over the last 5 years and allowing me to complete my dissertation in their lab. It has been a privilege to learn from their expertise in the field of EPR.

The work described in this dissertation was financially supported through a National Science Foundation (NSF) Graduate Research Fellowship as well as NSF IDBR 0753018 awarded to Gareth and Sandra Eaton.

I would especially like to thank Dr. Mark Tseitlin for devoting countless hours teaching me the theory of EPR. Richard Quine and George Rinard deserve special thanks for designing and building most of the instrumentation that I used for research.

Dr. Gerald Rosen (of the University of Maryland) was also a tremendous source of support and expertise for the spin-trapping experiments presented in this dissertation.

Virginia Meyer also deserves special thanks for her help with the rapid-scan measurements of α,γ-bisdiphenylene-β-phenylallyl (BDPA), irradiated quartz, diamond, and hydrogentated silicon samples.

I would especially like to thank all of my wonderful family and friends who have stepped in and gave me help and encouragement when I needed it most. Thank you also to my wonderful parents and siblings who always supported me. Thank you especially to Suze, Stacey, Mary Lynn, Alana, and Katie for your help with Lisa, it truly does take a village to raise a child. Finally, I will be forever grateful for my wonderful husband, Vance. Without your love and day-to-day support, I would never have been able to finish this work.

Table of Contents

List of Tables

List of Figures

List of Schemes

Abbreviations used in text

NMR	nuclear magnetic resonance
^{15}N-mHTCPO	4-hydro-3-carbamoyl-2,2,5,5-tetra-perdeuteromethyl-pyrrolin-1-^{15}N-oxyl-d_{12}
^{15}N-PDT	4-oxo-2,2,6,6-tetra-perdeuteromethyl-piperidinyl-^{15}N-oxyl-d_{16}
A	scan rate
a-Si:H	amorphous hydrogenated silicon
AC	alternating current
B_0	static magnetic field
B_1	amplitude of applied magnetic field from the microwave source
BDPA	α,γ-bisdiphenylene-β-phenylallyl
BHI	brain heart infusion
BMPO	5-tert-Butoxycarbonyl-5-methyl-1-pyrroline-N-oxide
BMPO-OOH	adduct of BMPO and superoxide
CFU	colony forming units
CTPO	3-carbamoyl-2,2,5,5-tetramethylpyrrolidin-1-yloxy
CVD	chemical vapor deposition
CW	continuous wave
dB	Decibel
db	dangling bonds
DMPO	5,5-dimethyl-1-pyrroline-N-oxide
DMPOX	5,5-dimethyl-2-pyrrolidone-N-oxyl
DNP	dynamic nuclear polarization
DPPH	2,2-diphenyl-1-picrylhydrazyl
DTPA	diethylenetriaminepentaacetic acid

ENDOR	electron-nuclear double resonance
EPR	electron paramagnetic resonance
FID	free induction decay
FT	Fourier transform
FWHM	full width at half max
G	gauss (unit of measurement of magnetic field, 1 G=10^{-4} T)
G_{pp}	gauss, peak-to-peak
$HO^{\bullet}$	hydroxyl radical
i.d.	inner diameter
IR	Infrared
L-band	microwave frequency from 1–2 GHz
LiPc	lithium phthalocyanine, radical containing solid
N_S^0	substitutional nitrogen centers
o.d.	outer diameter
$O_2^{\bullet -}$	Superoxide
OX63	methyl tris(8-carboxy-2,2,6,6-tetra(hydroxyethyl)-benzo[1,2-d:4,5-d']bis(1,3)-dithiol-4-yl)-tripotassium salt
PBS	phosphate buffered saline solution
ppm	parts per million
Q	quality factor of resonator
Q-band	microwave frequency from 33–50 GHz
r.f.	radio frequency
RCD	resonated coil driver
RMS	root mean square
S/N	signal-to-noise ratio

SEM	scanning electron microscope
SOD	superoxide dismutase
SPU	signal processing unit (Bruker trademark)
SRT	shot repetition time
T_1	spin-lattice relaxation time
T_2	spin-spin relaxation time
T_2*	time constant for damping of FID
T_D	spectral diffusion time
T_m	Phase memory time
Trityl	tertiary carbon-centered radical, see OX63 for example
TWT	traveling wave tube
VHF	very high frequency (30-300 MHz, in this dissertation it usually refers to 250 MHz)
X-band	frequency from 8–12.4 GHz
ΔB_{pp}	peak-to-peak linewidth in G
Λ	resonator efficiency (G/√Watt)
ω_0	source frequency
ω_L	Larmor frequency
ω_{res}	frequency of the resonator

Chapter 1: Motivation and Basics of EPR

1.1 Motivation for Studying Rapid-scan EPR

Important information can be extracted from EPR (electron paramagnetic resonance) experiments including imaging of oxygen concentrations in tissue [1], distances in proteins [2], studying transient radicals such as superoxide via spin-trapping [3], and much more. Rapid-scan is appealing because of its fast data acquisition and unlike pulsed EPR, data can be obtained at microwave powers available in conventional continuous wave (CW) EPR spectrometers.

Although rapid-scan NMR (nuclear magnetic resonance) has been observed for over 60 years [4, 5], rapid-scan EPR was invented in the Eaton lab relatively recently. Initially, X-band (~9 GHz) rapid-scan was a novel method that is still in the developmental stages. The initial goal was to understand the benefits of rapid-scan EPR relative to more mainstream methods such as CW and pulse EPR. The fast data acquisition of rapid-scan EPR made it promising as a technique that would enhance signal-to-noise (S/N) in a short amount of time.

In this thesis, rapid-scan EPR demonstrated a signal-to-noise enhancement relative to other EPR techniques when applied to samples with long longitudinal relaxation time T_1 (N_s^0 defects in diamond, $N@C_{60}$, and amorphous hydrogenated silicon) as well as nitroxyl radicals and spin-trap adducts. Magnetically concentrated samples were also

studied with rapid-scan EPR. For BDPA, insight into relaxation processes were determined that were not evident from pulse and CW techniques alone.

1.2 Resonance

In physics, resonance is defined as the tendency of a system to oscillate with a larger amplitude at certain natural frequencies than at other frequencies [6]. The increase in amplitude at resonant frequencies is observed because energy is being transferred to the system under the most favorable conditions. Resonant frequencies were first characterized for mechanical systems such as pendulums by Galileo in the early 17^{th} century [7, 8]. Resonance is observed for all types of vibrations or waves including mechanical, acoustic, molecular, and electromagnetic vibrations.

The resonance condition can also be thought of as the coupling of two systems so that energy flows between the two systems under the most favorable conditions [9]. In quantum mechanics, resonance is the coupling of two quantum mechanical states such as the stationary state of an atom and an oscillatory source of energy such as a photon. This coupling is strongest when the energy of the oscillatory source matches the energy difference between two stationary states of the atom. In spectroscopy, a photon is absorbed or emitted when the resonance condition in satisfied. Different types and frequency ranges of spectroscopy study different stationary states in atoms or molecules. UV-Vis spectroscopy uses a source of light in the visible and adjacent ranges (10–800 nm wavelength) that correspond to the energy separation of electronic transitions for molecules. Infrared (IR) spectroscopy has a range of energies that corresponds to the

vibrational states of molecules. In spectroscopy, the resonance phenomenon allows us to probe many different types of stationary states in quantum mechanical systems.

1.3 Electron Spin

Electrons are elementary particles that are characterized by an inherent angular momentum called spin. Classically, electrons are thought of as spinning tops, however, because electrons are quantum particles their behavior is governed by the rules of quantum mechanics. To understand the magnetic resonance phenomenon, it is important to note that an electron in the presence of a constant external magnetic field exists in one of two states α or β, whose projections are parallel and anti-parallel to the external field. These states differ only in the orientation of the angular momentum vector, but not the magnitude. The spin vector is typically denoted by $\boldsymbol{S}$. Magnetic moments are represented in units of $\hbar$, for which the magnitude of $\boldsymbol{S}$ is $\sqrt{S(S+1)}$, where S=1/2 is the electron spin quantum number [10]. The typical convention is to consider the α and β states as those having definite components S_z along the z-axis of the Cartesian frame, where z is the direction of the external magnetic field. For a single electron, S_z is either ½ (α state) or –½ (β state). For this basic EPR discussion, these states will be labeled as $M_s^{+1/2}$ (α state) and $M_s^{-1/2}$ (β state).

1.4 Zeeman Effect

EPR studies the interactions of an unpaired electron with an external magnetic field (B_0), local magnetic fields produced by the surrounding nuclear and electron spins, and orbital motion of the electron itself [11]. EPR was first discovered by Zavoisky in 1944 studying paramagnetic salts such as $MnSO_4$ [12, 13]. As mentioned previously, a

single unpaired electron, with no neighboring nuclei, has two allowed energy states $M_s^{+1/2}$ and $M_s^{-1/2}$ (Figure 1.1). In the absence of a magnetic field, these two spin states are degenerate and there is an equal population in the $M_s^{+1/2}$ and $M_s^{-1/2}$ states. However, when a magnetic field is applied, the spin can align with or against the magnetic field. The state with parallel orientation $M_s^{+1/2}$ has larger energy than the state with anti-parallel orientation $M_s^{-1/2}$. The difference between the energies of these two states is shown in Equation 1.1.

$$\Delta E = g\beta B = h\nu \tag{1.1}$$

where h is Planck's constant, a physical constant reflecting the size of one quantum of energy at a specific electromagnetic frequency, υ. The g-factor is denoted by g, β_e is the Bohr magneton, a natural unit of the electron's magnetic moment, and Δm_s is the change in spin state, which according to selection rules must be ±1. The gyromagnetic ratio of the electron is given by $-g\beta_e$ [10]. The spin states splitting in energy in the presence of a magnetic field is called the Zeeman effect. Because of the Boltzmann distribution for the spin ensemble, there is a temperature dependent difference in population of the two states, with more spins in the lower energy state. It is this difference that makes observation of the resonance possible.

The resonance condition is satisfied when the energy that is required to cause a transition between the two spin states is equal to $h\upsilon$. The resonance condition may be achieved in two ways: varying the magnetic field strength or varying the microwave frequency ([11]. In CW EPR, it is customary to hold the microwave frequency constant

and sweep the magnetic field through resonance because of resonator bandwidth limits [14]. The resonator bandwidth is defined as

$$BW_{res} = \frac{\nu_{res}}{Q} \tag{1.2}$$

where ν_{res} is the microwave frequency and Q is the quality factor of the resonator. Thus, the bandwidth can be increased by either lowering the Q or increasing the resonant frequency. One example of a frequency-swept experiment is collecting spectra at W-band (94 GHz) with low Q resonator [14]. At the most common microwave frequency in EPR, X-band (~9.6 GHz), there is not sufficient resonator bandwidth to employ a frequency sweep that is large enough to be useful for most spectra. Because of the limit in resonator bandwidth, most EPR spectrometers operate at constant microwave frequency and scan the magnetic field (Figure 1.1). The majority of this thesis will focus on field-swept EPR.

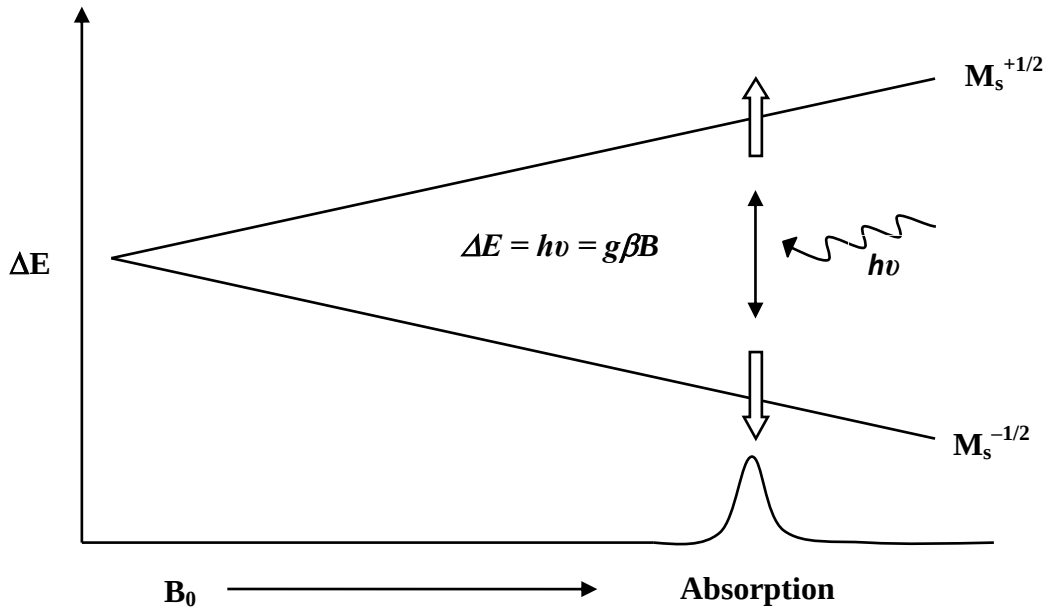

Figure 1.1. Zeeman energy splitting for an unpaired electron in a magnetic field. The splitting between the parallel (M_s = +1/2) and the antiparallel state (M_s = –1/2) is proportional to the applied magnetic field (B_0).

Chapter 2: Information extracted from EPR

The information desired from an experiment will direct the type of experiment performed. Applications of EPR range from studying the structure of biological molecular systems to studying the physical nature of magnetism (Salikhov, 2011). The following sections discuss typical information extracted from an EPR experiment.

2.1 *g*-Factor and Spin-Orbit Coupling

Because a spectrum can be obtained at different microwave frequencies, the field at which resonance occurs is not unique. The *g*-factor (Equation 2.1), however, can be used as a characteristic of a compound because it is independent of frequency.

$$g = \frac{h\nu}{\beta_e B_0} \tag{2.1}$$

The intrinsic spin angular momentum of a free electron is associated with a *g* factor of 2.00232, which is called g_e [15]. The g-factor is characteristic of the environment of a spin, specifically the spin-orbit coupling. In quantum mechanics, the orbital and spin angular momenta are represented by the operators $\hbar\boldsymbol{L}$ and ħS respectively (Salikhov, 2011). The orbital and spin magnetic moments of electrons are represented by the operators in Equation 2.2,

$$\mu_0 = -g_0\beta_e L \quad \textbf{and} \quad \mu_S = -g_e\beta_e S \tag{2.2}$$

The g-factors are different for the spin (g_e= 2.0023) and orbital (g_o = 1) moments. The total magnetic moment depends on the spin-orbit coupling. Because the ground state of most molecules (including radicals) have small orbital angular momentum, the expected *g*-factor in these cases is close to the free-electron value [15]. However, there is often mixing of orbital angular momentum of excited states into the ground state that creates a local magnetic field, which causes the *g*-factor to differ from the free-electron value. The *g*-factor can be isotropic (orientation independent) or anisotropic (dependent on the orientation of B_0 with respect to the molecular axis). Rapid tumbling can average anisotropic components of the *g*-factor and give an isotropic spectrum.

2.2 Hyperfine Splitting and Spin Density

Because the deviation of the g-value from the free-electron value is often small, it sometimes is not enough to uniquely characterize a radical species [16]. This is especially true if the experiment is carried out at lower frequencies such as VHF or L-band. The hyperfine structure often provides a more conspicuous signature to characterize the sample. The hyperfine structure that arises from the interaction of the electron with neighboring nuclei can be used to characterize a radical. The magnetic field at the electron is composed of contributions from the external magnetic field and a contribution from the magnetic moment of neighboring nuclei on electron spins [17]. Nuclei with spin zero, including ^{12}C and ^{16}O, are non-magnetic, however, many nuclei, including ^{1}H, ^{14}N, ^{13}C, have spin $I \geq ½$ and possess a magnetic moment [10].

The interaction of an unpaired electron with neighboring nuclear-dipole moments results in splitting of the electron spin resonance line. This phenomenon is called

hyperfine splitting [15]. The number of hyperfine lines is equal to $2nI+1$, where n is the number of symmetry equivalent nuclei and I is the nuclear spin [11]. B_I—the local magnetic field due to the coupling with the nucleus—is dependent upon the type of nucleus as well as the spin density around the nucleus. The larger B_I, the larger the hyperfine splitting is observed.

Hyperfine interactions are either isotropic (independent of the field orientation), or anisotropic [17]. If the unpaired electron is localized in a spherically symmetric s-orbital, the hyperfine coupling will be isotropic. Anisotropic coupling arises from an electron localized in a p-, d-, or f- orbital. Anisotropic hyperfine can appear isotropic if the radical is tumbling rapidly, which is the case for many radicals in solution. The fundamentals of nuclear hyperfine splittings are discussed in the text by Wertz and Bolton [15]. Because hyperfine couplings are related to the spin density of the unpaired electron on an atom, these values are often used to clarify the structure of the paramagnetic species.

2.3 Electron Relaxation Times

In EPR, relaxation is the process of reaching the equilibrium macroscopic magnetization in a given direction [18]. This occurs as a result of interactions between the spin system and its environment [19]. The relaxation time is defined as the time constant for a single exponential signal decay that describes the relaxation. By measuring electron relaxation times, a better understanding of the environment of the spin is obtained.

2.3.1. Spin-lattice relaxation time, T_1.

Also called the longitudinal relaxation time, T_1 is the relaxation time for magnetization along the z-axis, which is defined as the direction of the static magnetic field B_0 [18]. This relaxation process is induced by fluctuating magnetic fields arising from motions in the environment [19]. In solids, longitudinal relaxation is caused by absorption or stimulated emission of phonons. Similarly, in liquids, the fluctuating fields are induced by molecular motion. The rate of spin-lattice relaxation can be related directly to the rate of tumbling in solution as long as the tumbling is below the Redfield limit where the motions are fast enough to average the anisotropic interactions that they modulate. T_1 values are typically measured by inversion recovery and saturation recovery experiments [19]. For more details on spin relaxation see the chapter in Biological Magnetic Resonance by Gareth and Sandra Eaton [20].

An inversion recovery experiment is a three pulse sequence that measures T_1 directly. First, a 180^o pulse flips the magnetization vector from +z to –z. After a time τ_1 (that is variable), a 90^o pulse is applied to flip the spins into the x-y plane. The spins are allowed to diphase in the x-y plane and a 180^o pulse is applied to refocus the spins to form a spin-echo. One of the issues with an inversion recovery experiment is that often the time constant obtained from this experiment is a combination of the spin-lattice relaxation time and spectral diffusion. However, with this complication, inversion recovery experiments are currently the most common way to obtain a value for the spin-lattice relaxation time.

In a saturation recovery experiment, the first pulse is a long lower power pulse that saturates the spin system [21]. CW, FID, or echo can be used to monitor the recovery. The purpose of the long low power pulse is to eliminate spectral diffusion.

2.3.2 Spin-spin relaxation time, T_2.

Also called the transverse relaxation time, T_2 is the relaxation time in the x-y plane, which is defined to be perpendicular to the static magnetic field, B_0 [18].

Transverse relaxation does not require an exchange of energy with the environment, but does require interaction with the environment so that the dynamics of the spins are no longer coherent. This interaction includes the exchange of energy between spins. The phase memory time (T_m) is associated with the decay of the coherence in a spin echo experiment. The T_m label is sometimes used interchangeably with T_2, however there may be other contributions to T_m such as from instantaneous diffusion (phenomenon that spins with the same resonance frequency before the microwave pulse can have different resonance frequencies after the pulse) that do not correspond to spin relaxation.

If a line is homogeneously broadened, the T_2 can be determined from the slow-scan CW linewidth (Equation 2.3)

$$\Delta B_{pp} = \frac{2}{\sqrt{3}\gamma T_2} = \frac{6.56x10^{-8}(G\cdot s)}{T_2(s)} \tag{2.3}$$

where ΔB_{pp} is the slow-scan peak-to-peak linewidth and γ is the gyromagnetic ratio. In many EPR samples, unresolved hyperfine splitting contribute to the linewidth. In these cases, the spectra are said to be inhomogeneously broadened. Equation 2.3 does not apply to inhomogeneously broadened lines.

In a typical spin echo experiment to measure T_2, the pulse sequence is a 90° ($\pi/2$) microwave pulse, followed at time τ_1 later, by a 180° (π) microwave pulse. The application of the 90° pulse rotates the magnetization vector into the x-y plane in the direction perpendicular from B_1. After the first pulse the spins begin to lose coherence due to differences in the frequencies at which the spins are precessing. The second pulse rotates the spins 180^o forming an echo signal after an additional time τ_1. This 2-pulse spin echo experiment measures losses of net magnetization in the x-y plane. The time constant associated with the loss of the net magnetixation in the x-y plane is the phase-memory relaxation time or T_m. T_m is measured by monitoring the decay of the spin echo amplitude as a function of τ_1. T_m values that are measured by spin-echo experiments are often reported interchangeably as T_2.

Spectral Diffusion Time, T_D. is a term that includes all processes that move the spin magnetization between positions in the EPR spectrum (Eaton and Eaton, 2000). Some examples of spectral diffusion processes include: motion of an anisotropic center, electron-electron exchange, and nuclear spin-flops. Spectral diffusion makes an especially large contribution when the lines in a spectrum overlap.

T_2.* (pronounced "T-two-star") is the time constant associated with all broadening mechanisms that contribute to the linewidth including inhomogeneous broadening. T_2* can be measured as the time constant associated with the overall damping of a free induction decay (FID) of the spin system response to a pulse.

2.4 Power Saturation Experiments.

Signal intensity is directly proportional to B_1 (the amplitude of applied magnetic field from the microwave source) if the signal is not saturated [22]. The saturation of an EPR signal is dependent upon the relaxation times (T_1 and T_2).

To understand power saturation, the steady-state solutions to the Bloch equations should be considered. There are three distinct frequencies in an EPR experiment: the frequency of the resonator (ω_{res}), the source frequency (ω_0), and the Larmor frequency (ω_L). The Larmor frequency is the frequency of the precession of the spins in the presence of the static magnetic field, B_0 (Equation 2.4).

$$\omega_L = \gamma B_0 \tag{2.4}$$

At resonance, the source frequency (ω_0) is equal to the Larmor frequency (ω_L). The vector model is often used to describe spin dynamics. The Bloch equations are a set of equations that describe the macroscopic electron magnetization vectors as a function of time relative to T_1 and T_2. Equations 2.5–2.7 are the steady-state solution of the Bloch Equations, that can be applied to a situation such as CW EPR [23] .

$$M_x = \frac{\omega_1 T_2^{\,2} \delta\omega}{1 + \omega_1^2 T_1 T_2 + (T_2 \delta\omega)^2} M_0 \tag{2.5}$$

$$M_y = \frac{\omega_1 T_2}{1 + \omega_1^2 T_1 T_2 + (T_2 \delta\omega)^2} M_0 \tag{2.6}$$

$$M_z = \frac{1 + T_2^{\,2} \delta\omega}{1 + \omega_1^2 T_1 T_2 + (T_2 \delta\omega)^2} M_0 \tag{2.7}$$

where $\omega_1 = \gamma B_1$, $\delta\omega = (\omega_0 - \omega_L)$, and M_0 is the equilibrium magnetization along the z-axis in the absence of excitation ($B_1=0$). At resonance (when the Larmor frequency equals the source frequency, or $\delta\omega = (\omega_0 - \omega_L) = 0$), the equations are simplified in the following manner (Equation 2.8–2.10):

$$M_{x,res} = 0 \tag{2.8}$$

$$M_{y,res} = \frac{\omega_1 T_2}{1 + \omega_1^2 T_1 T_2} M_0 \tag{2.9}$$

$$M_{z,res} = \frac{1}{1 + \omega_1^2 T_1 T_2} M_0 \tag{2.10}$$

At resonance, the magnetization along the x-axis goes to zero. The component along the y axis is the largest. Power saturation can be understood from the Bloch equations. If B_1 is too large (i.e. the power is too high), M_y and M_z approach zero, thus the signal intensity decreases.

The populations of the two spin states (spin up and down) can be used to understand power saturation. If the applied B_1 is too high, the peak height in the absorption spectrum is decreased due to the reduction in the population difference between the two spin states. This occurs when the rate of energy absorption is comparable to or greater than the rate of relaxation between the two energy levels. For this reason, samples with longer relaxation times saturate at lower powers.

The shape of a power saturation curve is often described by a saturation factor, *s*, which is extracted from equation 2.10 and shown in Equation 2.11.

$$s = \frac{1}{1 + \gamma^2 B_1^2 T_1 T_2} \tag{2.11}$$

where s is the saturation factor, γ is the gyromagnetic ratio, B_1 is the magnetic field from the microwave source, T_1 is the spin-lattice relaxation time, and T_2 is the spin-spin relaxation time. Figure 6.3 is an example of a power saturation curve.

Because of the relationship between the saturation factor and relaxation times, power saturation curves can be measured to determine relaxation times [24]. These power saturation experiments give additional insight into the environment of the spins [25]. Power saturation curves can also be measured to determine the linear response region for a particular sample in a particular spectrometer. To obtain spectra in which the signal is proportional to the number of spins, the power should be selected that is in the linear response region of the power saturation curve. This information allows an experimentalist to select an appropriate power for a particular experiment. In this dissertation, power saturation curves were measured as a method of characterizing each rapid-scan experiment.

Equation 2.11 is useful for describing the saturation behavior for a single spin packet, which can be extended to a homogeneously broadened line. For homogeneous broadening, the energy absorbed from the microwave field is distributed to all the spins and thermal equilibrium of the spin system is maintained through resonance if B_1 is in the linear region. However, in a typical EPR experiment, there is an ensemble of spins that often exhibit inhomogeneous broadening. The Portis group demonstrated that a power saturation curve will have different shapes if the EPR line is a superposition of multiple spin packets. This case is defined as inhomogeneous broadening [22]. Examples of inhomogeneous broadening include hyperfine interactions, anisotropy broadening,

dipolar interaction between spins with different Larmor frequencies, and inhomogeneities in the applied magnetic field. The type of inhomogeneous broadening will result in different shapes of the power saturation curve.

2.5 Determination of Resonator Efficiency

Although the key variable is B_1 a power saturation curve often is plotted as the signal intensity as a function of the square root of power because that is what the spectrometer reads out. Incident power can be converted to B_1 using the relationship $B_1 = \Lambda * \sqrt{P}$. The resonator efficiency, Λ, is the conversion efficiency of incident power to B_1, the microwave magnetic field amplitude at the sample.

The efficiency of the resonator (Λ) can be measured directly by simulating the power saturation curve (using SATMON) [26] if the T_1 and T_2 relaxation times are known. Since Λ is proportional to $\sqrt{Q}$, the value for a particular resonator is dependent on sample size, microwave loss, sample positioning, and resonator tuning. If the resonator efficiency is calculated for a known Q (or quality factor, which will be discussed in further detail in section 3.3), the efficiency at different values of Q can be determined with Equation 2.12 [27]

$$\frac{\Lambda_1}{\Lambda_2} = \left(\frac{Q_1}{Q_2} \right)^{1/2} \tag{2.12}$$

For the ^{15}N-mHCTPO sample, Λ = 0.48 G/$\sqrt{}$watt for the dielectric resonator was determined by simulating a CW power saturation curve with SATMON, a locally-written Fortran program [26]. Table 2.1 is a summary of the resonator efficiencies for the SHQ and dielectric resonator at several different Q values. Measured values matched well

with values predicted by Equation 2.12. These efficiency values were used to convert the power saturation curves in this dissertation to plots of signal intensity as a function of B_1. This allowed for comparison between different instruments such as the EMX and E500T.

Table 2.1. Summary of resonator efficiencies for a variety of samples. The Q for the E500-T resonator was measured with the pulser circuit [28].

Resonator	Sample	Q	Efficiency (G/sqrt(Watt))
Dielectric-E500	Empty-Bruker	4000	4.0[a]
	Empty-I measured	9000	3.8[c]
	mHCTPO sample	150	0.48[b]
	1 Capillary Tube H_2O	835	1.1[c]
	3 Capillary Tube H_2O	325	0.7[c]
	Hydrogenated Si	9000	3.8[c]
	Diamond w/ water	400	0.8[c]
	$N@C_{60}$ w/water	250	0.6[c]
EMX-SHQ	Empty-Bruker	7500	2.0[a]
	Empty	9000	2.0[b]
	1 Capillary Tube H_2O	3000	1.2[c]
	3 Capillary Tube H_2O	1000	0.7[c]

[a]Efficiency as reported by Bruker in manual provided with resonator.
[b]Efficiency measured by simulating power saturation curve with SATMON program.
[c]Scaled efficiencies based on the ratio of the square root of the Q values.

Chapter 3: Introduction to Rapid-scan EPR

3.1 Background of Rapid-Scan EPR

Rapid-scan EPR is analogous to rapid-scan NMR experiments that were first performed by Bloembergen, Purcell, and Pound [5]. In these experiments transient effects in the form of "wiggles" were observed after the magnetic field passed through resonance and attributed to relaxation effects [4]. Later, it was shown that these lineshape distortions observed as "wiggles" could be deconvolved to obtain absorption NMR spectra [29].

Transient "wiggles" also were observed in early EPR experiments, and are an example of "passage effects". The term passage effects has been used in a broader way by Weger to describe various factors that cause traces to give misleading values of linewidth and relaxation times [30]. In the Eaton lab, one use of the term "passage effects" is to describe the distortions in the lineshape that are observed when the magnetic field is scanned through a line in a time that is short relative to T_2. The passage effects may not always be observed if the line is inhomogenously broadened even though the effect occurs for individual spin packets. These distortions are not always observed as wiggles, but still require deconvolution to obtain an undistorted lineshape.

Because there is not enough time for the spins to relax, spins that were previously excited as well as current spins are observed. This is why deconvolution

(Section 3.7) is needed: to decouple time-domain signals from different spin packets into a meaningful magnetic field domain spectrum. In this case, to observe passage effects, the field must be scanned through the line in a time that is short relative to T_2*, which is the relaxation time that describes the overall envelope of lines including inhomogeneous broadening.

The first observation of the wiggle form of passage effects in EPR was by Beeler's research group while studying the sodium line in liquid ammonia [31]. The early literature mainly focuses on the adiabatic passage of electron spins. Adiabatic rapid passage effects were observed early on in irradiated LiF [32, 33]. Weger published an extensive review on passage effects in magnetic resonance, both adiabatic and non-adiabatic [30].

In thermodynamics, if a process has no transfer of heat, it is labeled adiabatic. However, the definition of adiabatic in EPR is slightly different. In EPR, adiabatic passage is when the $|d\delta/dt| << |\gamma B_1|$ where $d\delta$ is the difference between the actual field and the resonance field in units of the magnitude of the oscillating field [34]. In this case, the spins follow the changes in B_1.

Passage effects are not unique to magnetic resonance. This type of phenomenon has been observed in rotational [35] and infrared [36] spectroscopy.

More recently, rapid-frequency-scan EPR was used to study nitroxyl radicals by Hyde's group at 94 GHz [14]. Using trapezoidal and triangular rapid frequency scans, wiggles were also observed in the signal response. Also, rapid-scan has been used in imaging experiments of nitroxyl radicals performed by the National Cancer Institute [37],

although the scans were not fast enough to cause oscillations on the trailing edge of the signals.

In the Eaton lab, rapid-scan EPR was initially investigated at X-band, but effort shifted to VHF (250 MHz) because of growing interest in developing methods for in vivo spectroscopy and imaging [38]. Triangular scans were used to drive the rapid magnetic field scans because of simplicity of hardware and the ability to use Fourier deconvolution to recover slow scan lineshapes from the rapid-scan signals [39]. Initially, rapid-scan EPR was applied to a trityl radical (T_2~11.5 μs) and deoxygenated LiPc (Lithium phthalocyanine) (T_2~2.5 μs) because of the potential of these samples for in vivo oximetry. Because of the relatively long spin-spin relaxation times of these samples, passage effects were observed with scan rates as low as 6 kG/s. These passage effects were simulated to determine T_2 of nitroxyl radicals at VHF [40]. Rapid-scan at VHF was also shown to be a quantitative measurement of spins provided that the system (sample, resonator, spectrometer, gain, etc.) is fully characterized [41].

3.2 Definition of Rapid-Scan EPR

As mentioned in the previous section, the term "rapid-scan" has been applied to a variety of different conditions. In the Eaton lab, the definition of the rapid-scan regime (for field-swept rapid-scan EPR) is that the magnetic field is swept through resonance in a time that is short relative to the electron spin-spin relaxation time (T_2). If T_2* is relatively long, this will result in oscillations in the signal response [42]. The decay of these oscillations is dependent upon the electron spin-spin relaxation time and inhomogeneous envelope (T_2*). Thus, information about the T_2 can be extracted from

simulations of rapid-scan spectra. Rapid-scan spectra can also be deconvolved to obtain the absorption spectra [43].

A vector model is useful when visualizing the physical processes during a rapid-scan EPR experiment. The magnetization vector is the vectorial sum of all of the magnetic moments in the sample. Typically CW EPR experiments are run in a slow-scan linear response regime where the magnetization is tipped by a very small angle [38]. The opposite extreme is a pulse experiment, where pulsed microwaves make a large effect on the orientation of the net magnetization vector (e.g., 90° and 180° pulses). In a rapid-scan experiment, the spins are tipped an intermediate amount.

In a rapid-scan experiment, as the magnetic field is scanned through resonance, the net magnetization vector is turned from the z-axis to include a xy component. The passage effects or wiggles that are observed are due to the oscillation of the xy-component of the magnetization. As mentioned in section 2.4, there are three distinct frequencies in an EPR experiment: the frequency of the resonator (ω_{res}), the source frequency (ω_0), and the Larmor frequency (ω_L). The Larmor frequency is the frequency of the precession of the spins in the presence of the static magnetic field, B_0 (Equation 2.5). At resonance, the source frequency (ω_0) is equal to the Larmor frequency. For magnetic resonance experiments, it is important to understand the rotating frame. In EPR, detection is at the source frequency, so the signal is relative to the reference frequency. In a rapid-scan experiment, B_0 rapidly changes with time and so does the frequency at which the spins precess (Equation 3.1).

$$\omega_L(t) = \gamma B_0(t) \tag{3.1}$$

As the field is swept faster and faster through resonance, the spins begin to precess at a frequency different from the source reference frequency. This difference is observed as the wiggles with accelerating frequency in the rapid-scan signal. The amplitude of the wiggles decay as the magnetization in the x-y plane returns to zero. Figure 3.1 is a depiction of the rapid-scan phenomena. The representation in Figure 3.1 uses the rotating frame of reference, which eliminates the time dependence of the microwave component that is perpendicular to the z-axis. There are two main contributions to the decay of the magnetization in the x-y plane: homogeneous and inhomogeneous broadening. For a line that is purely relaxation determined, the lineshape is Lorentzian, and the magnetization in the x-y plane decays with T_2 as the time constant.

Inhomogeneous broadening occurs when unresolved hyperfine coupling or g anisotropy contributes to the lineshape. When inhomogeneous broadening is present in a sample, the decay of the wiggles is dependent upon T_2^*. When the lineshape is dominated by inhomogenous broadening, it is often Gaussian. Lineshapes may also be intermediate between Lorentzian and Gaussian, and referred to as a Voight lineshape.

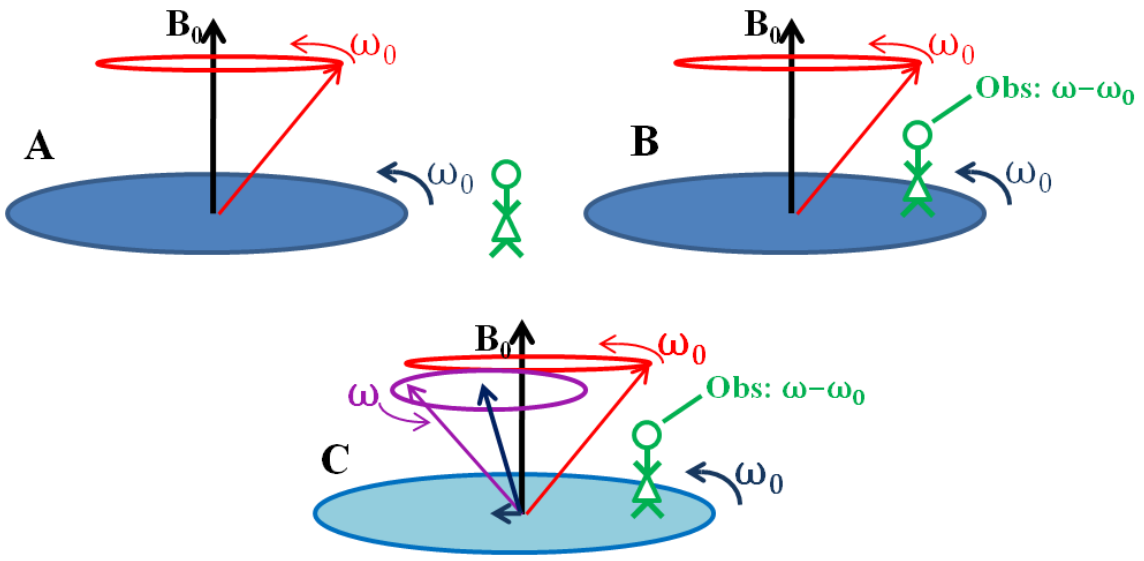

Figure 3.1. Comparison between laboratory and rotating frame of reference for rapid-scan EPR. (A) When the observer is in the laboratory frame of reference (off of the carousel) the frequency observed is the actual frequency the spin is precessing at, which is true at resonance. This figure shows the situation when the source frequency is equal to the Larmor frequency. (B) The observer is now rotating at the source frequency, so the observed frequency of the spin is the difference between the actual frequency at which the spin precesses and the Larmor frequency. (C) In a rapid-scan experiment, the departure from the source frequency is detected.

3.3 Instrumentation of a typical EPR Spectrometer

Basic spectroscopy requires three things: a source of radiation, a sample and a detector [44]. In magnetic resonance, an external magnetic field is also required. X-band (~9 GHz) CW spectrometers are the most common in the field of EPR [17]. All CW spectrometers have a few critical components including: a resonator, microwave bridge to direct the microwaves and to detect the signal, and a magnet to produce external magnetic field [10].

Most current spectrometers use a solid-state source called a Gunn diode. The output power of the microwave source cannot be varied easily [11]. Therefore, a variable

attenuator is important as it allows the microwave power that gets to the sample to be controlled in a precise and accurate way.

Resonators are used to enhance weak signals from the sample [11]. A cavity is a typical resonator in CW EPR, which admits microwaves through an iris [15] that is used to match the resonator to the transmission line and minimize reflection (critical coupling). There are many other common resonator designs including: loop-gap, dielectric, and cross loop. The frequency of the source is tuned to the appropriate resonant frequency of the cavity, which depends on the resonator geometry and the sample. The corresponding resonant wavelengths are related to the dimensions of the resonator. Resonance means that the resonator efficiently stores the microwave energy. Therefore, at the resonant frequency, microwaves remain inside the resonator and are not reflected back when the resonator is critically coupled to the transmission line. Resonators are characterized by their quality factor Q, which indicates how efficiently microwave energy is stored:

$$Q = \frac{2\pi(energy\ stored)}{energy\ dissipated\ per\ cycle} \tag{3.2}$$

As Q increases, the sensitivity of the spectrometer increases because the detected signal increases. The resonator Q can also be expressed in terms of the bandwidth of the resonator (Equation 1.2). Thus, the higher the *Q*, the lower the bandwidth. As will be discussed in detail later, the *Q* is important in rapid-scan EPR, where signals have a larger bandwidth then in CW EPR. The importance of *Q* will be further discussed in section 3.5.

For CW spectrometers, the direct detection of the absorption signal results in low signal to noise (S/N) [15]. To reduce the source noise, the EPR signal is encoded by modulating the magnetic, which results in an alternating signal at the output of the microwave detector. The signal is detected using a lock-in amplifier. The result is a first-derivative spectrum. This type of detection is referred to as phase-sensitive detection. For this type of detection, a modulation frequency and amplitude must be chosen. Phase-sensitive detection is advantageous because it can improve the S/N by several orders of magnitude [11], however, if modulation frequency and amplitude are not appropriately chosen, broadening of the EPR signal can occur. Signal intensity increases as the modulation amplitude is increased. To get the most accurate information about the lineshape, the modulation amplitude should be less than about 10% of the peak-to-peak linewidth. Passage effects may be observed if the modulation frequency is too high relative to $1/T_2$*

3.4 Differences between Rapid-scan and CW EPR

There are several differences between conventional CW and rapid-scan EPR including: signal detection, scan rate, shape of signal, resonator Q, and power saturation. In CW EPR, the modulated magnetic field ($B_0 + B_m cos(2\pi f_m t)$) is swept through resonance slowly relative to the relaxation times (T_1 and T_2), and the signal is detected with phase sensitive detection at the modulation frequency [42]. The magnetic field is modulated at a frequency, f_m.

For CW EPR, the magnetic field is scanned through resonance in a time that is long relative to relaxation times [38]. Conversely, in rapid-scan EPR, the field is swept

through resonance in a time that is short relative to the electron spin-spin relaxation time, the field is not modulated, and the signal is detected directly. If the rate of change of field is faster than the T_2^* then passage effects are observed [45]. The term 'rapid-scan' has also been used to describe scan rates that are faster than in commercial spectrometers. One earlier definition of "rapid" refers to the regime where the inequality 3.5 is satisfied [30].

$$\frac{B_1}{\left(\frac{dB_0}{dt}\right)\left(T_1T_2\right)^{0.5}} < 1 \tag{3.5}$$

In the experiments in this dissertation, rapid-scan is defined as a condition where the field is scanned through resonance in a time short relative to T_2 (Equation 3.6)

$$\frac{LW}{a} < T_2 \tag{3.6}$$

where *LW* is the linewidth of the signal in gauss. When this rapid field scan condition is satisfied, a S/N enhancement is observed. This phenomenon will be discussed in further detail in chapters 6–8. To observe passage effects (wiggles) distorting the absorption spectra, T_2 must be replaced by T_2^* in Equation 3.6.

Rapid-scan signals may have higher frequency components compared with CW, and require a larger resonator bandwidth. In CW EPR, the highest Q consistent with source stability is desired to increase the S/N. Samples that are lossy reduce the Q and are difficult to measure with CW EPR for this reason. However, in rapid-scan experiments, a loss in intensity due to low Q may be compensated by using a faster rate and a larger B_1. Thus, it is often advantageous to study a lossy sample with rapid-scan

EPR rather than CW. For samples that are not lossy, rapid-scan can still be advantageous [46]. If the Q of the resonator is too high, a lossy solvent may be added to lower the Q to prevent distortions in the rapid-scan signal. If a lossy solvent is added to provide enough bandwidth, the overall improvement in S/N with rapid-scan over CW will decrease.

However, having a lower Q, reduces source noise. At low powers, noise is caused by the diode detector, which is not dependent on power. However, at higher powers the main cause of noise is the source, which varies as the square root of power. The power where the transition from noise that is independent of power to dependent on power occurs is a function of Q [47], because the source noise is amplified at higher Q's. Low Q in rapid-scan EPR may be a disadvantage because of the white noise increase that is a result of a larger resonator bandwidth. However, because the Q is much lower, less source noise is observed. The magnitude of the source noise is also dependent on the quality of the source and the first-stage amplifier.

For rapid-scan experiments on the E500T the standard deviation of the noise in the center of deconvolved spectra was measured as a function of source power (Figure 3.2). For three replicate data sets the noise was independent of power below ~50 mW. From 50 to 200 mW there was an increase in noise of about 33%. These results indicate that for powers greater than about 50 mW, the noise is dominated by the source. As resonator Q increases, source noise becomes significant at lower powers [47]. Because a low Q (~150) was used for many of the rapid-scan experiments, the source noise only becomes significant at very high powers. It is important to note, that these results were

obtained with a reflection resonator. Source noise is much less of a problem when a cross loop resonator is used.

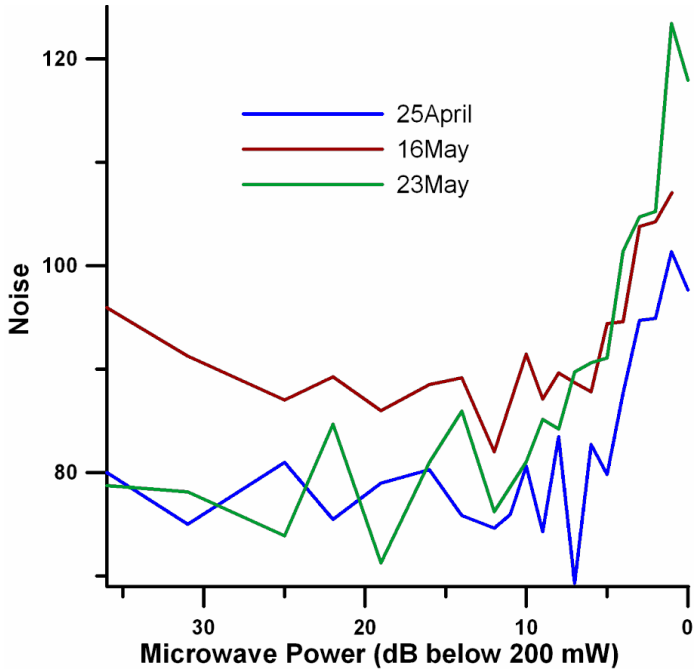

Figure 3.2. Noise as a function of incident power for rapid-scan EPR data collected with a critically-coupled FlexLine ER4118X–MD5 dielectric resonator with Q lowered to ~150. Data were observed at ~4.6 MG/s.

Because the magnetic field is on resonance for a relatively short time in a rapid-scan experiment, the energy absorbed by the spins, for the same microwave B_1, is less than in conventional CW spectra, and the signal does not saturate as readily. The higher the rapid-scan rate, the less time the magnetic field is on resonance, which allows spectra to be run at higher powers without distortion by power saturation. Examples are shown in Section 6.1.4.

3.5 Rapid-scan Hardware

The main difference between the hardware in CW and rapid-scan EPR, is the scan coils and coil driver that are used to create the rapid magnetic field sweep. As mentioned in section 3.7.1, a linear rapid-scan driver was originally used for simplicity in deconvolution. Sinusoidal scans with resonated coils permit wider sweeps at lower scan driver voltages, but only recently the method to deconvolve the passage effects from rapid sinusoidal scans has been developed [43]. Once the method for deconvolving the sinusoidal rapid-scan was developed, the design and construction of a resonated sinusoidal coil driver soon followed [48].

The scan coils are resonated via a circuit (Figure 3.3), consisting of a capacitor (*C*) and an inductor (*L*) also called an *LC* circuit.

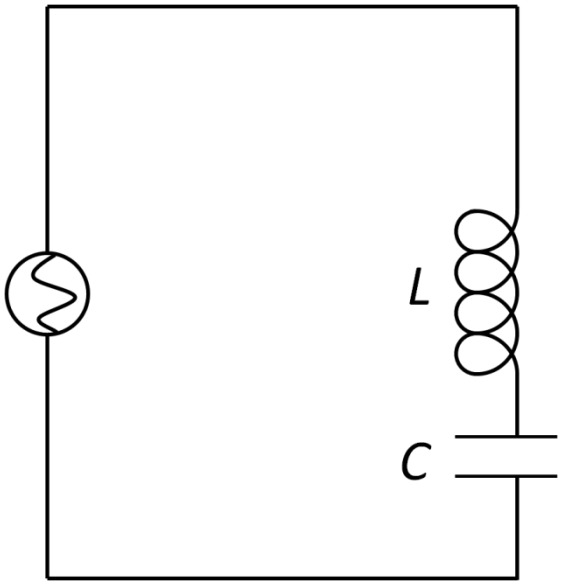

Figure 3.3. Simplified diagram for an *LC* circuit. In the case of the rapid-scan coil driver, the source is the resonated coil driver box, the coils that define the inductance are the scan coils, and the capacitors stand alone in their own box, because of the high voltages present and to make capacitor interchange easy.

An *LC* circuit is the electrical analog of a mass-spring oscillator (University Physics Arfken, 1989, pg 679). The charge on the capacitor in an LC circuit oscillates at a frequency given by Equation 3.7

$$f = \left(\frac{1}{2\pi}\right)\sqrt{\frac{1}{LC}} \tag{3.7}$$

The purpose of an *LC* circuit is two-fold: by resonating the scan coils the reactive components are removed, which allows the coils to be driven with much less voltage and resonating the coils ensures a near-perfect sinusoidal scan, which is necessary for proper deconvolution.

A variety of coils were used with the resonated coil driver, but the best results have been demonstrated by using Litz wire coils. Litz wire coils reduce the skin effect and the proximity effect. The skin effect is the phenomenon that electrical current tends to occupy the surface or "skin" of the wire. Because of this, a large percentage of the solid copper wire goes unused. By using Litz wire (many small wires encased by a larger wire), the total surface occupied by the current increases and the AC resistance decreases. The proximity effect is the phenomenon that coils in close proximity to one another induce eddy currents in each other, which also increases resistance. Thus, Litz wire coils are advantageous because the frequency dependence of the AC resistance is about a factor of 6 lower than for the solid wire coils [48]. This reduction in ac resistance reduces the power dissipated in the coils by a factor of 6, which decreases heating. When used on the X-band iron-core magnet the performance of the Litz wire coils was improved by installing aluminum plates on the poles of the magnet. With the Litz wire coils, sweep widths of up to 60 G at 100% duty cycle are possible. The 100% duty cycles

made possible with the Litz wire coils significantly improved the speed at which data could be collected. With the solid copper coils, a burst mode was used because of heating of the amplifiers in the scan coil driver. In burst mode, the scan coils are driven for only a fraction of the total time, with a wait time between bursts. The ratio of scan time to total time is the duty cycle. In burst mode the scans and the spins must come to equilibrium before the rapid-scan spectrum is collected, which reduces the effective time used for data collection. For a 50% duty cycle the time for data acquisition was only about 5%.

3.5.1. Modifications of standard spectrometer for rapid-scan EPR.

Starting from a bridge equipped for transient recording, very little if any modifications would be required. However, starting from a standard X-band CW spectrometer a high speed dual channel digitizer is required. If there is a signal processing unit (SPU) or SpecJet II in the system either of these will work, but the SPU bandwidth should be increased from the present 30 MHz to at least 60 MHz, preferably 75 MHz. The SPU is somewhat slower than SpecJet II when averaging fewer than 2048 traces, presumably due to data transfer rates. When averaging larger numbers of scans the two digitizers approach the same time efficiency.

A trigger from the modulation drive system to the SPU or SpecJet II is required. If the system has a signal channel module the output on the front panel that is a square wave synchronized to the modulation frequency can be used. Conventionally, the trigger was phased to be at the start of the up-field scan. If the up-down sense is ambiguous a switch could be provided to reverse the scan if it is wrong. The up-field direction can easily be

determined from a simple EPR test. Imagine a single line sample such as LiPc. Typically, a rapid-scan experiment is started with the signal centered at the resonant field so that the up and down scans are equidistant apart (red triangles in Figure 3.4). If the center field is then shifted significantly lower, the up and down scans will shift upward on the sinusoid, represented by the green circles in Figure 3.4. The upfield scans will move to the right, while the down field scans will move to the left. By doing this simple test, it can be determined which scans are upfield and which are downfield.

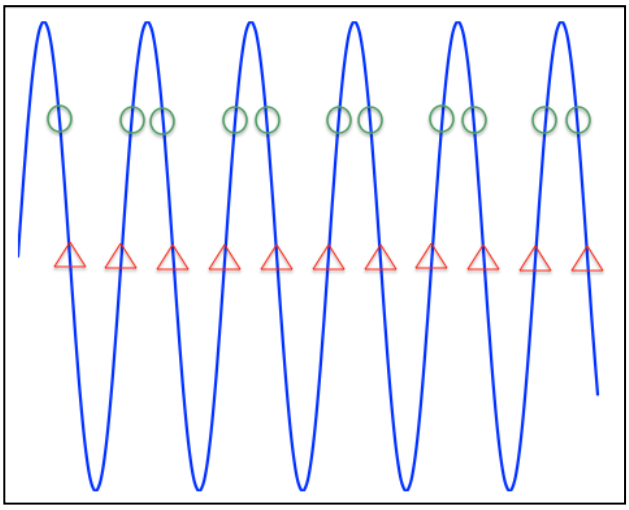

Figure 3.4. Graphical representation of test to distinguish up and down scans. Blue sinusoidal wave represents sinusoidal waveform. Red triangles represent the rapid-scans when the field is centered on the resonant field. When the field is shifted down, the scans move up on the sinusoid (represented by the green circles).

For rapid-scan EPR, a quadrature detection system is required. If starting from a CW-only bridge this will have to be added and provision made to switch it in and out.

A high-bandwidth dual channel video amplifier is required. Preferably the bandwidth would be adjustable in several steps from a few hundred kHz to at least twice

the maximum digitizer sampling rate. An alternative to the video amplifier bandwidth selections would be the use of an external programmable low-pass filter placed between the output of the video amplifier and the input to the digitizer, such as Krohn-Hite model 3995 LP Butterworth dual channel filter. The standard video gains used for pulse EPR in the range of 30 to 66 dB are appropriate. The video amplifier should be AC coupled with a low frequency cut-off of no higher than 20 Hz.

For primary data acquisition and averaging the standard data collection software for SPU or SpecJet II is adequate. However, to deconvolve the RS spectrum to obtain the slow scan spectrum, additional post-processing software is required. In addition, post-processing simulation software is also useful to compare the experimental time-domain data with its simulation.

3.6 Signal and Resonator Bandwidth

Rapid-scan signals may have higher frequency components than CW, and may require a larger resonator bandwidth depending on linewidths, relaxation times, and speed of the rapid-scans. The bandwidth required for a given experiment is based upon the linewidth and the scan rate of the magnetic field (Equation 3.8). To prevent distortion of the rapid-scan signal, a larger resonator bandwidth (lower Q) is required at faster scan rates. Figure 5.4 is an example of spectra collected at several different rates for the same sample.

The signal bandwidth necessary to prevent distortions in the rapid-scan signal can be estimated using Equation 3.8.

$$BW_{signal} = \frac{N \cdot a}{\sqrt{3}\pi\Delta B_{pp}} \tag{3.8}$$

$$a = \pi w f \tag{3.9}$$

where N is a constant often selected to be 5–6 (which accounts for 5–6 lifetimes for T_2^* exponential decay), a is the scan rate in G/s (defined for a sinusoidal scan by Equation 3.9 where w is the width of the scan and f is the scan frequency), and ΔB_{pp} is the peak-to-peak linewidth of the derivative line in gauss. If the signal bandwidth is limited by the choice of parameters such that the oscillations are damped, broadening occurs in the deconvolved line. The bandwidth requirement depends on the extent to which broadening is acceptable.

In practice, a rate is selected for a particular sample that is conservative relative to the rate suggested by Equation 3.8. Because N is a difficult parameter to select a priori, a conservative value for N will be initially selected (such as 10). Data are collected and deconvolved and the rate is decreased until a limiting value for the linewidth is observed. The rate is then increased until a small amount of broadening is observed. At this rate, the highest S/N per unit time will be observed while maintaining linewidth fidelity.

In a rapid-scan experiment, the bandwidth for the spectrometer is typically limited by the resonator bandwidth, which is defined by Equation 1.2. The video amplifier in the bridge could also limit the bandwidth, but this is typically not the case. In this dissertation, most of the rapid-scan data was collected at X-band with either the E580 or the E500T. The E500-T (X-band) and E580 (operated at X-band) have two bandwidth settings in the video amplifier, 20 and 200 MHz.

In a rapid-scan experiment, if B_0 is scanned upfield, the Larmor frequency increases, so the observed frequencies are from the reference to the upper limit of the resonator bandwidth. When the scan is downfield, the observed frequencies are from the reference frequency to the lower limit of resonator bandwidth. Thus, only half of the total resonator bandwidth is available for a given scan direction (see Equation 3.10).

$$BW_{available} = \frac{1}{2} BW_{resonator} = \frac{\nu_{res}}{Q} \tag{3.10}$$

This phenomenon was demonstrated by studying rapid-scan of a trityl signal. CD_3 trityl, which has a T_2~11 μs, and a full-width at half height of 30 mG was chosen to illustrate this concept. The rapid-scan experiment was performed with a scan frequency of 8 kHz, a scan width of 10.0 G, microwave frequency of 256.309 MHz, and a Q~50. Using Equation 3.8 (with an *N* of 5), the signal bandwidth for this experiment is 8.5 MHz. The Q of the resonator is 50, therefore the full bandwidth at 256.309 MHz is 5.12 MHz, and the half-bandwidth is 2.56 MHz. To determine which bandwidth was actually limiting the signal, a Krohn-Hite model 3955 LP Butterworth dual channel filter was used to adjust the bandwidth of the signal to the digitizer. If the bandwidth available to the rapid-scan signal was ~5 MHz, when the bandwidth was decreased below 5 MHz with the Krohn-Hite filter, damping of the signal should be observed. However, if the bandwidth available was ~2.5 MHz, no effect on the spectrum should be observed until the filter bandwidth is lowered below 2.5 MHz.

Rapid-scan EPR signals were measured at Krohn-Hite settings of 8, 5, 4, 3, 2.5, and 2 MHz. No significant difference in the signal between 8, 5, and 4 MHz was observed. When the bandwidth was decreased 3 MHz, a significant difference was

visible. Once the Krohn-Hite was set to less than half bandwidth of the resonator, the signal changed significantly. Figure 3.5 shows the difference between 8, 4, and 2 MHz.

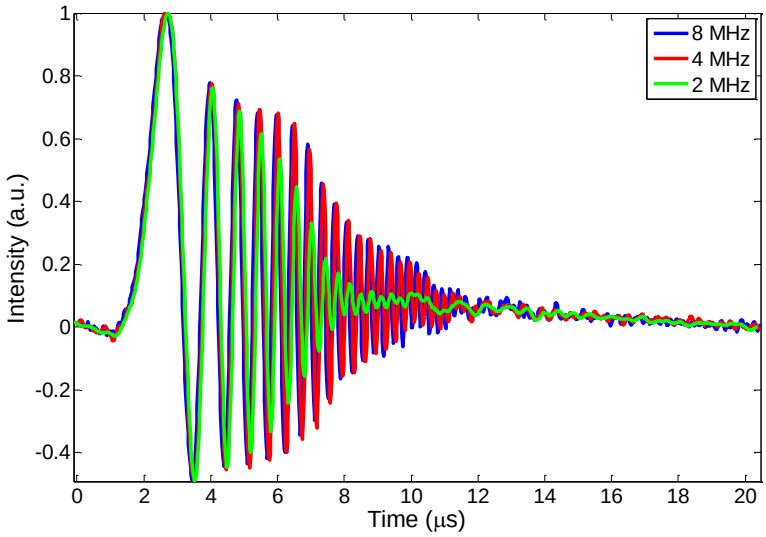

Figure 3.5. Comparison of rapid-scan EPR spectra of the CD_3 trityl radical with Krohn-Hite filter settings of 8, 4 and 2 MHz.

When calculating appropriate rates to run rapid-scan EPR to prevent distortions in the line, the bandwidth available is only ½ the resonator bandwidth (Equation 3.10).

3.7 Rapid-scan Deconvolution

3.7.1. Introduction

In this dissertation, deconvolution refers to the process of extracting a slow-scan conventional spectrum from a rapid-scan spectrum. The triangular deconvolution procedure was developed for experiments where the rapid-scan magnetic field was generated by a linear coil driver [39]. More recently sinusoidal fields have been used to achieve faster rapid-scan rates. These experiments were feasible after the development of the sinusoidal deconvolution procedure by Mark Tseitlin in the Eaton lab.

The rapid-scan signal, after multiplication by the sinusoidal driving function (Equation 3.11) is the convolution (multiplication in the Fourier domain) of the sinusoidal driving function and the absorption spectrum [43]. The driving function is defined by Equation 3.11, which describes how phase of the excitation relative to the waveform changes with time.

$$d_{\sin}(t) = \exp\left\{+j\gamma_e B_m\left[\frac{\sin(2\pi f_m t)}{2\pi f_m}\right]\right\} \tag{3.11}$$

B_m is half the peak-to-peak amplitude of the scan and f_m is the scan frequency. The absorption spectrum is obtained by division in the Fourier domain, followed by reverse Fourier transformation. To have a successful deconvolution, one must know the driving function accurately (including the scan width and frequency).

3.7.2. Calibrating Scan Width

Because an accurate understanding of the driving function is critical to successful deconvolution, the scan width should be calibrated. To calibrate the scan width, several spectra are collected with a sample with a known hyperfine splitting, such as ^{15}N-mHCTPO. The scan width is varied in the deconvolution until the splitting in the deconvolved rapid-scan spectrum matches the known splitting. An alternative method of calibrating the scan width is to step the field off resonance by a known amount (such as 5 G). It the scan width is known correctly, the deconvolved rapid-scan spectrum will be offset by 5 gauss.

Chapter 4: Rapid-scan method testing

One of the main focuses of this project has been to develop the hardware necessary to perform rapid-scan EPR experiments. The instrument design and construction were done by other members of the group including Dr. George Rinard and Richard Quine. This chapter will focus on testing of rapid-scan EPR instruments.

4.1 Q-measurement Circuit

4.1.1. Introduction

Because the EPR signal voltage is proportional to resonator Q [49], it is important to know the Q to do quantitative EPR experiments [11]. As mentioned previously, it is also important to know the Q in rapid-scan EPR. If Q is too high relative to the signal bandwidth, the resonator filters the rapid-scan signals and distorts spectra. Knowing the Q allows accurate, undistorted rapid-scan spectra to be collected.

There are two fundamental methods to determine the Q: by transient decay and by determination of the frequency bandwidth of the resonator [50]. The transient decay method is commonly used in pulsed EPR because the hardware is in place to create pulses and measure the transient response [28]. The analysis of this type of measurement depends on what type of detector is being used. For a crystal detector, the Q is described by Equation 4.1 assuming that the voltage output is linear in microwave power incident on the crystal.

$$Q_L = 2\pi\nu\tau \tag{4.1}$$

where τ is the ring-down time constant and ν is the resonator frequency. For a double-balanced mixer, the output signals are linear in voltage rather than power. The Q measured with a double-balanced mixed is described by Equation 4.2.

$$Q_L = \pi\nu\tau \tag{4.2}$$

Because the decay is a single exponential, only the time for a decay of 1/e needs to be measured to determine the Q [28]. However, if the Q is extremely low, the decay may be difficult to measure accurately due to limits in the response time of the detection device or the oscilloscope.

4.1.2. Methods

This work primarily focused on the testing of the circuit designed and built by Richard Quine. For a complete discussion on the engineering of this instrument, see Quine's [28] paper.

The power ring-down signal was collected via a LeCroy scope for a critically coupled resonator with several different Q settings from 100–1800 (Figure 4.1). These Q values were achieved by introducing different amounts of a lossy solvent (water) into the resonator in an EPR tube. The ring-down signal was also collected for different coupling settings such as critically and over-coupled (Figure 4.2). In figure 4.2, the full width of the pulse is displayed. The four traces show the change in the reflected power as a function of Q and coupling. To measure Q, the response at the end of the pulse is analyzed (Figure 4.1).

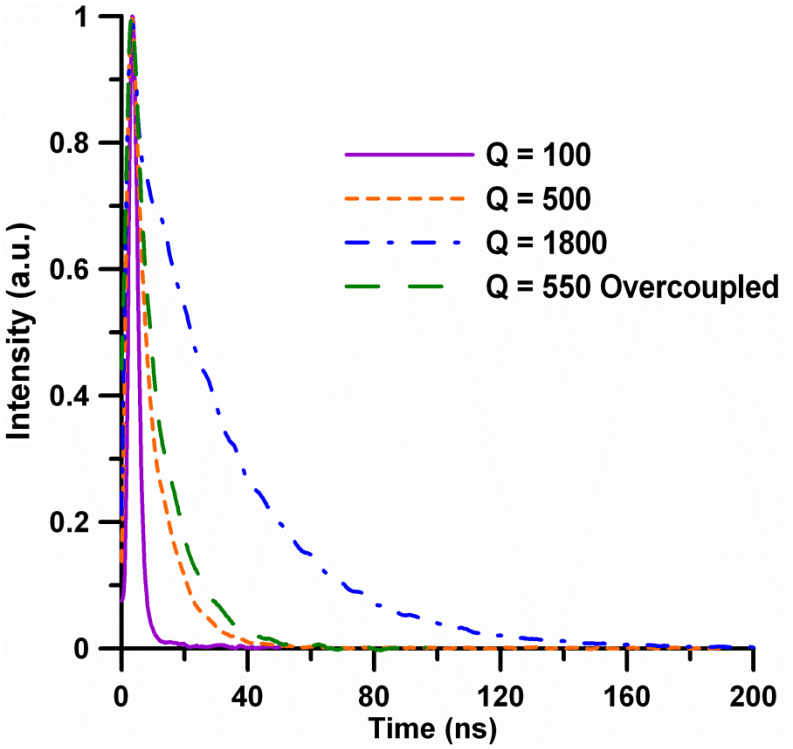

Figure 4.1. Reflected power ring-down for several Q settings, zoomed in on the end of the pulse. Reflected power ring-down signal obtained with the circuit in the X-band E500T bridge. **(fuchsia line)** Critically coupled resonator with a 0.16 mm tube of water added to the resonator (Q ≈ 100). **(orange dashed)** Critically coupled resonator with a 0.8 mm tube of water added to the resonator (Q ≈ 500). **(blue dashed)** Critically coupled resonator with a non-lossy sample in the resonator (Q ≈ 1800). **(green dashed)** Over coupled resonator with non-lossy sample in the resonator (Q ≈ 550). These waveforms were obtained at a spectrometer power attenuation setting of 15 dB where 0 dB is ca. 200 mw (+23 dBm).

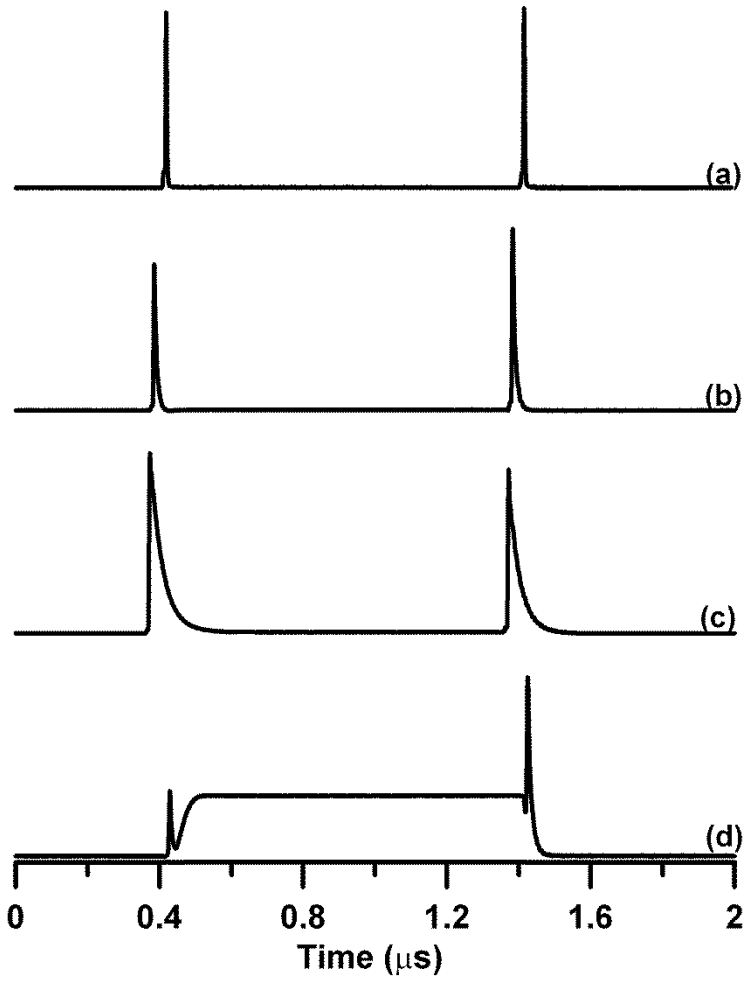

Figure 4.2. Reflected power ring-down signal obtained with the circuit in the X-band E500T bridge. **(a)** Critically coupled resonator with a 0.16 mm tube of water added to the resonator (Q ≈ 100). **(b)** Critically coupled resonator with a 0.8 mm tube of water added to the resonator (Q ≈ 500). **(c)** Critically coupled resonator with a non-lossy sample in the resonator (Q ≈ 1800). **(d)** Over coupled resonator with non-lossy sample in the resonator (Q ≈ 550). These waveforms were obtained at a spectrometer power attenuation setting of 15 dB where 0 dB is ca. 200 mw (+23 dBm).

4.1.3. Discussion

The measured Q values matched up with the value of Q necessary to simulate distorted rapid-scan spectra at higher Q values (>150). However, at lower Q values, some discrepancies were observed. These discrepancies were attributed to the limitations

in the oscilloscopes measuring the ring down. An apparent ring-down time constant of 1.2 ns was observed when measuring an open circuit (no resonator connected) with a 400 MHz bandwidth oscilloscope and 0.83 ns with a 500 MHz scope. This indicates that measurements of resonators with a ring-down time constant of less than 2.5 ns (Q~150 at X-band) would not give an accurate Q.

This circuit can also be used as an aid for tuning the resonator. Figure 4.2 a–c shows that when the resonator is critically coupled, the center of the pulse is nearly at the baseline (i.e. no reflected power). This type of pattern can be achieved by adjusting both the coupling and microwave frequency.

4.2 Determining best Resonator and Rapid-scan Coils

4.2.1. Introduction

Developing rapid-scan EPR at X-band has required experimentation with several different set-ups. Initially, the coils in an ENDOR resonator were used to achieve very high scan rates (up to 1 GG/s) to study α,γ-bisdiphenylene-β-phenylallyl (BDPA) and 2,2-diphenyl-1-picrylhydrazyl (DPPH) (Chapter 5). A critically-coupled Bruker ER4118X-MD4 pulse ENDOR resonator was rotated such that the field resulting from the ENDOR coils was parallel to the B_0 magnetic field [51]. This set up worked well for a sample that was very small and point-like. However, for more extended solution samples, larger coils are required to achieve a homogeneous field throughout the sample. In this section, some of the different coils and resonators that were tried to determine the best set up will be discussed.

Rapid-scan (RS) EPR can be done using standard cavity modulation coils and the standard CW modulation coil driver. However, certain limitations will apply, and some modifications to a standard CW spectrometer will be needed, as outlined below.

4.2.2. Methods

^{15}N-mHCTPO sample. ^{15}N-mHTCPO (4-hydro-3-carbamoyl-2,2,5,5-tetra-perdeuteromethyl-pyrrolin-1-^{15}N-oxyl-d_{12}) was used routinely for testing of different hardware. This nitroxyl radical was prepared as previously described [52] and provided by Prof. Halpern (University of Chicago). A solution of 0.1 mM ^{15}N-mHTCPO in 80/20 v/v Ethanol/water was placed in a 4 mm o.d. x 3 mm i.d. quartz tube, and had a height of 3 mm, resulting in a 3x3 mm cylindrical shape, which gave a resonator Q ~150. The sample was degassed by performing six freeze-pump-thaw cycles and then was flame sealed. This concentration is in a range where the contribution to relaxation from collisions is very small [1].

4.2.3. Results and Discussion

Comparison of standard modulation coils with extended coils. There are limitations in the use of standard Bruker modulation coils and drivers for rapid-scan EPR due to the small size of these coils. Standard modulation coils are about 25 mm diameter; this limits the homogeneous field region produced by the coils. Considerable distortion in rapid-scan spectra taken with standard modulation coils was observed for extended samples. Figures 4.3–4.6 and the following discussion illustrate this problem.

For scan width control and calibration, the standard automated method of resonating and calibrating the modulation coils is probably adequate (section 3.7), but it

should be noted that precise knowledge of the scan rate is required for accurate deconvolution of the RS spectrum.

Dielectric resonator with Bruker modulation coils. The rapid-scan time-domain spectrum of the low field line for 0.1 mM ^{15}N-mHCTPO in 80/20 ethanol/water solution in the dielectric resonator with resonated modulation coils at ~29 kHz with ~30 G scan width is shown in Figure 4.3A. Good agreement between the pseudomodulated-deconvoluted rapid-scan spectra with the CW spectrum was observed for the low-field line (see Figure 4.3 C, D) but not for the full spectrum (Figure 4.4 B, C). The broadening observed in Figure 4.4 B is most likely a result of the sample size relative to the size of the modulation coils because the field may not be homogeneous over the sample.

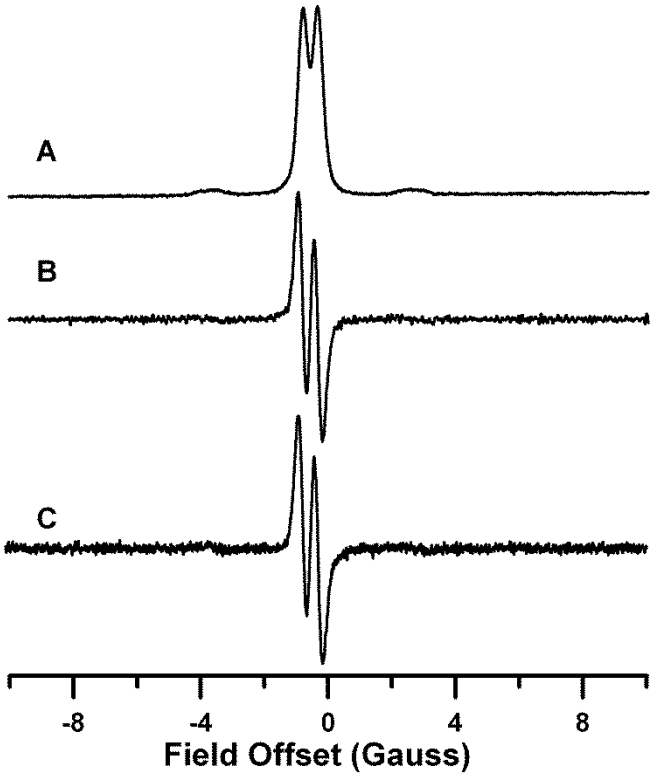

Figure 4.3. Comparison of deconvolved rapid-scan and CW spectra of the low-field line for a 3mm ^{15}N-mHCTPO sample, obtained with standard modulation coils. (A) Deconvolved rapid-scan spectrum of 0.1 mM mHCTPO solution with 20 G scan width, and 29.7 kHz scan frequency. 1024 averages were collected with resonator Q~150 and 2 mW power (0.02G B_1). (B) First derivative spectrum obtained by pseudomodulation of the signal in A. (C) Single scan of a field-modulated first-derivative CW EPR spectrum of the same sample.

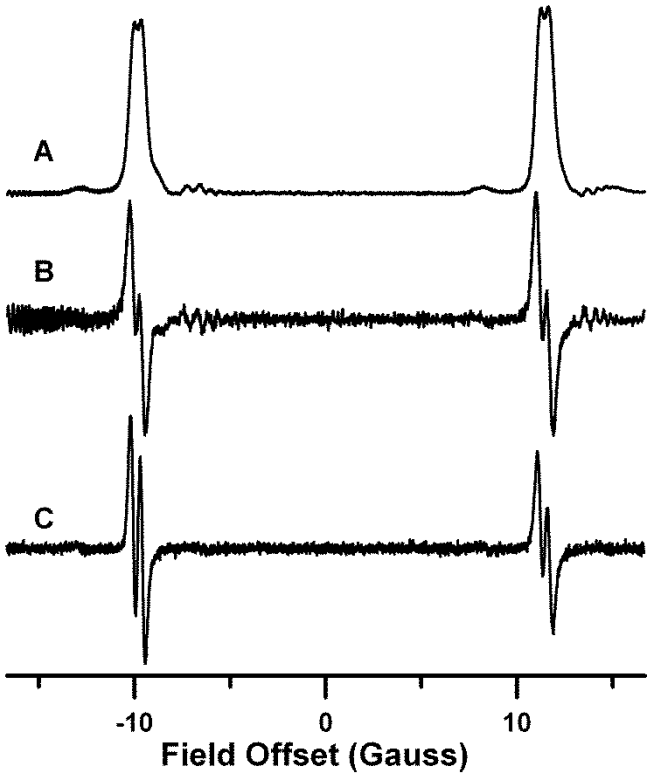

Figure 4.4. Comparison of deconvolved rapid-scan and CW spectra of 3 mm ^{15}N-mHCTPO sample, obtained with standard modulation coils. (A) Deconvolved rapid-scan spectrum of 0.1 mM mHCTPO solution with 55 G scan width, and 29.7 kHz scan frequency (~5.1 MG/s). 1024 averages were collected with resonator Q~150 and 2 mW power (0.02G B_1). (B) First derivative spectrum obtained by pseudomodulation of the signal in A. (C) Single scan of a field-modulated first-derivative CW EPR spectrum of degassed 0.2 mM mHCTPO solution. 40 G sweep width, 0.05 G modulation amplitude.

Dielectric resonator with larger external coils. The rapid-scan spectrum of the low-field line for the same 3 mm 0.1 mM mHCTPO as previously described is shown in Figure 4.6A. This is a better experimental set up, that does not cause as much broadening. Good agreement is observed between the pseudomodulated-deconvoluted rapid-scan spectrum with the CW for the low-field line (Figure 4.5 C,D) and for the full spectrum (Figure 4.6 A,B).

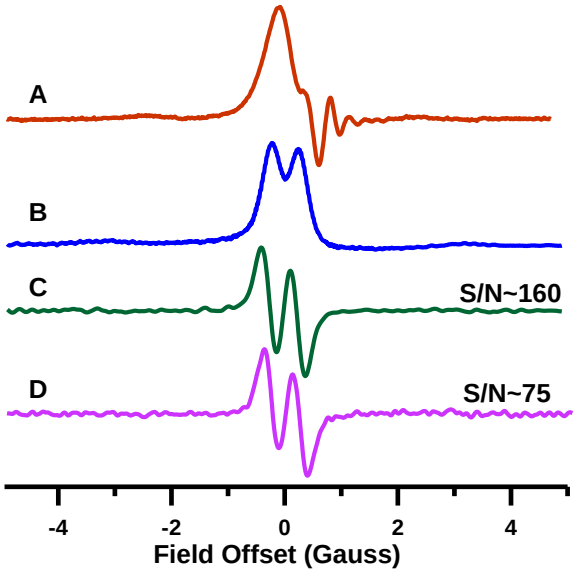

Figure 4.5. Comparison of rapid-scan and conventional CW EPR spectra of a 3mm 0.1 M mHCTPO sample. Magnetic field scans were from low field to high field using 9.5 cm external coils. (A) As-recorded sinusoidal rapid-scan signal obtained with a scan rate of 1.8 MG/s. 1024 averages were recorded in about 0.9 seconds using SpecJet II. The incident microwave power was about 80 mW (0.14 G B_1). (B) Slow-scan absorption spectrum obtained by deconvolution of signal in A. (C) First derivative spectrum obtained by pseudomodulation of the signal in B. (D) Single scan of a conventional field-modulated first-derivative CW EPR spectrum of the same sample, obtained in 0.9 sec using about 5 mW incident microwave power, 10 kHz modulation frequency and 0.13 G modulation amplitude. Modulation amplitude, power, and filter were chosen to maximize signal while allowing less than 2% broadening of the linewidth. Operated with a 50% duty cycle.

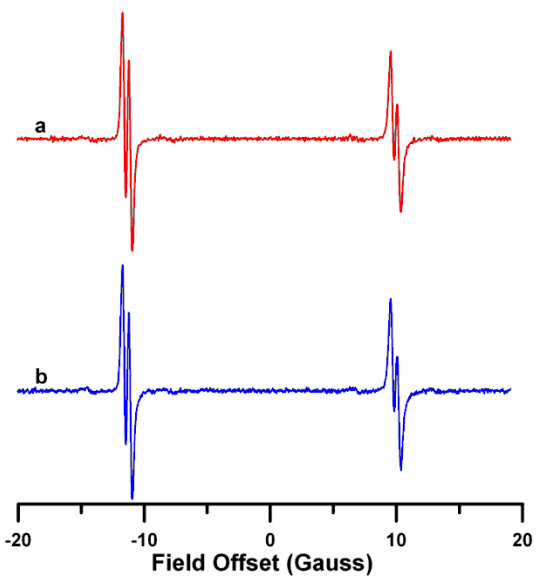

Figure 4.6. Comparison between pseudomodulated, deconvolved rapid-scan and slow scan spectrum of degassed 0.1 mM mHCTPO solution. (a) CW spectrum. 40 G sweep width, 0.05 G modulation amplitude, 5 mW microwave power. (b) Pseudomodulated, deconvolved rapid-scan spectra of a degassed 0.1 mM mHCTPO solution with 55 G scan width, and 29.7 kHz scan frequency (~5.1 MG/s). 1024 averages were collected with resonator Q~150 and 2 mW power (0.02G B_1).

The data shown in Figures 4.4 and 4.6 were obtained with about the same frequency and sweep width. The only difference was the size of the coils that were used to create the rapid magnetic field scans. The improvement in resolution observed with the external coils is attributed to the size of the coils. The 9.5 cm external circular coils are large relative to the sample size, creating a more homogenous field over the sample.

There are hardware limitations on the maximum scan rates. For Bruker modulation coils, the maximum field available from the standard system is 40 Gpp at 100 kHz, which produces a maximum scan rate of about 12.5 MG/s. For narrow lines and long T_2* this is fully adequate. However, for short T_2* and broad lines it may not be adequate to reach the RS regime.

Although the standard modulation coils themselves are robust enough to handle 40 Gpp continuously, their proximity to the resonator can sometimes cause r.f. tuning drift when run continuously due to heating of the resonator assembly. Since the power goes down as the square of the ratio of a reduction in sweep width this limitation only occurs at the very highest sweep widths.

R.F. drift begins to occur at about 1 W in the modulation coils or about 20 Gpp at 100 kHz. Because the a.c. resistance is less at lower frequencies the coils dissipate less power at the same sweep width for lower frequencies.

Dielectric resonator with Litz wire external coils. The Litz wire coils greatly improved the speed of data collection by allowing operation of 100% duty cycles. Figure 4.7 shows the rapid-scan of mHCTPO when using the Litz wire coils (section 3.4). The agreement between CW and the derivative of the deconvolved rapid-scan spectrum is good.

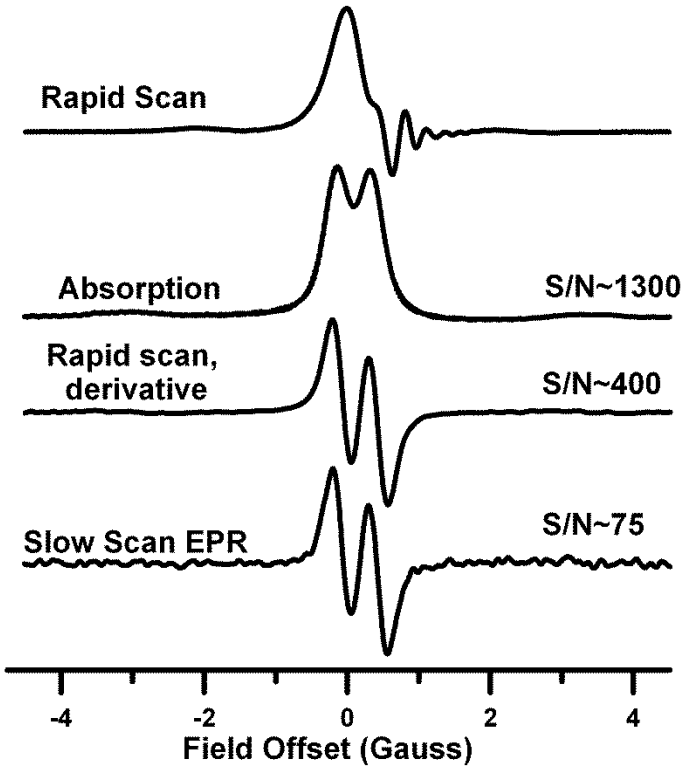

Figure 4.7. Comparison of rapid-scan and conventional CW EPR spectra of the low-field nitrogen hyperfine line of ^{15}N-mHCTPO collected with Litz wire coils at 100% duty cycle. (Rapid-scan) As-recorded sinusoidal rapid-scan signal obtained with a scan rate of 1.8 MG/s and microwave power about 80 mW (B_1= 0.14 G). 12000 averages were recorded in about 0.9 sec. (Absorption) Slow-scan absorption spectrum obtained by deconvolution. (Rapid-scan, derivative) First derivative. (Slow Scan EPR) Single scan of a conventional field-modulated first-derivative CW EPR spectrum of the same sample, obtained in 0.9 sec using 5 mW power, 10 kHz modulation frequency and 0.13 G modulation amplitude. Modulation amplitude, power, and filter were chosen to maximize signal amplitude with less than 2% broadening.

Conclusions. Currently, the best set up for X-band rapid-scan experiments is with the external Litz wire coils with the dielectric resonator. This allows for the most homogeneous field across the sample, and the Litz wire coils allow higher sweep rates to be achieved at 100% duty cycle.

4.3 Testing of Sinusoidal Coil Driver

4.3.1. Introduction

Sinusoidal scans allow rapid-scan to be run at faster scan rates than with linear (triangular) rapid field scans. This is because the amplifier power requirements for the electronics are lower for sinusoidal scans with resonated coils than with linear scans [48]. Because the scan rate changes during the scan, the deconvolution for sinusoidal rapid-scan EPR is more complicated than for linear rapid-scan. The sinusoidal deconvolution procedure was developed in the Eaton lab [43], which permitted routinely acquiring and analyzing sinusoidal rapid-scan EPR. For the sinusoidal deconvolution procedure to work properly, one must accurately know the driving function (the function that describes the rapid magnetic field scan). Therefore, a lot of effort went into determining how accurately sinusoidal the scans were.

Section 3.4 introduced the basics of the hardware for the rapid-scan coil driver that was developed. Richard Quine developed and built the coil driver while my primary efforts were to test different coil drivers and rapid-scan coils to determine ways to improve the experiment. For a full discussion on the electrical engineering and design see the paper that gives a full description of the coil driver that is denoted as RCD3 [48].

4.3.2. Methods

Samples. The ^{15}N-mHCTPO sample was the same 3 mm 0.1 M sample as previously described (section 4.2.2). The jitter of the coil driver was tested with a small LiPc sample. A very strong LiPc sample was chosen, so that good signal-to-noise (S/N) would be achieved with just one scan. 2-D experiments were set up so that 50 spectra

were collected consecutively. This experiment was performed at several different sweep widths.

Spectroscopy. Rapid-scan signals were collected on a Bruker custom E500T X-band spectrometer. Signal acquisition was via a Bruker signal processing unit (SPU) for CW spectra and a SpecJetII fast digitizer for rapid-scan signals. A critically-coupled FlexLine ER4118X–MD5 dielectric resonator was used to minimize eddy currents induced by the rapidly-changing magnetic fields. The pulse ring down method described in section 4.1 was used to measure the resonator Q. The waveform was measured with a Tektronix model AM-503 current probe and was simulated with a sine wave.

4.3.3. Results and Discussion

Before the final version of the resonated coil driver was built (RCD3), several earlier versions were tested (RCD1 and RCD2). Initially, there was an unknown source of EPR signal broadening that was assigned to jitter, based on the following results. The larger sweep width, the larger the discrepancy between the RCD1 and RCD2 that was observed (Figure 4.8 and 4.9 A–C). The standard deviations are summarized in Table 4.1. The standard deviations were also measured with spectrometer AFC both ON and OFF. Little difference in standard deviation was observed when the ACF was turned off.

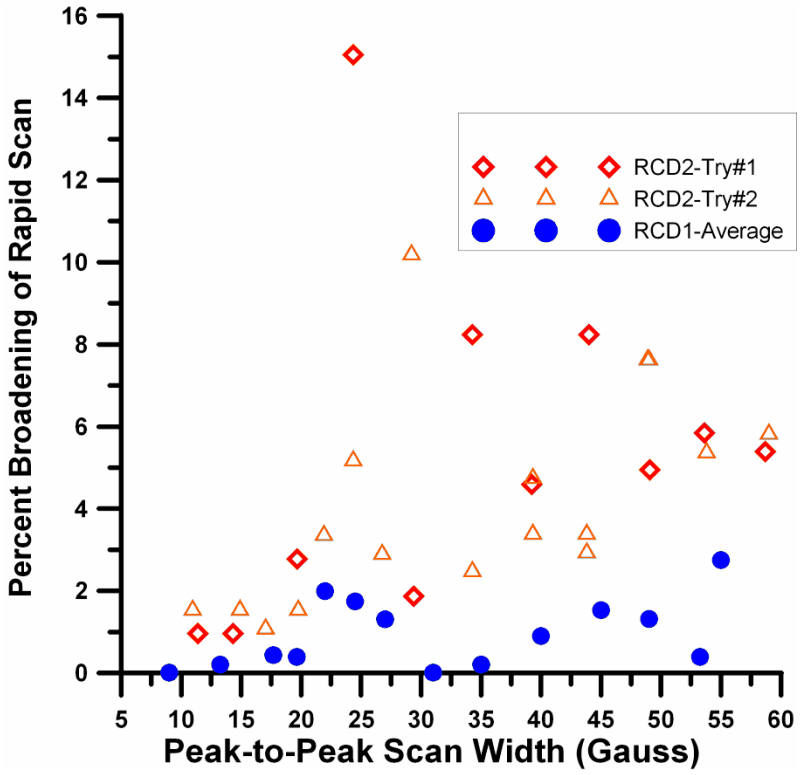

Figure 4.8. Percent broadening of deconvolved pseudomodulated rapid-scan spectrum of the low field line of ^{15}N-mHCTPO when compared to the CW spectrum. Broadening was measured as a function of sinusoidal scan width obtained with RCD1 or RCD2. For every data point, the resonance was centered in the sinusoidal scan.

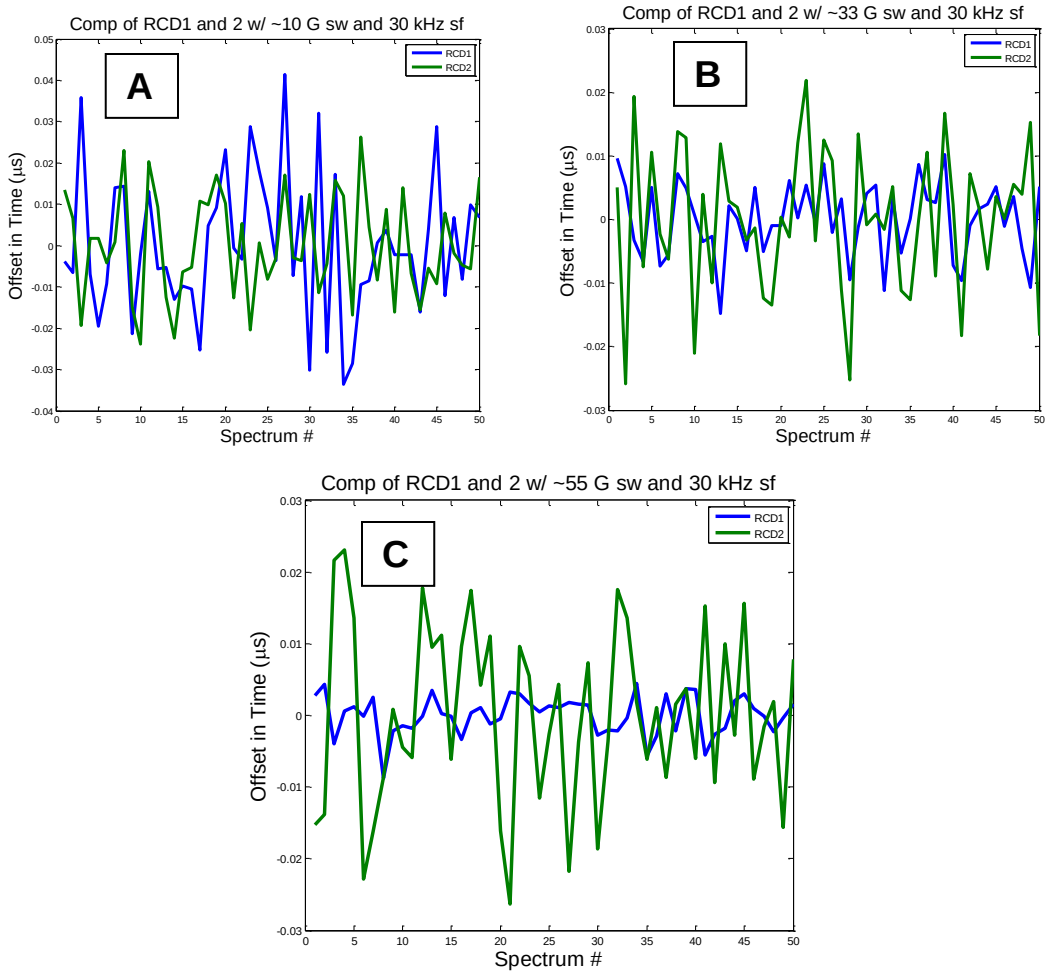

Figure 4.9. Comparison of position offset of rapid-scan spectrum (from mean position) between RCD1 and RCD2 for a deoxygenated LiPc sample at 3 different sweepwidths. 2-D rapid-scan data were collected with 3430 G center field, 30 kHz scan frequency, and (A) ~10 G scan width (scan rate ~1 MG/s), (B) ~33 G scan width (scan rate ~3 MG/s), (C) 55 G scan width (scan rate ~1 MG/s). Spectra were collected consecutively. For each individual spectrum, a single scan was collected with resonator Q~200 and 33dB power.

Table 4.1. Comparison of standard deviation of position of resonance of LiPc at several different settings of sweep width. Standard deviations in time were multiplied by the rate to get a standard deviation in gauss.

Sweep Width (Gauss)	RCD1-stdev (mG)	RCD2-stdev (mG)
10 (AFC ON)	17	11
33 (AFC ON)	20	33
33 (AFC OFF)	17	30
55 (AFC ON)	18	66
55 (AFC OFF)	23	67

There is more jitter in the signal position for the early model of RCD2 at higher sweep widths than RCD1. The apparent jitter of the resonance position could be due to either horizontal time jitter, vertical amplitude jitter of the scan voltage, or both.

To distinguish between these two types of jitter, data were collected with (i) resonance positioned at the center field and (ii) a center field offset (roughly 2/3 of the half sweep width away from the center field). For RCD1, the standard deviation increased with offset, indicating that the jitter may be due to vertical amplitude jitter (Figure 4.10 A–C). However, for RCD2, no dependence of the standard deviation with offset was observed (Figure 4.11 A–C). These comparisons showed that the jitter observed for RCD2 is mainly due to horizontal time jitter. The standard deviations measured are summarized in Table 4.2.

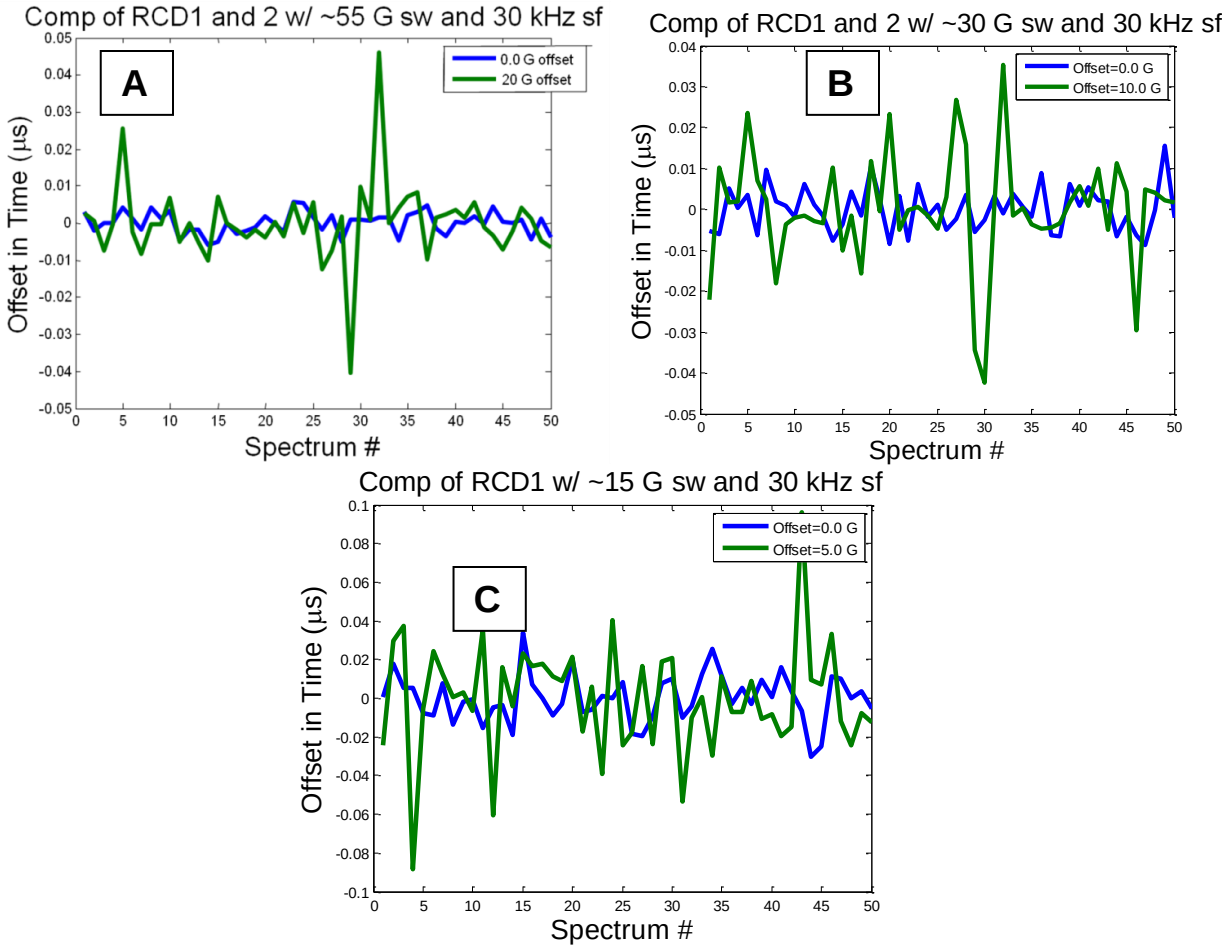

Figure 4.10. Comparison of position offset of rapid-scan spectrum (from mean position) for (i) the line centered in the scan and (ii) offset by 2/3 of the amplitude of the half sweep width for RCD1 with a deoxygenated LiPc sample at 3 different sweepwidths. 2-D rapid-scan data were collected with 3430 G center field and offsets shown in individual panels, 30 kHz scan frequency, and (A) ~55 G scan width (scan rate ~5.5 MG/s), (B) ~33 G scan width (scan rate ~3 MG/s), (C) 15 G scan width (scan rate ~1.5 MG/s). Spectra were collected consecutively. For each spectrum, 1 scan was collected with resonator Q~200 and 33dB power.

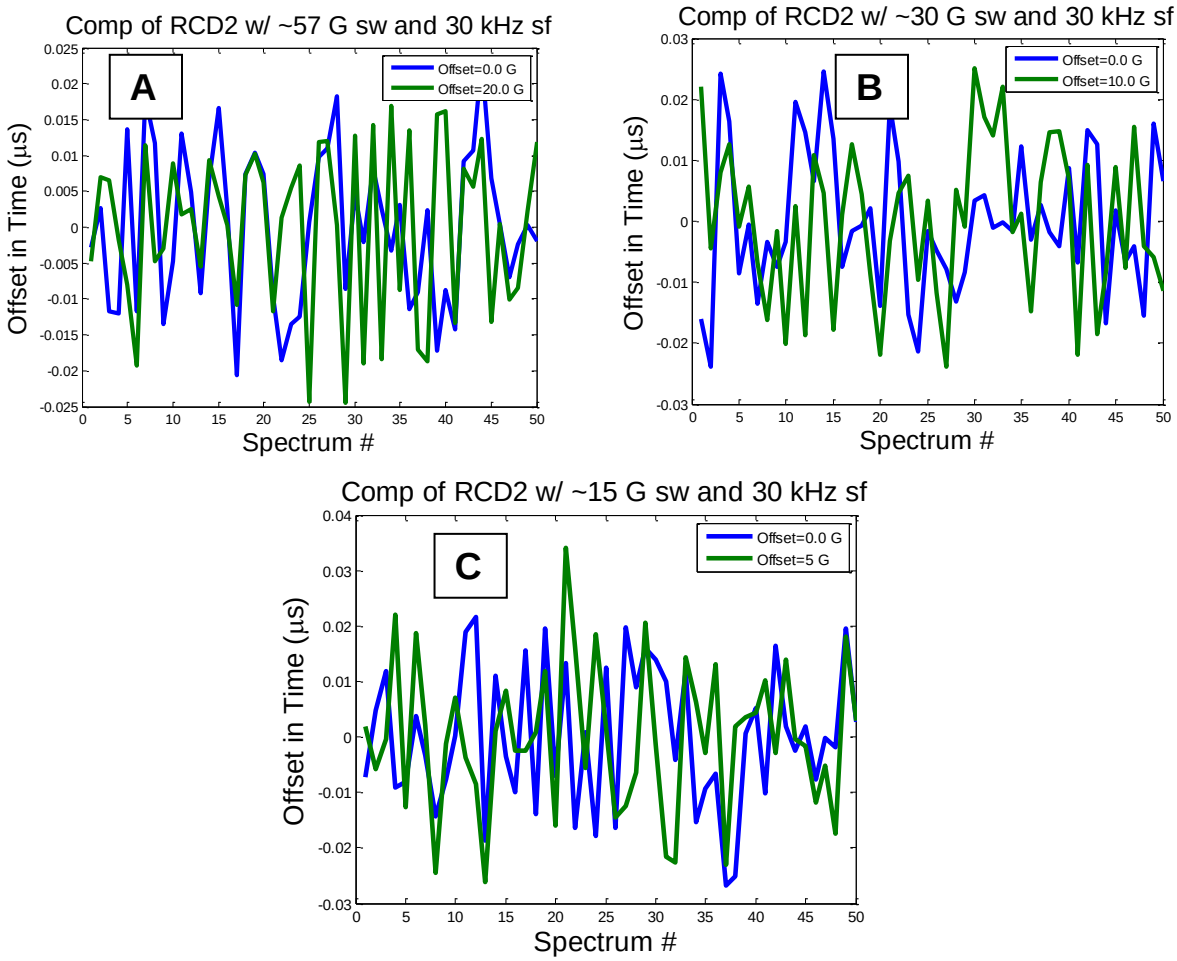

Figure 4.11. Comparison of position offset of rapid-scan spectrum (from mean position) for (i) the line centered in the scan and (ii) offset by 2/3 of the half amplitude of the sweep width for RCD2 with a deoxygenated LiPc sample at 3 different sweepwidths. 2-D rapid-scan data was collected with 3430 G center field and offsets shown in individual panels, 30 kHz scan frequency, and (A) ~55 G scan width (scan rate ~5.5 MG/s), (B) ~33 G scan width (scan rate ~3 MG/s), (C) 10 G scan width (scan rate ~1 MG/s). Spectra were collected consecutively. For each spectrum, 1 scan was collected with resonator Q~200 and 33dB power.

Table 4.2. Comparison of standard deviation of position of resonance of LiPc for RCD1 and RCD2 with (i) resonance centered or (ii) offset by 2/3 of the scan amplitude (half of the peak-to-peak amplitude). Standard deviations in time were multiplied by the rate to get a standard deviation in gauss.

Sweep Width (Gauss)	RCD1-stdev (mG)	RCD2-stdev (mG)
15 (CF- 0.0 G offset)	18	17
15 (CF-5.0 G offset)	41	18
33 (CF- 0.0 G offset)	17	32
33 (CF- 10.0 G offset)	40	34
55 (CF- 0.0 G offset)	15	60
55 (CF- 20.0 G offset)	53	65

More jitter is observed for RCD2 than RCD1 at larger sweep widths. The absolute time jitter for RCD1 actually decreases with increasing sweepwidth. The absolute time jitter for RCD2 stays fairly constant with increasing sweepwidth, so the field standard deviation increases with rate. The jitter for RCD1 is dependent on the center field offset, indicating that vertical amplitude jitter was observed. The jitter for RCD2 is not dependent on the center field offset, which suggests that this jitter is due primarily to horizontal time jitter.

Figure 4.12 shows the comparison between the sinusoidal waveform and a simulated sine wave. The residuals between the current waveform and the simulated sine wave were multiplied by 50. This figure shows that the current waveform is very nearly sinusoidal. The total harmonic distortion, which is calculated by taking the ratio of the

RMS (root mean square) of the residuals to the sine wave RMS value and multiplying by 100) is 0.6%. This very low distortion is attributed to the resonated type circuit that is used in this design.

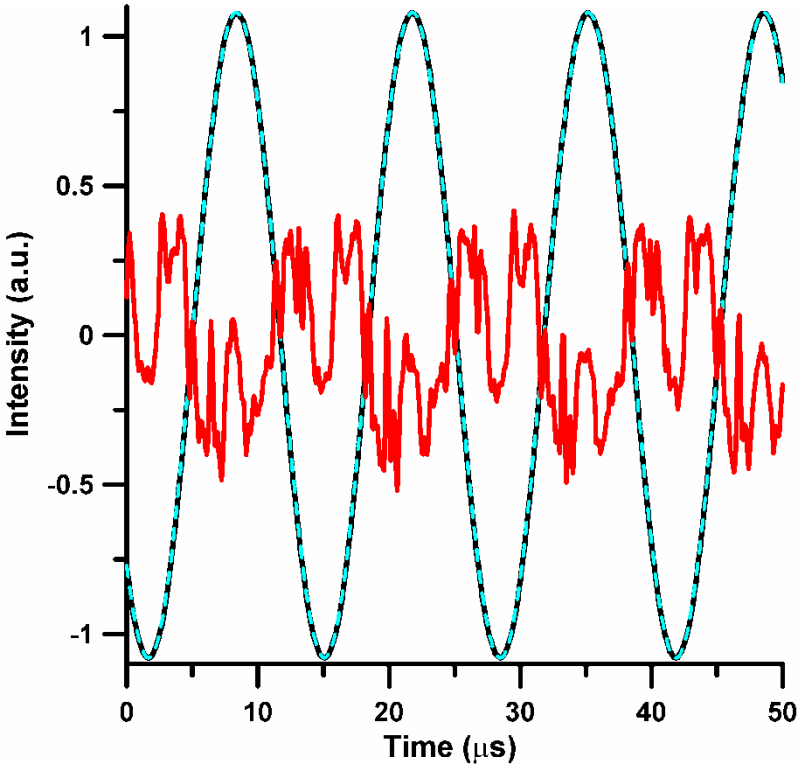

Figure 4.12. Comparison of current waveform (black) measured with Tektronix model AM-503 current probe and simulated sine wave (blue dashed) with a scan frequency of 74.5 kHz and scan amplitude of 2.20 App (~26 Gpp). The red trace is the difference between the current waveform and the simulated sinwave multiplied by 50.

Figure 4.13 is an example of a comparison between the derivative of a deconvolved rapid-scan spectrum with a conventional CW EPR spectrum for an aqueous ^{15}N-PDT (4-oxo-2,2,6,6-tetra-perdeuteromethyl-piperidinyl-^{15}N-oxyl-d_{16}) sample. The good agreement of the deconvolved rapid-scan spectrum with the CW spectrum further illustrates that the rapid magnetic field scan is nearly sinusoidal. Not only does the linewidth match up very well with the CW, but also the positions of the ^{13}C hyperfine

lines also match well. If the driving function had not been close to sinusoidal, a good deconvolution would not have been obtained when a sinusoidal function was assumed.

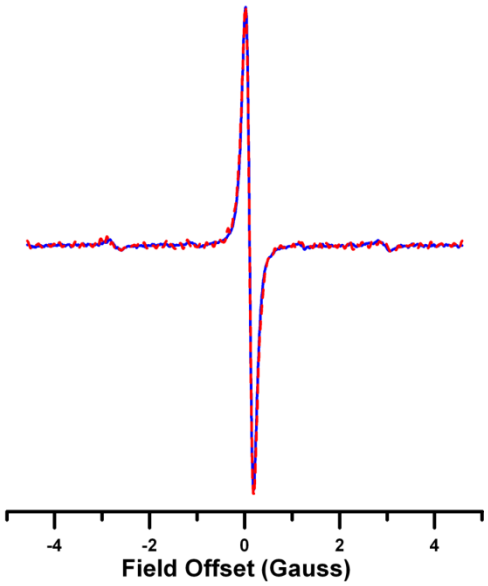

Figure 4.13. Segments of spectra of the low-field nitrogen hyperfine line for degassed 0.2 mM ^{15}N-PDT solution. (blue line) CW spectrum obtained with 45 G sweep width, 0.02 G modulation amplitude, 82 sec scan time, and 0.3 mW power. (red dashed line) Pseudomodulated, deconvolved rapid-scan spectrum obtained with 9.15 G scan width, and 29.7 kHz scan frequency (scan rate of ~0.85 MG/s). 1024 averages were collected in ~1 sec. with resonator Q~150 and 2 mW power (0.02 G B_1).

4.4 Sinusoidal Background Removal

4.4.1. Introduction

In sinusoidal field-swept rapid-scan EPR, the rapidly-changing magnetic field creates background signals mainly at the scan frequency [53]. A first approach to removing this background was to record the off-resonance signal and subtract it from the on-resonance signal. This method is problematic because it doubles the amount of time to record the signal, and it increases the random noise. Also, the background signal may be field-dependent which would further increase the noise following a background

subtraction. Dr. Mark Tseitlin in the Eaton lab developed a novel background removal procedure for sinusoidal rapid-scan experiments that does not require an off-resonance spectrum. This method assumes that the background is sinusoidal, which appears to be consistent with experiments. My contribution to this work was to test the background removal procedure in MATLAB to determine if any improvement could be made.

For a complete discussion on the theory behind the software used to remove the sinusoidal background, please see the recent paper [53] on the subject.

4.4.2. Methods

Sample Preparation. Xanthine oxidase, hypoxanthine, superoxide dismutase (SOD), horse heart ferricytchrome c, and diethylenetriaminepentaacetic acid (DTPA) were purchased from Sigma-Aldrich (St. Louis, MO). Dr. Gerald Rosen at the University of Maryland generously supplied the spin trap, 5-tert-butoxycarbonyl-5-methyl-1-pyrroline N-oxide (BMPO) [54]. Solutions were made in a 50 mM sodium phosphate solution (with 1 mM DTPA added), buffered to a pH~7.4. Superoxide was generated by a 2 μM hypoxanthine/ 0.04 units/mL xanthine oxidase solution ($O_2^{\cdot -}$ production rate of ~2 μM/ min measured SOD-inhibited reduction of ferricytochrome C). The BMPO (50 mM) formed an adduct with the superoxide that was detected with EPR.

Spectroscopy. Rapid-scans at X-band were obtained on a Bruker E500T transient spectrometer using a dielectric resonator. The scan parameters for spin-trapped superoxide were H_m = 55 G and F_m= 50645 Hz.

4.4.3. Results and Discussion

The background subtraction procedure to rapid-scan data for spin-trapped superoxide (BMPO-OOH) was applied at X-band for a case where the background is large compared with a relatively weak EPR signal (Figure 4.14). The real and imaginary components of the signal, after subtraction of the calculated complex background signal, are shown in Figure 4.14d.

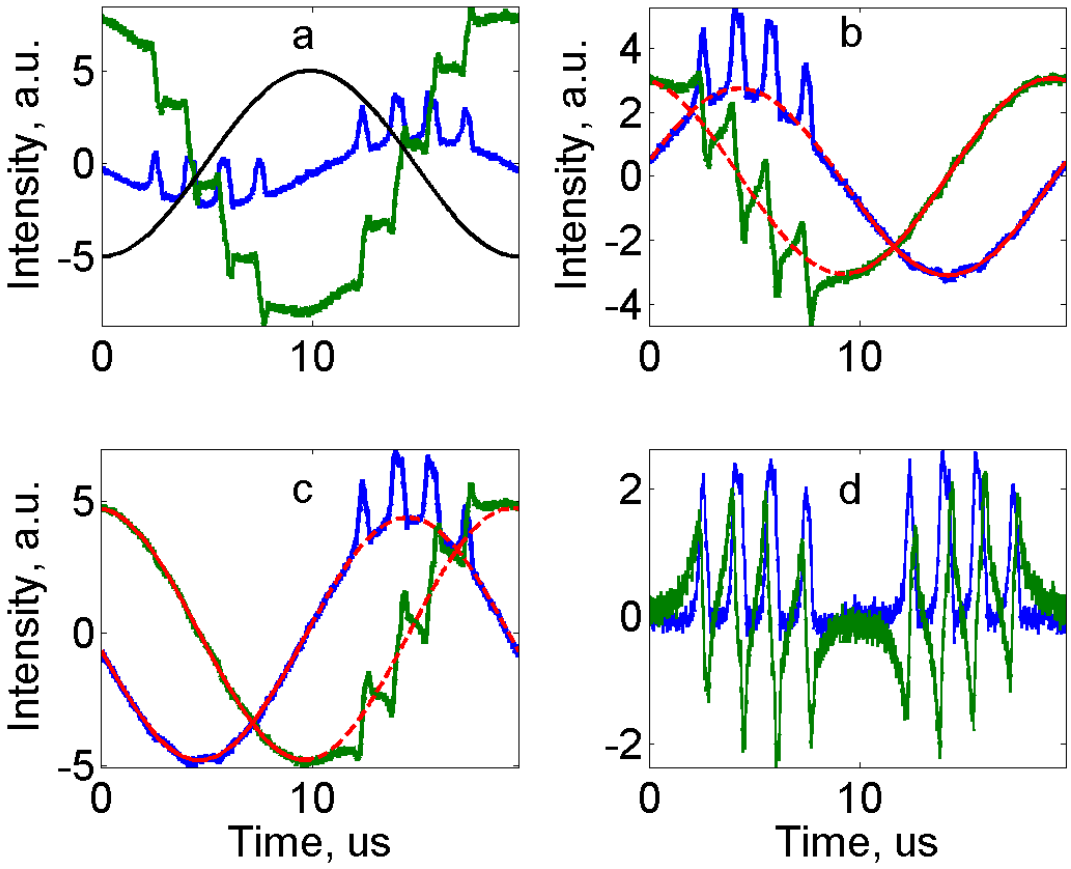

Figure 4.14. Application of background subtraction procedure to spectra of BMPO-OOH. The signals in the two channels are shown in blue and green. a) Experimental data for a full cycle of sinusoidal scan overlaid on the magnetic field scan waveform (black). b) Up-field scan c) Down-field scan. For both the up and down scans, the fitted background (solid red) was extrapolated into the half-cycle that includes the EPR signal (dashed red). d) Results after background subtraction.

This background removal procedure assumes that the background is primarily the first harmonic, and partially second harmonic of the scan frequency. The procedure is based on the notion that you can separate the up and down scans in the frequency domain and return back to the time domain with 2 signals (Figure 4.14 B&C). Once in the time domain, you have two signals each with a separate background to make fitting of the background easier. Once the background has been fit and the two halves are recombined, it is subtracted from the signal.

For a sharp signal like BMPO-OOH it might be argued that the sinusoidal background could be defined even in the presence of the signal. However, EPR imaging is an important application of rapid-scan EPR. For imaging experiments, the signal is often substantially broadened and difficult to distinguish from background.

This background removal procedure has been used for a variety of samples for which data are shown in the remainder of the dissertation. When applying this method, it is important to distinguish between the up and down scan (the field direction), which can be determined by changing the center field and observing the direction of the shift of the line. This background correction also corrects for non-orthogonality of the detection system.

Chapter 5: Relaxation information extracted from magnetically concentrated samples with rapid-scan EPR.

5.1 Introduction

Magnetically concentrated samples: BDPA (α,γ-bisdiphenylene-β-phenylallyl), LiPc (Lithium phthalocyanine), and DPPH (2,2-diphenyl-1-picrylhydrazyl) (Scheme 5.1) are useful to test rapid-scans because they have narrow and approximately Lorentzian lines. These samples have T_2 relaxation times around 100 ns. Because these samples are point-like particles, the T_2 were measured using echo decay with a gradient applied (using an iron Allen wrench in the field) to suppress the FID. BDPA in air was measured to have a bulk relaxation time of 130 ns while LiPc has a T_2~80 ns, and DPPH a T_2~100 ns. The EPR lines for these samples are narrow because of the exchange narrowing phenomenon [55]. An interchange of spin state between two electron spins does not alter the total magnetic moment of the sample, but exchange interaction allows an electron of a definite spin to jump rapidly from one molecule to another [56]. This has the effect of averaging out electron dipole-dipole interactions that would otherwise yield a broad spectral line. These samples were studied by rapid-scan EPR to determine how well the spin-spin relaxation time could be extracted from the data.

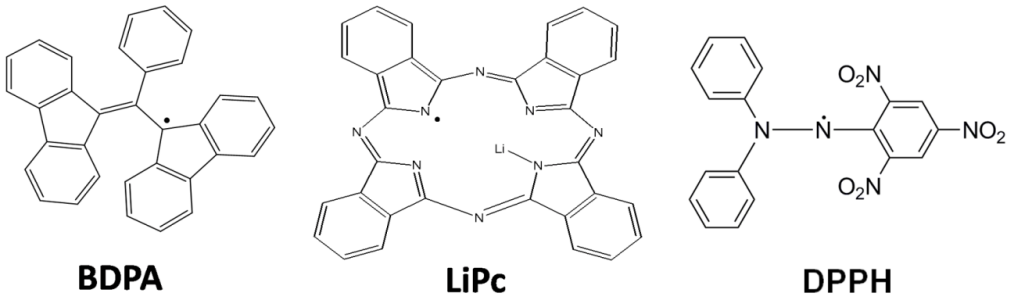

Scheme 5.1. Structures of BDPA (*α,γ*-bisdiphenylene-β-phenylallyl), LiPc (Lithium phthalocyanine), and DPPH (2,2-diphenyl-1-picrylhydrazyl).

5.2 LiPc

5.2.1. Introduction

LiPc is a nitrogen-centered radical that was developed initially by Turek's group [57] and has been used as a probe for EPR oximetry experiments [58]. LiPc is often used as a standard in the Eaton lab. LiPc is a strong sample that has an almost perfectly Lorentzian lineshape that is fairly narrow in air. These characteristics make it an appealing sample for testing method development and has been used extensively in developing rapid-scan EPR and imaging [39]. In the previous chapter, LiPc was used to characterize jitter in the resonated coil driver.

5.2.2. Methods

Sample Preparation. LiPc was prepared electrochemically following the literature procedures [57] and was generously provided by Prof. Swartz, Dartmouth University. Needle-like crystals of LiPc were selected for the measurements.

EPR Spectroscopy. Rapid-scan and CW signals were recorded on a Bruker E500T transient X-band spectrometer. The microwave bridge has a 200 MHz bandwidth video

amplifier. Signal acquisition was via a SpecJet II digitizer. A critically-coupled Bruker ER4118X-MD4 pulse ENDOR resonator was rotated such that the field resulting from the ENDOR coils was parallel to the B_0 magnetic field. Resonator Q was measured using pulse ring down with a locally-designed addition to the bridge [28] and with an HP 8719D network analyzer (as described in section 4.1). To avoid excess heating of the ENDOR coils, the sine wave for the magnetic field scans was generated with a Tektronix AWG2021 arbitrary waveform generator, operating in burst mode. The duty cycle was about 1%. The center field was selected to be close to resonance.

5.2.3. Results and Discussion

Because LiPc has a nearly Lorentzian line, the spin-spin relaxation time was estimated from the linewidth to be about 80 ns. Figure 5.1 shows the comparison between the experimentally obtained and simulated rapid-scan spectrum for this sample. Simulation of this spectrum gave a T_2 of 82 ns, which is in good agreement with the value extracted from the CW spectrum.

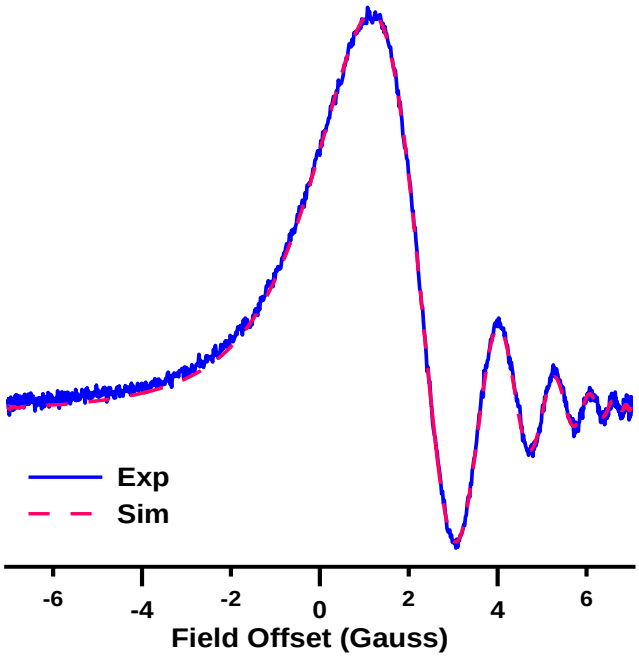

Figure 5.1. Comparison of simulated and experimental rapid-scan of LiPc. (Blue) 22 MG/s rapid-scan spectrum of LiPc. Q~200, 500 kHz scan frequency, 14 G scan width, and 0.2 mW power. (Pink Dashed) Simulation of rapid-scan spectrum, which gave a spin-spin relaxation time of 82 ns.

The LiPc sample demonstrated that determination of T_2 by simulation of rapid-scan spectra is possible. While LiPc is a straightforward case because of very small inhomogeneous broadening, this concept can be applied to more complex samples to determine the spin-spin relaxation time.

5.3 BDPA

5.3.1. Introduction

Measurement of the relaxation times for BDPA was attempted with rapid-scan EPR. However, BDPA turned out to be much more complicated than its Lorentzian line suggested. The work with BDPA was summarized in the 2011 paper [51].

The stable organic radical BDPA (α,γ-bisdiphenylene-β-phenylallyl) was first synthesized in 1957 [59], and has since been widely used in EPR. Because of its intense EPR signal, magnetically-concentrated solid BDPA was previously used in the development of novel methods to study unpaired electrons [60-63]. BDPA is also widely used in dynamic nuclear polarization NMR studies [64, 65].

BDPA was initially chosen to study X-band rapid-scan EPR because it has an intense narrow EPR signal. Also, BDPA had a homogeneously broadened line so it was assumed that the T_2 could be measured directly from the CW lineshape (Equation 2.3). Through rapid-scan EPR experiments, the crystalline BDPA:benzene complex was shown to be heterogeneous, and should therefore be used with caution as a standard sample.

5.3.2. Methods

Samples. The 1:1 BDPA:benzene complex was purchased from Sigma Aldrich (batch #00226KM). Two bottles were purchased from Sigma Aldrich and they both had the same batch number. Small particles of BDPA were selected and placed in 0.8 mm i.d pyrex capillaries, which were supported in 4 mm o.d. quartz EPR tubes. Most experiments were performed with air-saturated samples. For rapid-scan experiments, ~0.1 mL of a 3:1 (by weight) ethanol-water mixture was placed in the annulus surrounding the capillary containing the BDPA sample, to lower resonator Q to about 200. If resonator Q is not sufficiently low, the limited resonator bandwidth may dominate the damping of the rapid-scan oscillations.

Oxygen and benzene were removed from selected BDPA samples to determine the impact on the CW linewidth and on electron spin-spin relaxation times. To remove

oxygen, samples were evacuated for about 5 hours, without heating. To remove benzene [66], samples were evacuated while heating at 90°C for about 7 hours. To characterize BDPA with reduced benzene content in the presence of air, air was reintroduced after the evacuated samples had cooled.

UV-Vis Experiments. UV-Vis experiments were performed to determine if variations in T_2 were due to impurities in the samples. T_2 was determined from CW lineshapes for 386 individual small BDPA particles. The distribution of T_2 is shown in Figure 5.2. The range of linewidths from these samples is shown in Figure 5.3. The particles were sorted, based on T_2, into separate containers. 1.0 mg of BDPA from containers with T_2 in four ranges (102–107 ns, 112–117 ns, 122–125 ns, 137–142 ns) was dissolved in chloroform to make four solutions with 30 μM concentrations. UV-Vis spectra were collected on a Varian Cary 100 Bio UV-Vis spectrometer with a wavelength range of 200–900 nm.

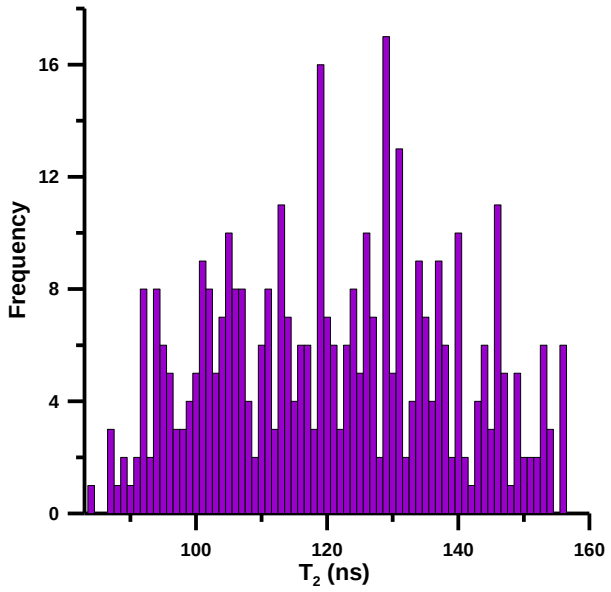

Figure 5.2. Distribution of T_2 for 386 BDPA particles, measured individually by CW linewidth on an EMX spectrometer.

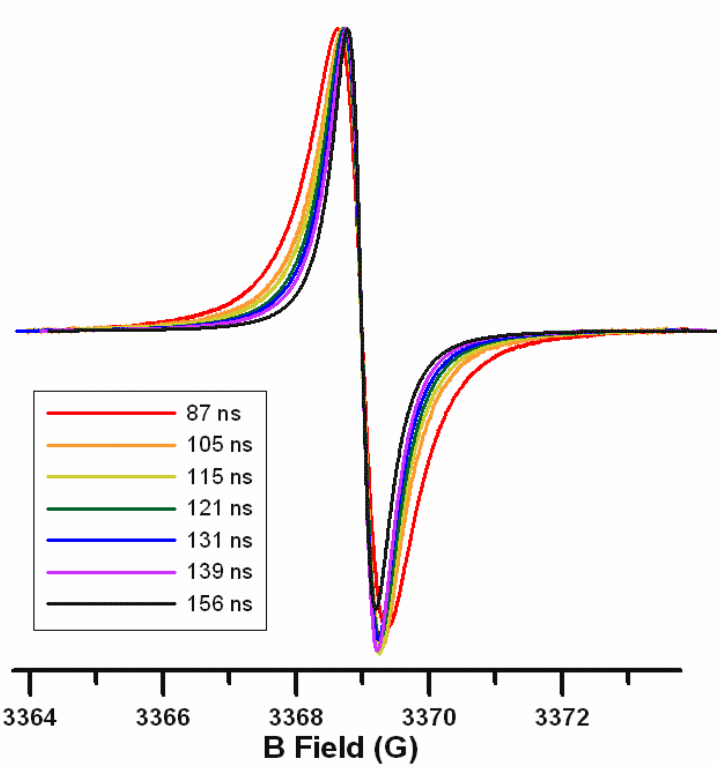

Figure 5.3. CW EPR for several selected BDPA particles, measured individually on an EMX spectrometer. 10.0 G sweep width, 0.08 G modulation amplitude, 30 KHz modulation frequency.

SEM Spectroscopy. To determine if particles with different T_2 had different physical characteristics, scanning electron microscope (SEM) images of selected BDPA particles were collected. Particles were placed in silver paint and SEM images were collected on a JEOL JSM-IC848a microscope with the help of Azure Avery from the Department of Physics and Astronomy at the University of Denver.

NMR Spectroscopy. NMR experiments were performed to determine if variations in T_2 were due to differences in benzene concentration in the samples. NMR experiments were performed on an Avance III 500 MHz Bruker spectrometer. Several sets of BDPA particles (sorted by T_2 or linewidth) were collected so that about 1.0 mg of BDPA dissolved in 0.5 mL of $CDCl_3$ was used for each measurement. Assuming the same

amount of $CHCl_3$ in all the $CDCl_3$, the integrals of the $CHCl_3$ and benzene peaks were compared as a function of the electron spin relaxation time.

EPR Spectroscopy. Rapid-scan signals were recorded on a Bruker E500T transient X-band spectrometer the same as described as in section 5.1 and the Bruker ENDOR resonator (section 5.2.2). The microwave bridge has a 200 MHz bandwidth video amplifier. Signal acquisition was via a SpecJet II digitizer.

For the BDPA experiments, sinusoidal scan frequencies ranged from 300 kHz to 1.5 MHz and scan widths varied from 17 to 60 G, which corresponds to rates at the center of the scan of 16 to 280 MG/s. The ENDOR coils can be used to generate sweep widths up to 70 G peak-to peak at scan frequencies exceeding 5 MHz, which corresponds to scan rates in excess of 1 GG/s. However, these rates are higher than are needed to characterize T_2 of BDPA and would have required significant decrease in resonator Q to record spectra with sufficient signal bandwidth.

The slow-scan spectra were recovered from the rapid-scan signals using Fourier deconvolution [43]. The first derivatives of the absorption signals recovered from the rapid-scans were calculated using a function analogous to the pseudomodulation method described by Hyde [67], and included a Butterworth filter to approximate the impact of the spectrometer time constant. Later, it was discovered that better signal (without an oscillating distortion) was achieved by using a numerical differentiation combined with a Butterworth filter rather than pseudomodulation.

To define the distribution of T_2 shown in Figure 5.2, CW spectra of small BDPA particles were collected on a Bruker EMX-plus X-band spectrometer at room temperature with a sweep width of 10 G, modulation frequency of 100 kHz, and modulation

amplitude of 0.08 G (Figure 5.3). The 100 kHz modulation frequency was used for convenience, although it caused some broadening of the narrowest lines. For the more precise comparisons of lineshapes with deconvolved rapid-scan spectra, CW spectra were obtained with a modulation frequency of 30 kHz.

Simulations. CW spectra were simulated with a Lorentzian lineshape using the shareware package Easyspin [68]. T_2 was calculated using Equation 1.5, which is valid only for unsaturated spectra with a Lorentzian lineshape that is relaxation determined. The simulations of the CW spectra are sensitive to T_2, with an uncertainty of about 2–3%. The uncertainty is based on the range of linewidths that appear to give similar agreement with the experimental data.

Simulations of the rapid-scan signals were performed by numerical integration of the Bloch equations [42] using a program written in MATLAB. The input parameters are magnetic field scan width, scan frequency, resonator Q, offset of the center of the scan from the resonant magnetic field, and T_2 relaxation time. For these simulations, all parameters were known except T_2, which was adjusted to fit the spectra. The uncertainty in T_2, about ±5%, was calculated from the confidence level of replicate measurements, converted to a percent. Factors that contribute to the uncertainty are variations in background, and uncertainty in the value of resonator Q. Uncertainties are greater for samples with weaker signals. T_2 obtained by simulation of the rapid-scan spectra was compared to T_2 calculated from the CW linewidths. Agreement between the results of the two methods indicates that systematic sources of error were minimized.

5.3.3. Results

EPR Spectra of BDPA. Although commercial BDPA is a crystalline solid, the particles do not appear to be single crystals, and there is a wide range of morphology. Therefore in the following discussion the designation 'particle' is used instead of 'crystal'. Rapid-scan experiments using multiple particles resulted in spectra that could not be simulated with a single T_2. Therefore attention was focused on individual particles and characterization of the differences among particles.

Sinusoidal rapid-scans of a BDPA particle at scan rates in the center of the scan of 18 to 60 MG/s are shown in Figure 5.4. The absorption signals are recorded by direct detection. As the scan rate increases, the signal broadens, the amplitude of the oscillations increases, and the number of oscillations increases [38]. The spacing between the peaks in the oscillation decreases as the magnetic field is scanned above or below resonance. The time constant for the damping is T_2 (because $T_2 \sim T_2^*$), which was determined by simulation.

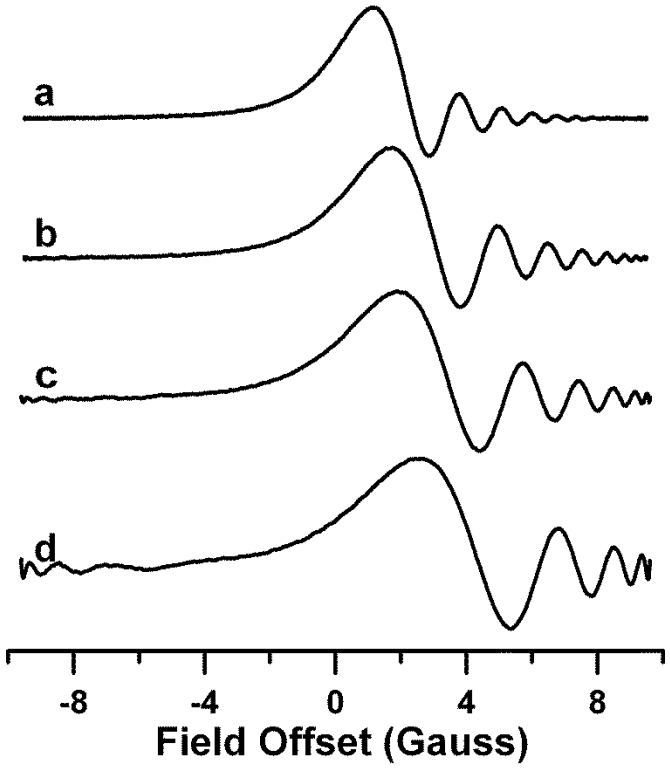

Figure 5.4. Rapid-scan spectra of a BDPA particle with T_2 = 88 ± 3 ns, obtained with constant 19 G scan width, and different scan frequencies. 10240 averages were collected with resonator Q~200 and 0.2 mW power. **a.** 300 kHz scan frequency (18 MG/s), recorded in ~30 sec. **b.** 500 kHz scan frequency (30. MG/s), recorded in ~20 sec. **c.** 700 kHz scan frequency (42 MG/s), recorded in ~15 sec. **d.** 1 MHz scan frequency (60 MG/s), recorded in ~10 seconds.

Rapid-scan spectra for BDPA particles 1–3, which have different T_2, recorded at a rate in the center of the scan of 16.25 MG/s are shown in Figure 5.5a. The shorter the T_2, the more quickly the oscillation decays. The effects of the sinusoidal rapid-scan on the EPR signals in Figure 5.5a can be deconvolved to recover the slow scan lineshapes, as shown in Figure 5.5b. The slow scan lineshapes obtained by deconvolution and conversion to the first-derivative display are in excellent agreement with traditionally recorded CW spectra obtained with 30 kHz modulation frequency. The use of 100 kHz modulation frequency for the CW spectra of BDPA causes small, but significant,

broadening, which became evident when the values of T_2 obtained by rapid-scan and CW lineshapes were compared. T_2 determined from rapid-scan and CW spectra for the three samples for which data are shown in Figure 5.4 are compared in Table 5.1.

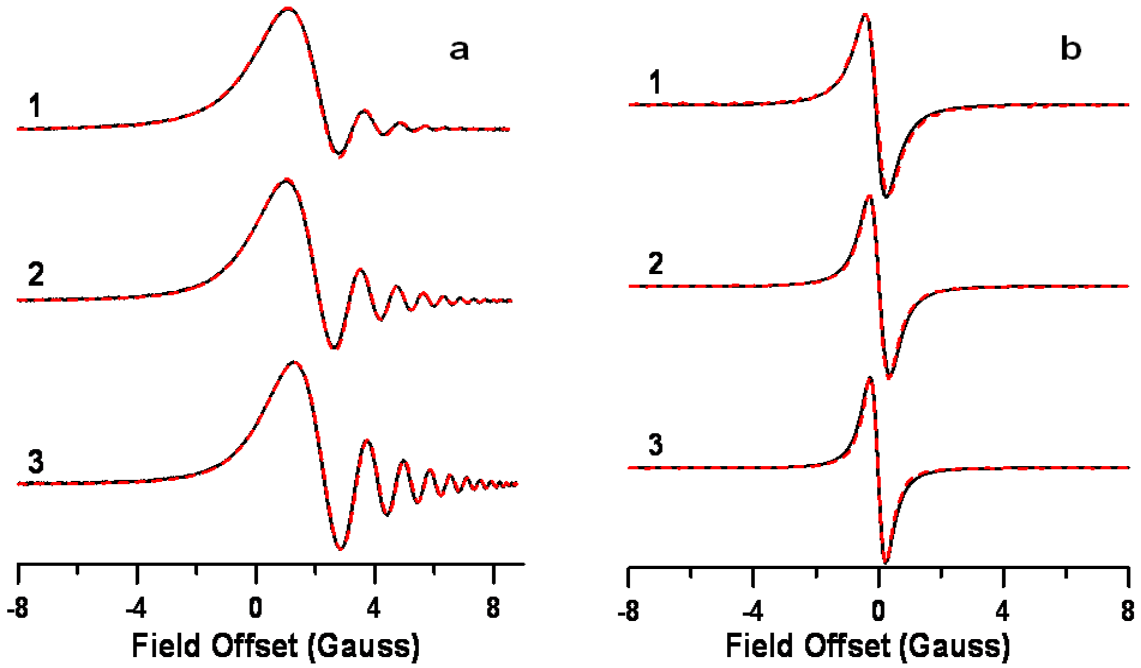

Figure 5.5. a. Rapid-scan EPR (black line) of BDPA particles 1 – 3 (with T_2 = 85, 110, and 141 ns, respectively) and simulations (red dashed line). Spectra were collected with resonator Q~200, 300 kHz scan frequency, 17.2 G scan width, scan rate 16.25 MG/s, 0.2 mW power and 10240 (samples 1 and 3) or 20480 scans (sample 2). **b.** Comparison of CW spectra (black line) with first derivative spectra obtained by pseudomodulation from the deconvolved rapid-scan spectra (red line). CW spectra were collected with 30 kHz modulation frequency, 0.08 G modulation amplitude, and 0.02 mW power. For sample 1, 4 averages were recorded in about 5.5 min. For samples 2 and 3 a single scan was recorded in 86 s.

Table 5.1. T_2 (ns) for three BDPA particles for which spectra are shown in Fig. 5.5

Sample	T_2 from rapid-scan EPR[a]	T_2 from CW EPR[b]
1	85	92
2	110	103
3	141	130

[a] Average uncertainty, calculated for replicates rapid-scan measurements, was ± 5%.
[b]Average uncertainty, calculated for replicate CW measurements, was ± 2%.

Effect of oxygen and benzene on relaxation times for BDPA particles. CW spectra were recorded for four BDPA samples that had been evacuated to remove oxygen and subsequently heated in vacuum to remove benzene. The samples were selected to have different initial linewidths in air. Table 5.2 shows the changes in the CW linewidths that were observed. Line 4 in Table 5.2 is the line width after air was allowed back in the sample after removal of benzene (by heating and evacuating). Removal of oxygen caused the largest decrease in linewidth for particle 4, which had the broadest initial linewidth. For particle 4, heating under vacuum to remove benzene caused little additional change in linewidth. For the other particles heating under vacuum resulted in distributions of linewidths and formation of components with substantially broadened lines. For all of the heated particles, exposure to air caused substantial broadening of the lines. The changes in lineshape from heating in vacuum were not reversible.

Table 5.2. Effect of oxygen and benzene on the linewidths (G) for four BDPA samples.

Particle	4	5	6	7
Original in air	0.68	0.53	0.49	0.42
Evacuated[b]	0.35	0.36	0.40	0.42
No benzene or O_2	0.38	0.28–1.5[b]	0.36 –1.4[b]	0.5–1.2[b]
No benzene, w/ Air	1.8	0.7–1.9[b]	1.6	1.5

[a]Evacuated for 4 hours at ambient temperature to remove O_2.
[b] These linewidths could not be fit with single Lorentzians, but appeared to be superpositions of multiple Lorentzians with widths in the tabulated range.

UV-Vis of BDPA in $CHCl_3$ and SEM images. UV-Vis spectra were recorded for BDPA particles with different ranges of T_2 (102–107 ns, 112–117 ns, 122–127 ns, 137–142 ns) dissolved in $CHCl_3$ (Figure 5.6). Each sample had λ_{max} = 488 nm and a weaker absorbance at λ = 874 nm, which is in good agreement with the literature [64], and there was no evidence of peaks characteristic of the diamagnetic carbanion precursor.

The SEM images of two different BDPA particles ($T_2 \sim 96$ ns and $T_2 \sim 152$ ns) are shown in Figure 5.7–5.12. The SEM images show that BDPA particles have many different crystal morphologies.

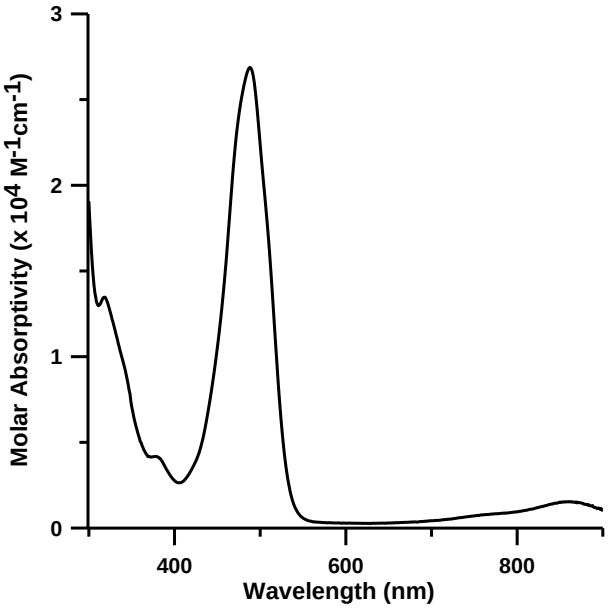

Figure 5.6. UV-Vis absorption spectrum in $CHCl_3$ solution of BDPA particles with T_2 in the range of 122 – 127 ns. λ_{max} =488 nm.

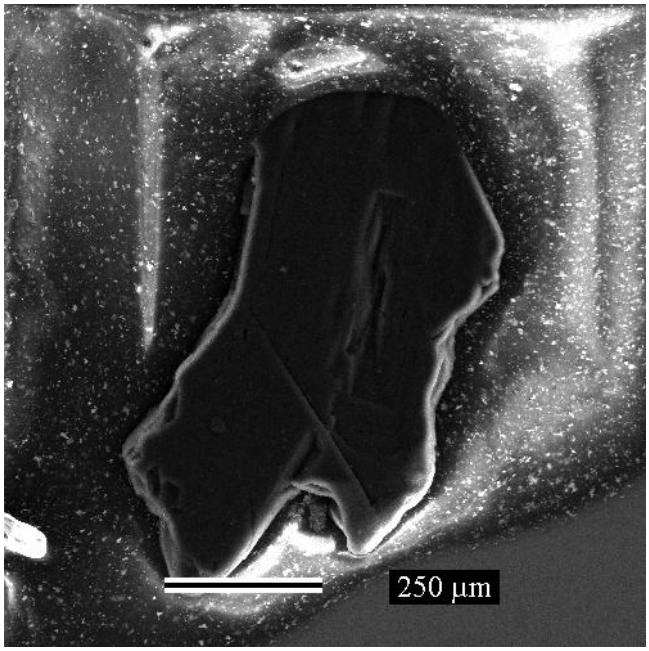

Figure 5.7. SEM Image of BDPA particle with T_2=96 ns, with 85x magnetization

.

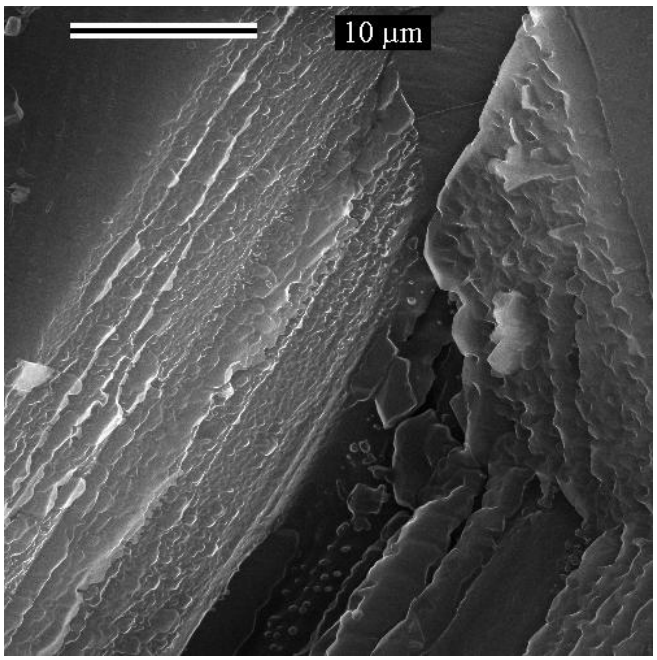

Figure 5.8. SEM Image of BDPA particle with T_2=96 ns (same particle as in 5.7), with 2500x magnetization.

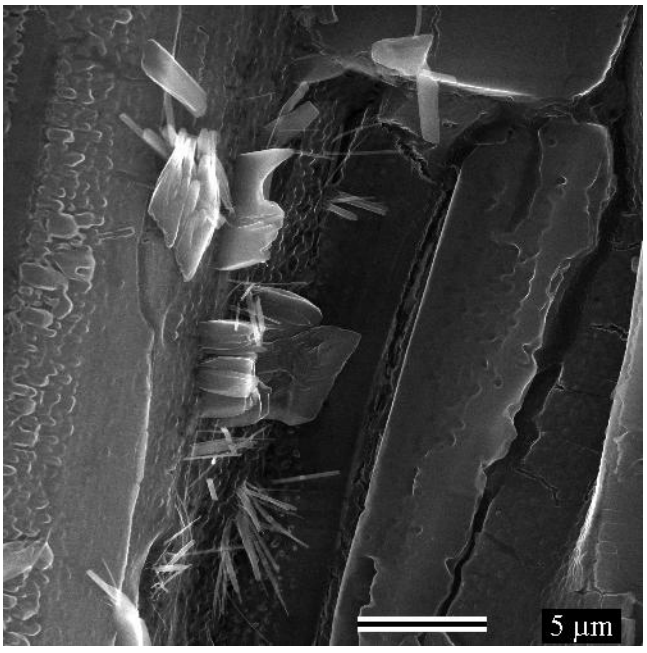

Figure 5.9. SEM Image of BDPA particle with T_2=96 ns (same particle as in 5.7 and 5.8), with 3500x magnetization.

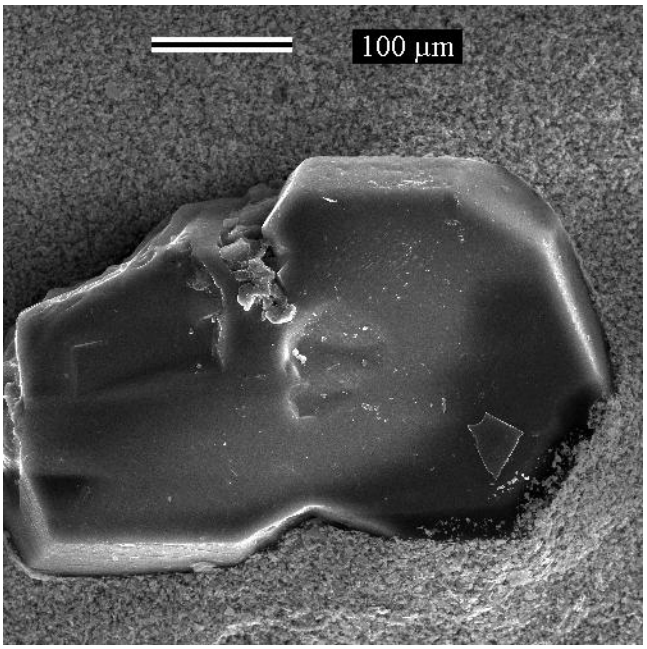

Figure 5.10. SEM Image of BDPA particle with T_2=152 ns, with 190x magnetization.

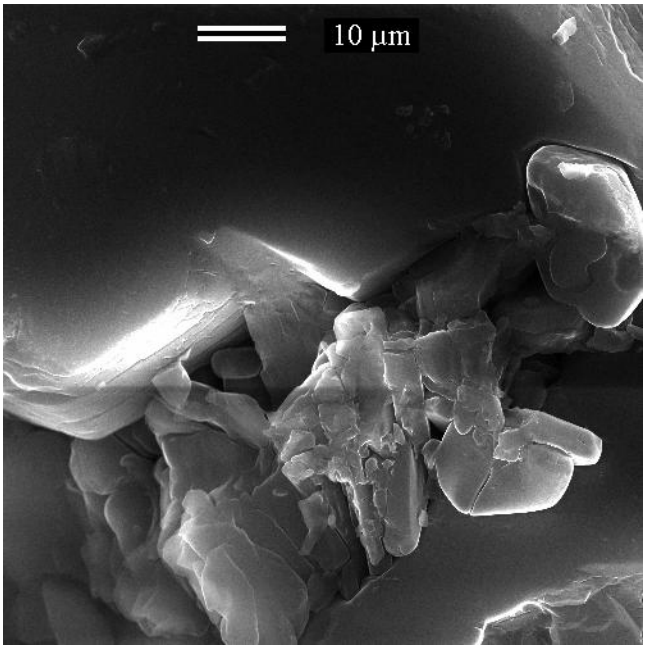

Figure 5.11. SEM Image of BDPA particle with T_2=152 ns (same particle as in 5.10), with 1200x magnetization.

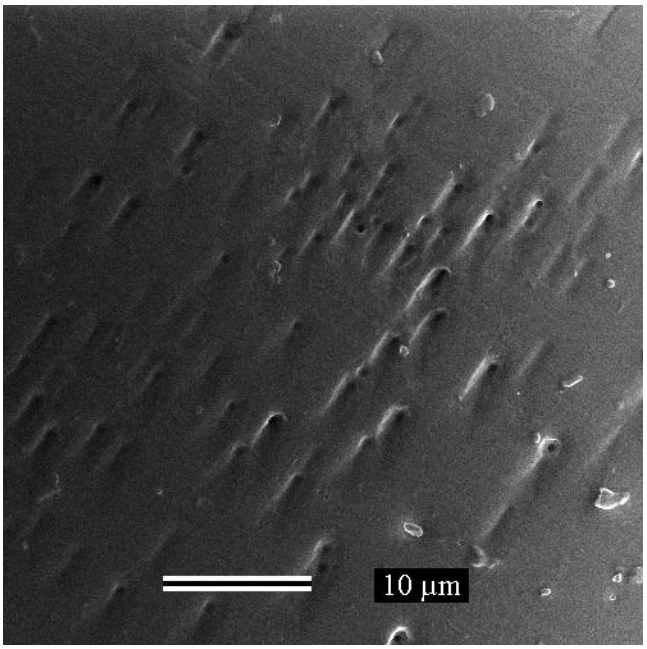

Figure 5.12. SEM Image of BDPA particle with T_2=152 ns (same particle as in 5.10 and 5.11), with 2000x magnetization.

NMR of BDPA in $CDCl_3$. Figure 5.13 shows the ratio of the integral of the benzene peak to the $CDCl_3$ peak. When compared to the $CDCl_3$ peak, the benzene increased as the T_2 increased. This suggests that an increased concentration of benzene was present in samples with longer relaxation times. The higher concentration of benzene may contribute to the exchange interactions among the concentrated BDPA. All NMR measurements were made with the same amount of $CDCl_3$ from the same bottle. However, this study was not a quantitative measure of the concentration of benzene present in the BDPA samples.

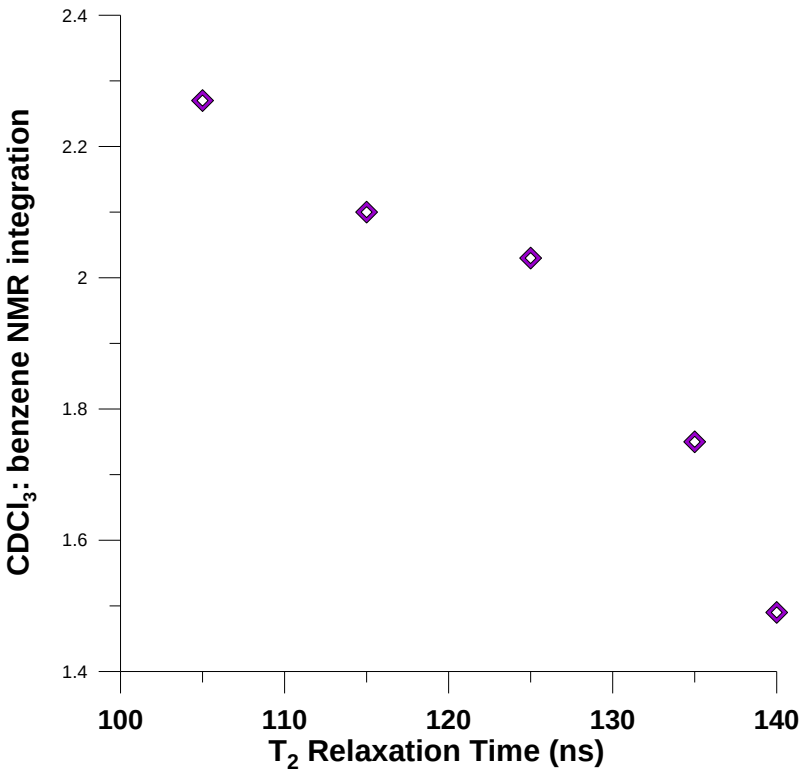

Figure 5.13. Ratio of the integrals of $CDCl_3$: benzene peaks as a function of T_2 of BDPA. Several sets of BDPA particles were collected so that about 1.0 mg of BDPA was dissolved in 0.5 mL of $CDCl_3$.

5.3.4. Comparison of information obtained by CW and rapid-scan EPR for BDPA

Determining T_2 of BDPA through simulations of CW and rapid-scan. The exchange-narrowed lineshape for solid 1:1 BDPA:benzene in the presence or absence of air (O_2) is Lorentzian, so T_2 can be calculated from the CW linewidth. Simulations with a Lorentzian lineshape were in reasonable agreement with experimental spectra of samples consisting of multiple particles. However, rapid-scan experiments using multiple particles resulted in spectra that could not be simulated with a single T_2. This result indicated that the spectrum of the bulk BDPA sample could not be represented by a single spin packet linewidth, and was actually a superposition of spin packets with a distribution of linewidths. From these simulations, rapid-scan EPR provided information

about BDPA that was less evident in the CW experiments. Although it might be expected that electron spin echo experiments would be helpful in determining T_2, the homogeneous broadening of the lines precluded echo formation because it was not practical to create an inhomogeneous field over the small particle. Common techniques of creating a gradient across a sample to facilitate echo formation were unsuccessful because of the small sizes of the particles.

Figure 5.5a illustrates that rapid-scan EPR spectra are sensitive to the T_2 of a sample. The T_2 required to simulate the rapid-scan spectra for individual particles matched well with T_2 determined from the linewidth of the CW spectrum obtained with 30 kHz modulation frequency (Table 5.1). The rapid-scan spectra also were deconvolved to obtain the slow scan spectra. The first derivative of the deconvolved rapid-scan spectra for particles 1, 2, and 3 agreed well with the conventionally-recorded CW spectra (Figure 5.5b).

Heterogeneity of BDPA. Individual BDPA particles have T_2 relaxation times ranging from 80–160 ns (Figure 5.2–5.3). The distribution in T_2 does not appear to be Gaussian so it is attributed to variations in physical properties. At X-band there does not appear to be a distribution in g values. Rotation of a particle with a goniometer through 180^o found linewidth variation only between 0.49 and 0.44 G. This small orientation dependence indicates that the distribution of linewidths implied by the relaxation times in Figure 5.2 is not a result of different orientations of the particles in the magnetic field. Data in Table 5.2 show that BDPA particles with a variety of T_2 are affected differently by the removal of oxygen as well as removal of both benzene and oxygen. BDPA particles with shorter T_2 are more sensitive to the removal of oxygen. These differences

may be due to morphology and/or benzene concentration. For the oximetric probe lithium phthalocyanine (LiPc) (section 5.1) there is a correlation between sensitivity to oxygen and crystal morphology [69]. SEM images (Figures 5.7–5.12) indicate that the BDPA particles have many different crystal morphologies. However, there does not appear to be a correlation between the shape of the particle and the T_2 for the particle. It is difficult to draw any conclusions from SEM images of the particles other than that the particles have multiple morphologies within a single particle.

It is important to note that evacuation of BDPA with or without heating to remove benzene was not a reversible process, for these particles. After removal of benzene and exposure to air, the lines for all samples are broader and linewidths are more heterogeneous than before evacuation. The irreversibility of evacuation indicates that structural changes are occurring.

Conclusions. The commercial BDPA complex with benzene (1:1) has different T_2 for various particles, which was first evident from the rapid-scan spectra. The rapid-scan spectroscopy gave insight into the spin-spin relaxation of BDPA that was not obvious from CW and pulse EPR techniques alone. Heterogeneity in the g-value of BDPA particles was not evident at X-band. The BDPA particles have differing T_2 due to differences in crystal morphology and/or the ratio of benzene:BDPA in the crystal, which impact the effectiveness of spin exchange. BDPA is a stable organic radical that has an intense signal, and is therefore appealing as a standard in EPR experiments and for use in DNP (dynamic nuclear polarization). However, rapid-scan spectra and CW experiments have demonstrated that the commercial 1:1 BDPA:benzene complex is a heterogenous

sample. If BDPA is chosen as a standard during the development of a new method, the heterogeneity of the material should be taken into account.

5.4 DPPH

5.4.1. Introduction

DPPH is a common standard in EPR spectroscopy [70]. DPPH is used as a field calibration standard, a quantitative standard, as well as a sample for method development. DPPH exists as the monoclinic as well as the triclinic crystal structure depending on the solvent from which it is crystallized. It was previously shown in the literature that the most intense and narrow line for DPPH was achieved when recrystallized from carbon disulfide [71].

DPPH was also chosen as a sample to help develop rapid-scan EPR at X-band because of its narrow, Lorentzian line when recrystallized from CS_2. Effort was taken to recrystalize DPPH to achieve the narrowest line possible. By recrystallizing commercial DPPH from CS_2 a change in linewidth from 2.0 G to 0.65 G was observed.

5.4.2. Methods

Spectroscopy. CW spectra were collected on a Varian E-9 spectrometer. Rapid-scan data were collected on an E580. The microwave bridge has a 200 MHz bandwidth video amplifier. Signal acquisition was via a SpecJet I digitizer. A critically-coupled Bruker ER4118X-MD4 pulse ENDOR resonator was rotated such that the field resulting from the ENDOR coils was parallel to the B_0 magnetic field (section 5.2.2). Resonator Q was measured using pulse ring down. To avoid excess heating of the ENDOR coils, the sine wave for the magnetic field scans was generated with a Tektronix AWG2021

arbitrary waveform generator, operating in burst mode. The duty cycle was about 1%. The center field was selected to be close to resonance. The scan rate at the center of a sinusoidal scan, which is used to describe spectra, is given by Equation 3.6.

Sample Preparation. Several different recrystallization techniques were tried to achieve the narrowest line for DPPH. DPPH was recrystallized twice to obtain narrow linewidths (Figure 5.15). About 100 mG of DPPH was dissolved in a minimum amount (~5 mL) of CS_2. Crystals were allowed to form by slow evaporation of solvent on the benchtop (no ice) to achieve more needle-like crystals. The first recrystallization was relatively fast (5-10 minutes for crystals to appear) while the second recrystallization took closer to an hour for crystals to come out of solution. In earlier attempts, ice or even dry ice was used to recrystallize the DPPH which gave a less crystalline form of DPPH and a broader line.

After recrystallization, samples were either purged with nitrogen (Figure 5.15) or evacuated for 24–48 hours (Figure 5.16).

5.4.3. Results and Discussion

Initially, the CW spectrum of commercial DPPH was recorded (see Figure 5.14). The commercial DPPH was a powdery sample that had a ΔB_{pp}~2.0 G. The best recrystallization technique was to simply allow long crystals to grow in CS_2 on the benchtop. Purging with nitrogen (Figure 5.15) after recrystallization gave a narrower lineshape that exhibited g anisotropy, whereas simply evacuating the sample gave a narrower signal with no evident g anisotropy (Figure 5.16).

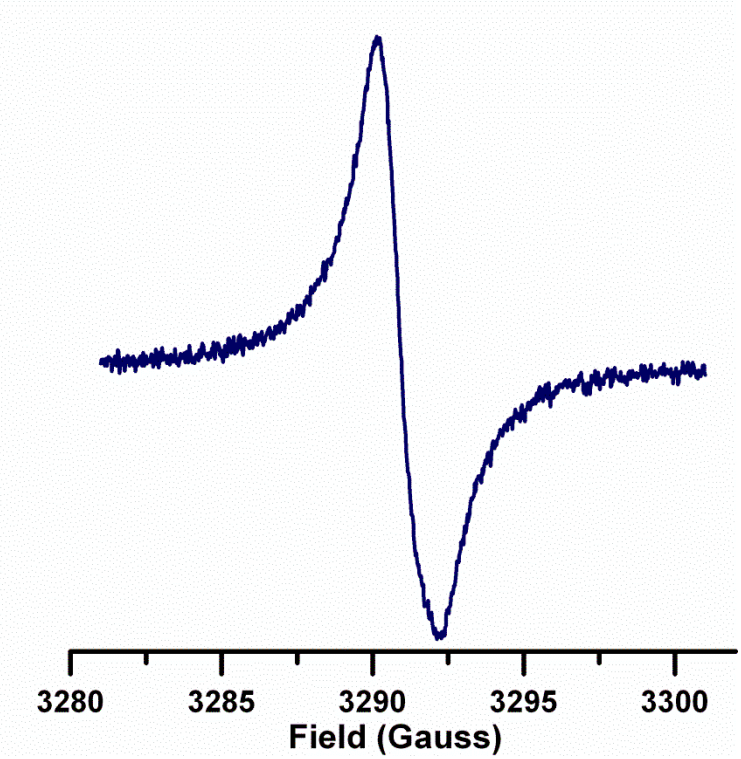

Figure 5.14. CW spectrum of commercial DPPH straight from the bottle in air. ΔB_{pp}~2.0 G. Center field: 3291.0 G, freq: 9.2311 GHz, microwave power: 0.2 mW, 0.1 G modulation amplitude, 100 kHz modulation frequency.

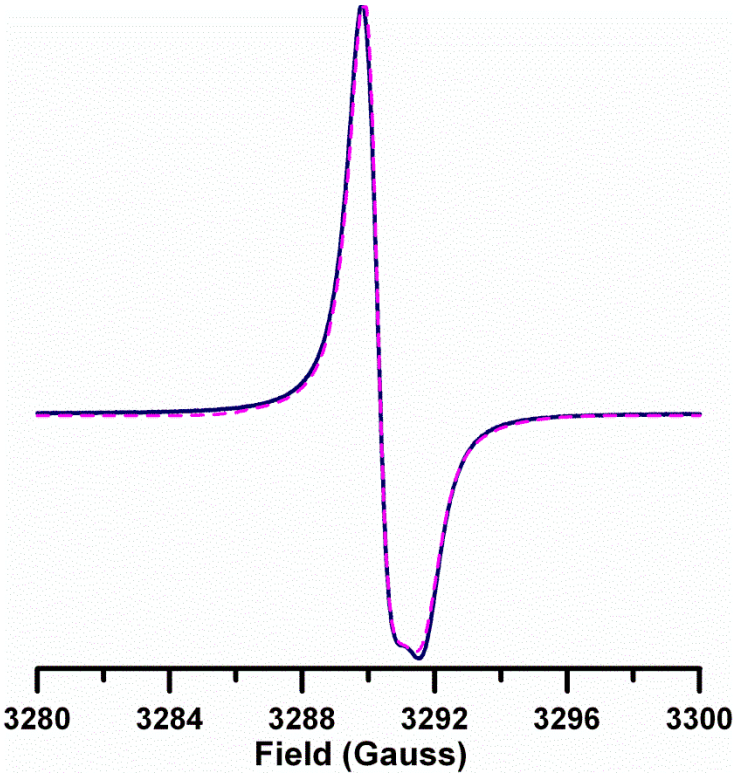

Figure 5.15. (Blue) CW spectrum of DPPH following recrystallization from CS_2 and purging with nitrogen. (Magenta dashed) Simulation using monmer program with linewidth of 0.9 G with g anisotropy. $g_{\perp}$~2.004 and $g_{||}$~2.0029.

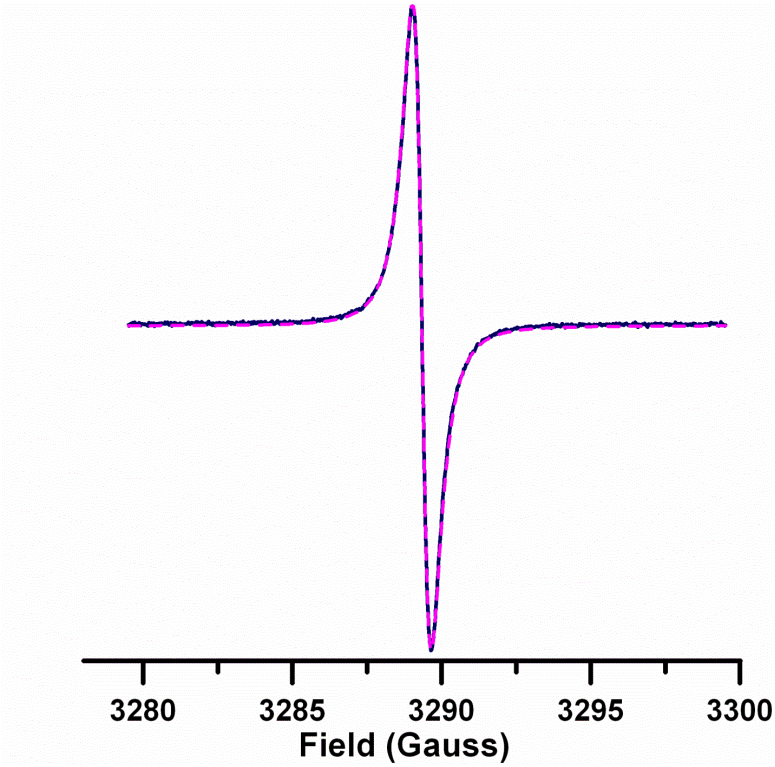

Figure 5.16. (Blue) CW spectrum of DPPH following recrystallization from CS_2 and evacuation. (Magenta dashed) Simulation using EPR2 with a Lorentzian line and a linewidth of 0.65 G.

Rapid-scan was attempted on the recrystallized sample that yielded a very narrow line (0.65 G), (Figure 5.17). This was done in the initial stages of the experiments with the ENDOR resonator, when the sweep rate limits were being pushed and tested. The scan rate of the spectrum in Figure 5.17 was very high, about 0.7 GG/s. These experiments were done to show the ability of the system to scan at such fast rates. The experimental data were limited by the SpecJet I digitizer, which has a maximum resolution of 4 ns. The simulation is not in good agreement with the data for several reasons. First, the spins did not have the opportunity to relax completely before scanning back through resonance. Second, the digitized signal has poor time-axis resolution and is

not a perfect representation of the signal response. Third, the resonator bandwidth was most likely filtering out some of the higher-frequency components of this signal. However, in spite of these limitations the best simulation of the rapid-scan spectrum used a T_2 that is consistent with the CW linewidth.

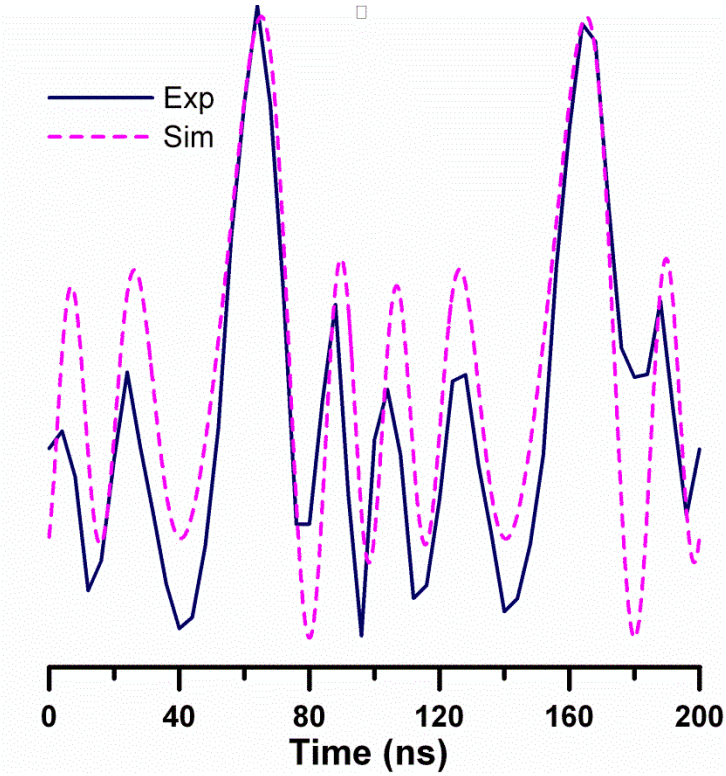

Figure 5.17. (Blue) Rapid-scan spectrum of DPPH following recrystallization and evacuation, collected with 5 MHz scan frequency, 43 G scan width (resulting in a rate of 670 MG/s) and 2 mW microwave power. (Magenta dashed) Simulation using Bloch Equations assuming a Lorentzian line with a T_2 ~100 ns. This relaxation time agrees with the linewidth (0.65 G).

5.5 Summary of rapid-scan of magnetically concentrated samples

BDPA, LiPc, and DPPH were helpful choices when initially developing rapid-scan at X-band. All of these samples are magnetically concentrated, resulting in strong signals

and narrow linewidths due to spin-spin exchange. LiPc was the most straightforward of the three samples. LiPc has an almost perfectly Lorentzian line with a T_2 of 80 ns. When LiPc is evacuated, it has a much longer T_2 (2.5 μs) and therefore narrower line [38]. With LiPc it was shown that rapid-scan spectra can be simulated to determine the spin-spin relaxation time. LiPc was also used to test deconvolution procedures and to troubleshoot spectrometers.

BDPA was a more complicated story than LiPc. The CW spectra of bulk BDPA could be simulated with a Lorentzian lineshape, suggesting that the linewidth was relaxation determined. However, rapid-scan experiments with bulk BDPA resulted in spectra that could not be simulated with a single T_2. This result indicated that the BDPA sample could not be represented by a single spin packet linewidth, and actually had a distribution of spin packet linewidths. From these simulations, rapid-scan EPR provided information about BDPA that was less evident in the CW experiments. BDPA showed that rapid-scan experiments can give insight into the relaxation of a sample that might not otherwise be evident with conventional CW EPR.

A crystal of DPPH that yielded a narrow Lorentzian linewidth can be obtained through recrystallization with CS_2. Further rapid-scan experiments with DPPH should be performed to gain further information about the relaxation of this sample. Specifically, rapid-scan spectra should be collected at a slower rate than shown in Figure 5.17, which would be more reasonable with the resonator bandwidth available.

Chapter 6: S/N comparison between rapid-scan and other EPR methods.

6.1 Materials samples with long relaxation times

6.1.1. Introduction.

One of the most exciting applications of rapid-scan EPR is to samples with long relaxation times. Our 2013 paper [72] summarizes the comparison between rapid-scan and CW for three of the samples (N@C60, amorphous hydrogenated silicon (a-Si:H), and neutral single substitutional nitrogen centers (N_S^0) in diamond) presented in this section. In 2011, we published a paper summarizing the comparison between rapid-scan and EPR methods for an irradiated quartz sample [73].

This section is focused on defect centers in solids, but the application of rapid-scan EPR to an OX63 (methyl tris(8-carboxy-2,2,6,6-tetra(hydroxyethyl)-benzo[1,2-d:4,5-d']bis(1,3)-dithiol-4-yl)-tripotassium salt) trityl sample will also be presented. The name "trityl" is given to paramagnetic compounds where the unpaired electron is primarily located on a tertiary carbon. Scheme 6.1 shows the structure of OX63.

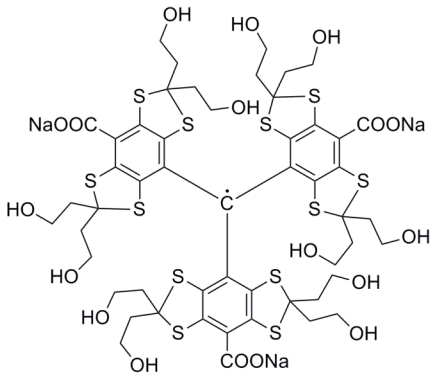

Scheme 6.1. Structure of methyl tris(8-carboxy-2,2,6,6-tetra(hydroxyethyl)-benzo[1,2-d:4,5-d']bis(1,3)-dithiol-4-yl)-tripotassium salt, also known as OX63.

Paramagnetic defect centers in solids that are important for many applications ranging from electronic devices[74, 75] to quantum computing [76-79] often are present in low concentrations and have long relaxation times, which makes characterization by electron paramagnetic resonance (EPR) challenging. For most magnetically dilute samples, as temperature is decreased below ambient, electron spin lattice relaxation times increase proportional to T^{-n} where $n > 2$ [20]. If temperature is decreased to increase the Boltzmann factor and thereby increase signal intensity, the increase in relaxation times often makes it more difficult to record unsaturated spectra that are free of passage effects, which negates the potential gains from increased Boltzmann factors. To enhance sensitivity for samples with long relaxation times, rapid-scan EPR can be used to collect EPR spectra.

In this section, *S/N* for spectra obtained by rapid-scan are compared with continuous wave (CW), field-swept echo detected, and Fourier Transform (FT) EPR with parameters selected to give less than 2% lineshape broadening. Five samples will be presented: amorphous hydrogenated silicon (a-Si:H) [80], 40 μM OX63, N@C_{60} [81], E'

defects in irradiated quartz, and neutral single substitutional nitrogen centers (N_S^0) in diamond [82]. In each sample the spin concentration is relatively low and the relaxation times at ambient temperature at X-band range from 3 to 2300 μs. For these samples we demonstrate that in the same data acquisition time, rapid-scan gives dramatically better *S/N* than CW or field-swept echo-detected EPR. Rapid-scan *S/N* also is better than FT EPR for N@C_{60} and comparable to FT EPR for N_S^0, without the need for the high source power that is required for pulse EPR. FTEPR could not be performed for a-Si:H because of the short T_2*. Further experiments should be performed to collect FTEPR for OX63 and the E' defects in irradiated quartz.

6.1.2. EPR Spectroscopy

The EPR spectra discussed in this section are collected on four different spectrometers. The CW spectra for all samples except the diamond sample were collected on a Bruker EMX-plus spectrometer. For the diamond sample, the CW spectra were collected on a EMX that had the ability to attenuate the power by 90 dB. Field-swept-echo spectra were collected on our locally built pulse spectrometer [83] . The FTEPR data were collected on the Bruker E580 spectrometer. All rapid-scan signals in this section were recorded on the Bruker E500T, which has a SpecJetII fast digitizer. A critically-coupled Bruker FlexLine ER4118X–MD5 dielectric resonator was used to minimize eddy currents induced by the rapidly-changing magnetic fields. The resonator *Q* was measured for each sample by pulse ring-down using a locally-designed addition to the bridge [28].

Power saturation curves were collected for all samples in this section by collecting CW and rapid-scan signals at a variety of powers (see section 2.4 for a

discussion on power saturation curves). Power saturation curves help determine signal enhancement with rapid-scan EPR relative to conventional CW and are needed to select powers that do not distort the signal.

6.1.3. Samples

Amorphous Hydrogenated Silicon. Undoped a-Si:H was deposited by standard plasma enhanced chemical vapor deposition (PECVD) according to a protocol used for thin film solar cell production [80, 84] provided by Alexander Schnegg at the Hemholtz institute in Berlin, Germany. The sample was 7.3 mg of fine powder contained within a 4 mm o.d. quartz tube. The number of spins in the sample was $(8.5\pm1.0)\text{x}10^{13}$. The paramagnetic states in a-Si:H are three-coordinated silicon atoms usually referred to as dangling bonds (db).

N@C_{60}. A 0.2% N@C_{60} in solid C_{60} sample was prepared by literature methods [85], and provided by Prof Aharon Blank, Technion, Israel. The solid was in a 0.8 mm capillary tube, supported in a 4 mm OD quartz tube.

Irradiated Quartz. The sample was a 2 mm diameter by 10 mm long rod of fused quartz (SiO_2) that had been irradiated to 240 kGy (24 MRad) with ^{60}Co γ rays. This sample is from the same batch as described in [86], which have spin concentrations of 5-$7\text{x}10^{17}$ spins/cm^3. Pulsed EPR of this sample yields an electron spin echo that is so strong that it fills the digitizer on a modern spectrometer with an essentially noise-free signal [86]. A weaker sample with about 30 times lower spin concentration has been prepared for signal-to-noise (S/N) quality control on modern pulsed EPR spectrometers

[87]. The Q was reduced to about 300 by putting water around the sample in a 4 mm OD quartz tube.

N_S^0 Defect in Diamond. A diamond sample with 20 ppb N_S^0 defects, grown by Chemical Vapor Deposition (CVD) [88], was purchased from Element Six Ltd (U. K.). The production and characterization of high purity single crystal CVD diamonds has been discussed [89]. The sample had dimensions of 4 x 4 x 2 mm and was wedged in a 4 mm OD Teflon tube. N_S^0 is one of the most common defects in synthetic diamond grown by either High Temperature High Pressure synthesis or CVD. This sample was provided by Prof. Mark Newton at the University of Warwick. There is a lattice distortion associated with N_S^0 due to the occupation of an N-C anti-bonding orbital by the extra electron (compared to carbon) of nitrogen. The unique N-C bond is about 25–30% longer than the normal C-C bond and the donor level is very deep (E_A = 1.7 eV). Much is known of the interaction of vacancies with nitrogen impurities. Charge transfer from the N_S^0 deep donor produces V^-: $V^0 + N_S^0 \rightarrow V^- + N_S^+$. Upon annealing above 900 K the stationary N_S^0 readily traps mobile vacancies to produce nitrogen vacancy (pair) complexes: $V^0 + N_S^0 \rightarrow (N_S\text{-}V)^0$ and $(N_S\text{-}V)^0 + N_S^0 \rightarrow (N_S\text{-}V)^-$. $(N_S\text{-}V)^-$ is one of the most intensively colored centers. It has a zero phonon line at 1.945 eV and the photoluminescence intensity is strongly modulated depending on whether the system is in the $m_S = \pm 1$ or $m_S = 0$ ground electron spin state, facilitating optically detected magnetic resonance on single defects at room temperature. It has recently been shown that $(N_S\text{-}V)^-$ can be grown into CVD diamond as a unit [79] as well as being produced as described above.

OX63 trityl sample. A 0.2 mM aqueous OX63 sample was obtained from Josh Biller, University of Denver. The radical was provided by Prof. Howard Halpern, University of Chicago. 200 μL of the 0.2 mM OX63 sample was mixed with 800 μL ethanol to reach a final concentration of 40 μM. The solution was transferred into a 4 mm quartz EPR tube until it reached a height of 4 mm. The sample was degassed in an analogous fashion to the nitroxyl radical solutions in section 6.2 by performing four freeze-pump-thaw cycles and then the tubes were flame sealed.

6.1.4. Results

Relaxation Times. The electron spin relaxation times are summarized in Table 6.1. The values of T_1 range from 11 μs for a-Si:H to 2300 μs for 20 ppb N_S^0 in diamond. Values of T_2 are from 2.8 μs for N@C_{60} to 230 μs for N_S^0 in diamond. For N@C_{60} the values of T_1 are shorter for the $m_I = \pm 1$ lines than for $m_I = 0$, but there is little m_I dependence of T_2 (Table 6.2). These values are orders of magnitude longer than for typical organic radicals in fluid solution at ambient temperature [20].

Table 6.1. Electron relaxation times, line widths, and microwave B_1 for CW and rapid-scan for paramagnetic centers in materials.

Sample	T_1 (μs)[a]	T_2 (μs)[a]	ΔB_{pp} (G)[a]	B_1 for CW[b] (mG)	B_1 for rapid-scan[b] (mG)	Rapid-scan rate (MG/s)
a-Si:H	11	3.3	6	35	200	3.9
40 μM OX63	14	5	0.16	~12	96	0.6
N@C_{60}	120 – 160	2.8	0.25	6	53	1.5
E' in irradiated fused quartz	200	20	~1[c]	17	220	4.7
N_S^0 in diamond[d]	2300	230	0.045	0.03	5.8	0.14

[a]Uncertainties are about ±5% for relaxation times and ±2% for line widths
[b] Selected to give less than 2% power broadening
[c] Lineshape is anisotropic
[d] Parameters are for nitrogen $m_I = 0$ line.

Table 6.2. Relaxation Times for N@C_{60}.[a]

	LF (μs)	CF (μs)	HF (μs)
T_1	118	161	117
T_2	2. 9	2.4	2.8

[a]Uncertainties are about ±5%

Power Saturation. Power saturation curves measured at the center of the spectra for a-Si:H, OX63, N@C_{60}, E' defects in irradiated quartz, and N_S^0 in diamond are shown in Figures 6.1–6.5. For the rapid-scans the signal amplitude after deconvolution was measured. To compare rapid-scan and CW spectra, the relative amplitudes were normalized to be the same at low B_1, in the linear response region.

For a-Si:H the dependence of signal amplitude on B_1 deviates from linearity above B_1 ~35 mG for the CW spectra, whereas for rapid-scans at a rate of 3.9 MG/s

deviation from linearity is above B_1 ~200 mG (Figure 6.1). At B_1 ~35 mG for CW and ~200 mG for rapid-scan the power broadening of the signal is about 2%.

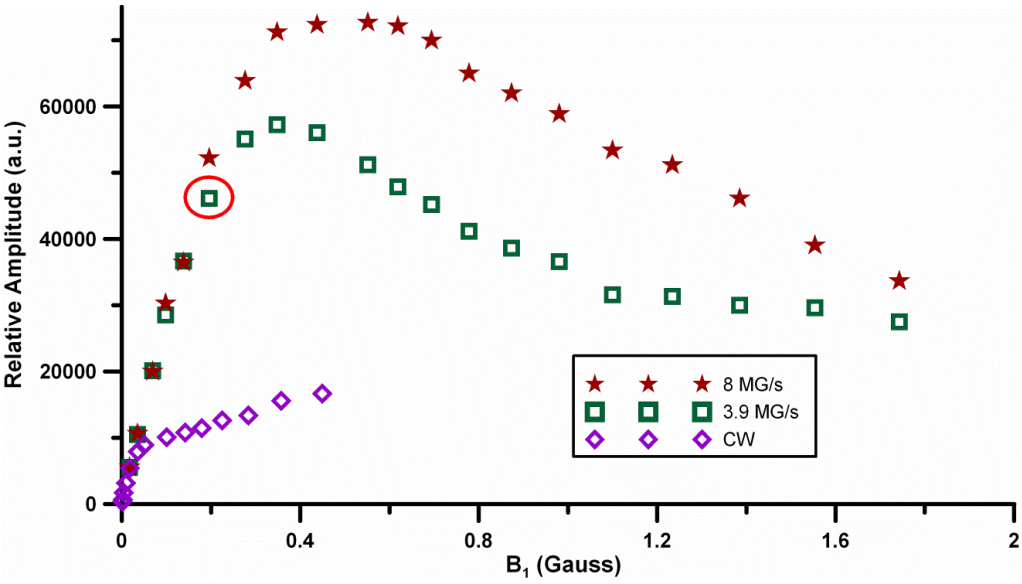

Figure 6.1. Power saturation curves for the a-Si:H sample obtained by CW and sinusoidal rapid-scan at two scan rates. The point that corresponds to the acquisition conditions for the rapid-scan spectra shown in Figure 6.6A is circled. Given the long relaxation times the shape of the CW saturation curve is almost certainly due to a mix of absorption and dispersion spectra.

For 40 μM OX63, both the CW and rapid-scan spectra were collected on the E500T spectrometer with the dielectric resonator. An approximate efficiency of 0.48 G/√(Watt) was used to discuss B_1 for this sample. However, these data were collected recently and a value for Q was not yet determined. Thus, the exact efficiency cannot be determined for this sample. The dependence of signal amplitude on the square root of power (B_1) deviates from linearity above 12 mG for CW spectra, whereas for rapid-scan at 0.6 at 0.6 MG/s, the signal deviated from linearity at 96 mG (Figure 6.2).

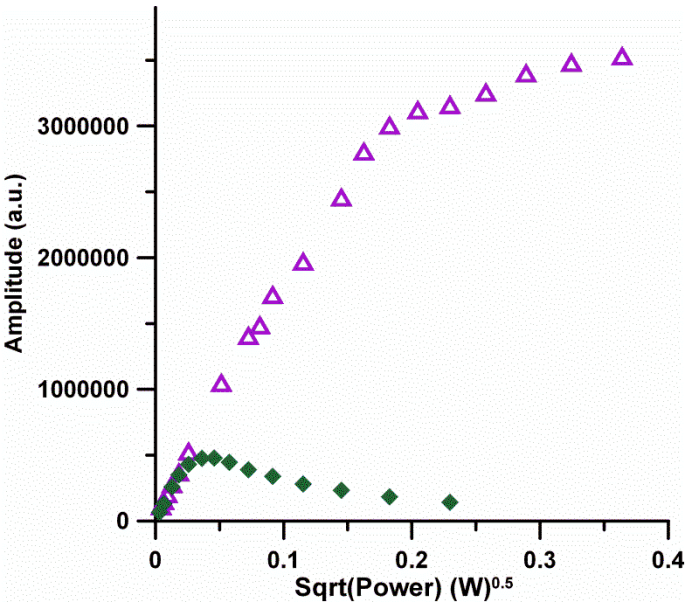

Figure 6.2. Amplitude of CW (green diamonds) and rapid-scan spectra (purple triangles) of OX63 as a function of square root of power. The rapid-scan frequency was ~13 kHz and the scan width was 14.3G (0.6 MG/s). Rapid-scan signals were 1024 averages collected in ~5 seconds. CW spectra were single scans, collected in ~30 seconds.

For $N@C_{60}$ the dependence of signal amplitude on B_1 deviates from linearity above B_1 ~6 mG for the CW spectra, whereas for rapid-scans at 5 MG/s deviation from linearity is above B_1 ~53 mG (Figure 6.3).

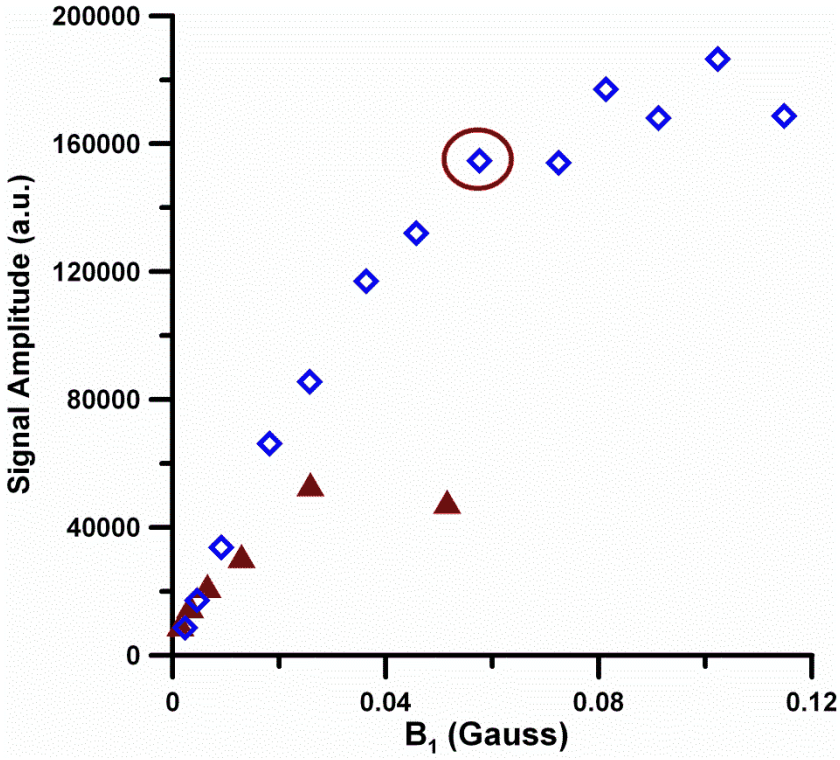

Figure 6.3. Power saturation curves for the N@C_{60} sample obtained by CW (filled triangles) and sinusoidal rapid-scan (open diamonds). The rapid-scan spectra were acquired at a scan rate of 1.5 MG/s. The point that corresponds to the acquisition conditions for the rapid-scan spectra shown in Figure 6.8A is circled.

At the time that the quartz data was collected, the EMX with the two power attenuators was not yet in the Eaton lab. The relaxation times of the E' defects in quartz are so long that passage effects caused distortions of the CW spectra at powers that would have been used to obtain a power saturation curve on the older E9, so only the rapid-scan power saturation curve is shown in Figure 6.4.

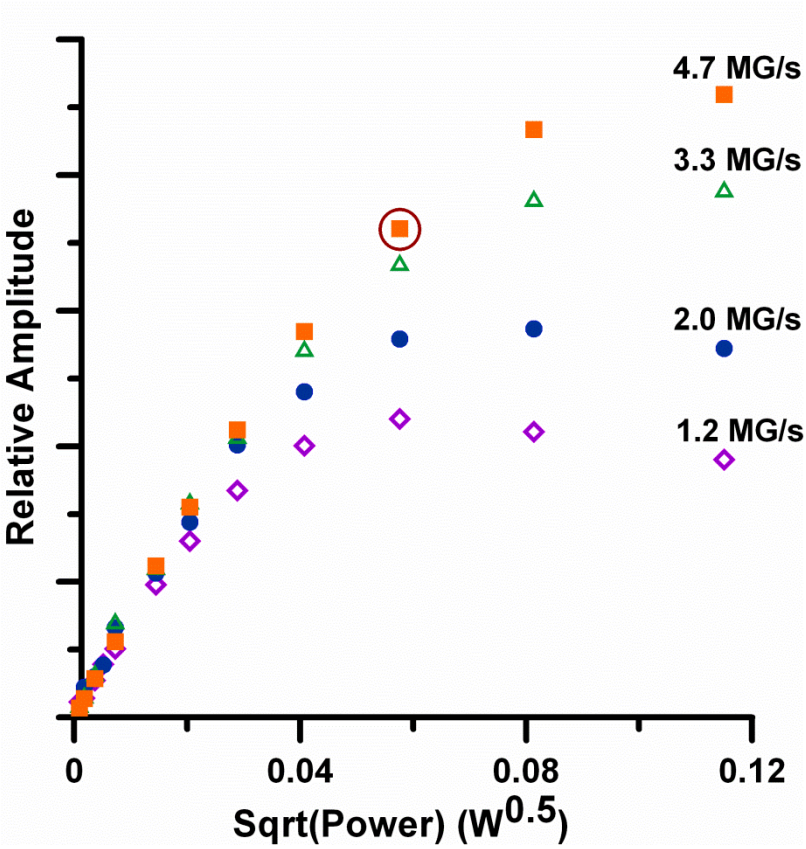

Figure 6.4. Power saturation curve for the center line of the spectrum of E' defects in irradiated quartz by rapid-scan at several different rates. The point that corresponds to the acquisition conditions for the spectrum shown in Figure 6.9A is circled.

For N_S^0 in diamond, (like the E' defects in quartz) the relaxation times are so long that passage effects caused distortions of the CW spectra at powers that would have been used to obtain a power saturation curve, so only the rapid-scan power saturation curve is shown in Figure 6.5. The amplitudes of extensively signal-averaged CW spectra at 70 dB attenuation (B_1 ~0.3 mG) were about twice as large as spectra at 76 dB, which indicates that the B_1 used to record the data in Figure 6.11E was in the linear response regime for the signal. The dependence of signal amplitude on B_1 for the CW spectra deviates from

linearity above about $B_1 \sim 0.25$ mG, however, for rapid-scan spectra at a scan rate of 0.14 MG/s deviation from linearity is observed above about $B_1 \sim 6$ mG (Figure 6.5).

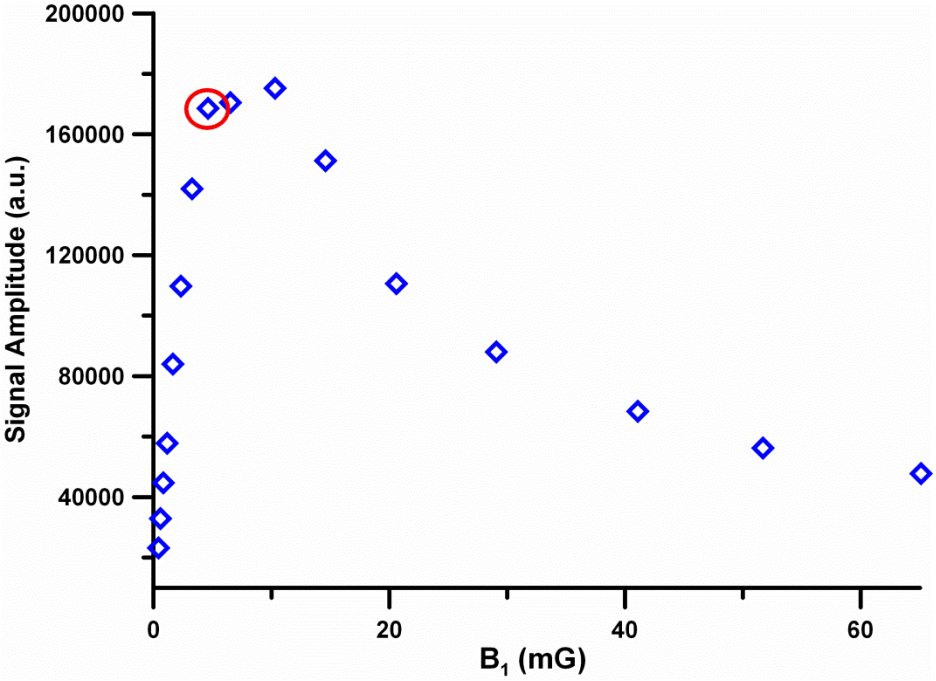

Figure 6.5. Power saturation curve for the center line of the spectrum of 20 ppb N_S^0 in diamond obtained by triangular rapid-scan at 0.14 MG/s. The point that corresponds to the acquisition conditions for the spectrum shown in Figure 6A is circled.

For the three samples, the B_1 that can be used for the same minimal power saturation decreases as T_1 and T_2 increase (Table 6.1). However for each of the samples, B_1 for rapid-scan is larger than for CW by factors of about 7 to 200. The ability to use higher B_1 without saturating the sample is a major advantage in improving *S/N*. As shown in Figures 6.1–6.5 the relative signal amplitude is substantially higher at the higher B_1 that can be used in rapid-scan than for the same degree of power saturation for CW spectra. Since rapid-scan spectra were obtained in the linear response regime, scan

periods less than T_1 do not decrease signal amplitudes, which is a major advantage relative to pulsed experiments.

Lineshapes. The spectra obtained by various EPR methods for a-Si:H, 40 μM OX63, 0.2% N@C_{60}, E' defects in irradiated quartz and the center line (nitrogen $m_I = 0$) of N_S^0 in diamond are shown in Figures 6.6–6.10 The a-Si:H sample had the broadest line width, $\Delta B_{pp} \approx 6$ G which corresponds to FWHM of the absorption spectrum of 10.2 G (Figure 6.6). The lineshapes obtained from rapid-scan, CW, and field-swept echo detected spectra are in good agreement. Since $T_2^* = 6.56 \times 10^{-8}$ (G s)/ΔB_{pp} this Lorentzian line width corresponds to $T_2^* \sim 10$ ns, which is too short relative to the deadtime of the E580 spectrometer to permit measurement of an FID as required for FTEPR.

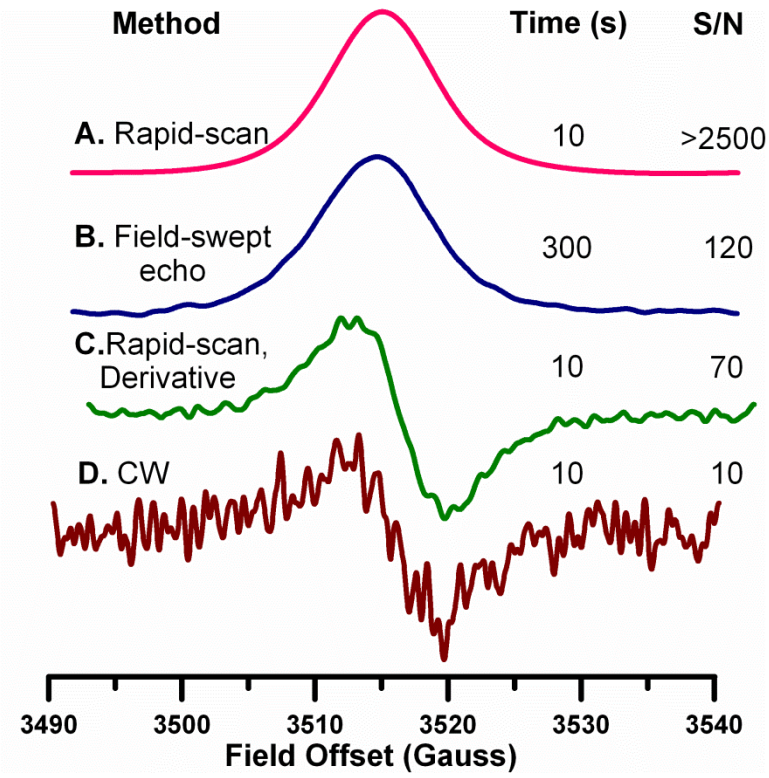

Figure 6.6. Comparison of spectra of a-Si:H. A) Slow-scan absorption spectrum obtained by deconvolution of sinusoidal rapid-scan signal acquired with a scan rate of 3.9 MG/s, 102400 averages, and B_1 = 200 mG. B) Field-swept echo detected spectrum obtained with constant 500 ns spacing between pulses, SRT (shot repetition time) = 100 μs, 1024 shots/point, 10 scans. C.) Derivative of deconvolved rapid-scan spectrum. D) Conventional field-modulated first-derivative CW EPR spectrum acquired with 2 G modulation amplitude at 30 kHz, and B_1 = 35 mG.

The peak-to-peak linewidth of OX63 is 160 mG (Figure 6.7). Good agrement for linewidth with CW and rapid-scan was observed. OX63 should be further studied to examine FTEPR and field-swept echo detected EPR for this sample.

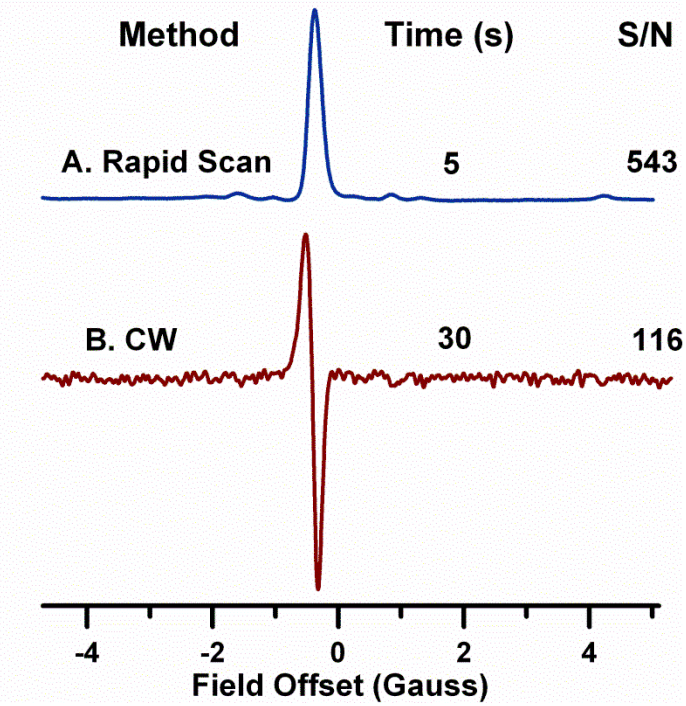

Figure 6.7. Comparison of rapid-scan and conventional CW EPR spectra of OX63. (A) Slow scan absorption spectrum obtained by deconvolution of rapid-scan signal obtained with a scan rate of 0.6 MG/s and microwave power about 40 mW (B_1= 90 mG B_1). 1024 averages were recorded in about 5 sec with a 100% pulse on/off duty cycle with a net duty cycle of 100%. B) Single scan of a conventional field-modulated first-derivative CW EPR spectrum of the same sample, obtained in 30 sec using 2 mW power, 10 kHz modulation frequency, and 50 mG modulation amplitude.

The spectrum of 0.2% N@C_{60} has three lines with a nitrogen hyperfine splitting of 5.7 G (Figure 6.8). There is good agreement between the absorption spectra obtained by rapid-scan (Figure 6.8A), field-swept echo decay (Figure 6.8B), and FT-EPR (Figure 6.8C). The first-derivative of the rapid-scan absorption spectrum (Figure 6.8D) has ΔB_{pp} = 0.23 G for the low field line, 0.25 G for the center line, and 0.28 G for the high field line (Figure 6.8E). These measurements are consistent with the literature [80] which reported the nitrogen hyperfine to be ~6 G and the CW line width at 0.2% doping to be ~0.25 G.

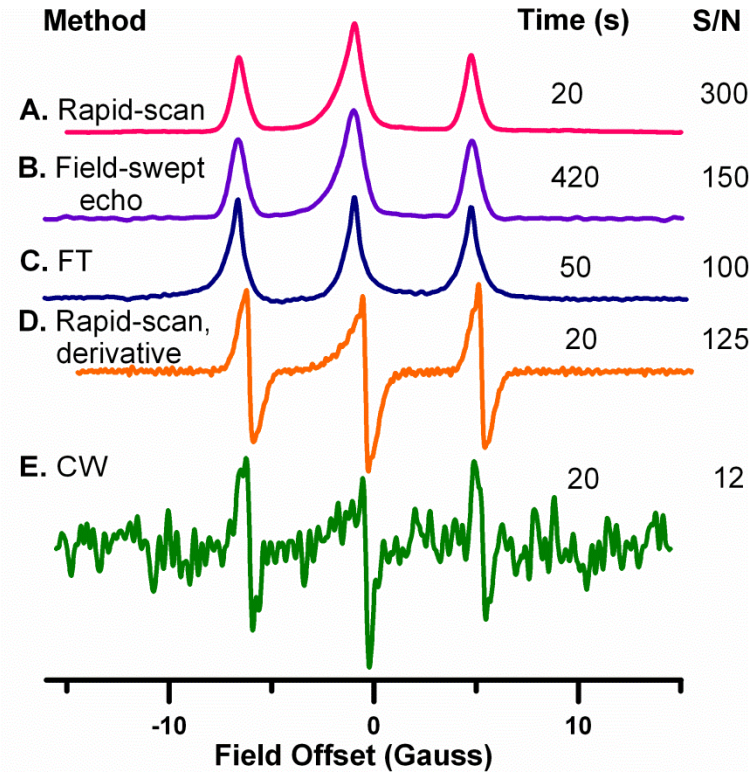

Figure 6.8. Comparison of spectra for 0.2% N@C_{60}. A) Slow-scan absorption spectrum obtained by deconvolution of sinusoidal rapid-scan signal acquired with a scan rate of 1.5 MG/s, 102400 averages, and B_1 = 53 mG. B.) Field-swept echo detected spectrum obtained with constant τ = 600 ns spacing between pulses, SRT = 200 μs, 1024 shots/pt, 2 scans. C) FT-EPR for data obtained with SRT = 200 μs, 90° tip angle, and 20,480 averages . D) Derivative of deconvolved rapid-scan spectrum. E) CW spectrum acquired with 0.1 G modulation amplitude at 30 kHz and B_1 = 6 mG.

CW spectra of the E′ defects are shown in Figure 6.9D. The spectrum has parallel and perpendicular components due to g-anisotropy. The power dependence of the E′ CW spectrum is difficult to characterize because the signal saturates so readily. At high microwave power, saturation and passage effects change the spectrum, causing it to look like an inverted absorption spectrum.

The rapid-scan oscillations are observed on the E′ signal as a small negative-going feature on the high-field side of the spectrum (Figure 6.9A). The g-value

dispersion of the defect centers results in interference of the oscillations from individual spin packets, so the rapid-scan response does not show as much oscillatory behavior as would be predicted for the known relaxation times [45, 86]. The slow scan absorption spectrum was obtained by deconvolution (Figure 6.9B). For comparison with the conventional spectrum (Figure 6.9D), pseudomodulation was used to calculate the first-derivative (Figure 6.9C).

The field-swept echo-detected spectrum of the E′ signal is shown in Figure 6.10A and the first derivative obtained by pseudomodulation is shown in Figure 6.10B.

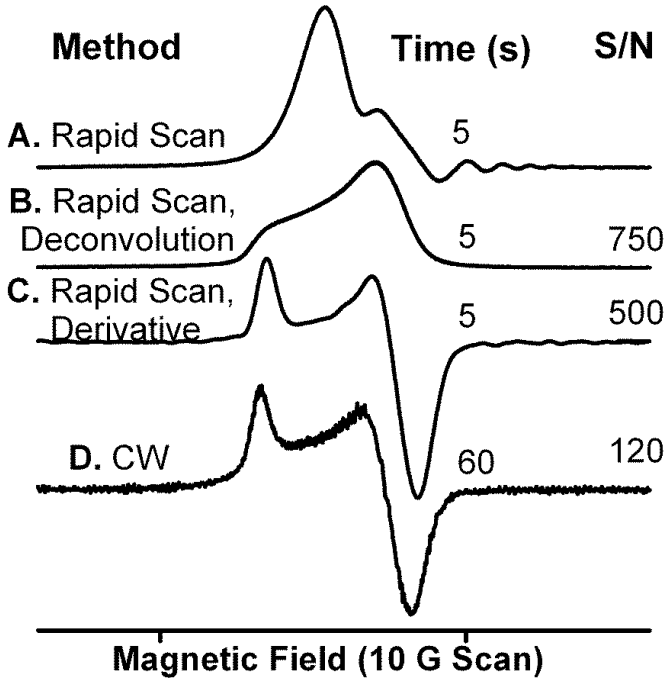

Figure 6.9. Comparison of rapid-scan and CW EPR spectra of E' center in irradiated fused quartz. a) As-recorded sinusoidal rapid-scan signal obtained with a scan rate of 4.7 MG/s. 1024 averages were recorded in about 5 sec. The incident microwave power was about 3.3 mW. b) Slow-scan absorption spectrum obtained by deconvolution of signal in a. c) First derivative spectrum obtained by pseudomodulation of the signal in b. d) Single scan of a conventional field-modulated first-derivative CW EPR spectrum of the same sample, obtained in 1 minute using about 0.02 mW incident microwave power (40 dB), 10 kHz modulation frequency and 0.05 G modulation amplitude.

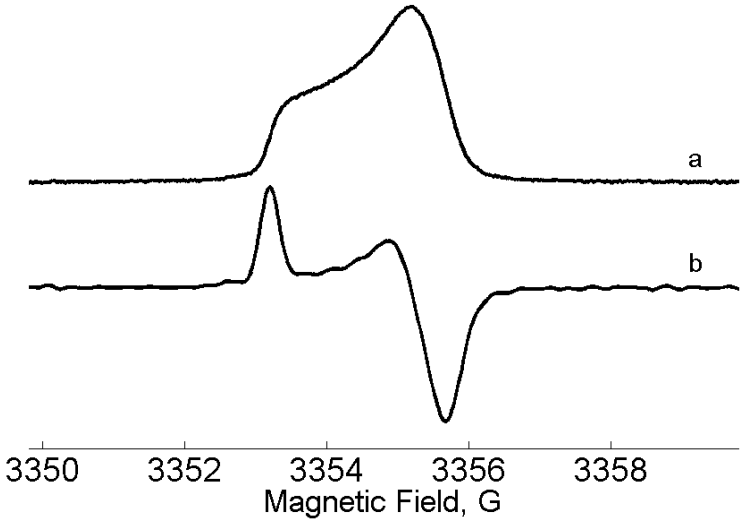

Figure 6.10. a) As-recorded X-band field-swept, echo-detected EPR spectrum of irradiated quartz, obtained with $\pi/2$ = 1024 ns, π = 2048 ns, 1 scan with 4 step phase cycling, power = 15 mW, 1024 points, 10 G sweep width, 2 ms pulse repetition time. Data were acquired in 20 seconds. b) First derivative spectrum obtained by pseudomodulation of the signal in a.

The $m_I = 0$ line for N_S^0 in diamond had the narrowest width, with FWHM of the absorption spectrum of 80 mG, and ΔB_{pp} ~45 mG (Figure 6.11). The ΔB_{pp} calculated from the first-derivative of the rapid-scan signal is in good agreement with the value determined from a CW spectrum obtained with extensive signal averaging. The low modulation amplitude and low power required to obtain undistorted spectra of this sample cause the *S/N* in the CW spectra to be poor. It is important to note that on a typical EMX CW spectrometer with only a standard 60 dB attenuator, the acquisition of a CW spectra would not have been possible because at 60 dB the lineshape is distorted by passage effects, even when the modulation frequency is 6 kHz. The field-swept echo-detected spectrum was broadened by about 30% due to limitations in the integrator gate (Figure 6.11B). The 45 mG Lorentzian lineshape for N_S^0 in diamond is much broader

than the spin-packet line width of about 0.4 mG calculated for T_2 ~200 μs. In diamond at concentrations higher than about ten atomic parts per million the EPR line width is linearly dependent on the paramagnetic defect concentration [90]. At lower concentrations the electron-nuclear dipolar contribution to the line width dominates and the width of the line is concentration independent. A limiting Gaussian line width of ΔB_{pp} = 100 mG had been predicted due to interaction with ^{13}C[90]. Approximately Lorentzian lineshapes are predicted when the concentration of interacting nuclear spins is less than about 3% [91, 92].

The data acquisition parameters for each method were selected to give minimal spectral broadening, so except for the broadening of the spin-echo detected spectra of N_S^0, the line widths obtained by various methods are in good agreement.

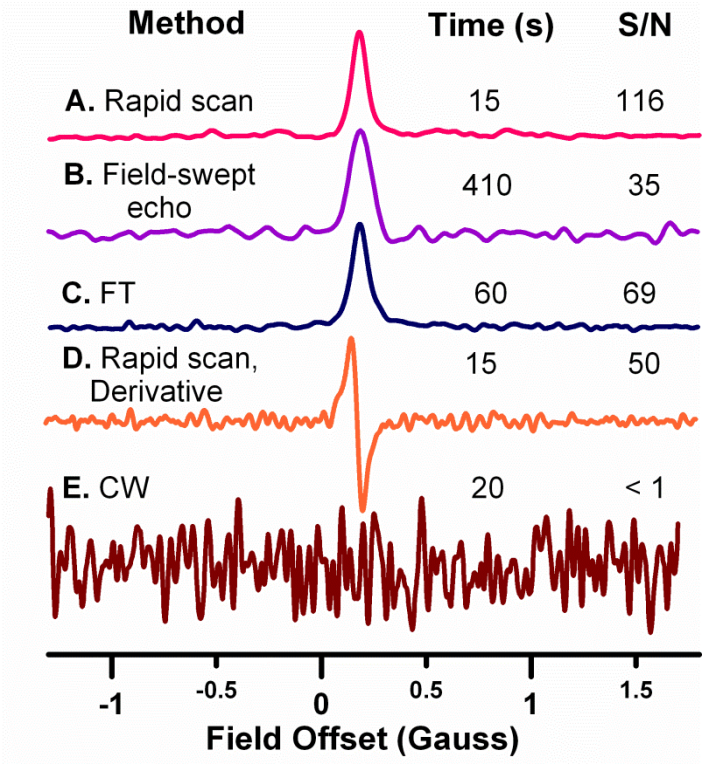

Figure 6.11 Comparison of spectra for the center line of N_S^0 in diamond. A) Slow-scan absorption spectrum obtained by deconvolution of triangular rapid-scan signal acquired with a scan rate of 0.14 MG/s, 102,400 averages, B_1 = 4 mG. B) Field-swept echo detected spectrum with a constant 600 ns spacing between pulses, SRT = 3 ms, 64 shots/pt, 1 scan. C) FT-EPR of data obtained with an SRT of 200 μs, 24° tip angle, and 40960 averages. D) Derivative of deconvolved rapid-scan spectrum. E) CW spectrum acquired with 0.05 G modulation amplitude at 6 kHz and B_1 = 0.25 mG, one scan.

Signal-to-noise. Spectra for a-Si:H (Figure 6.6), 40 μM OX63 (Figure 6.7), N@C_{60} (Figure 6.8), E' defects in quartz (Figure 6.9), and N_S^0 in diamond (Figure 6.10) show significantly higher *S/N* for rapid-scans than for CW obtained in the same amount of time. For all samples but OX63 (field-swept echo-detected was not collected for this sample), system limitations for the field swept echo experiments prevented data acquisition in the same short times that were used for rapid-scan and CW EPR, but even

with longer data acquisition times the *S/N* by echo detection was not as good as for rapid-scan.

The *S/N* and data acquisition times for the four methods are summarized in Table 6.3. The CW spectra were obtained on a Bruker EMX because the *S/N* for CW was higher than on the E500T. Improvement in the *S/N* for CW spectra on the E500T would probably also improve the *S/N* for rapid-scan. To compare *S/N* for experiments with different acquisition times, the *S/N* per $\sqrt{t}$ was calculated (Table 6.3), which takes into account the fact that *S/N* increases proportional to the $\sqrt{n}$ where n is the number of scans. For each of the samples the relative *S/N* improved in the order CW < echo detected < FT ≤ rapid-scan. The improvements for rapid-scan relative to CW ranged from 25 for $N@C_{60}$ to > 250 for a-Si:H. The much larger advantage for a-Si:H occurs because although relaxation times are long, the signal is inhomogeneously broadened and therefore the rapid-scan experiments could be performed without lowering resonator *Q*. For the other samples the CW experiments were performed at higher *Q* than the rapid-scan experiments. These advantages of rapid-scan EPR relative to CW and spin-echo detected EPR are typical of what can be expected for samples with long spin lattice relaxation times.

The quartz sample used for the comparison had a relatively high dose. For irradiated fused quartz T_1 is approximately independent of dose, and T_2 becomes longer as dose is decreased, with values approaching T_1 at low dose [45] The longer T_2 at lower doses means that passage effects are an even greater problem at lower doses. Thus the

advantages of rapid-scan over CW spectroscopy will be greater at lower doses than shown in the high-dose example.

Table 6.3. Data acquisition times, *S/N*, and relative *S/N*.

Sample	Method	Acquisition Time (seconds)	*S/N* [a]	*S/N* per sqrt(sec) relative to CW
a-Si:H				
	CW	10	10	1
	Field-swept echo	300	120	2.2
	Rapid-scan	10	>2500	>250
40 μM OX63				
	CW	30	116	1
	Rapid-scan	5	543	11.5
0.2 % N@C_{60}				
	CW	20	12	1
	Field-swept echo	420	150	2.7
	FT-EPR	50	100	5.3
	Rapid-scan	20	300	25
E' in Irrad. Quartz				
	CW	60	120	1
	Field-swept echo	20	400	6
	Rapid-scan	5	500	14.4
N_S^0 in diamond				
	CW	20	<1	1
	Field-swept echo	240	64	>18[b]
	FT-EPR	30	160	>130
	Rapid-scan	15	116	>140

[a] *S/N* is peak-to-peak signal amplitude (for CW) or signal amplitude (all other EPR methods) divided by rms noise.

[b]The field swept echo detected spectra were recorded with a conservative $SRT \sim 4\ T_1$. If $SRT \sim 1.4\ T_1$ had been used, the *S/N* per sqrt(sec) relative to CW would have been >~14.

The *S/N* for rapid-scan compared with FTEPR is strongly sample dependent. For a-Si:H T_2* (~ 10 ns) is too short relative to the instrument deadtime to permit FTEPR.

For $N@C_{60}$ the S/N for FTEPR spectra obtained with 90^o pulses and SRT = 1.4 T_1 was about a factor of 5 poorer than for rapid-scan. The T_1 for $N@C_{60}$ is too short, relative to the shortest SRT available on the spectrometer, to take advantage of potential signal enhancement using Ernst angle pulses [93]. However, even it that had been possible, it would only enhance *S/N* by about 60%, and the *S/N* for FTEPR would still be substantially lower than by rapid-scan. For N_S^0 in diamond the FTEPR experiments were performed with SRT ~0.1 T_1 and an Ernst angle of 26^o, which gave *S/N* comparable to that for rapid-scan.

Comparisons in Table 6.3 are based on the absorption signal for the rapid-scan, FT, and echo detected spectra with the conventional first-derivative CW spectrum. As shown in Figures 6.6 to 6.11, taking the derivative of the absorption spectrum increases the high frequency noise. Uncertainty analysis has shown that if the *S/N* is the same, the number of spins can be calculated from the absorption spectrum about twice as accurately as from the first derivative signal so the absorption signal is advantageous for spin quantitation [46].

6.1.5 Discussion

S/N. There are several reasons why rapid-scan gives improved *S/N* relative to CW EPR. During the rapid-scans, the energy absorbed by the spins for the same microwave B_1 is less than in CW EPR, so the signal does not saturate as readily. Because higher B_1 can be used, higher *S/N* can be obtained by rapid-scan than by CW EPR. The signals in the real and imaginary channels of a quadrature detector are combined to further improve the *S/N* ratio by up to a factor of $\sqrt{2}$ [94]. In addition, the full amplitude of the absorption

signal is detected in each scan, unlike CW where modulation broadening limits the magnitude of the modulation. Coherent averaging in rapid-scan spectroscopy functions like a narrow-banded comb filter in the frequency domain, which substantially decreases noise [95]. Unlike echo-detected EPR, in rapid-scan it is not necessary to form a spin echo, so measurements can be performed with good signal intensity even if T_2 is short. The problems inherent in spectrometer deadtime that restrict FT EPR to samples with long T_2* are avoided. Unlike pulsed EPR, high power amplifiers are not needed.

The experiments discussed here were designed to maximize *S/N* while minimizing the line broadening. For each of the methods employed, *S/N* can be increased at the expense of lineshape broadening. For some measurements signal broadening may be an acceptable price to pay for improved *S/N*. It is therefore important to understand the different trade-offs that exist for the various experiments.

In CW experiments, the parameters that can be adjusted to improve *S/N* are modulation amplitude, power, and the time constant for the low-pass filter. The *S/N* increases with increasing modulation amplitude, however if the modulation amplitude is too high, the signal broadens. Similarly, *S/N* can be increased by increasing B_1 up to the peak of the power saturation curve, but this occurs at the expense of power broadening. A low-pass filter can decrease high frequency noise, but increased filtering also can broaden the line.

For rapid-scan experiments the field scan rate and microwave power can be varied. More scans can be averaged per unit time at faster scan frequencies. The faster the scan rate, the larger the B_1 that can be used for the same degree of power saturation. However if the scan rate becomes fast enough that the signal bandwidth exceeds the

resonator bandwidth the signal is broadened. The constraints on the low-pass filter are similar to those for CW.

The integrator gate and the shot repetition time impact the *S/N* for a field-swept echo detected spectrum. For $N@C_{60}$ the *SRT* was $1.4T_1$ which gives approximately the maximum echo per unit time. For N_S^0 in diamond a more conservative SRT of 4 T_1 was used. The S/N in the echo detected spectra is strongly dependent on the length of the integrator gate. If the integrator gate is narrow relative to the echo, the *S/N* is enhanced, but lines are broadened because of truncation of low frequency components of the signal. Conversely, a broad integrator gate includes more low frequency components of the signal and gives narrower lines. There are hardware limitations on timing of field-swept echo-detected experiments at X-band using pulsed TWT amplifiers in commercial spectrometers.

The S/N of the FTEPR signal can be maximized by adjusting the *SRT* and decreasing the flip angle using the Ernst angle calculation. However hardware limitations on SRT limit this approach. One advantage of FT for narrow signals is that the complete spectrum can be acquired with a single pulse.

This report discusses applications of rapid-scan to a few samples with long electron spin relaxation times at ambient temperatures. There are many other important classes of samples that have long electron spin relaxation times at the temperatures for which EPR data is required, and for which rapid-scan is expected to provide significant advantages relative to other EPR methods. Decreasing temperature increases the difference in Boltzmann populations between $m_S = \pm 1/2$ electron spin states which has the potential to increase the intensity of the EPR signal. This is particularly important for

species present at low concentrations. However electron spin lattice relaxation times for most magnetically dilute samples increase proportional to T^n with $n \geq 2$. The longer relaxation times limit the B_1 that can be used to record CW spectra and limit the repetition times that can be used in pulsed experiments. Thus for CW and pulse experiments the rapid increase in T_1 with decreasing temperature can more than offset the potential advantage of higher Boltzmann populations at lower temperatures.

The rapid-scan drivers in the Eaton laboratory currently can generate scan widths up to about 80 G, with a tradeoff between scan width and scan frequency [48, 96]. These scan widths are sufficient to record spectra for a wide range of organic radicals. Work by Hyde et al is focused on splicing together multiple rapid-scan segments to record wider EPR spectra [91, 92]. Improved methods for recording broad spectra are currently being developed in the Eaton lab.

Device-limiting paramagnetic states at functional interfaces or in thin film electronic devices may be present in low concentrations [75]. Electrically detected magnetic resonance is expected to have higher sensitivity than rapid-scan for these sites but spin quantitation is difficult [97]. Organic co-factors in biomolecules including protein-derived radicals, semiquinones, or flavins typically are present in low concentrations, and have very long relaxation times at cryogenic temperatures. Intermediates that are studied by freeze quenching reactions also are present in low concentrations.

Higher magnetic fields/frequencies are predicted to be advantageous for rapid-scans for several reasons. At higher frequency the same resonator Q corresponds to a

higher bandwidth which permits faster scans without signal broadening. Greater g value dispersion often results in broader lines, which increases T_2* and permits the use of higher Q and/or faster scans. The smaller size of higher frequency resonators means that sample sizes are smaller, so the size of the scan coils can be decreased which decreases the power required for a scan and facilitates wider scans.

For spin quantitation rapid-scan has the additional advantage that the number of unpaired electrons can be determined more accurately from the absorption spectrum than from the first derivative spectrum that is recorded in traditional CW experiments.

The enhancements in *S/N* observed for the materials samples examined in this study thus have implications for a wide range of applications both in materials science and biomedicine.

Conclusion. Samples with relatively long relaxation times are difficult to measure with conventional CW and echo-detected field-swept EPR. There are limitations to the use of FTEPR when T_2* is short and when spectral bandwidth is large. For comparable selections of parameters required to obtain accurate line shapes and quantitative signal intensities, rapid-scan yields higher *S/N* than CW or field-swept echo-detected EPR. The advantage of rapid-scan relative to FTEPR is strongly sample dependent. Table 6.3 summarizes the *S/N* enhancement observed with rapid-scan EPR for a-Si:H, OX63, N@C_{60}, E' defects in irradiated quartz, and N_S^0 in diamond. Rapid-scan is a straight-forward alternative to CW EPR that allows spectra of samples with long relaxation times to be acquired with improved *S/N* and without the need for high power amplifiers.

6.2 Nitroxyl Radicals

6.2.1. Introduction

Many organic radicals are transient in solution. The term "persistent" refers to a radical that has a lifetime significantly greater than a methyl radical under the same conditions [98]. The persistence of a radical depends on its environment. Nitroxyl radicals or nitroxides are remarkably persistent due to resonance delocalization and steric shielding of the unpaired electron [3]. Because of the increased lifetimes of nitroxyl radicals when compared to other organic radicals, these molecules have been the subject of in-depth study by EPR. Nitroxyl radicals have been widely used used *in vivo* EPR imaging [99], spin labeling [16], spin trapping [100], and many other fields.

In this section, the enhancement of S/N of nitroxyl radicals in lossy solutions with rapid-scan relative to traditional CW is demonstrated. This work was also summarized in our 2012 paper [101]. Three radicals were used for these experiments:
CTPO (3-carbamoyl-2,2,5,5-tetramethylpyrrolidin-1-yloxy), ^{15}N-mHCTPO (4-hydro-3-carbamoyl-2,2,5,5-tetra-perdeuteromethyl-pyrrolin-1-^{15}N-oxyl-d_{12}) and ^{15}N-PDT (4-oxo-2,2,6,6-tetra-perdeuteromethyl-piperidinyl-^{15}N-oxyl-d_{16}) (Scheme 6.2).

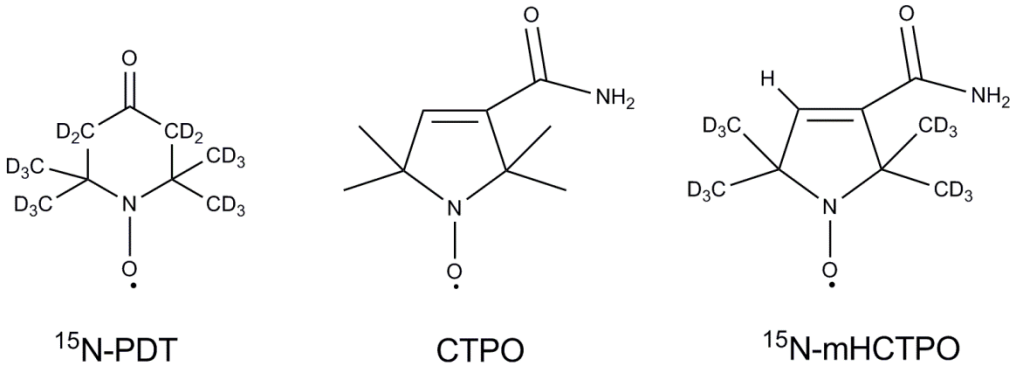

Scheme 6.2. Structures of ^{15}N-PDT (4-oxo-2,2,6,6-tetra-perdeuteromethyl-piperidinyl-^{15}N-oxyl-d_{16}), CTPO (3-carbamoyl-2,2,5,5-tetramethylpyrrolidin-1-yloxy), and ^{15}N-mHCTPO (4-hydro-3-carbamoyl-2,2,5,5-tetra-perdeuteromethyl-pyrrolin-1-^{15}N-oxyl-d_{12}).

6.2.2. Methods

Sample Preparation. ^{15}N-PDT with 98% isotope purity was purchased from CDN Isotopes (Quebec, Canada). ^{15}N-mHTCPO was prepared as previously described [52] and provided by Prof. Halpern (University of Chicago). Solutions in 80/20 EtOH/H_2O were 0.2 mM for ^{15}N-PDT and 0.1 mM for ^{15}N-mHTCPO. These concentrations are in a range where the contribution to relaxation from collisions is very small [1]. The samples, in 4 mm o.d. x 3 mm i.d. quartz tubes, had heights of 3 mm, resulting in 3x3 mm cylindrical shapes. The height was selected to decrease the impact of distortions in the signal due to nonuniformities in the rapidly-scanned fields. Both samples were degassed by performing six freeze-pump-thaw cycles and then the tubes were flame sealed.

EPR Spectroscopy. CW spectra and rapid-scan signals were obtained on a Bruker custom E500T X-band spectrometer. The microwave bridge had bandwidth options of 20 or 200 MHz. Signal acquisition was via a Bruker signal processing unit (SPU) for CW spectra and a SpecJetII fast digitizer for rapid-scan signals. For CW spectra the

modulation frequency and amplitude were chosen to minimize lineshape distortions. The microwave B_1 was calculated from incident power as described in section 5.2. A critically-coupled FlexLine ER4118X–MD5 dielectric resonator was used to minimize eddy currents induced by the rapidly-changing magnetic fields. Resonator Q was measured using the pulse ring down method with a locally-designed addition to the bridge [28]. The 80/20 EtOH/H_2O solutions lowered the resonator Q to about 150, which corresponds to a resonator 3 dB bandwidth of 64 MHz at about 9.7 GHz (Equation 6.1).

$$BW_{res} = \frac{\upsilon}{res} \tag{6.1}$$

where υ is the resonator frequency. As discussed in section 3.5, because the field is sequentially scanned up and down in a rapid-scan experiment, only half of the resonator bandwidth is available for the signal in either half cycle. The resonator Q that is required to minimize distortion of a signal with a bandwidth BW_{signal} is:

$$Q = \frac{\upsilon}{2 \cdot BW_{signal}} \tag{6.2}$$

where BW_{signal} is approximated by equation 3.5.

Although the rapid-scan regime is defined in terms of T_2, calculation of signal bandwidth requires inclusion of inhomogeneous broadening and is expressed in terms of T_2*. For hyperfine split spectra and other complex lineshapes an approximate T_2^* based on the overall rate of damping of the FID should be used in Equation 3.5. The goal is to avoid filtering out the high-frequency components of the spectrum. A more precise estimate of signal bandwidth can be obtained by Fourier transformation of the rapid-scan signal.

A locally-designed magnetic field scan driver created sinusoidal scans with 9.5 cm diameter circular coils outside the resonator, aligned coaxially with the main magnetic field. To avoid excessive heating of the amplifier in this scan driver, the sine wave for the magnetic field scans was generated in bursts with a duty cycle of 33 or 50%. To permit equilibration of the hardware and spin response, the rapid-scan signals were digitized only after the 5th cycle of each burst, which corresponds to a duty cycle for data acquisition of about 4%. This fractional duty cycle method was required by the type of scan driver and coils available at the time of this experiment.

The center field of the scan was selected to be close to resonance. In a sinusoidal scan, the scan rate is a function of the offset from the center of the scan. Scan rates were designated by the rate at the center, which is given by Equation 3.9. The scan frequency ranged from 10 to 60 kHz, and scan widths ranged from 5 to 60 G. The rapid-scan signal, after multiplication by the sinusoidal driving function, is the convolution of the slow scan spectrum with the driving function [43]. The slow-scan spectra were recovered by deconvolution, using the Fourier transforms of the data and the driving function [43]. The up- and down-field half cycles of the sinusoidal scans were analyzed separately. To facilitate comparison with conventional CW spectra, a pseudomodulation procedure [67] was used to recover the first derivative spectrum. This procedure included a fourth-order low pass Butterworth filter [102]. Filtering was done with the MatLab "butter" routine and the value of the adjustable parameter, W_n, was selected to give less than 2% broadening (W_n=0.12).

The T_1 and T_2 for ^{15}N-PDT and ^{15}N-mHCTPO in 80/20 EtOH/H_2O were measured using three-pulse inversion recovery and two-pulse electron spin echo decay,

respectively, on a locally-built pulsed spectrometer [83]. The T_2 values for the low field lines of ^{15}N-mHCTPO and ^{15}N-PDT are 0.70 and 0.61 μs, respectively. The T_1 values for the low field line of ^{15}N-mHCTPO and ^{15}N-PDT are 1.2 and 0.79 μs, respectively. The estimated uncertainties for T_1 and T_2 are about 3%. The T_2^* for ^{15}N-PDT, measured from a single pulse FID, was 0.43 ± 0.03 μs. This value of T_2^* is about 13% larger than would have been calculated using Equation 2.3, which approximates the inhomogeneously broadened ΔB_{pp} (0.175 G) as a Lorentzian. For ^{15}N-mHCTPO the partially resolved ring proton hyperfine coupling causes a more complicated decay of the FID, so T_2^* = 0.26 μs was estimated from the inhomogeneously broadened linewidth of ΔB_{pp} (0.256 G).

Simulations. Simulations of the rapid-scan signals were performed by numerical integration of the Bloch equations and summation of the contributions from multiple spin packets. The input parameters were magnetic field scan width, scan frequency, resonator Q, offset of the center of the scan from the resonant magnetic field, T_1, T_2, and B_1. Two approaches were used to determine the weightings of the spin packets that model the inhomogeneous broadening. (i) For spectra obtained with small enough B_1 that saturation effects were negligible, the inhomogeneous broadening was approximated by a set of spin packets with relative amplitudes calculated using a Voigt function [39]. The parameters for the Voigt function were determined by fitting the rising edge of the signal. An uncertainty of about ±7% was estimated for the inhomogeneous broadening. (ii) For the power saturation curves the known deuterium hyperfine splittings [1] were used to calculate the positions of individual spin packets relative to the center of the spectrum. The field offsets for the centers of the spectra were measured from the experimental

rapid-scan spectra obtained by deconvolution. Changes in offsets within a data set were attributed to frequency drift arising from changes in the temperature of the resonator. The simulated rapid-scan spectra were deconvolved, and the amplitudes were measured. The calculations were performed for each experimental combination of scan width and scan frequency. To determine the dependence of the maximum amplitude in the power saturation curve on scan rate, power saturation curves also were simulated for scan rates between 300 kG/s and 10 MG/s.

6.2.3. Results

The rapid-scan spectra of ^{15}N-PDT (Figure 6.12) exhibit characteristic oscillations on the trailing edge of the signal. The values of T_2 obtained by simulation of the spectra were in good agreement with values obtained directly by spin echo.

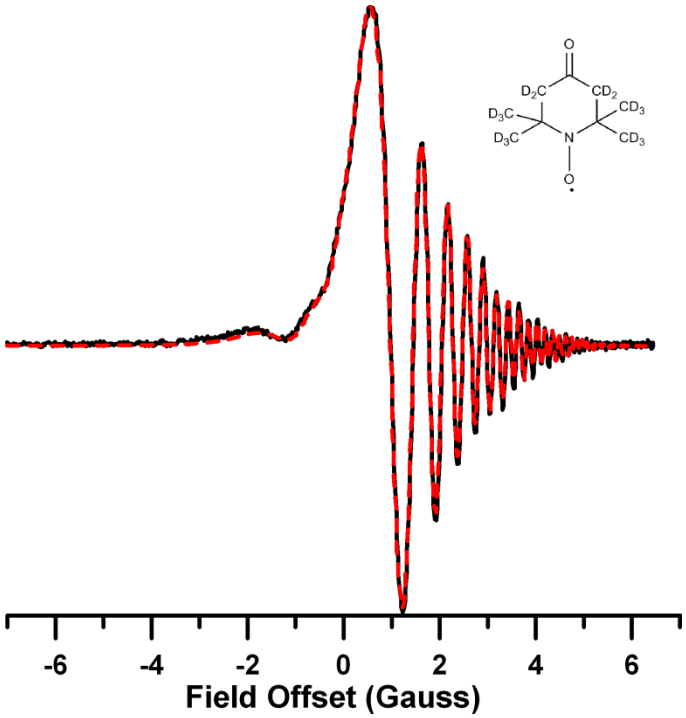

Figure 6.12. (black line) Segment of an X-band sinusosidal rapid-scan spectrum of the low-field nitrogen hyperfine line for a degassed 0.2 mM ^{15}N-PDT solution, obtained with 55 G scan width, 3419 G center field, and 29.7 kHz scan frequency (scan rate ~5.1 MG/s) with a 50% pulse on/ off duty cycle and a net duty cycle of 4% for data acquisition. 1024 averages were collected with resonator Q~150 and 2 mW power (B_1 = 0.02 G), which is well below the peak in the power saturation curve (red dashed line). Simulation obtained with T_2 = 0.61 μs and 75 mG inhomogeneous broadening.

The slow-scan absorption spectrum for ^{15}N-PDT was obtained from the data in Figure 6.12 by deconvolution. For comparison with the conventional spectrum, pseudomodulation was used to calculate the first-derivative, which is in good agreement with the CW spectrum (Figure 6.13).

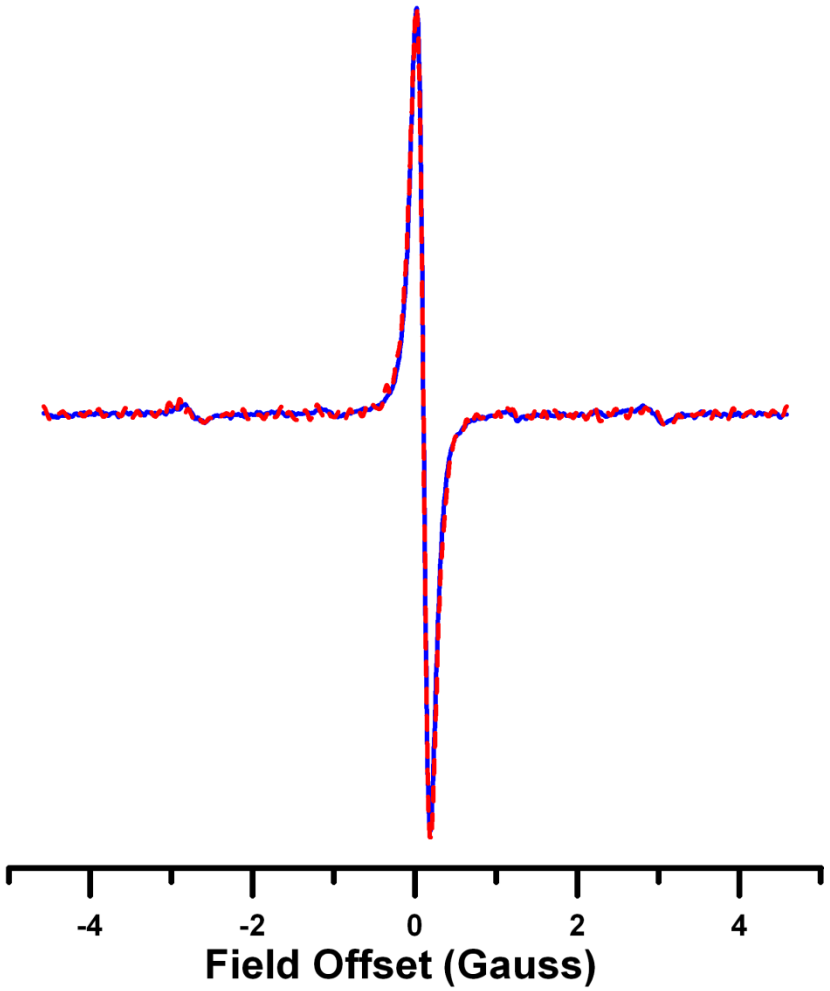

Figure 6.13. Segments of spectra of the low-field nitrogen hyperfine line for degassed 0.2 mM ^{15}N-PDT solution. (blue line) CW spectrum obtained with 45 G sweep width, 0.02 G modulation amplitude, 82 sec scan time, and 0.3 mW power with a 50% pulse on/ off duty cycle with a net duty cycle of 4%. (red dashed line) Pseudomodulated, deconvolved rapid-scan spectrum obtained with 9.15 G scan width, and 29.7 kHz scan frequency (scan rate of ~0.85 MG/s). 1024 averages were collected in ~1 sec. with resonator Q~150 and 2 mW power (B_1 = 0.02 G).

The experimental and calculated dependence of the amplitude of the rapid-scan signals on microwave power for ^{15}N-mHCTPO for three rapid-scan rates is significantly different than for a CW spectrum (Figure 6.14). As the scan rate is increased, the region in which the signal amplitude increases linearly with power extends to higher power and the maximum signal amplitude increases (Figure 6.14). A similar dependence of power

saturation on scan rate was observed for ^{15}N-PDT (Figure 6.15) and for signals in materials samples (Section 6.1).

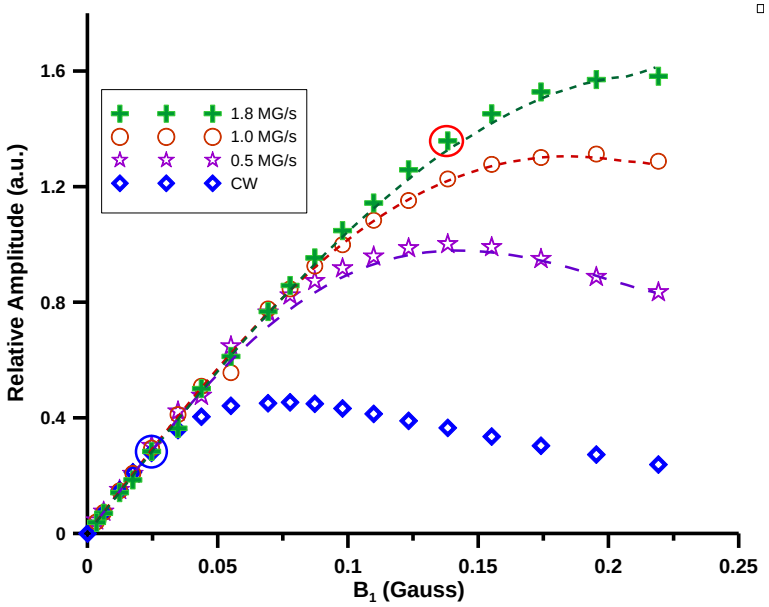

Figure 6.14. Amplitude of CW and rapid-scan spectra of the low-field nitrogen hyperfine line of 0.1 mM ^{15}N-mHCTPO solution as a function of microwave B_1. The scan widths were ~10 G and rapid-scan frequencies were 15.9, 31.5, or 57.4 KHz. Rapid-scan signals were 1024 averages, collected in less than 1 second. CW spectra were collected with single scan acquired in ~82 seconds. The y-axis scale is the same for all of the rapid-scans. The amplitude of the CW spectra is scaled to match that obtained for the rapid-scans at low B_1. The dashed lines represent the calculated power saturation curves, which were simulated by solving the Bloch equations. The point that corresponds to the acquisition conditions for the spectra shown in Figure 6.17A–C is circled in red, and the point that corresponds to the low-power CW spectrum in Figure 6.17D is circled in blue.

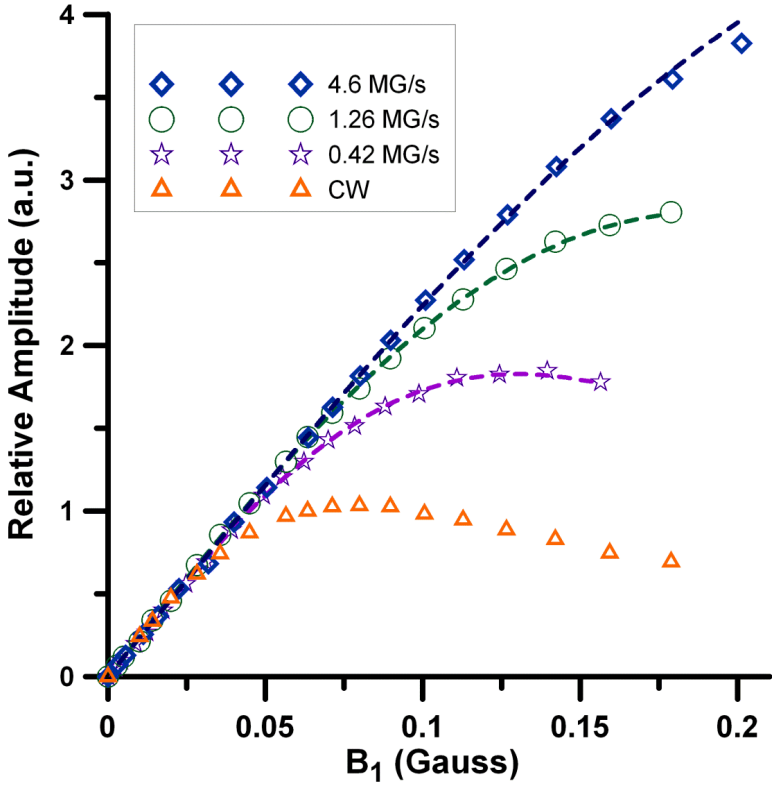

Figure 6.15. Amplitude of CW and rapid-scan spectra of the low-field nitrogen hyperfine line for 0.2 mM ^{15}N-PDT solution as a function of microwave B_1. The rapid-scan frequency was ~30 kHz and the scan width was varied. Rapid-scan signals were 1024 averages, collected in less than 1 second. CW spectra were single scans, collected in ~82 seconds. The y-axis scale is the same for all of the rapid-scans. The dashed lines represent the calculated power saturation curves, which were simulated by solving the Bloch equations. The amplitude of the CW spectra is scaled to match that obtained for the rapid-scans at low B_1.

The maximum signal amplitudes in simulated power saturation curves as a function of scan rate for ^{15}N-mHCTPO are shown in Figure 6.16B. The regime in which the rapid-scan signal amplitude is enhanced is defined by Equation 6.5, which points out that higher powers can be used for faster scans.

$$\frac{B_1}{\left(\frac{dB_0}{dt}\right)(T_1T_2)^{0.5}} < 1 \qquad (6.5)$$

where dB_0/dt is the scan rate [4, 30, 38]. The maximum amplitude in the calculated power saturation curves becomes dependent on scan rate (Figure 6.5A) when the left hand side of Equation 6.5 decreases below 1, which confirms that the benefit of scanning faster occurs within the rapid-scan regime. At log(rate)~7, the maximum amplitude of the power saturation curve begins to decrease (Figure 6.5A). The decrease in amplitude is observed at this rate because of relaxation time limitations. If the scan rate is too fast, the magnetization has not fully come to equilibrium before the next excitation. To achieve the increased signal amplitudes at higher scan rates requires higher B_1 (Figure 6.16B).

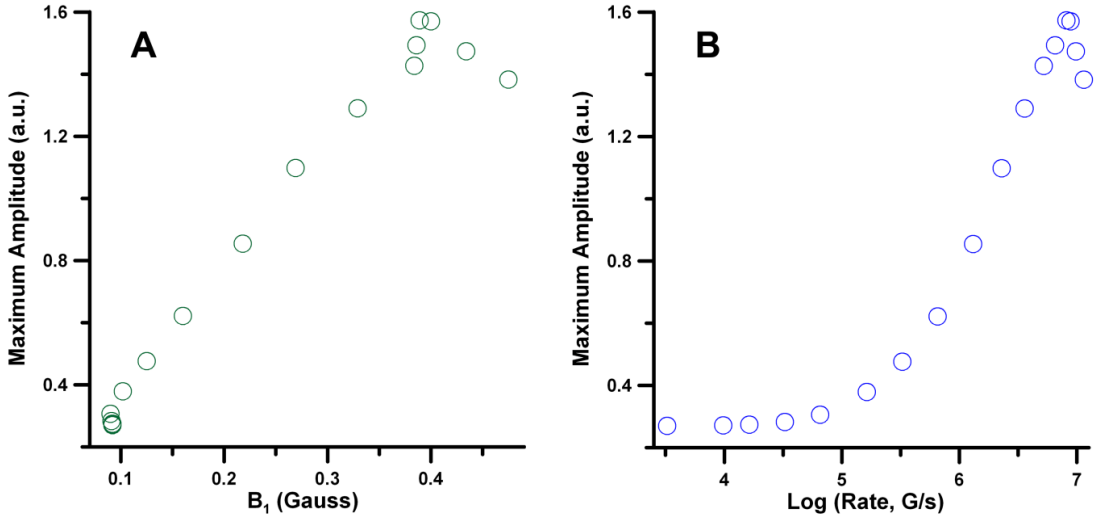

Figure 6.16. Simulation for ^{15}N-mHCTPO of the maximum intensities in the power saturation curves as a function of rate (B). The B_1 required to achieve these amplitudes is shown in (A). Scan width was ~10 G and scan frequency was varied from 0.1 to 350 kHz.

The S/N per unit time for CW and rapid-scan was compared for the ^{15}N-mHCTPO sample (Figure 6.17). The power, modulation amplitude, and a fourth order

low pass Butterworth filter setting for the CW spectrum were selected to cause no more than ~2% broadening (W_n=0.11). The conversion time selected for the CW experiment was 0.9 ms for 1024 points to give a sweep time of 0.92 seconds. The rapid-scan data with the fastest rate shown in Figure 6.14 (1.8 MG/s) were chosen for the comparison. The power and Butterworth filter setting for the rapid-scan spectrum were selected to also limit signal broadening to ~2%. The ~57 kHz scan frequency allowed 1024 scans to be averaged in 0.9 seconds. The rapid-scan and CW experiments had about the same data acquisition time, and the filter bandwidths appropriate for each scan were selected, so the S/N was compared directly. By using rapid-scan EPR, the S/N was improved by about a factor of 2 (Figure 6.17) for the derivative spectra.

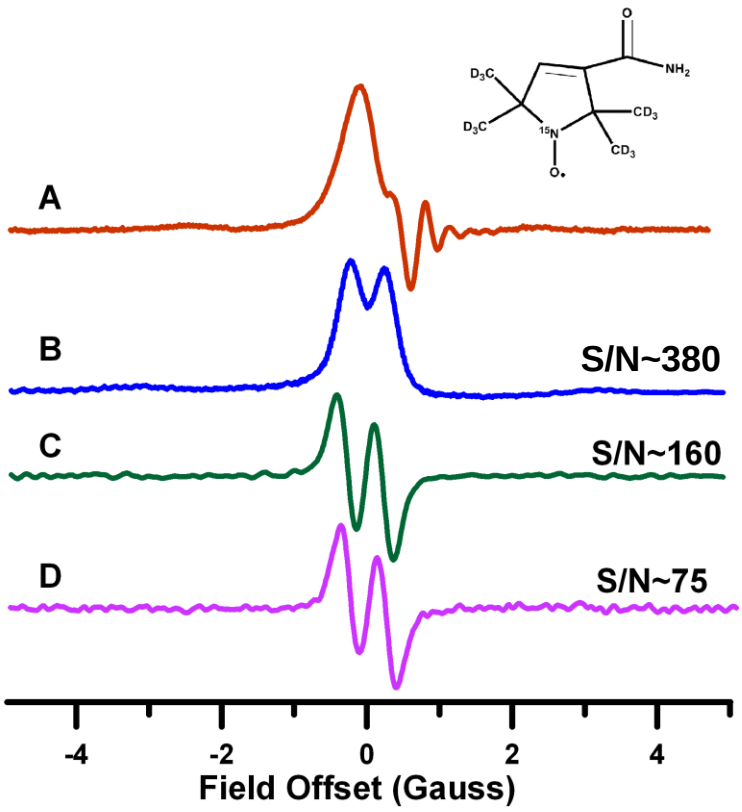

Figure 6.17. Comparison of rapid-scan and conventional CW EPR spectra of the low-field nitrogen hyperfine line of ^{15}N-mHCTPO. (A) As-recorded sinusoidal rapid-scan signal obtained with a scan rate of 1.8 MG/s and microwave power about 80 mW (B_1= 0.14 G B_1). 1024 averages were recorded in about 0.9 sec with a 50% pulse on/ off duty cycle with a net duty cycle of 4% for data acquisition. B) Slow-scan absorption spectrum obtained by deconvolution of signal in A. C) First derivative spectrum obtained by pseudomodulation of the signal in B. D) Single scan of a conventional field-modulated first-derivative CW EPR spectrum of the same sample, obtained in 0.9 sec using 5 mW power, 10 kHz modulation frequency and 0.13 G modulation amplitude. Modulation amplitude, power, and filter were chosen to maximize signal amplitude with less than 2% broadening.

After the Litz wire coils (Section 4.2.3) were installed, and it was possible to operate with 100% duty cycle, a repeat experiment was performed and an even greater improvement in S/N was observed. The S/N for the absorption is about 18x better than for the CW first derivative spectrum.

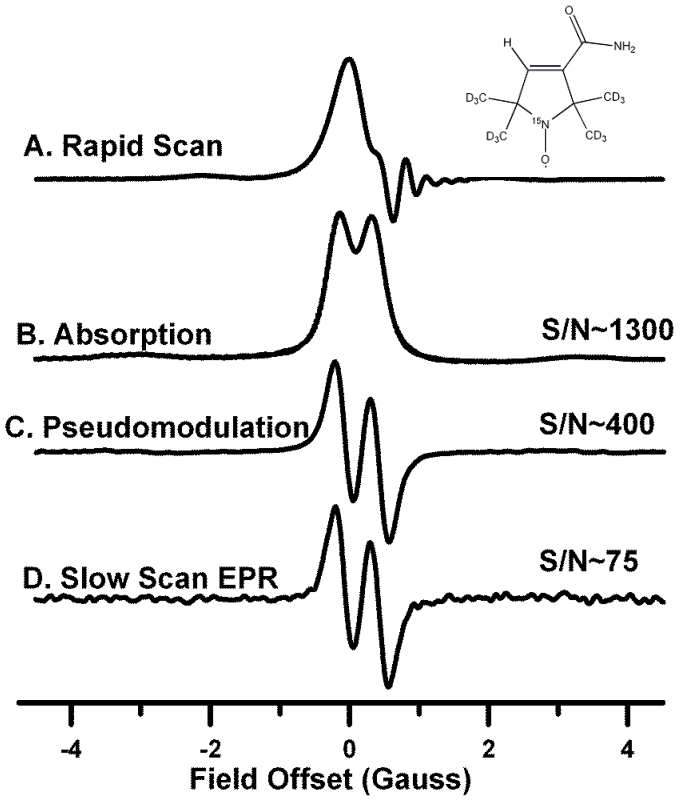

Figure 6.18. Comparison of rapid-scan and conventional CW EPR spectra of the low-field nitrogen hyperfine line of ^{15}N-mHCTPO with Litz wire coils. (A) As-recorded sinusoidal rapid-scan signal obtained with a scan rate of 1.8 MG/s and microwave power about 80 mW (B_1= 0.14 G B_1). 12000 averages were recorded in about 0.9 sec with a 100% pulse on/ off duty cycle with a net duty cycle of 100%. B) Slow-scan absorption spectrum obtained by deconvolution of signal in A. C) First derivative spectrum obtained by pseudomodulation of the signal in B. D) Single scan of a conventional field-modulated first-derivative CW EPR spectrum of the same sample, obtained in 0.9 sec using 5 mW power, 10 kHz modulation frequency and 0.13 G modulation amplitude. Modulation amplitude, power, and filter were chosen to maximize signal amplitude with less than 2% broadening (same spectrum as Figure 6.6 D).

6.2.4. Discussion

Power saturation curves for ^{15}N-mHCTPO (Figure 6.14) and ^{15}N-PDT (Figure 6.15) demonstrate that unsaturated rapid-scan spectra can be acquired at higher powers and with higher signal amplitude for the same acquisition time than conventional CW

EPR. For a given sample, the bridge and resonator bandwidth were held constant for all measurements, and experiments were performed in a range where noise was independent of power. The signal bandwidth increases linearly with scan rate (Equation 3.5) which requires a higher detection bandwidth for faster scans. If noise is approximately 'white', it increases proportional to the square root of bandwidth. If the scan rate is doubled, and if the data acquisition system is 100% efficient, then twice as many scans can be averaged in the same time. Since noise decreases with the square root of the number of scans, the increase in detector bandwidth is, in principle, compensated by the larger number of scans. The maximum scan rate that does not distort the lineshape is inversely proportional to resonator Q. Signal amplitude is proportional to the square root of Q. Lossy samples inherently lower the resonator Q, which provides larger bandwidths that are needed for rapid-scans. If a sample is non-lossy, then lowering the Q to permit rapid-scans could offset the advantage of scanning faster.

The 0.2 mM ^{15}N-PDT sample has a ΔB_{pp}~175 mG and a T_2*=430 ns±30 ns. It was studied at scan rates up to 4.6 MG/s, which gives BW_{signal} (Equation 3.8) ~28 MHz. The bridge bandwidth was set at 200 MHz. The required BW_{res} is ~56 MHz, and at υ~9.67 GHz this corresponds to a Q~175. The resonator Q for this experiment was 200. The deconvolved rapid-scan spectra at the fastest rate exhibited slight broadening (~3%) even in the linear power region, which is attributed to resonator Q. The rapid-scan spectra could still be accurately simulated by accounting for the effect of resonator Q.

The 0.1 mM ^{15}N-mHCTPO sample has a ΔB_{pp}~256 mG for the inhomogeneously broadened proton-hyperfine split lines, and was studied at scan rates up to 1.8 MG/s. T_2^* is about 0.26 μs. The BW_{signal} (Equation 3.8) the highest rate is ~6.5 MHz, which requires

BW_{res} of ~13 MHz. At υ~9.67 GHz this corresponds to a Q~430. The actual Q for this experiment was 150. Thus, for the ^{15}N-mHCTPO experiment, there was an excess of resonator bandwidth. The bridge bandwidth was set at 20 MHz. No broadening was observed in the deconvolved ^{15}N-mHCTPO rapid-scan spectra within the linear power region.

When comparing the signal-to-noise of the solid copper coil data for ^{15}N-mHCTPO with CW EPR, the S/N increased by a factor of 2 with rapid-scan (Figure 6.17) when comparing the two derivative spectra. When the spectra are compared in their native state, rapid-scan gave a 5x enhancement in S/N. The coils were then switched to the Litz wire coils with the aluminum plates in the spectrometer, 100% duty cycles were achieved. With this set up a S/N enhancement of over 5x was achieved (Figure 6.18) when comparing derivative spectra. When comparing the data in its native state, rapid-scan gave an enhancement of a factor of 17.

Chapter 7: Applying EPR to Spin Trapping Experiments.

7.1 Developing X-band Rapid-scan EPR as a method of detecting Spin Trap Adducts.

7.1.1 Introduction.

Motivation. In the late 1960s, when the significance of biologically generated free radicals, such as superoxide ($O_2^{\bullet-}$), was in its infancy, a new technique for identifying these reactive species was developed called spin trapping [100]. Superoxide ($O_2^{\bullet-}$) is well known for its role in the Fenton reaction and in oxidative stress [103]. It is generated by a broad spectrum of enzymes and has been shown to be an important cell signalling agent, controlling a variety of physiological functions [104, 105]. Yet our knowledge of these signalling events is currently based only on in vitro models. For example, it has been shown that $O_2^{\bullet-}$ generated by the metabolism of xanthine by xanthine oxidase can promote the germination of *B. anthacis* endospores [106]. Similar findings were obtained using activated macrophages [107]. Although these models are highly suggestive of an important cell signalling role for $O_2^{\bullet-}$, it has not been possible to confirm the analogous pathways in vivo. Improving the sensitivity of detection of $O_2^{\bullet-}$ requires improved methodology. The research described in this chapter, and in the corresponding journal article [108], is an important step toward detection of $O_2^{\bullet-}$ in cells by EPR.

Reactive oxygen species, including hydroxyl ($HO^{\bullet}$) and superoxide ($O_2^{\bullet-}$) radicals, have lifetimes at ambient temperature that are too short to be detected directly by EPR. The spin-trapping technique in which a short-lived radical reacts with a nitrone or nitroso-compound to form a more stable radical (Scheme 7.1) was developed in the late 1960's [100, 109]. For many years 5,5-dimethyl-1-pyrroline-N-oxide (DMPO) (Scheme 7.1) was the nitrone of choice for detecting $O_2^{\bullet-}$ and $HO^{\bullet}$ because of the characteristic EPR spectra of the adducts DMPO-OOH and DMPO-OH [110, 111]. DMPO has played a pivotal role in identifying $O_2^{\bullet-}$ in many enzymatic reactions, including nitric oxide synthases [112-115]. More recently, spin traps have been synthesized with either a diethoxyphosphoryl (DEPMPO) [116] or ester group, such as 5-*tert*-butoxycarbonyl-5-methyl-1-pyrroline-N-oxide (BMPO) [54, 117, 118]. BMPO (Scheme 7.1) has a larger rate constant for trapping $O_2^{\bullet-}$ than DMPO, and BMPO-OOH exhibits a longer half-life than DMPO-OOH [54]. However, even with improvements in spin traps, the low rate of formation of $O_2^{\bullet-}$ in vivo makes prospects of detection by EPR extremely challenging.

Scheme 7.1. Spin trapping reagents and reaction. The half-life for several spin-trap adducts are listed [3, 54].

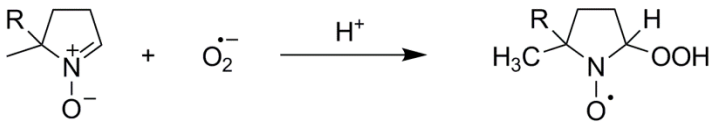

R = CH_3, DMPO
R = $P(O)(OEt)_2$, DEPMPO
R = $CO_2C(CH_3)_3$, BMPO

R = CH_3, DMPO-OOH, $t_{1/2}$=66 s @ pH 7.4
R = $P(O)(OEt)_2$, DEPMPO-OOH, $t_{1/2}$=18 min @ pH 7.0
R = $CO_2C(CH_3)_3$, BMPO-OOH, $t_{1/2}$= 22 min @ pH 7.4

CW EPR has been the method of choice for most spin trapping experiments. Analogous to nuclear magnetic resonance, Fourier transform (FT) EPR has the potential to improve sensitivity of EPR. However, electron spin relaxation times are orders of magnitude shorter than nuclear spin relaxation times, which limit the utility of FT EPR. Electron spin relaxation times for spin-trapped radicals are expected to be similar to those for more stable nitroxyl radicals. Although T_2 for rapidly tumbling nitroxyl radicals in de-oxygenated aqueous solutions is about 0.5 μs [1], unresolved hyperfine splittings and collisions with O_2 reduce T_2^* (the effective decay time for a free induction decay) to less than 100 ns. These short T_2^* values are less than the deadtime of most pulsed EPR spectrometers, which drastically reduces detected signal intensity, and makes the S/N per unit time for FTEPR spectra of spin-trapped radicals poorer than for CW.

In this chapter, the improvement in S/N for BMPO-OOH recorded by rapid-scan relative to CW EPR will be demonstrated. The oxidation of hypoxanthine by xanthine oxidase was used as a continuous enzymatic source of $O_2^{\bullet-}$, with rates of generation in the range of 0.1–6 μM/min. To demonstrate applicability to a living organism, rapid-scan EPR with BMPO as the spin trap was used to detect $O_2^{\bullet-}$ produced by *Enterococcus faecalis*. *E. faecalis* is a human intestinal commensal that has been shown previously to produce extracellular $O_2^{\bullet-}$ [119]. Rapid-scan EPR spectroscopy, combined with the best of the current generation of spin traps, permits characterization of $O_2^{\bullet-}$ generated at rates similar to those that would be observed in isolated cells. The low concentrations of BMPO-OOH that can be observed by rapid-scan are undetectable by CW EPR in the same data acquisition time.

Measuring rate of superoxide production. Understanding the rate of superoxide production is an important aspect of characterizing rapid-scan of spin trap adducts. The initial tests were done by generating superoxide with a simple hypoxanthine/xanthine oxidase system and trapping superoxide with BMPO. The rate of superoxide generation was measured by observing the reduction of ferricytochrome *c* via UV-Vis spectroscopy.

Superoxide radicals can reduce ferricytochrome *c* by univalent electron transfer (Equation 7.1).

$$2O_2^{-\bullet} + cyt^{3+} \rightarrow cyt^{2+} + O_2 \tag{7.1}$$

In the presence of superoxide dismutase (SOD), an additional decay occurs for superoxide (Equation 7.2).

$$2O_2^{-\bullet} + SOD + 2H_2O \longrightarrow 2O_2 + H_2O_2 + 2OH^- \tag{7.2}$$

It has been shown previously that the initial rates of ferricytochrome *c* reduction at various finite concentrations of the cytochrome *c* [120] can be determined by measuring the initial reaction rate.

Initial rates of the reduction of ferricytochrome c were measured by observing the growth of the peak at 549 nm as a function of time with an extinction coefficient of 21 $mM^{-1}cm^{-1}$. The growth of this peak was observed for 10 minutes for each concentration of cytochrome *c*. The initial rate was measured by fitting a line to the first 3 minutes of each curve.

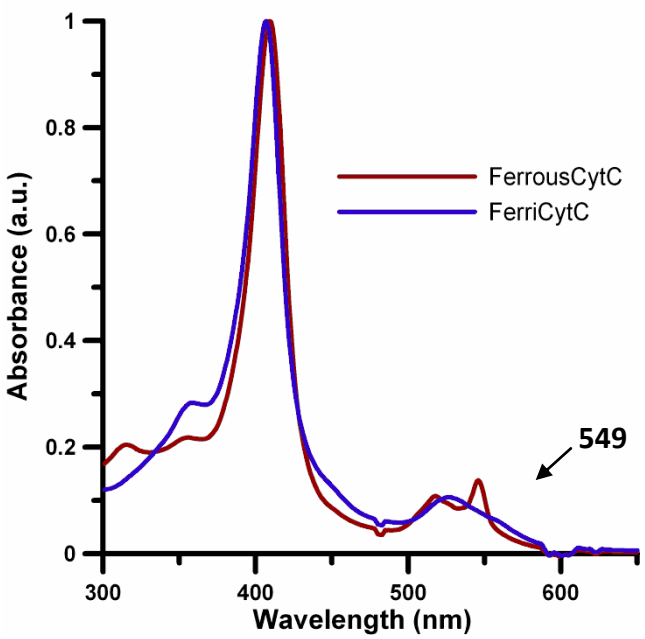

Figure 7.1. UV-Vis spectra for both oxidation states of cytochrome *c*. The native state, ferricytochrome *c* (Fe^{3+}), is reduced by superoxide radical to make ferrocytochrome *c*. The absorbance of the peak at 549 nm is monitored to determine the rate of production of superoxide.

7.1.2. *Methods.*

The BMPO spin trap was synthesized as described in the literature [54] and provided by Prof. Gerald Rosen, University of Maryland. Xanthine oxidase (EC 1.1.3.22), hypoxanthine, superoxide dismutase (SOD), horse heart ferricytochrome c, and diethylenetriaminepentaacetic acid (DTPA) were purchased from Sigma – Aldrich (St. Louis, MO). *Enterococcus Faecalis* ATTC strain 19443 was purchased from Carolina Biological Supply Company (Burlington NC). Brain heart infusion agar (BHI) was purchased from Fischer Scientific. Samples for EPR spectroscopy were contained in 0.8 mm inner diameter pyrex capillaries, supported in 4 mm outer diameter quartz EPR tubes.

For methodology validation, $O_2^{\bullet-}$ was generated using hypoxanthine and xanthine oxidase at pH 7.4 [121]. Typically, xanthine oxidase (0.04 U/mL) was added to pH about 7.4 sodium phosphate buffer (50 mM) containing DTPA (1 mM) and hypoxanthine (0.5 – 400 μM, final concentration) to achieve rates of $O_2^{\bullet-}$ formation that ranged from 0.1 to 6.0 μM/min. The superoxide production rate was estimated by monitoring the SOD-inhibitable reduction of ferricytochrome c (80 μM) at room temperature [120]. Spin trapping was performed by addition of 100 mM BMPO in pH ~ 7.4 phosphate buffered saline (50 mM, PBS) containing 1 mM DTPA to the solution of hypoxanthine and xanthine oxidase to achieve a final BMPO concentration of 50 mM in the reaction mixture. EPR spectra were recorded 10 min after mixing reagents. The half-life of BMPO-OOH at ambient temperature is reported to be about 23 min [122]. Solutions for control experiments contained SOD (30 U/mL).

The procedure for growing *Enterococcus faecalis* for spin trapping experiments was similar to that described in the literature [119, 123, 124]. The bacterial culture was spread onto brain heart infusion (BHI) agar to isolate a single colony. The spread plates were incubated at 37° C for 16 hours. Depending on the concentration of the bacteria, the spreading procedure had to be repeated until a single colony could be easily isolated. A single colony was touched with a pipet tip and scraped into a culture tube with 3 mL of liquid BHI media. All steps with bacteria open to the air were carried out in a BSL-2 hood provided generously by Dr. Scott Barbee, Department of Biological Sciences.

Once in the culture tube, the bacteria were incubated and shaken for 16 hours at 37° C. After 16 hours, the bacterial culture had an opaque color and was placed on ice to slow growth. Bacteria were then washed (in the BSL-2 hood) with phosphate buffered saline (PBS) buffered to a pH of 7.4. and spun down with a centrifuge with 10000 RPM 8600 RCF for 2 min. The bacteria-containing pellets were washed with PBS and spun again and then resuspended in the PBS solution.

The rate of formation of $O_2^{\bullet-}$ by *E. faecalis* in the presence of 10 mM glucose was estimated to be 0.1 nmoles/min/1.0x10^6 colony forming units (CFU) by monitoring the SOD-inhibitable reduction of ferricytochrome c (80 μM) at room temperature.

Bacteria were enumerated using two methods. (i) The optical density (O.D.) at 620 nm was measured at several dilutions and a molar absorptivity of 2.0 x10^9 CFU O.D.$^{-1}$ mL^{-1} was used to convert OD to CFU. (ii) Each of the suspensions of bacteria was further diluted by a factor of 100,000 and 10 μL was plated on brain heart infusion agar. The individual colonies that formed overnight (at 37° C) were counted to determine the average number of CFU per mL. A calibration curve was created that related optical density and CFU/mL as well as the superoxide production rate. UV-Vis with ferricytochrome c was used to determine the rate of production of superoxide by bacteria in the presence of 10 mM of glucose for a set of dilutions.

CW EPR spectra were obtained on a Bruker EMX-plus X-band (9.5 GHz) EPR spectrometer with a super high quality factor (SHQ) resonator. With these samples in the resonator, the Q was ~ 3000 and the resonator efficiency (B_1 /√W) is 1.2 [125, 126]. Although the peak-to-peak first-derivative linewidths for individual hyperfine lines are

about 0.75 G, spectra were over-modulated with modulation amplitude about 0.75 G. The 20 mW microwave power (B_1 =170 mG) was too high to be in the regime where signal amplitude increases linearly with the square root of power. High modulation amplitude and microwave power were used to maximize the signal amplitude, although these parameters broaden the lines and decrease resolution of the small hyperfine splittings.

Rapid-scan EPR spectra were obtained on a custom Bruker E500T X-band spectrometer with a dielectric ER4118X-MD5 resonator. In the dielectric resonator the B_1 excites spins over a sample height of about 1 cm, which is about half as large as in the SHQ resonator. In comparing performance of CW and rapid-scan, this approximately factor of 2 difference in the number of spins detected was not taken into account. The samples lowered the resonator Q, measured with a locally-designed addition to the bridge [127], to about 850. Sinusoidal scans were generated with a locally-designed and built scan driver [48], that includes interchangeable capacitors to resonate the scan-coil circuit. Litz wire coils with 7.6 cm average diameter were mounted outside the resonator, coaxially with the main magnetic field. The scan frequency was about 51 kHz and the scan widths were between 50 and 60 G. The signal amplitude for BMPO-OOH changes too rapidly to permit acquisition of a power saturation curve. Based on the power saturation behavior for stable nitroxyl radicals in aqueous solution [125], a microwave power of ~53 mW (B_1 = 250 mG) was selected to maximize signal amplitude with less than 2% line broadening. Data were acquired in segments containing 1 to 12 cycles of the sinusoidal scans. These segments were averaged 100k times. Background correction [128], sinusoidal deconvolution [43], combination of signals in real and imaginary

channels [94], and combination of up-field and down-field scans were performed, to obtain the spectra shown in Figures 7.4 to 7.6.

A fourth-order Butterworth filter was applied to both the CW and rapid-scan data to decrease noise. The filter parameter was selected to broaden the signals by less than 2%.

7.1.3. *Results and Discussion*

Figure 7.2 is a comparison of the derivative spectrum of BMPO-OOH collected by rapid-scan and CW EPR. These spectra were collected at about the same power. Figure 7.2 demonstrates that much better resolution of hyperfine structure can be achieved with rapid-scan over CW EPR, for the same data acquisition time.

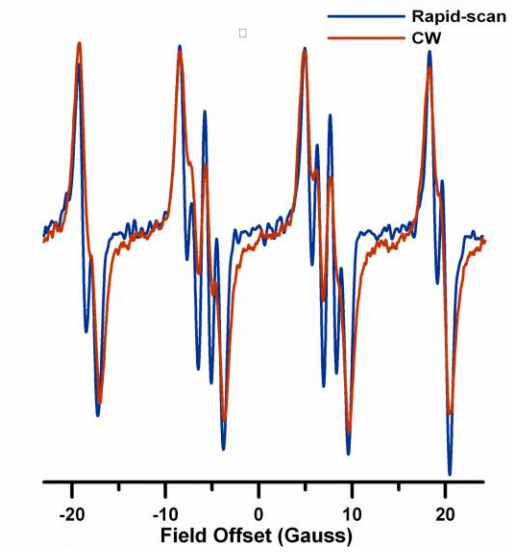

Figure 7.2. Comparison of 6 MG/s rapid-scan and CW spectra of BMPO-OOH. (Blue Trace) 30 kHz scan frequency, 62 G scan width, and 20 mW power, collected in 42 seconds. (Orange Trace) Collected on a Bruker EMX-plus spectrometer. 1.0 G mod amp, 20 mW power, 10 KHz mod frequency, 60 G sweep width.

Considerable thought and effort were put towards determining the best way to accurately compare rapid-scan and CW EPR for spin-trapped adducts. The Eaton lab collectively determined to compare CW and rapid-scan each collected with the appropriate parameters that yielded the highest S/N with an allowed percentage of broadening and on the spectrometer with the best currently available performance. Thus, CW spectra of BMPO-OOH were obtained with a Bruker X-band (9.5 GHz) EMX Plus and a SHQ resonator that represents the current state of the art. Rapid-scan spectra were recorded on a custom Bruker X-band E500T with a dielectric resonator.

CW and rapid-scan spectra for BMPO-OOH produced by 6 μM/min generation of $O_2^{\bullet-}$ (Figure 7.3) are shown as the conventional first-derivative spectrum (Figure 7.3A) and the first integral of the CW spectrum (Figure 7.3B). Figure 7.3C is the deconvolved rapid-scan spectrum, which was obtained in 10% of the time that was used for the CW spectrum (Figure 7.3A). Rapid-scan spectra are presented as the absorption signal, because that is the form in which data are recorded. Both CW and rapid-scan spectra for BMPO-OOH exhibited the characteristic 12-line pattern that arises from nearly equal splittings by one nitrogen with A_N = 13.23 G and one proton with A_H = 11.8 G, and nearly equal populations of two isomers [54]. There is good agreement between the nuclear hyperfine splittings observed in the CW and rapid-scan spectra [54]. The smaller splittings are better resolved in the rapid-scan absorption spectrum (Fig. 7.3C) than in the first integral of the CW spectrum (Figure 7.3B), because the high modulation amplitude and power used to obtain the CW spectrum broadened the lines. Since magnetic field modulation is not used to record the rapid-scan spectrum, this source of line broadening

is avoided. The time on resonance is shorter for rapid-scan than for CW, so higher microwave B_1 can be used without causing power broadening [101]. However, the spectra in Figure 7.3 were obtained by the two methods with about the same B_1. Further improvement in the S/N for the rapid-scan spectrum could have been achieved by using higher power.

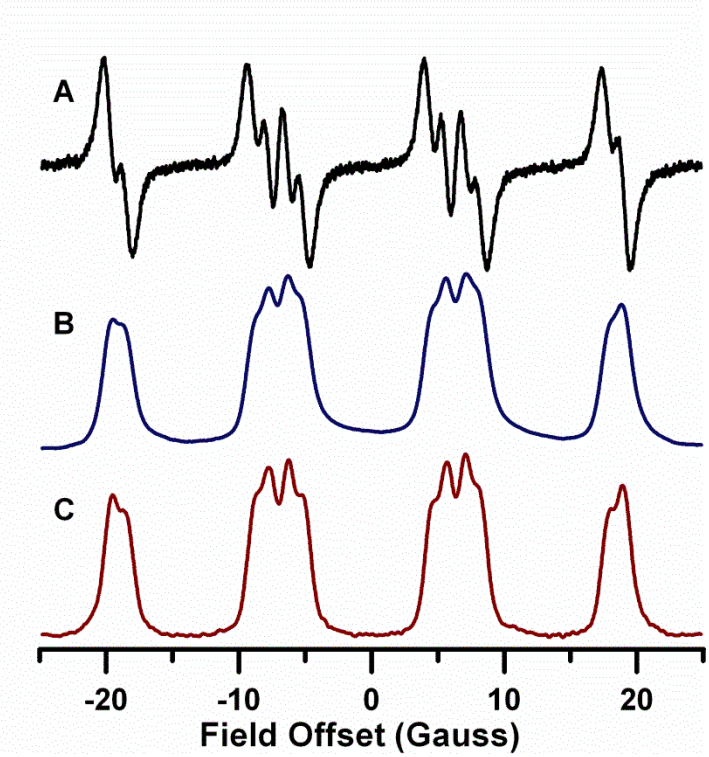

Figure 7.3. Comparison of CW and rapid-scan spectra of BMPO-OOH in solution with a $O_2^{\bullet-}$ production rate of 6 μM/min, recorded 10 min after mixing reagents. $O_2^{\bullet-}$ was produced by a mixture of hypoxanthine/xanthine oxidase. A) CW spectrum obtained with 55 G sweep width, 0.75 G modulation amplitude, single 42 s scan, 20 ms time constant, and 20 mW (B_1 = 170 mG) microwave power. B) The first integral of spectrum in part A. C) Deconvolved rapid-scan spectrum obtained with 55 G scan width, 51 kHz scan frequency, 20 mW (B_1 = 150 mG) microwave power, 100 k averages with one cycle averaged, and a total time of ~4 seconds.

CW and rapid-scan spectra in Figure 7.4 were obtained in 30 s of data acquisition time for a formation rate of 0.1 µM/min $O_2^{\bullet-}$, which is 60 times lower than the superoxide formation rate in Figure 7.3. In the CW spectrum (Figure 7.4A) there is barely a hint of the BMPO-OOH signal. By contrast the rapid-scan spectrum in the same 30 s of data acquisition time has a signal-to-noise of about 10 (Figure 7.4B). Based on the comparison in Figure 7.4, it is evident that rapid-scan EPR permits detection of BMPO-OOH with good lineshape fidelity at low production rates that are inaccessible by CW EPR in the same data acquisition time. The ability of rapid-scan EPR to collect high S/N data in a short amount of time relative to CW will allow for higher resolution in time dependent EPR experiments and be very important for EPR imaging.

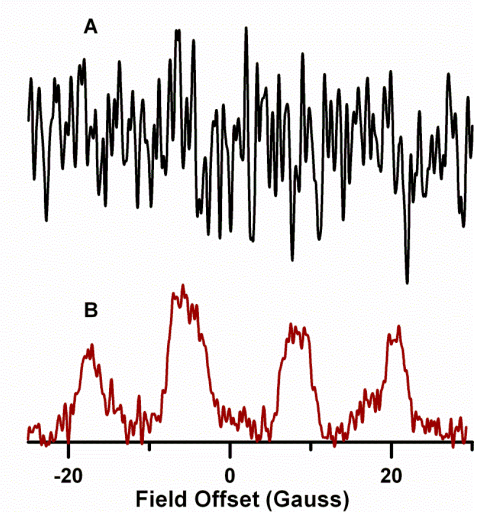

Figure 7.4. Comparison of CW and rapid-scan spectra of BMPO-OOH in solution with a $O_2^{\bullet-}$ production rate of 0.1 µM/min, recorded 10 min after mixing reagents. The concentration of BMPO-OOH is ~0.3 µM. A) CW spectrum obtained with 55 G sweep width, 0.75 G modulation amplitude, single 30 s scan, 15 ms conversion time, 10 ms time constant, and 20 mW (B_1 = 170 mG) microwave power. B) Deconvolved rapid-scan spectrum obtained with 55 G scan width, 51 kHz scan frequency, 53 mW (B_1 = 250 mG) microwave power, segments consisting of 12 sinusoidal cycles were averaged 100k times with a total data acquisition time of ~30 seconds.

Rapid-scan EPR was applied to a bacterial system, the extracellular production of $O_2^{\bullet-}$ by *E. faecalis,* at a rate of 0.1 nmoles/min per $1.0x10^6$ CFU/mL (Figure 7.5). At this rate of $O_2^{\bullet-}$ production it was difficult to determine whether the EPR spectrum of BMPO-OOH was present in the CW spectrum (Figure 7.5A). By contrast the characteristic BMPO-OOH signal is clearly discernible in the rapid-scan spectrum with a signal-to-noise of about 42 (Figure 7.5B). The data in Figure 7.5 demonstrate the improved sensitivity of rapid-scan relative to CW EPR in a living system.

There are several reasons why rapid-scan yields better S/N than CW EPR. (i) In every scan the full amplitude of the signal is detected by rapid-scan, unlike conventional spectroscopy where the signal amplitude that is detected is limited by the modulation amplitude and increasing the modulation amplitude causes broadening of the line. (ii) In the rapid-scan spectrum the magnetic field is on resonance for a shorter period of time than in the conventional CW spectrum so higher microwave power can be used without saturation of the signal [38, 73, 101]. (iii) In the rapid-scans the absorption and dispersion signal are combined, which gives up to a $\sqrt{2}$ improvement in signal-to-noise [94]. The net result of these factors is a major improvement in S/N that is especially important at low radical concentrations. As shown in Fig. 7.4 and 7.5, improved S/N can make the difference between detecting and not detecting an EPR signal. In addition, if the S/N is the same, the number of spins can be calculated from the absorption spectrum about twice as accurately as from the first derivative signal [46].

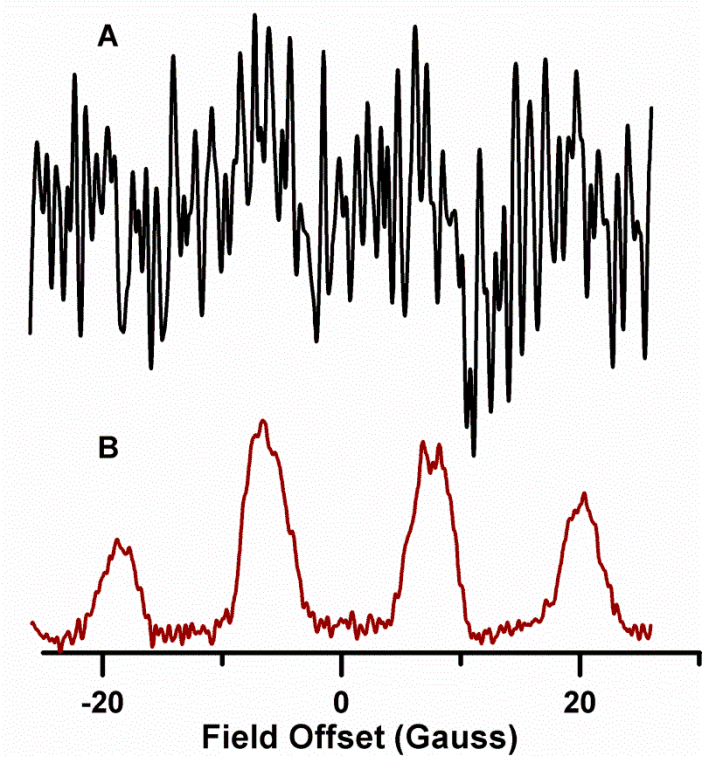

Figure 7.5. Comparison of CW and rapid-scan spectra of BMPO-OOH in a suspension of *E. faecalis* with $2x10^6$ CFU/mL and a $O_2^{\bullet-}$ production rate of 0.2 μM/min, recorded 10 min after mixing reagents. The concentration of BMPO-OOH is ~0.5 μM. A) CW spectrum obtained with 55 G sweep width, 0.75 G modulation amplitude, single 30 s scan, 15 ms conversion time, 10 ms time constant, and 20 mW (B_1 = 170 mG) microwave power. B) Deconvolved rapid-scan spectrum obtained with 55 G scan width, 51 kHz scan frequency, 53 mW (B_1 = 250 mG) microwave power, segments consisting of 12 sinusoidal cycles were averaged 100k times, with a total data acquisition time of ~30 seconds.

7.2 Applying EPR to study spin trapped radicals in plasmas.

7.2.1. *Introduction*

The experiments discussed in this section are a result of a collaboration with Dr. Mark Golkowski's group at University of Colorado-Denver. Graduate student Reed Plimpton and others built the nonthermal plasma apparatus. My role was the spectroscopy and data analysis. The results of these experiments were reported in our 2013 paper [129].

Nonthermal plasmas and their use within the biomedical community are subjects of increasing clinical and industrial attention with a multitude of specific device designs described in the literature [130-132]. Due to the short-lived nature of many of the chemical species produced in nonthermal plasma discharges, most apparatuses are engineered for so-called direct exposure, where the plasma discharge is in direct contact or very close proximity to the biological sample [133]. A few configurations, however, have explored the so-called indirect exposure approach where an atmospheric pressure air stream passes through a plasma discharge and only later makes contact with a biological sample (Watts et al., 2006; Gołkowski et al., 2012; Liu et al., 2008). The advantages offered by the indirect method of delivery include independence from surface geometry, removal of patient and operator from proximity to the plasma discharge, as well as more flexibility in the adjustment of operating parameters.

Despite the growing number of documented experiments, a pressing issue facing the biomedical exploitation of nonthermal plasmas is the need to understand the chemical and biological processes induced in the cell/tissue environment. Efforts to explore these mechanisms have mostly concentrated on down-stream indicators of efficacy such as

bacterial inactivation percentages, absence of gross pathological complication, direct tissue and wound metrics, or optical observations of treated cells [134, 135]. There is growing interest in exploring biochemical mechanisms and kinematics of nonthermal plasma exposures [136, 137]. The efforts to understand nonthermal plasma chemistry have paralleled the identification of the primary species of interest for therapeutic effect. The diversity of bacteria in the clinical environment offers the prospect of situation-specific application of a plasma device [138, 139]. Specifically, different families of reactive species are found to provide differing bactericidal efficacies as a function of the infection strain or application environment [140]. The use of indirect nonthermal plasma-based devices introduces a range of potential parameters, in addition to the electrical properties of the plasma, for the engineering of the plasma induced chemical cocktail [141].

Though numerical simulation of the reactive plasma-created species is a well-established research tool, comparatively little direct observational data specific to their medical use at atmospheric pressure is available [142]. The primary difficulty of these measurements relates to the short lifetimes of the more reactive species as well as a broad array of species and simultaneous reactions present. Recent advances in spectroscopic technology have allowed for broadband and near-real-time measurements of the plasma treated atmospheric pressure air streams [143, 144]. In particular, the ability of EPR spectroscopy to identify specific short lived radicals offers a new avenue for the direct measurement of surface and liquid contact chemistry involved in nonthermal plasma interactions [145, 146]

In this section, the chemistry induced by an indirect nonthermal plasma device with hydrogen peroxide additives is presented [129]. Previous reports on this device have demonstrated its ability to deliver an assortment of chemical species at a distance of up to two meters from the plasma discharge. This low-cost design has demonstrated sterilization results, including deactivation of spores and biofilms, comparable to direct plasma methods as well as a lack of adverse effect on murine skin (Gołkowski et al, 2012). Here, the detection of the hydroxyl radical in the plasma induced effluent more than a meter downstream from the discharge through the use of EPR spectroscopy is presented. The detection is evidence for the generation of hydroxyl radicals in secondary chemical processes away from the discharge.

7.2.2. *Materials and Methods*

Nonthermal Plasma Device Description. The nonthermal plasma device investigated in this chapter was built by Golkowski's group and is a modified version of the hardware described by Gołkowski [135]. The main distinction of the device from other nonthermal plasma hardware for biological applications is the use of air as the working gas, the addition of hydrogen peroxide, and a closed loop flow. See the paper for further details on the components of the plasma device [129].

When operated without the addition of hydrogen peroxide, the device is known to generate approximately 800 ppm of ozone, 20 ppm of N_2O and 11 ppm of NO_2. Hydrogen peroxide was added by placing a 30% hydrogen peroxide solution in the stream of the plasma. With the addition of the hydrogen peroxide solution, the air stream (gas phase) concentrations change to ozone: ~350 ppm, H_2O_2: ~400 ppm, N_2O: 11 ppm and NO_2: 11 ppm [135]. The humidity of the effluent was measured using a thermoset

polymer capacitive sensor (HIH-5030, Honeywell) integrated into the sterilization chamber. The closed loop flow of the device allows for the creation of conditions significantly different from the outside atmosphere. The relative humidity was varied from 36–75% in the presence of hydrogen peroxide/plasma mix and 22-90% in the plasma only state (no hydrogen peroxide additive) by adding Drierite to the chamber. The output of the humidity sensor was measured using a LabJack U3 data acquisition unit (Lakewood, CO) and sampled at a frequency of 1 kHz.

Electron Paramagnetic Resonance Spectroscopy. 5,5-Dimethyl-1-Pyrroline-N-Oxide (DMPO) and diethylenetriaminepentaacetic acid (DTPA) were purchased (Sigma Aldrich, St. Louis, MO). The spin trap 5-tert-butoxycarbonyl 5-methyl-1-pyrroline N-oxide (BMPO) was a gift from Prof. Gerald Rosen, University of Maryland. Spin trapping was performed by diverting a relatively small volume of gas (~1/5 total, Figure 7.6) and bubbling it through DMPO (50 mM) or BMPO in a sodium phosphate buffer (50 mM) containing DTPA (1 mM) for 30 seconds. The sample was briefly mixed by vortexing, and an aliquant transferred to a 0.8 mm ID Pyrex capillary by capillary action. The Pyrex capillary was supported in a 4 mm OD quartz EPR tube. CW EPR spectra were obtained on a Bruker EMX-plus X-band (9.5 GHz) EPR spectrometer with a SHQ resonator at a Q-factor of about 3000. The time between the end of bubbling effluent into the spin trap solution and the start of EPR signal acquisition was about 1 min. Spectra were collected with 1.0 G modulation amplitude, 100 kHz modulation frequency, and 20 mW microwave power. For each humidity, three samples were prepared and measured by EPR. The double integrals of the DMPO-OH spectra were compared with those of TEMPOL (4-hydroxy-2,2,6,6-tetramethylpiperidin-1-oxyl) solutions ranging from 0.3–5

μM measured under identical settings to estimate the absolute concentration of hydroxyl spin adduct.

Studies of bacterial viability and statistical analyses were performed to further characterize the effectiveness of plasma device. See Gowkowski's paper for further details on these topics [129, 135].

7.2.3. *Results*

Spectroscopic Analysis. The most significant result of this investigation is the detection of the hydroxyl radical using the DMPO and BMPO spin traps. Figure 7.6 shows the comparison of the control and 30 second exposure spectra. Figure 7.6B shows the characteristic spectrum of DMPO-OH. Detection of the hydroxyl radical in the delivered effluent was additionally confirmed using the BMPO spin trap (Figure 7.6C). The points shown as blue asterisks in Figure 7.7 are the radical concentrations for the plasma only operational mode of the device (without hydrogen peroxide additives) as a function of relative humidity. The range of humidities examined was limited by the engineering of the device, specifically the use of ambient air. The wick assembly and the concentration of the hydrogen peroxide in the reservoir were constant. The radical concentration is in the range of 1-15 ppm and increases with humidity. The increase of radical concentration with humidity is statistically significant for both the plasma treatments. The radical concentration points in Figure 7.7 suggest a saturation of concentration at around 67% humidity and a departure from a linear relationship.

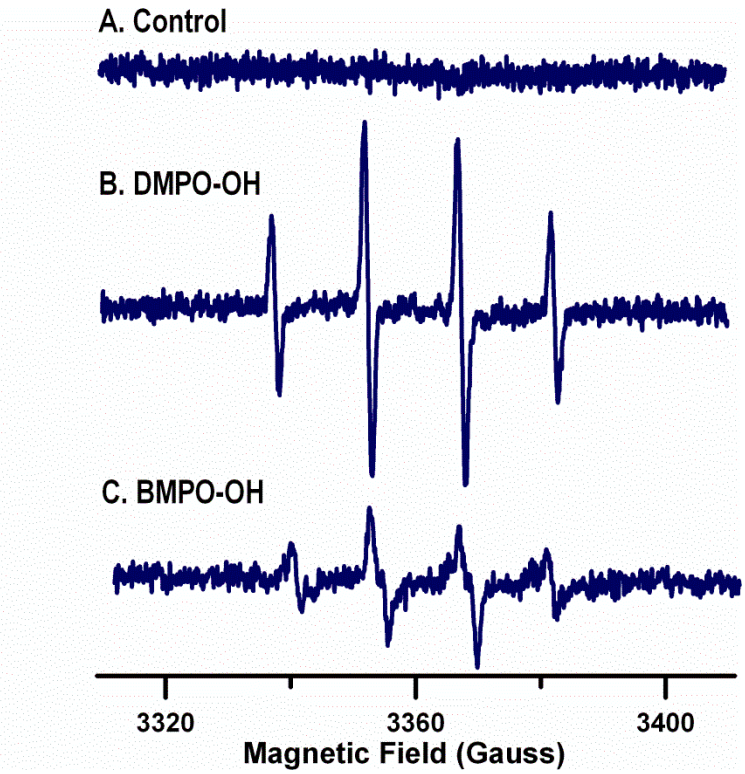

Figure 7.6 CW EPR spectra for hydroxyl radical detection. (A) Control signal, spin trap solution without the addition of plasma. (B) DMPO-OH spectrum obtained with 1.0 G modulation amplitude, 100 kHz modulation frequency, and 20 mW microwave power. (C) BMPO-OH spectrum obtained with 1.0 G modulation amplitude, 100 kHz modulation frequency, and 20 mW microwave power. Double integrals of the detected signals for spin adducts are proportional to concentrations of hydroxyl radicals trapped.

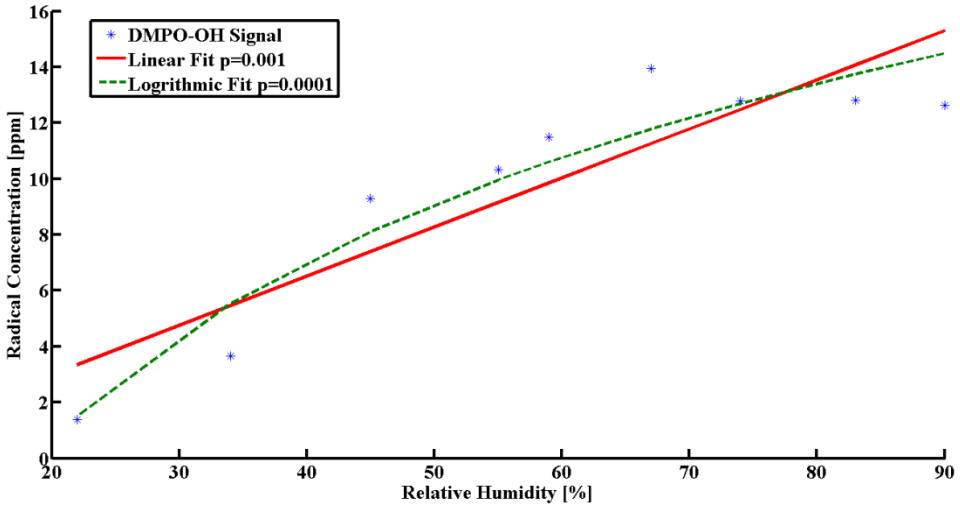

Figure 7.7. Radical concentration [OH•] measured by CW EPR as a function of humidity.

When the exposure time of the spin trap solution to the discharge effluent was increased by a factor of four to 2 min, the oxidation of DMPO to DMPOX (5,5-dimethyl-2-pyrrolidone-N-oxyl) was observed in place of the trapped radical, DMPO-OH (Figure 7.8 and 7.9). This result demonstrates the strong oxidizing ability of ozone. The spectrum was assigned to DMPOX by inputting the hyperfine coupling constants into the NIH spin trap database (https://dir-apps.niehs.nih.gov/stdb/index.cfm).

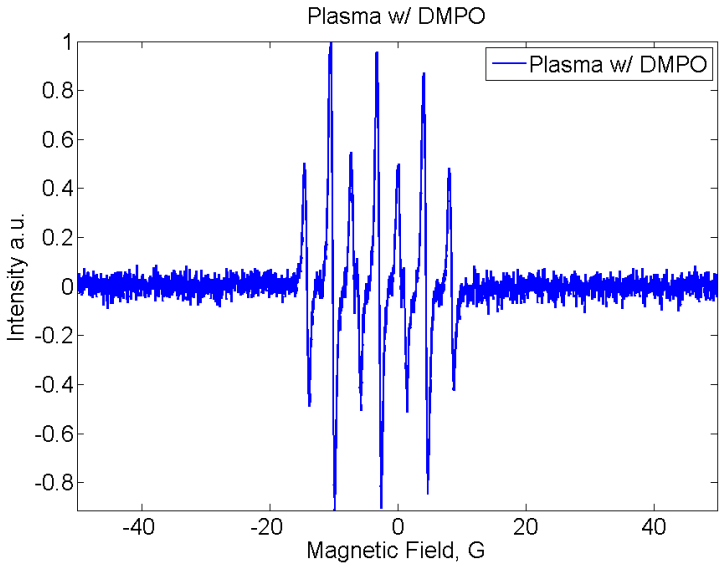

Figure 7.8. CW EPR of aqueous DMPO solution exposed to ozone-generating plasma for 2 min, resulted in oxidation to DMPOX. Spectrum was obtained with 100 G sweep width, 0.75 G modulation amplitude, 1 scan, 80 second scan time, 20 ms conversion time, 20 ms time constant, and 20 mW microwave power.

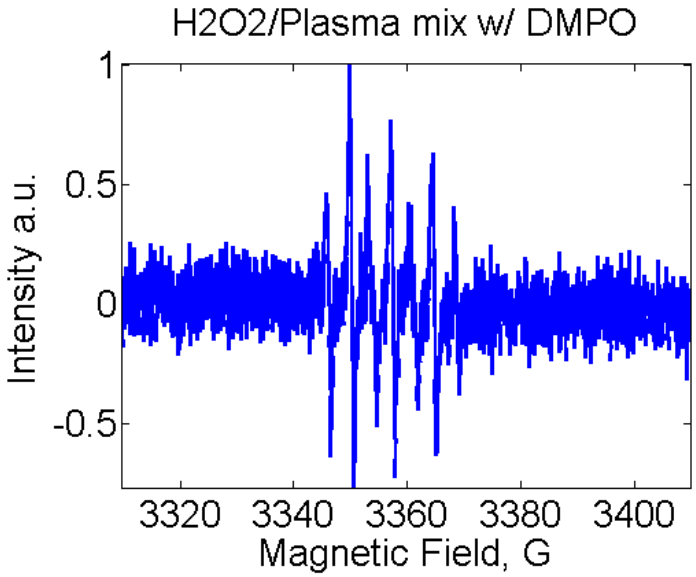

Figure 7.9. CW spectrum was obtained with 100 G sweep width, 0.75 G modulation amplitude, 1 average, 80 second scan time, 20 ms conversion time, 20 ms time constant, and 20 mW microwave power. Signal is a mixture of DMPO-OH and oxidized DMPO (DMPOX).

7.2.4. *Discussion*

Hydroxyl radical detection. An often cited disadvantage of the indirect delivery of plasma effluent is the perceived preclusion of delivering short-lived reactive species such as the radicals produced in a discharge. The EPR spin trapping experiments demonstrate that hydroxyl radical ($OH^{\bullet}$) is present in the solutions that are treated with the plasma effluent, which raises the question of the source for the radicals. Hydroxyl radical is a reactive oxygen species (ROS) that is created in nonthermal plasmas [147] and is short lived, with an average gas-phase lifetime of one second [148]. The device described in this report has an indirect delivery of effluent with ~1.5 meters between the discharge source and spin trap solution where the hydroxyl radical is detected. Because of this distance, it is unlikely that hydroxyl radicals created in the plasma discharge reach the spin trap solution to be detected by EPR. It is more likely that the trapped radicals are generated by secondary reactions of the species formed in the discharge.

As stated previously, the non-thermal discharge produces 800 ppm ozone, 20 ppm of N_2O and 11 ppm of NO_2. The decrease in ozone concentration upon the addition of H_2O_2 [135] is attributed to elevated water concentration in the air stream that is passed through the discharge and has been documented to decrease ozone production. In the discharge, breakdown of water generates $H^{\cdot}$, H_2, H_2O_2, H_3O^+, and OH^- [149, 150]. However, Gołkowski et al. (2012) have shown that for this device, negligible amounts of H_2O_2 are generated directly in the DBD suggesting that water molecules are not directly dissociated in significant quantity.

Although ozone in the effluent decreases with increasing humidity, hydroxyl radical production increases with increasing humidity. Therefore, water is a key part of the mechanism of hydroxyl radical production. The water content is constant at the point where the discharge is bubbled into the spin trap solution. Thus, the dependence of $OH^{\bullet}$ on humidity suggests that the chemistry relevant to hydroxyl production occurs in the gas phase before the discharge stream reaches the spin trap solution.

A possible mechanism [151] is the aqueous chemistry of ozone shown in Equation 7.3 and 7.4.

$$O_3 + e^- \rightarrow O_3^- \qquad k=3.6\text{x}10^{10}\ \text{L mol}^{-1}\,\text{s}^{-1} \quad (7.3)$$

$$O_3^- + H_2O \rightarrow OH^{\bullet} + OH^- + O_2 \qquad k=15\ \text{L mol}^{-1}\,\text{s}^{-1} \quad (7.4)$$

It is proposed that ozonide is produced in the discharge through Equation (7.3) or additionally through reaction with ozone and the superoxide radical. Because of ozonide's relatively slow reaction with water (Equation (7.4)), and relatively long lifetime of several seconds the ozonide may travel the ~1.5 meter path before reacting with water to form the hydroxyl radical that is detected in the spin trap solution. The lifetime of ozonide and the likelihood of the process of Equations (7.3) and (7.4) is increased in the presence of water, including microscopic water droplets. The concentration of water in the closed loop flow is significant, and although the bulk humidity never reached 100% in our tests, it is possible that the local humidity may have been higher allowing aerosol-type droplets to form. Water thus plays the dual role of reacting directly with ozonide in Equation (7.4) and also extending the lifetime of the ozonide anion in the system.

Ozone is also a strong oxidizer. Figures 7.8 and 7.9 showed that the oxidation of DMPO to DMPOX (5,5-dimethyl-2-pyrrolidone-N-oxyl) was observed instead of the trapped radical, DMPO-OH when DMPO was exposed to ozone for 2 min. This shows that increasing ozone could have competing effects – generation of hydroxyl radicals and destruction of the spin trap.

When H_2O_2 is added to the discharge system, both ozone and H_2O_2 are present in the effluent. Ozone can react with H_2O_2 to form hydroxyl radical in what is commonly designated as peroxone chemistry [152, 153], although there is uncertainty about the stoichiometry of the reaction. This reaction could be an additional source of hydroxyl radicals in the spin trapping solution. The similarity in concentrations of trapped hydroxyl radicals in the presence and absence of H_2O_2 suggests that peroxone chemistry is not the dominant contribution to formation of trapped radicals.

When H_2O_2 is added to the discharge system, the reaction of H_2O_2 with Fe^{2+}/Fe^{3+} (Fenton chemistry) also may play a role in generation of hydroxyl radicals. The solutions for the trapping experiments did not contain intentional iron and contained the chelator DTPA to decrease the availability of adventitious iron, so Fenton chemistry is unlikely to contribute to hydroxyl radical formation in the spin trapping solutions.

It is important to note that spin trapping experiments only capture a small fraction of the radicals present. The actual concentration of $OH^{\bullet}$ delivered to the treatment site is significantly higher than the ppm values reported in Figure 7.7 Although it is impossible to unequivocally exclude other more elaborate mechanisms of hydroxyl radical

production, the mechanisms described are the most likely in the context of our observed delivery of hydroxyl radicals at a significant distance from the discharge.

Conclusion. The direct observation of hydroxyl radical delivery to a remote treatment site more than a meter from the plasma discharge was reported for the first time in our paper [129]. Secondary reactions of stable (ozone) and semi-stable (ozonide) species present in the device effluent provide the proposed mechanism for the production of ·OH.

Future work will include expansion of humidity and spectroscopic measurements to more fully probe the humidity dependence of other species, especially potential contributions from the hydroperoxyl pathways at the higher operational humidity levels. This study focused on the hydroxyl radical, but a similar investigation could be performed for the equally biologically and medically significant nitric oxide (NO) radical. Optimization of plasma induced chemical cocktails for specific medical treatments and therapies is feasible even for setups where the discharge is removed from the sample.

Chapter 8: Quartz as a S/N standard for pulse EPR.

8.1 Introduction

For CW EPR, the weak pitch sample has long been the standard for spectrometer quality assurance [154]. Early in the development of pulsed EPR, an irradiated (24 MRad, 240 kGy) fused quartz sample was proposed as a standard [86]. Improvements in spectrometer sensitivity, and the continued use of 8-bit digitizers necessitate a replacement standard with a weaker signal to define signal amplitude and noise for a single echo. One such sample is a 2 mm diameter, 10 mm long fused quartz rod irradiated to 1 kGy. This small sample has utility for a variety of measurements. For resonators that use standard 4 mm o.d. sample tubes (at X-band or lower frequency), a long 4 mm o.d. rod of irradiated (261 Gy) fused quartz can be positioned reproducibly more easily than the small cylinder. With the increasing importance of Q-band pulsed EPR, a standard for Q-band is also needed. A 1.6 mm o.d. rod irradiated to 261 Gy was produced for this purpose. The pair of samples permits comparison of X-band and Q-band pulsed EPR performance, monitoring performance of pulsed EPR spectrometers as a function of time to be sure of continued good performance, and for interlaboratory comparisons. The 1.6 mm o.d. and 4 mm o.d. 261 Gy fused quartz rods are commercially available from Wilmad.

8.2 Methods

Samples. The 100 mm long, 4 mm o.d. and 1.6 mm o.d. fused quartz rods were irradiated by NIST to a dose of 261 Gy with ^{60}Co gamma (Figure 8.1). Defect levels were chosen to give X-band S/N in a useful range for single spin echoes. The dimensions are selected to fit Bruker FlexLine X-band and Q-band EPR resonators, but they can be used with other resonators for quality tests. A set of 6 samples labeled 1–6 was studied at X-band. A set of 7 samples labeled 1–7 was studied at Q-band.

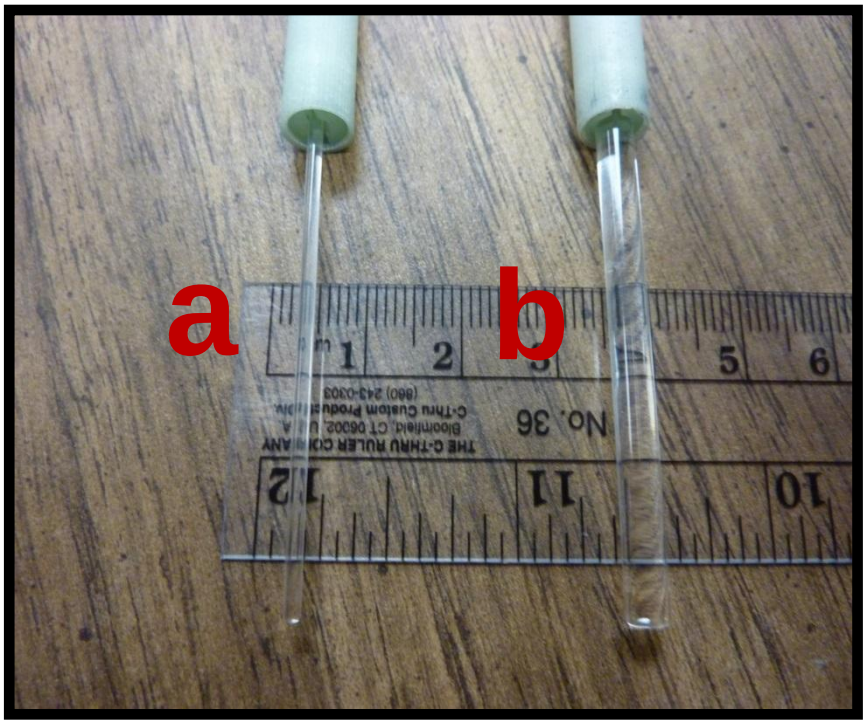

Figure 8.1. Q-band (a) and X-band (b) irradiated quartz samples in Bruker FlexLine sample holders.

Spectroscopy. X-band S/N measurements of the spin-echo were made with both the ER4118 X-MD5 dielectric resonator (empty-critically-coupled Q~10,000) and the ER4118 X-MS5 split-ring resonator (empty-critically-coupled Q~2000) on the E580, and

with the ER4118 X-MS5 split-ring resonator on the homebuilt ESE (only sample #1 was measured for the homebuilt ESE). The sample was positioned to extend through the resonator. The sample was rotated to the position that gave the highest microwave frequency. On the E580, the 2-pulse spin echo was created using the graphical user interface "Easy" software. The echo was digitized via XEPR, and then transferred to Excel or Matlab to perform S/N measurements. The noise reported is the standard deviation of a portion of the baseline after the echo. For the homebuilt ESE, not as many replicates for the measurement were made, but the S/N was ~29 for a gain=20, Q~400, BW=20 MHz, and $\pi/2$=20 ns.

Resonator Q was measured by pulse ringdown, and the coupling was adjusted to give about the same Q for each of the measurements.

Ralph Weber and Carl Patrick independently measured S/N measurements of the 261 Gray irradiated fused quartz samples at both X and Q-band.

Several recommendations are given by the Eaton lab when using one of these samples to test a pulse spectrometer including: 1.) Select a reproducible sample position by rotating the sample to the position at which the resonator frequency is the highest. 2.) Overcouple the resonator to a Q of about 425 to 450 and measure the Q by ringdown after a pulse. 3.) Create a spin echo with 40 and 80 ns $\pi/2$ and π pulses, separated by 1 microsecond. 4.) Use a pulse repetition rate of 2 ms or longer. 5.) Select the magnetic field to give the maximum spin echo. 6.) use a detector bandwidth of 20 MHz. 7.) Digitize a single echo and several microseconds of baseline after the echo. When applying these recommendations to Q-band, the only main difference is the overcoupling.

A Q-band resonator may only be able to be overcoupled to 650, but simply use the maximum overcoupling setting.

8.3 Results and Discussion

Figure 8.2 is an example of an X-band field-swept echo detected spectrum for the irradiated quartz signal-to-noise standard. Figure 8.3 is an echo of the same sample, which is an example of the type of spectrum used to calculate S/N values.

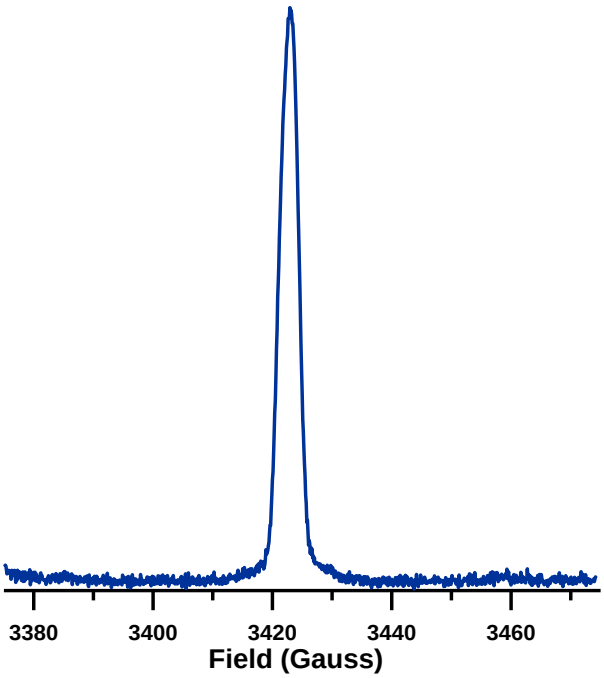

Figure 8.2. X-band field-swept echo of a 261 Gy irradiated quartz sample obtained using a Bruker E580 with $\pi/2$=40 ns @ 4 dB power attenuation, d_1=1000 ns, SRT=2 ms,1 scan with 4-step phase cycling, 5 shots/point, Q~425, and 20 MHz bandwidth.

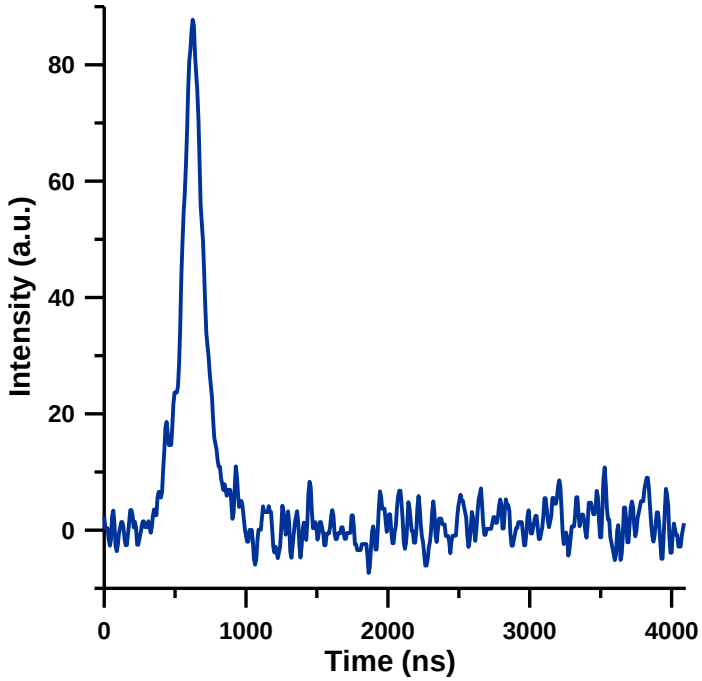

Figure 8.3. X-band spin-echo of a 4 mm 261 Gy irradiated quartz sample obtained using a Bruker E580 with π/2=40 ns @ 16 dB power attenuation, dx=400 ns, SRT=2 ms,Q~425, and 20 MHz bandwidth. 1 scan, S/N= 27.

Figure 8.4 and 8.5 are Q-band field-swept echo and spin-echo spectra of the irradiated quartz sample respectively.

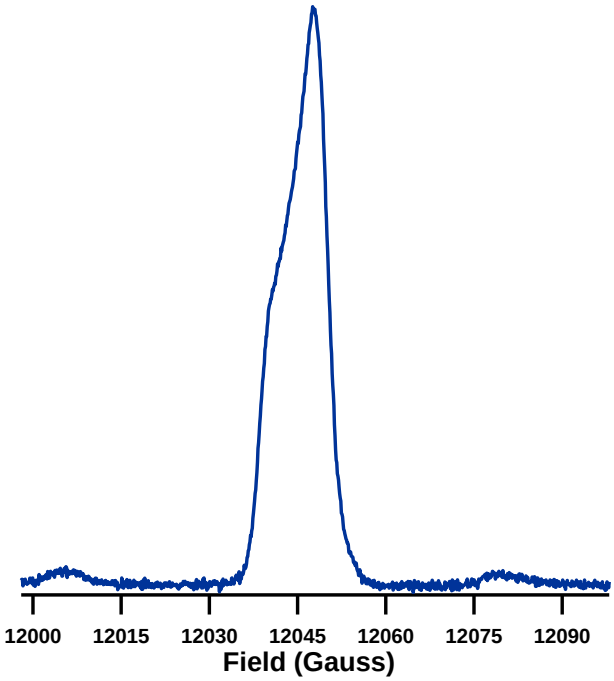

Figure 8.4. Q-band field-swept echo of a 261 Gy irradiated quartz sample obtained using a Bruker E580 with $\pi/2$=40 ns @ 4 dB power, d_1=1000 ns, SRT=2 ms, 1 scan with 4-step phase cycling, 5 shots/point, Q~650, d_1=1000 and 20 MHz bandwidth.

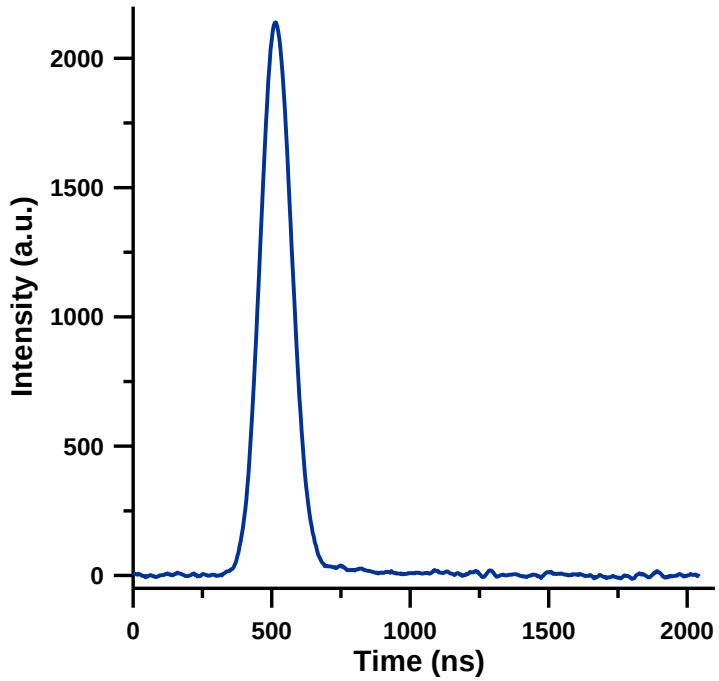

Figure 8.5. Figure 4. Q-band spin-echo echo of a 261 Gy irradiated quartz sample obtained using a Bruker E580 with $\pi/2$=40 ns @ 4 dB power, d_1=1000 ns, dx=400 ns, SRT=2 ms,Q~650, and 20 MHz bandwidth. S/N was calculated with 16 averages, and S/N value was divided by 4. 1 scan, S/N=74.

Table 8.1 summarizes the S/N values obtained with six different irradiated quartz samples on the E580 with a 90^o pulse of 20 ns. Table 8.2 summarizes the S/N values obtained with six different irradiated quartz samples on the E580 with a 90^o pulse of 40 ns.

Table 8.1. X-band spin-echo S/N measurements of six 4 mm 261 Gy irradiated quartz samples with the dielectric resonator (MD5). The Q was ~450. $\pi/2$ = 20 ns @ 16 dB pulse power attenuation. The MW bandwidth was 20 MHz for all measurements in the table below. The MW amplifier was turned ON. Standard deviations (stdev) and confidence intervals (CI) are also listed.

Sample	1	2	3	4	5	6
Average S/N	**30**	**30**	**28**	**33**	**29**	**30**
Stdev	4	2	1	3	4	3
CI	3	2	1	2	3	2

Table 8.2. X-band spin-echo S/N measurements of six 4 mm 261 Gy irradiated quartz samples with the dielectric resonator (MD5). The Q was ~450. $\pi/2$ = 40 ns @ 22 dB pulse power attenuation. The MW bandwidth was 20 MHz for all measurements in the table below. The MW amplifier was turned ON. Standard deviations (stdev) and confidence intervals (CI) are also listed.

Sample	1	2	3	4	5	6
Average S/N	**32**	**27**	**24**	**33**	**25**	**25**
Stdev	3	3	2	3	3	2
CI	5	4	3	5	4	3

The average S/N for all samples with the dielectric resonator is ~30 for $\pi/2$=20 ns and ~27 for $\pi/2$=40 ns. S/N measurements were also collected with the split ring resonator (Table 8.3–8.4). This resonator is much more sensitive to sample positioning. The sample was rotated to the highest possible frequency. For the split-ring resonator, the average for S/N for all six samples is ~25 for $\pi/2$=20 ns and ~22 for $\pi/2$=40 ns. Thus, the dielectric resonator has a 17% increase in S/N for $\pi/2$=20 ns and a 20% increase for $\pi/2$=40 ns. A summary of measurements at X and Q-band is shown in Table 8.6.

Table 8.3. X-band spin-echo S/N measurements of six 4 mm 261 Gy irradiated quartz samples with the split-ring resonator (MS5). The Q for ~425. $\pi/2$ = 20 ns @ 16 dB pulse power attenuation. The MW bandwidth was 20 MHz for all measurements in the table below. The MW amplifier was turned ON. Standard deviations (stdev) and confidence intervals (CI) are also listed.

Sample	1	2	3	4	5	6
Average S/N	**27**	**27**	**22**	**26**	**23**	**24**
stdev	2	3	3	3	3	2
CI	1	2	1	1	1	1

Table 8.4. X-band spin-echo S/N measurements of six 4 mm 261 Gy irradiated quartz samples with the split-ring resonator (MS5). The Q for ~440. $\pi/2$ = 40 ns @ 23 dB pulse power attenuation. The MW bandwidth was 20 MHz for all measurements in the table below. The MW amplifier was turned ON. Standard deviations (stdev) and confidence intervals (CI) are also listed.

Sample	1	2	3	4	5	6
Average S/N	**26**	**24**	**20**	**21**	**21**	**20**
Stdev	3	3	2	3	3	2
CI	5	4	3	5	4	3

Table 8.5 is a summary of the Q-band S/N measurements of the spin-echo with the Q-band ER 5107D2 0602 resonator. These experiments were ran with $\pi/2$ = 40 ns because of present limitations with pulse power (the spectrometer has a 1 Watt amplifier).

Table 8.5. Q-band spin-echo S/N measurements of six 4 mm 261 Gy irradiated quartz samples with the Q-band ER 5107D2 0602 resonator. The Q for these measurements was ~650. $\pi/2$ = 40 ns @ 4 dB pulse power attenuation. The MW bandwidth was 20 MHz for all measurements in the table below. S/N values were calculated with 16 averages, and S/N value was divided by 4. The S/N was too high to yield well-defined noise with single pulses, so 16 averages were used to increase the effective number of bits. Standard deviations (stdev) and confidence intervals (CI) are also listed.

Sample	1	2	3	4	5	6	7
average	**71**	**66**	**73**	**69**	**79**	**74**	**81**
stdev	8	4	6	10	13	3	8
CI	12	6	9	16	21	5	12

The average S/N for the quartz sample at Q-band is ~73. The S/N at Q-band is about 2.4 times the S/N at X-band. A summary of both the Q-band and X-band S/N measurements is given in Table 8.6.

Table 8.6. Summary of S/N measurements for four different resonators. Standard deviations (stdev) and confidence intervals (CI) are also listed.

	E580: dielectric	E580: dielectric	E580: Split Ring	E580: Split Ring	HB ESE: split-ring	Q-band
Resonator Q	450	450	425	440	400	650
Detector BW	20	20	20	20	20	20
π/2 pulse	20	40	20	40	20	40
S/N	**30**	**27**	**24**	**22**	**29**	**73**

Table 8.7 is a summary of the S/N measurements made by Bruker. Tables 8 and 8.9 summarize the comparison between Denver and Bruker.

Table 8.7. Summary of S/N measurements for four different resonators obtained by Bruker Biospin.

	R.W. MS5	R.W. MD5	C.P. MS5	C.P. Prague	C.P. Q-band	C.P. Q-band
Resonator Q	450	450	440	440	630	630
Detector BW	20	20	20	20	20	20
π/2 pulse	20	40	20	40	20	40
S/N	**14**	**21**	**23**	**22**	**72**	**51**

Table 8.8. Interlaboratory[a] comparison of spectrometer performance (S/N) with irradiated fused quartz samples. 'Suggested conditions' were used for these measurements.

	R.W. MD5	Denver MD5	C.P. MS5	Denver MS5	C.P. Q-band	Denver Q-band
Resonator Q	450	450	440	425	630	650
Detector BW	20	20	20	20	20	20
$\pi/2$ pulse	40	20	20	20	40	40
S/N	**21**	**30**	**23**	**24**	**51**	**73**

[a]R.W is Ralph Weber, Bruker BioSpin Billerica and C.P. is Carl Patrick, Bruker BioSpin Germany

Table 8.9. Interlaboratory comparison of spectrometer performance (S/N) with irradiated fused quartz samples. 'Suggested conditions' were used for these measurements.

Resonator	Denver	Bruker (Billerica)	Bruker (Germany)
ER4118X-MD5	27	21	–
ER4118X-MS5	22	14	23
ER5107D2	73	–	51

Conclusion. A standard with a weaker signal (compared with the 240 kGy irradiated fused quartz sample) is needed to define signal amplitude and noise for a single echo. A 261 Gy irradiated fused quartz sample can be used as a signal-to-noise standard for pulse EPR at both X and Q-band. These irradiated fused quartz rods are useful for monitoring performance of pulsed EPR spectrometers as a function of time to be sure of continued good performance, and for interlaboratory comparisons.

Chapter 9: The "Unfinished" chapter

Introduction. This chapter is devoted to the experiments that were begun, but were not finished. The goal of this chapter is to be a starting point for future experimentalists who would like to continue this work. While every chapter of this dissertation could be added upon, these are topics that did not easily fit into any of the other chapters. Two of these projects were performed in collaboration with undergraduate students working in the Eaton group.

9.1. Cr doped in K_3NbO_8

9.1.1. Introduction

In an effort to find a standard for dosimetry experiments at L-band, Cr doped in K_3NbO_8 was synthesized. The main criteria for a dosimetry standard is a g-value different that is sufficiently different from g ~ 2 so that the spectra of the standard and the sample of interest (irradiated teeth) do not overlap. Cr doped into K_3NbO_8 has been previously used as a g-factor, spin concentration, and field calibration standard for high field EPR spectroscopy [155]. Cr(V) samples are of interest because they possess *g*-values from 1.943–1.986, which is a substantial difference when performing experiments at relatively high fields. X-band and L-band CW EPR spectra of single crystals of Cr doped in K_3NbO_8 were obtained. The EPR spectra of these crystals were strongly dependent on the orientation of the crystal relative to the B_0 field, which agreed with

literature [155]. This project was done jointly with Jackie Toomey. Syntheses were done primarily by Jackie. My role was supervision and assistance with spectroscopy.

9.1.2. Methods

Samples. Cr doped into K_3NbO_8 was synthesized based on the procedures in the literature [155, 156]. Yellow single crystals of 0.5 % Cr doped in K_3NbO_8 were obtained. Several methods of analyzing the crystals were attempted including crushing the single crystals of Cr doped in K_3NbO_8 as well as growing very small crystals of this material to make a sample that was not as orientation dependent. Neither approach was successful because many small crystallite particles did not give a clean EPR spectrum. When the crystals were ground until they became a fine powder, a chemical change occurred and a signal was no longer observed.

K_3NbO_8 with no Cr added was prepared following a similar procedure as previously described. Larger crystals of the K_3NbO_8 that did not have any Cr added were grown.

Spectroscopy. Both X-Band and L-Band CW EPR spectra were obtained of this Cr standard along with a 15 Gy irradiated tooth sample. X-band experiments were performed on the EMX-plus and L-band spectra were collected on the multi-frequency spectrometer.

9.1.3. Results and Discussion

X-band. Figure 9.1 is the CW spectrum of a 0.5 % Cr doped in K_3NbO_8 single yellow crystal aligned vertically in the EPR tube so that the long axis is perpendicular to the external magnetic field.

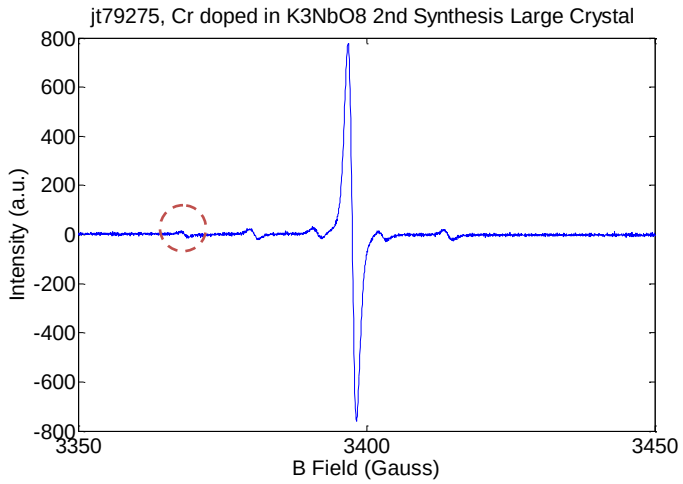

Figure 9.1. 9.4 GHz CW spectrum of Cr doped in K_3NbO_8 long axis aligned perpendicular to B_0. 20 mW power, 0.5 G modulation amplitude, 10 scans, 3397.5 G center field. Circled with a dashed line is a peak most likely due to a defect center in the crystal structure, g = 2.0027. The linewidth for the center and ^{53}Cr hyperfine lines is ~1.5 G.

The peak in the center of the spectrum is due to isotopes of Cr with I = 0. The four peaks that area approximately symmetrically positioned about the center are due to ^{53}Cr with I = 3/2. The peak occurring at the lowest field is due to a defect center. This experimental spectrum matches fairly well with to the spectrum in a previously published paper [155]. This comparison between literature and experiment is also summarized in Table 9.1. The presence of the extra peak observed in the spectrum cannot be confirmed by the literature spectrum because it is out of the range of the data in the literature.

Figure 9.2 is a CW spectrum of a crystal with its long axis aligned parallel to the B_0 magnetic field.

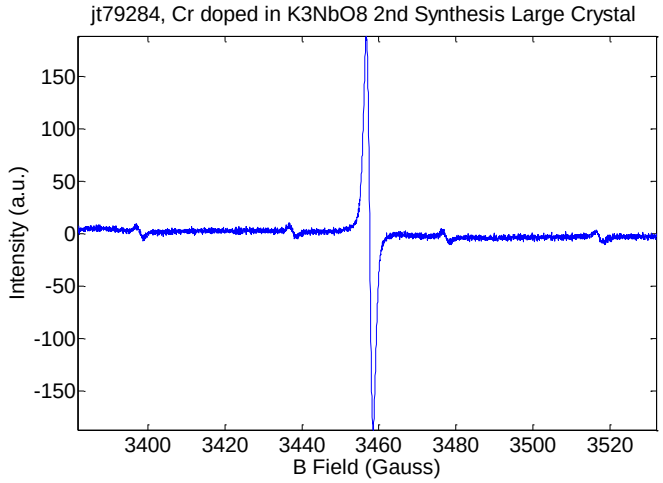

Figure 9.2. 9.4 GHz CW spectrum of Cr doped in K_3NbO_8. 20 mW power, 0.5 G modulation amplitude, 10 scans, 3457.5 G center field. The linewidth for the center and hyperfine peaks is ~1.5 G.

When the crystal is aligned parallel, the g value changed significantly ($g_{\perp}$ = 1.9855, g_{II} = 1.9434). Also, when the crystal was aligned parallel to the magnetic field, the extra peak (hypothesized to be due to a defect center) was no longer evident. Figure 9.2 also matches with the spectrum in the literature for the crystal aligned parallel to the Zeeman field, which is summarized in Table 9.1.

The orientation dependence was further studied by crushing the Cr doped in K_3NbO_8 crystals into smaller pieces, and recording a CW spectrum (Figure 9.3).

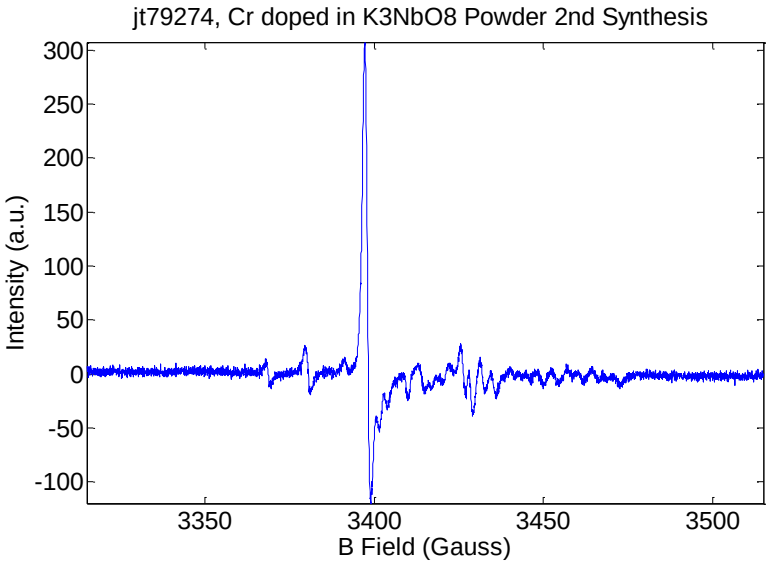

Figure 9.3. 9.4 GHz CW spectrum of crushed Cr doped in K_3NbO_8. 20 mW power, 0.5 G modulation amplitude, 10 scans. The linewidth for the center and hyperfine peaks is ~1.5 G.

From Figure 9.3 it is evident that the CW spectra of Cr doped in K_3NbO_8 is highly orientation dependent and although the sample was crushed, this spectrum looks to be a mixture of crystallite particles with different orientations. To achieve a more homogeneous sample, the sample was crushed even more until the sample became a powder. Unfortunately, when the sample was ground into a powder, the S/N decreased significantly (Figure 9.4). It is possible that some type of chemical change occurred while the sample was ground vigorously.

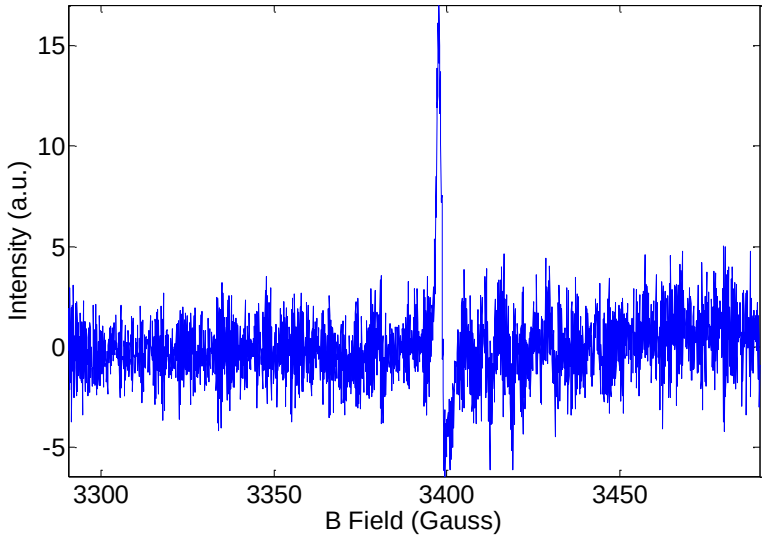

Figure 9.4. 9.4 GHz CW spectrum of powder Cr doped in K_3NbO_8. 20 mW power, 0.5 G modulation amplitude, 10 scans, g= 1.9851. The linewidth for the center and hyperfine peaks is ~1.5 G.

The g value for the powder sample also matched up with the literature value (Table 9.1). The powder sample has the advantage that it is more homogeneous and less orientation dependent, however, the S/N seems to be lower for the powder sample compared to the single crystal sample, so more sample may be required if this were to be used as a standard in the dosimetry experiments.

Table 9.1. Comparison of g and A values for 0.5% Cr doped in K_3NbO_8.

	Single Crystal	Crystal Lit Value	Powder	Powder Lit Value
$g_{\perp}$	1.9855	1.9851	1.9851	1.98508
g_{II}	1.9434	1.9427	—	—
$^{53}A_{\perp}$	11.36	11.49	—	—
$^{53}A_{II}$	39.80	39.56	—	—

To understand the source of the extra peak that was observed in Figure 9.1, K_3NbO_8 with no Cr added was prepared. CW spectra of bulk (several crystals) K_3NbO_8 w/o Cr was measured with X-band EPR spectroscopy (Figure 9.5). The bulk K_3NbO_8 has a large EPR signal, that looks very similar to the EPR spectra of crushed Cr doped in K_3NbO_8 (see Figure 9.3).

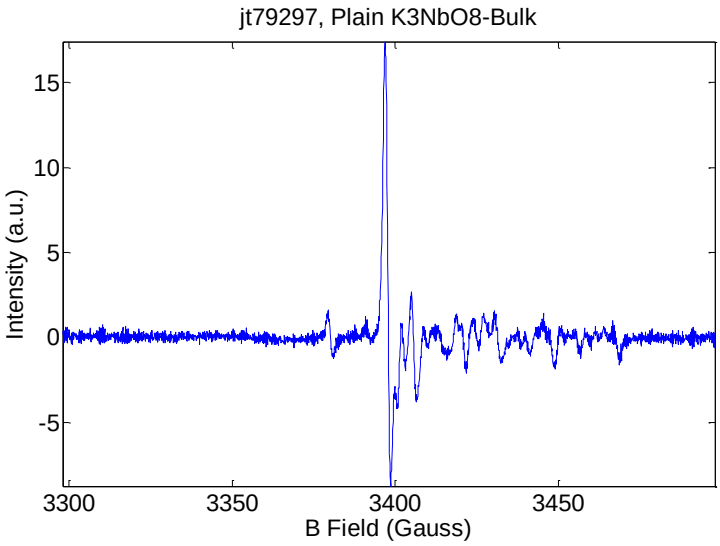

Figure 9.5. 9.4 GHz CW spectrum of bulk K_3NbO_8. 20 mW power, 0.5 G modulation amplitude, 10 scans, g= 1.9851 (for main peak). The linewidth for the center and hyperfine peaks is ~1.5 G.

Chromium is known to be an impurity in high purity niobium compounds [157, 158]. Chromium is a relevant trace impurity in niobium because chromium has a relatively high overall concentration in nature which is difficult to remove completely by certain purification procedures. An average of about 10 ppb Cr was found in the niobium oxide in materials that were labeled "super pure."

Larger crystals of the K_3NbO_8 that did not have any Cr added were grown. The CW EPR spectrum for K_3NbO_8 crystal oriented perpendicular to the field can be seen in

Figure 9.6. For this sample, the small extra peak that was evident in the K_3NbO_8 that had Cr doped into it (Figure 9.1) was not observed. The source of the extra peak in Figure 9.1 is unknown. There is a possibility that the extra peak observed in Figure 9.1 is a defect center that was only visible when the Cr had been added. The S/N for the spectrum in Figure 9.6 is lower than that of Figure 9.1, which should be expected because the sample for Figure 9.6 did not have any Cr added.

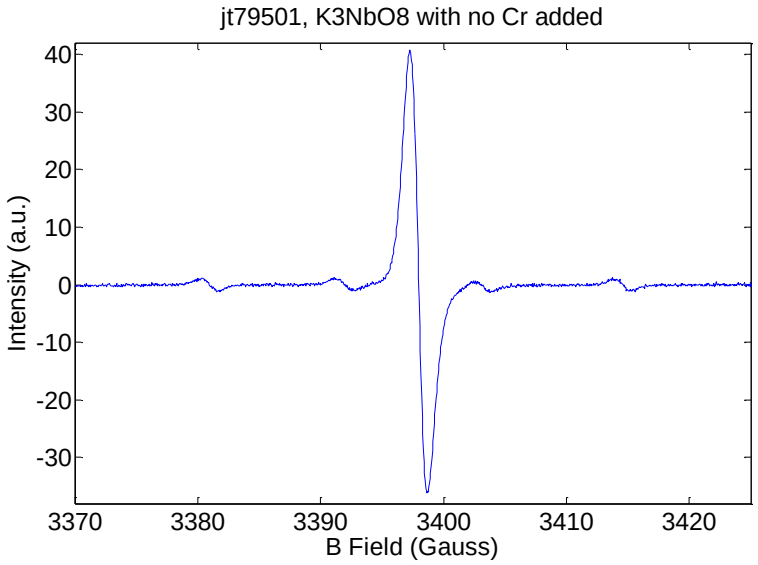

Figure 9.6. 9.4 GHz CW spectrum of Cr in plain K_3NbO_8 with long axis aligned perpendicular to B_0. 2.0 mW power, 0.75 G modulation amplitude, 20 scans, 3398.27 G center field. The linewidth for the center and hyperfine peaks is ~1.5 G.

The plain K_3NbO_8 crystal also was oriented parallel to the B_0 magnetic field (Figure 9.7 & 9.8). The crystal orientation represented by Figure 9.7 is probably not quite parallel to B_0, because the hyperfine coupling constants are not quite as large as what has been reported in the literature (A=35 vs literature A=39.5)

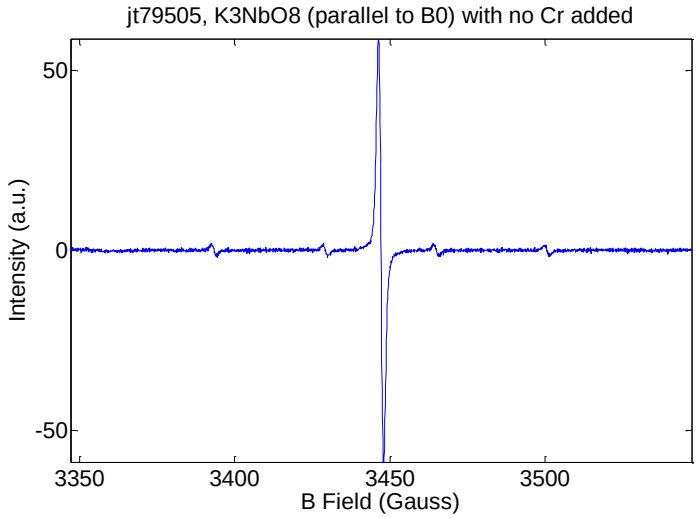

Figure 9.7. 9.4 GHz CW spectrum of a plain K_3NbO_8 crystal oriented almost parallel to B_0. 2.0 mW power, 0.75 G modulation amplitude, 20 scans, 3447.5 G center field. The linewidth for the center and hyperfine peaks is ~1.5 G.

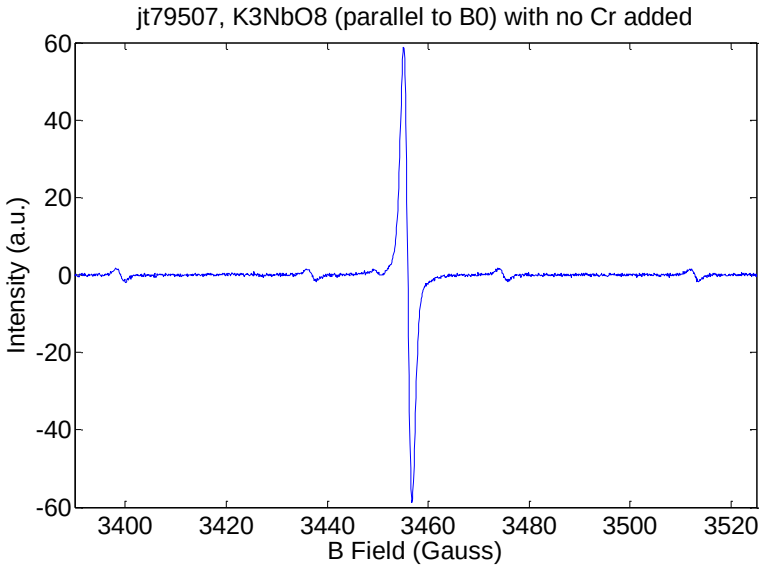

Figure 9.8. 9.4 GHz CW spectrum of a plain K_3NbO_8 crystal oriented close to parallel to B_0. 2.0 mW power, 0.75 G modulation amplitude, 20 scans, 3447.5 G center field. The linewidth value for the center and side peaks is ~1.5 G.

The crystal orientation for the data in Figure 9.8 is close to a parallel position, but not exactly. Hyperfine values are close to the literature (A=38.1, A_{lit}=39.56), but a little

smaller. The reason for this discrepancy is probably because the crystal was not oriented exactly parallel to the magnetic field.

L-band. An L-band spectrum of the chromium (doped in K_3NbO_8) spectrum at 1.5 GHz is shown in Figure 9.9. The g value at L-band for the center line was 1.984, which is very close to the g value of 1.985 that was measured at X-Band. DPPH was used as a g-value standard.

The smaller peaks due to the ^{53}Cr isotope are not visible either due to the large amount of noise in the EPR spectrum (Figure 9.9) or the Breit Rabi effect [15].

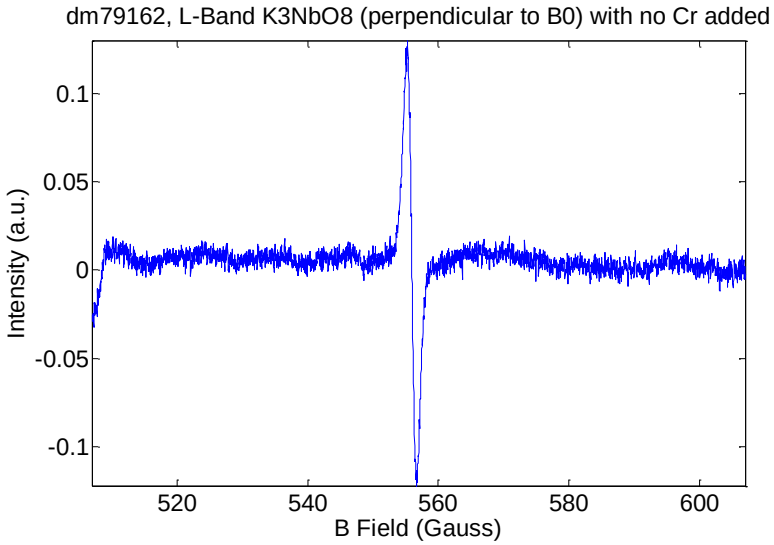

Figure 9.9. 1.543721 GHz CW spectrum of Cr doped in K_3NbO_8 with long axis aligned perpendicular to B_0 (aligned vertically in tube). 5.0 mW power, ~0.8 G modulation amplitude (not calibrated), 24 scans, 557 G center field. The linewidth is ~1.5 G. The *g*-value~1.984

X-band EPR of Cr doped in K_3NbO_8 compared with irradiated Teeth. Figure 9.10 is an X-band EPR spectrum of a 15Gy irradiated tooth sample alongside a Cr doped in K_3NbO_8 crystal, which was used as a standard. This particular crystal of Cr doped in K_3NbO_8 is a good standard for CW EPR of irradiated teeth because the two samples have

similar strength, and therefore similar S/N. (This is the same crystal of Cr doped in K_3NbO_8 that was used for Figure 9.2.)

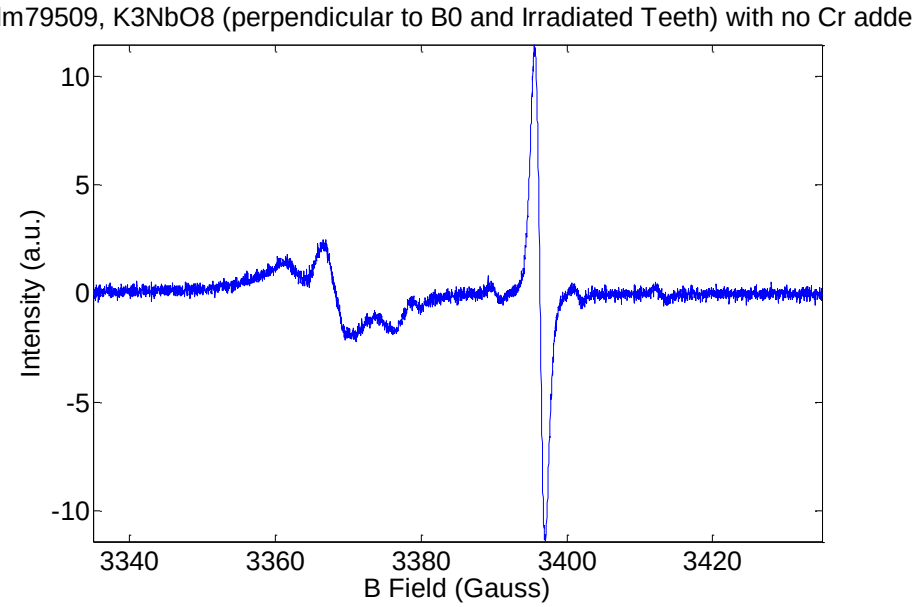

Figure 9.10. 9.4 GHz CW spectrum of 15 Gy irradiated teeth and a Cr doped in K_3NbO_8 crystal oriented perpendicular to B_0 (vertical in the EPR tube). 0.20 mW power, 1.0 G modulation amplitude, 10 scans, 3385 G center field, and 100 G sweep width. The linewidth for the teeth is 14 G for the entire signal and 4 G for the inner linewidth. The linewidth for the Cr is ~1.5 G.

The g value for the signal from the irradiated tooth sample is 2.002, while the g values for the K_3NbO_8 sample were about the same as the $g_\perp$ values listed in Table 9.1. At X-band the signals from the standard and the irradiated tooth sample do not overlap. The only disadvantage for using the Cr in K_3NbO_8 sample oriented vertically in the tube (axis of the crystal perpendicular to the field) as a standard, is that the lowest field chromium hyperfine peak has a position close to that of the tooth (1.995) sample, so that the peaks slightly overlap. When this crystal is oriented parallel to the B_0 magnetic field, there is a ~60 G shift of the center field to higher fields. For the parallel orientation, there is much

less of an overlap of the tooth signal and the Cr signal, however, it is much more difficult to reproducibly align the axis of the crystal parallel to the B_0 field compared to the perpendicular orientation. This is because it is easier to align a crystal vertically in an EPR tube rather than align a horizontal crystal exactly parallel to the B_0 field. The difficulty of properly aligning the crystal parallel to the magnetic field is an important consideration and could be reason not to use the Cr doped in K_3NbO_8 crystals as a standard for dosimetry experiments.

L-band EPR of Cr doped in K_3NbO_8 and Teeth. Figure 9.11 is an L-Band EPR spectrum of the Cr doped in K_3NbO_8 and 15 Gy irradiated tooth sample. The same sample that was used for Figure 9.10 was used for Figure 9.11 (the Cr doped in K_3NbO_8 was still oriented vertical in the EPR tube or perpendicular to the B_0 field).

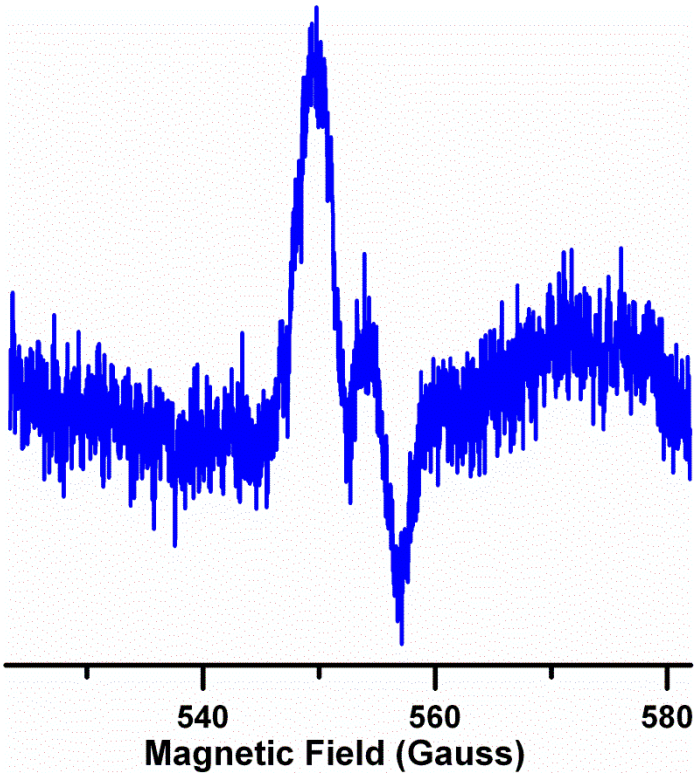

Figure 9.11. 1.54 GHz CW spectrum of 15 Gy irradiated tooth sample and a Cr doped in K_3NbO_8 crystal oriented perpendicular to B_0 (vertical in the EPR tube). 5 mW power, 4.0 G modulation amplitude, 40 scans, 552 G center field, and 60 G sweep width (dm79178).

It is evident from Figure 9.11 that the Cr and tooth signals overlap substantially at L-band, which is the field/frequency combination that currently is used for the tooth dosimeter. The tooth signal is at a field of about 550 G, while the Cr signal is at a field of about 555 G. As mentioned previously, the problem with the Cr doped in K_3NbO_8 crystal oriented perpendicular to B_0 (vertical in the EPR tube) is that there was a small amount of overlap between the teeth and the Cr signal at X-band, which becomes a lot of overlap at L-Band. To prevent this overlap, the crystal should be oriented parallel to the B_0 field, which is very difficult to perform reproducibly, and thus Cr doped in K_3NbO_8 may not be an ideal standard for the dosimetry project.

To show that these peaks are truly overlapping, the Cr sample was removed from the teeth to see how this would affect the EPR spectrum (Figure 9.12). Figure 9.12 clearly shows that one of the major peaks that was removed, which was caused by the Cr sample.

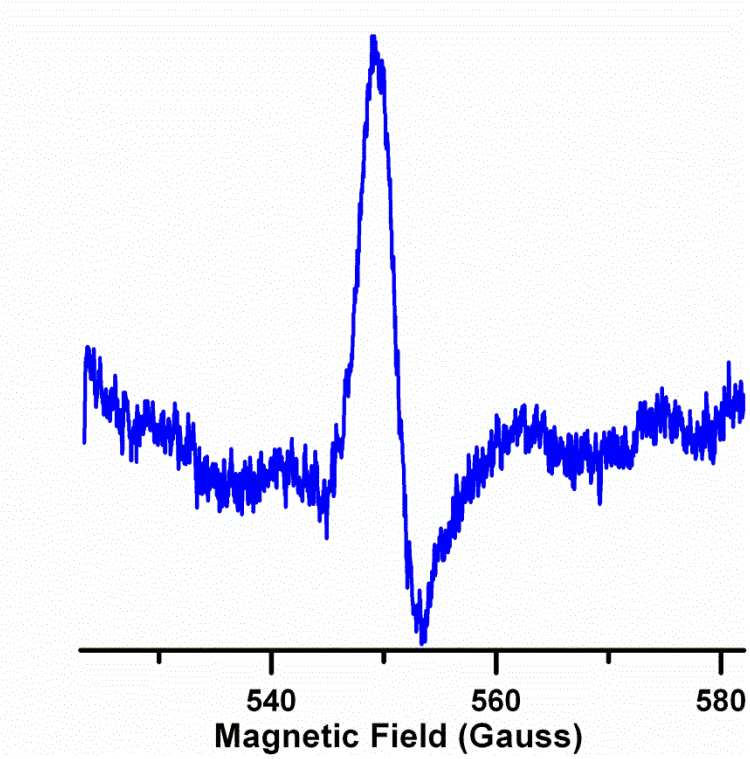

Figure 9.12. 1.54 GHz CW spectrum 15 Gy irradiated tooth sample. 5 mW power, 4.0 G mod amp, 40 scans, 552 G center field, and 60 G sweep width (dm79179). The linewidth is about 4 G.

9.1.4. Summary

Jackie was able to synthesize 0.5% Cr doped in K_3NbO_8, with spectra that matched up with what is in the literature. The spectra of 0.5% Cr doped in K_3NbO_8 crystals are very dependent on the orientation of the crystal in the magnetic field. The L-

band spectrum for this sample was also obtained. The linewidth for the Cr doped in K_3NbO_8 was the same at both X-band and L-band (~1.5 G).

Powder spectra of 0.5% Cr doped in K_3NbO_8 are probably not a better choice for dosimetry experiments because when the crystals are ground, there seems to be some sort of chemical change so that the intensity of the signal decreases significantly. Thus, the powder sample is also problematic because the spectra for this sample are dependent on the extent that the crystals are crushed. The powder sample has the advantage that it is more homogeneous and less orientation dependent, however, the S/N seems to be lower for the powder sample compared to the single crystal sample, so more sample may be required if this were to be used as a standard in the dosimetry experiments.

Jackie also prepared K_3NbO_8 crystals with no Cr added, which had a large Cr signal due to a Cr impurity in the niobium oxide. These spectra matched up pretty well with the spectra of the 0.5% Cr doped in K_3NbO_8 spectra.

Both X-Band and L-Band CW EPR spectra were obtained of this Cr standard with the 15 Gy irradiated tooth sample to see if this compound can be used as a standard for tooth dosimetry experiments. Because of the difficulties orienting this sample, as well as the overlap of the tooth and tCr signals, this sample is most likely not the best material to use for a standard in dosimetry experiments.

9.2. Rapid-scan at VHF

9.2.1. Introduction

To design nitroxyl radicals to be the best possible probes for *in vivo* EPR imaging, one must understand all factors that contribute to improving the S/N [1]. In Biller's 2011

paper, patterns that guide the design and selection of nitroxyl radicals for imaging experiments were presented.

In this section, VHF rapid-scan EPR of two nitroxyl radicals that were designed and synthesized by Dr. Gerald Rosen are presented. The goal of this work was to determine which of these nitroxyl radicals would be better for rapid-scan imaging at VHF.

9.2.2 Methods

Samples. The dueterated/ ^{15}N (referred to as RDN15) and hydrogenated ^{14}N version (RSN14) of the radical shown in scheme 9.1 were synthesized by Dr. Gerald Rosen at the University of Maryland. Aqueous 0.18 and 0.49 mM solutions were prepared for each of these radicals. The solution was placed in 16 mm quartz tubes. Solutions were purged with nitrogen.

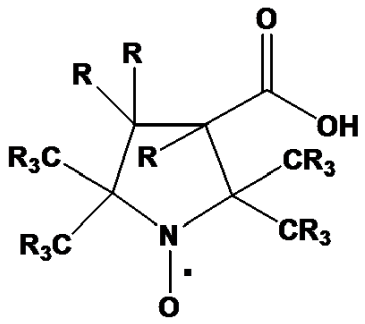

Scheme 9.1. Radical synthesized by Dr. Rosen. For RDN15, R=D and N=^{15}N. For RSN14, R=H and N=^{14}N.

Spectroscopy. Rapid-scan of Dr. Rosen's ^{14}N nitroxyl radical was collected at VHF on the Bruker E540 in March of 2009 and repeated in March of 2012. Triangular rapid-scan signals were generated with a locally designed linear coil driver. Scan

frequencies ranged from 5 to 20 kHz and sweep width (peak-to-peak) ranged from 10–30 G.

9.2.3. Results

2009 Results. Deconvolution of rapid-scan spectra of the center line of a 0.49 mM aqueous solution of RSN14 is shown in Figure 9.13. The FWHM~1.38 G. Figure 9.14 is the deconvolution of the rapid-scan data for the low field line of a 0.49 mM aqueous RDN15 sample, which has a FWHM of 0.6 G. Figure 9.15 is the deconvolution of the rapid-scan data for the low field line of a 0.18 mM aqueous RDN15 sample, which has a FWHM of 0.67 G.

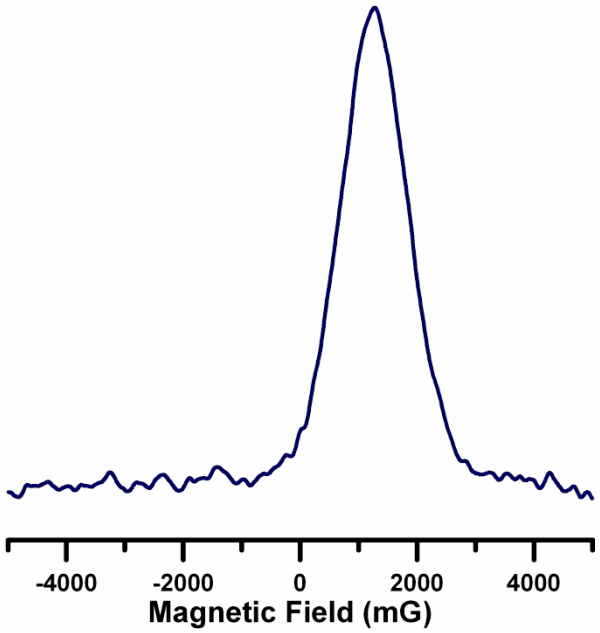

Figure 9.13. 2009 VHF deconvolution of rapid-scan of center line of aqueous 0.49 mM RSN14 sample on E540. 15 G sweep width , 99328 averages, 10 kHz modulation frequency. FWHM 1.38 G.

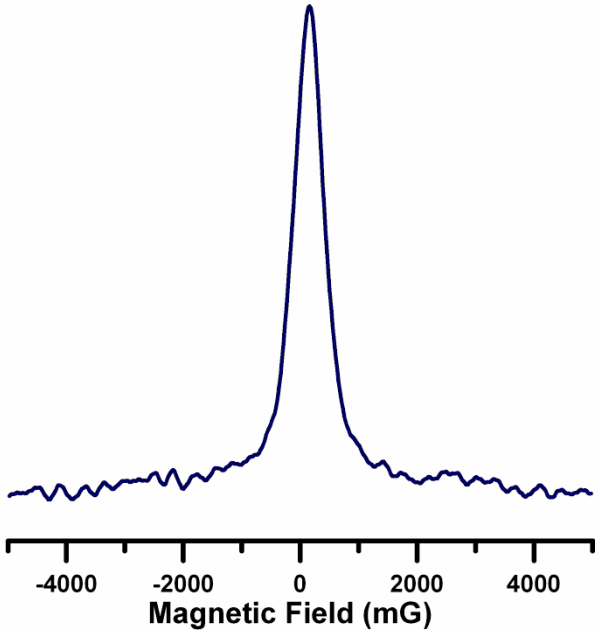

Figure 9.14. 2009 VHF deconvolution of rapid-scan of low-field line of aqueous 0.49 mM RDN15 sample on E540. 30 G sweep width , 100K averages, 20 kHz modulation frequency. FWHM 0.6 G

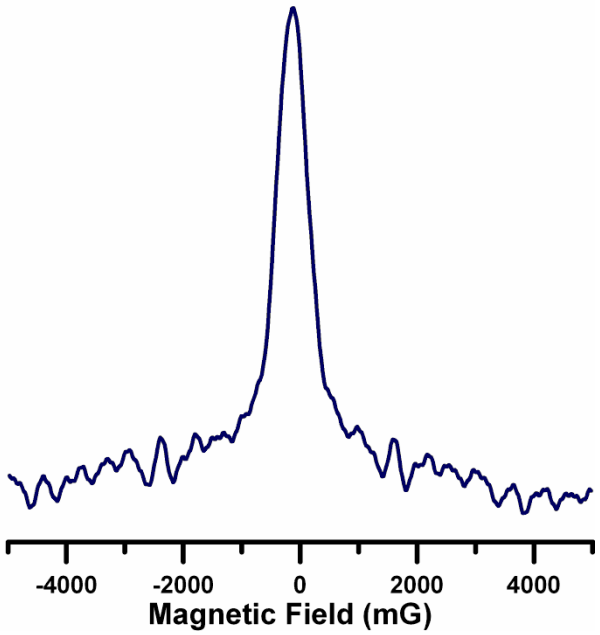

Figure 9.15. 2009 VHF deconvolution of rapid-scan of low-field line an aqueous 0.18 mM RDN15 sample on E540. 30 G SW, 500 K avgs, 20 kHz modulation frequency. FWHM 0.67 G

2012 Results. Deconvolution of rapid-scan spectra of the low-field line of a 0.18 mM aqueous solution of RDN15 is shown in Figure 9.16. The FWHM~0.56 G. Figure 9.17 is the deconvolution of the rapid-scan data for the low field line of a 0.18 mM aqueous RDN15 sample, which has a FWHM of 0.52 G.

The FWHM for each of these samples (from both 2012 and 2009) is summarized in Table 9.2.

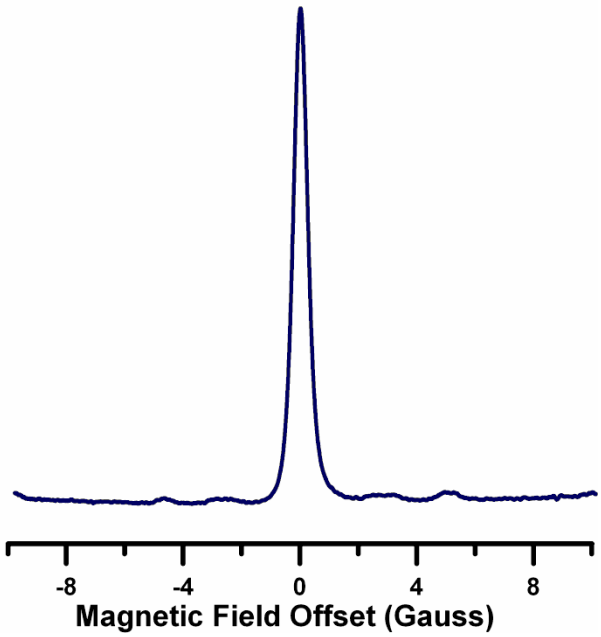

Figure 9.16. 2012 VHF deconvolution of rapid-scan of low-field line of 0.48 mM RDN15 sample on E540. 20 G sweep width, 100 K avgs, 5 kHz modulation frequency. FWHM 0.56 G

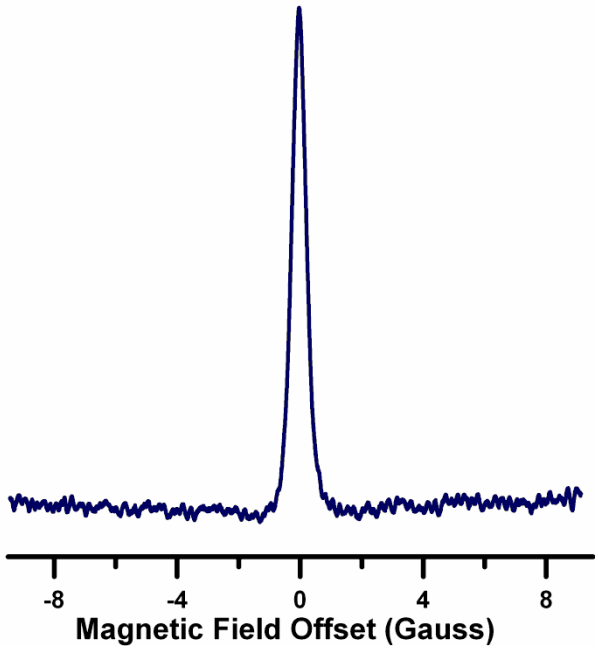

Figure 9.17. 2012 VHF deconvolution of rapid-scan of low-field line of an aqueous 0.18 mM RDN15 sample on E540. 20 G sweep width, 100 K avgs, 5 kHz modulation frequency. FWHM 0.52 G

Table 9.2. FWHM (in Gauss) measured for the Rosen nitroxyl radicals using rapid-scan at VHF.

Sample Concentration (mM)	RSN14 -2009- (Center Line)	RDN15 -2009- (Low Field Line)	RDN15 -2012- (Low Field Line)
0.49	1.38	0.6	0.56
0.18	–	0.67	0.52

The cause of the broadening in the 2009 data is unknown. The normalized power saturation curve (for rapid-scan) for both 0.18 and 0.48 mM RDN15 is shown in Figure 9.18.

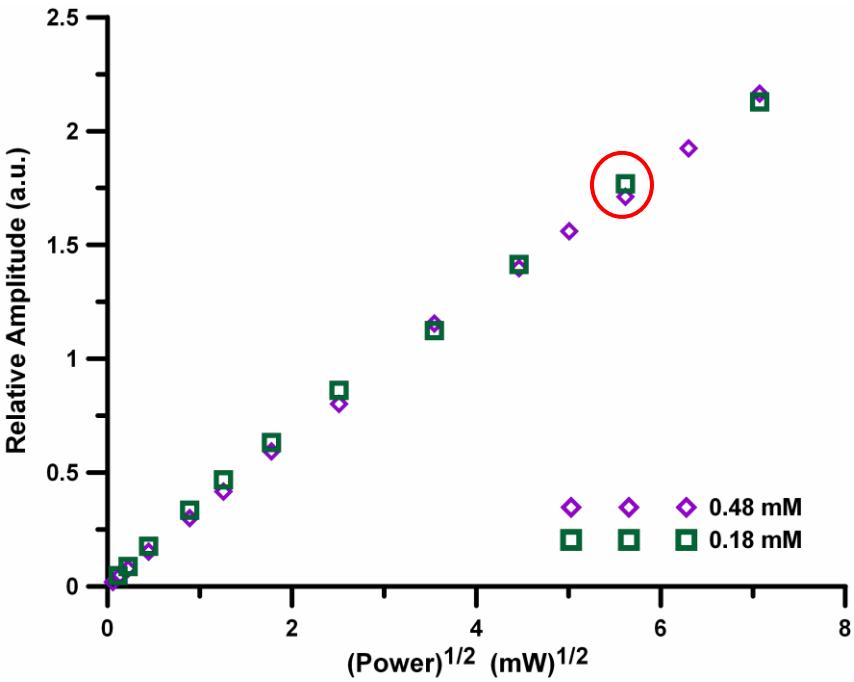

Figure 9.18. Rapid-scan spectra of the RDN15 samples were obtained as a function of incident microwave power while scanning the magnetic field through resonance at 300 kG/s. The points that correspond to the acquisition conditions for the spectra shown in Figure 9.16–9.17 are circled in red.

Conclusions. The RDN15 sample has a much narrower linewidth, and would be more suitable for imaging experiments compared to the RSN14 sample.

9.3. Rapid-scan of Manganese samples.

9.3.1. Introduction

Mn^{2+} has a nuclear spin of 5/2; if an unpaired electron couples to this nucleus, a splitting pattern consisting of 6 lines will result. Manganese was studied as a possible sample to test the limitations of rapid-scan EPR. Because of the large hyperfine splitting, this type of spectrum is particularly difficult with rapid-scan EPR spectroscopy.

9.3.2. Methods.

Sample. Mn^{2+} doped in CaO was provided from Dr. Ira Goldberg, Thousand Oaks, CA.

*Spectroscopy.*CW EPR spectra were collected on a Bruker EMX-plus spectrometer with an SHQ resonator. Rapid-scan EPR spectra were collected with a Bruker E500T spectrometer with a dielectric resonator.

9.3.3. Results and Discussion

The CW spectrum for Mn^{2+} doped in CaO is shown in Figure 9.19. The linewidth for the individual lines are roughly 2 G. The hyperfine splitting is roughly 70 gauss.

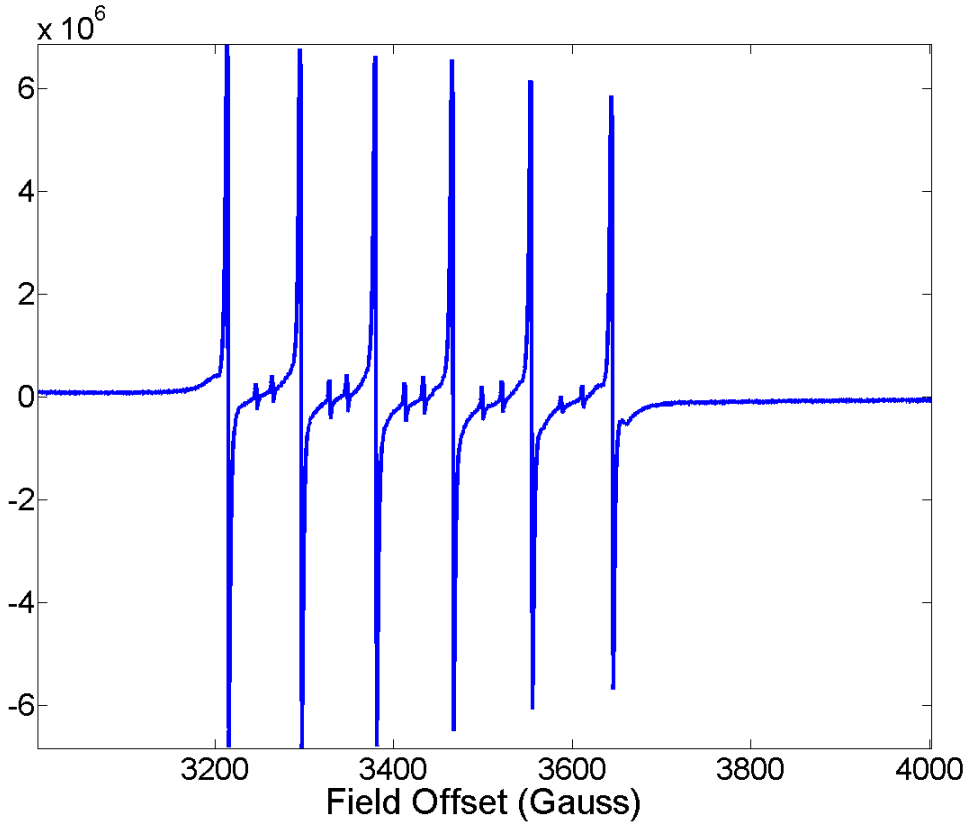

Figure 9.19. CW spectrum of Mn^{2+} doped in CaO, collected with 0.3 G modulation amplitude, 100 KHz modulation frequency, 21 mW power, 21 second time constant, and 1000 G sweep width.

Rapid-scan spectra of Mn^{2+} doped in CaO is shown in Figure 9.20. This spectrum represents some preliminary results where the conditions (specifically the power) are not particularly ideal for the relaxation time of the sample.

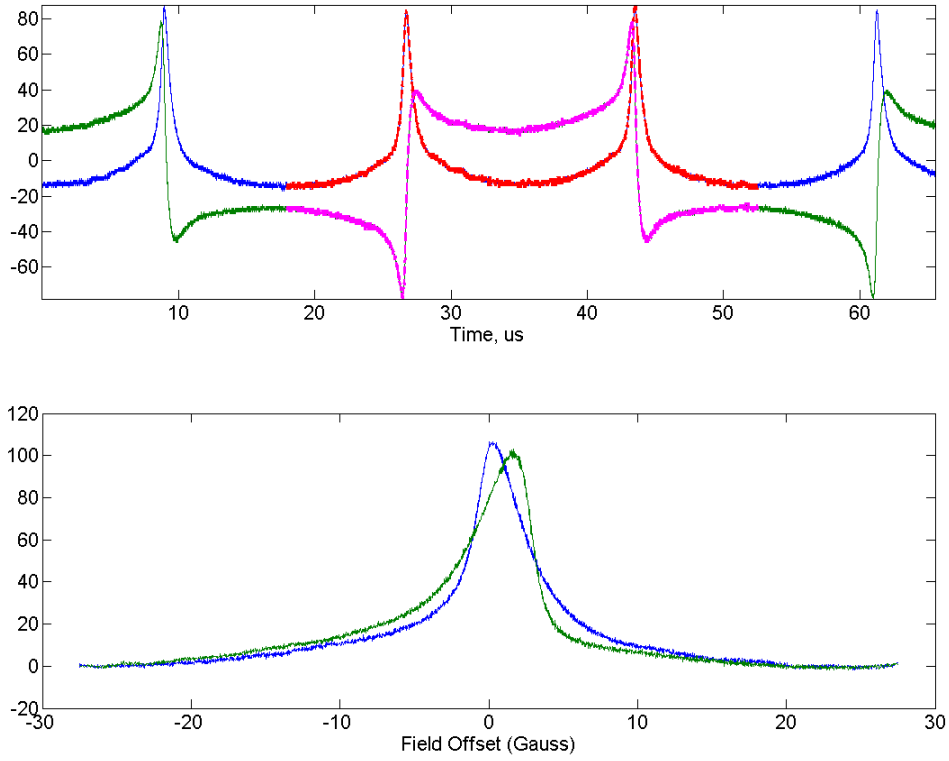

Figure 9.20. Rapid-scan spectrum of Mn^{2+} doped in CaO. 57 G scan width, 28.956 kHz scan frequency, and 2.1 mW power. (Top Panel) Time domain rapid-scan signal. (Bottom Panel) Up (blue) and down (green) scans after deconvolution.

Typically, when the rapid-scan spectrum is deconvolved, the up and down spectrum should match. However, the bottom panel of Figure 9.20 is an example where the up and down scans do not match. This mismatch is most-likely due to power saturation. The deconvolution algorithm can only accurately work in the linear power response region. Once the signal is partially power saturated, the deconvolution no longer yields accurate results. This preliminary experiment was not optimized.

9.4. CW Spectra of metal complexes and nitroxyl radical at Q- X- and L-Band Frequencies

9.4.1. Introduction

The goal of the work in this chapter was to demonstrate differences in the EPR spectra at the L-band frequency of 1.5 GHz, X-band frequency of 9.5 GHz and the Q-band frequency of 34 GHz, and to understand why these changes are occurring. *In vivo* magnetic resonance spectroscopy, including magnetic resonance imaging (MRI), utilizes lower frequency microwaves to effectively penetrate bodily tissues and provide superior contrast and image quality. Frequency dependence of EPR spectra is important for understanding *in vivo* EPR spectroscopy. This work was done in collaboration with Michelle Collier. She prepared the samples. My role was supervision and assistance with spectroscopy and data interpretation.

The frequency dependence of four samples is studied in this section: TEMPO (2,2,6,6-tetramethylpiperidine-1-oxyl), Vanadyl$(acac)_2$ (vanadyl bis(acetylacetonate)), Aquo-vanadyl ion ($VO(H_2O)_5^{2+}$), and $Cu(dtc)_2$ (copper(II) bis(diethyldithiocarbamate)). The structures of these compounds are shown in Scheme 9.2. A nuclear spin in the vicinity of an unpaired electron splits the signal into multiple lines, with a spacing that is called the hyperfine coupling constant, A. For interactions with one nuclear spin the number of lines is 2I+1. When A is much less than the external magnetic field B, the hyperfine lines are equally spaced. When A is similar to the external field strength, the splittings are unequal due to the Breit Rabi effect [15]. At lower resonance frequencies the magnetic field is smaller, so hyperfine lines are unequally spaced.

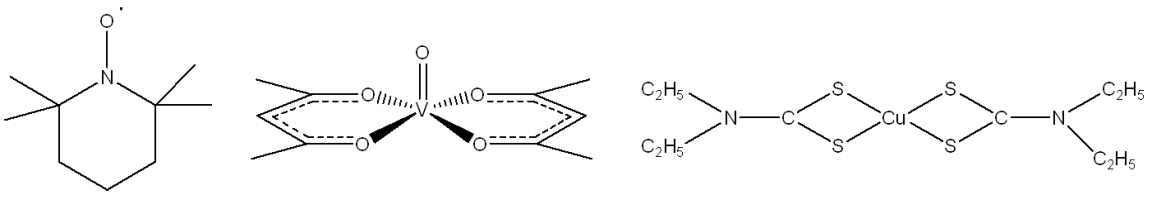

Scheme 9.2. Chemical structures for TEMPO (2,2,6,6-tetramethylpiperidine-1-oxyl), Vanadyl(acac)$_2$ (vanadyl bis(acetylacetonate)), and Cu(dtc)$_2$ (copper(II) bis(diethyldithiocarbamate)).

9.4.2. Methods.

Samples. TEMPO was purchased from Sigma Aldrich (St. Louis, MO). A 2 mM toluene solution of TEMPO was prepared and transferred into teflon tubing supported in a 4 mm quartz tube to be studied at X-band. Nitrogen gas was purged through the sample during analysis to remove O_2. A 2 mM toluene solution in a 25 mm quartz tube was studied at L-band. Nitrogen gas was purged through sample before analysis, but not during.

Vanadyl(acac)$_2$ (vanadyl bis(acetylacetonate)) was synthesized by Michelle Collier according to the literature [159]. A 2 mM toluene solution in toluene in a 4 mm quartz tube was prepared to be studied at X-band. A 2 mM toluene solution in a 25 mm quartz tube was prepared to be studied at L-band.

Aquo-vanadyl ion ($VO(H_2O)_5^{2+}$) was prepared by Michelle Collier by dissolving Vanadium oxysulfate in 25 mL deionized H_2O to make a 20 mM solution. The 20 mM solution was transferred to a 20 mm quartz tube to be studied at L-band. A 2 mM solution in a small capillary tube, supported in a 4 mm quartz tube was studied at X-band. A 2 mM sample was prepared in a pyrex capillary tube and was studied at Q-band.

$Cu(dtc)_2$ (copper(II) bis(diethyldithiocarbamate)) was synthesized by Michelle Collier according to the literature [160] and recrystallized for purification. 0.24 g sodium diethylcarbamate salt was dissolved in water and was added to 0.135 g of copper sulfate dissolved in water in a 40 mL beaker. A coffee colored solution with a dark precipitate was produced. The precipitate was filtered through a porcelain funnel and air dried for 24 hours. The solid was recrystallized by dissolving it in a minimum amount (5 mL) of hot chloroform and then placing the solutions on ice. 280 mg of black $Cu(dtc)_2$ crystals were produced. A 2mM toluene solution of $Cu(dtc)_2$ was prepared in a 4 mm quartz tube to be studied at X-band. A 2 mM toluene solution of $Cu(dtc)_2$ was prepared in a 25 mm quartz tube to be studied at L-band.

Spectroscopy and Simulations. CW EPR spectra were obtained on a Varian E-9 X-band (9.5 GHz) EPR spectrometer and a homebuilt L-band spectrometer. CW spectra were simulated using three programs: Bruker software XSophe, the shareware package EasySpin [68], or the locally written program Asym, which calculates the tumbling correlation time based on the Kivelson linewidth theory [161]. Spectra were primarily simulated with Asym, but X-band spectra were simulated with EasySpin and L-band were simulated with XSophe for comparison.

9.4.3. Results and Discussion.

A comparison between the X-band and L-band CW spectra of TEMPO is shown in Figure 9.21. The hyperfine coupling to the I = 1 nitrogen nucleus is relatively small so lines are nearly equally spaced at both L-band and X-band.

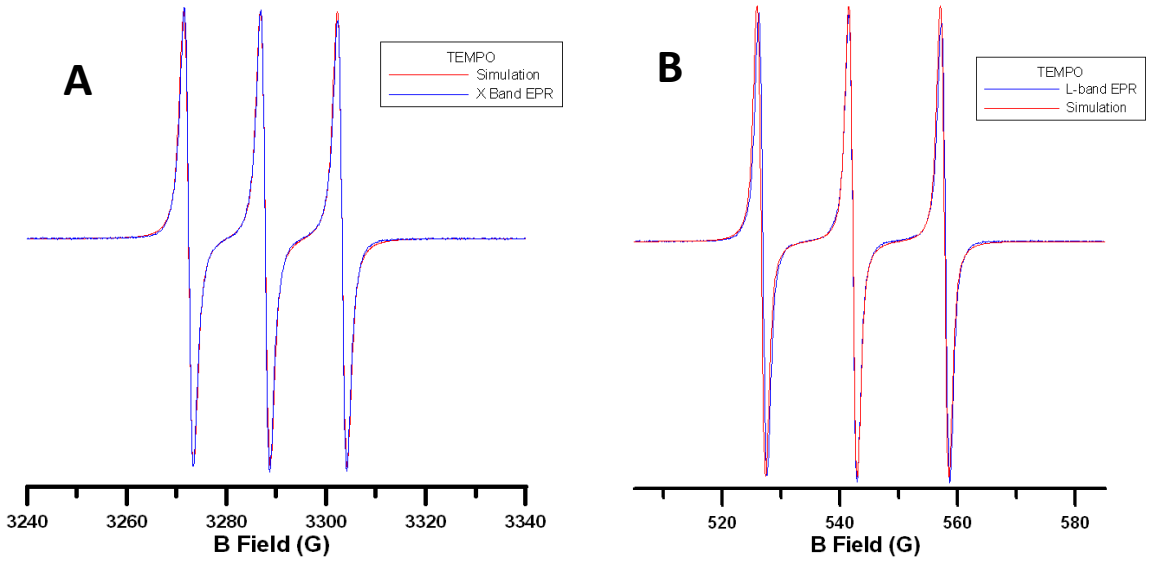

Figure 9.21. Comparison of X- and L-band CW spectrum of 2 mM TEMPO in toluene. (A) X-band CW spectrum collected with 0.5 G modulation amplitude, 100 KHz modulation frequency, 2 mW power, and 100 G sweep width. (B) L-band spectrum collected at a frequency of 1.5218 GHz, 30 dB, 80 G sweep width, and a sweep time of 120 s.

The comparison between X- and L-band CW EPR for vanadyl(acac)$_2$ is shown in Figure 9.22 while the comparison for aquo vanadyl is shown in Figure 9.23. The effects of changing the frequency (and field) are dramatic for the vanadyl(acac)$_2$ and the aquo vanadyl because of vanadium's large nuclear spin (I = 3.5) and the large hyperfine splitting. Differences in linewidths and peak heights are due to incomplete motional averaging.

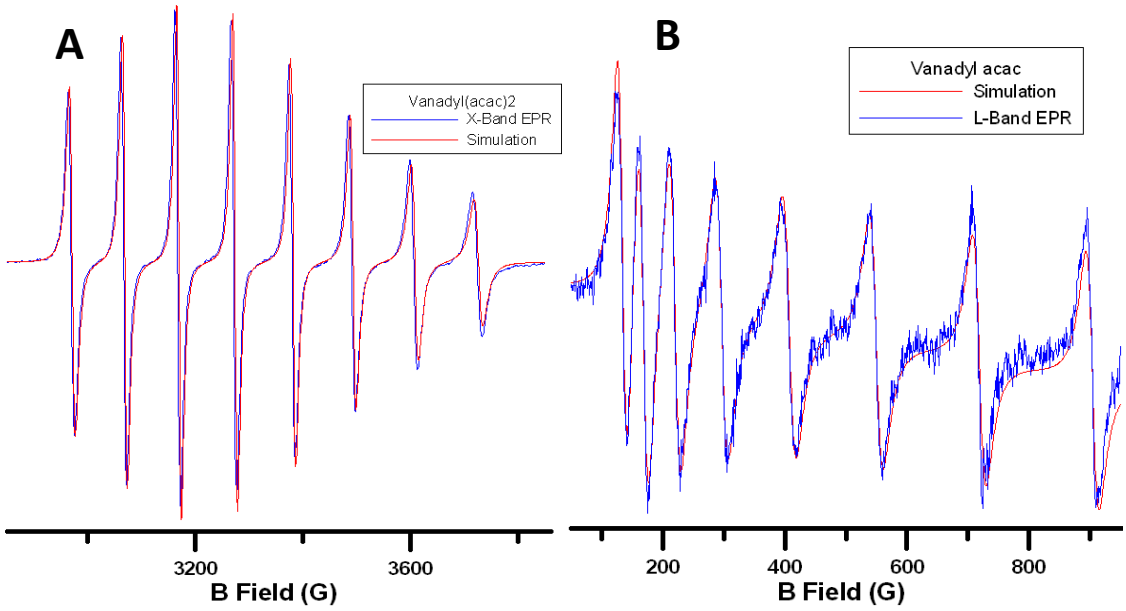

Figure 9.22. Comparison of X- and L-band CW spectrum of 2 mM vanadyl(acac)$_2$ in toluene. (A) X-band CW spectrum collected with 1 G modulation amplitude, 100 KHz modulation frequency, 5 mW power, and 1000 G sweep width. (B) L-band spectrum collected at a frequency of 1.5218 GHz, 30 dB, 900 G sweep width, and a sweep time of 120 s.

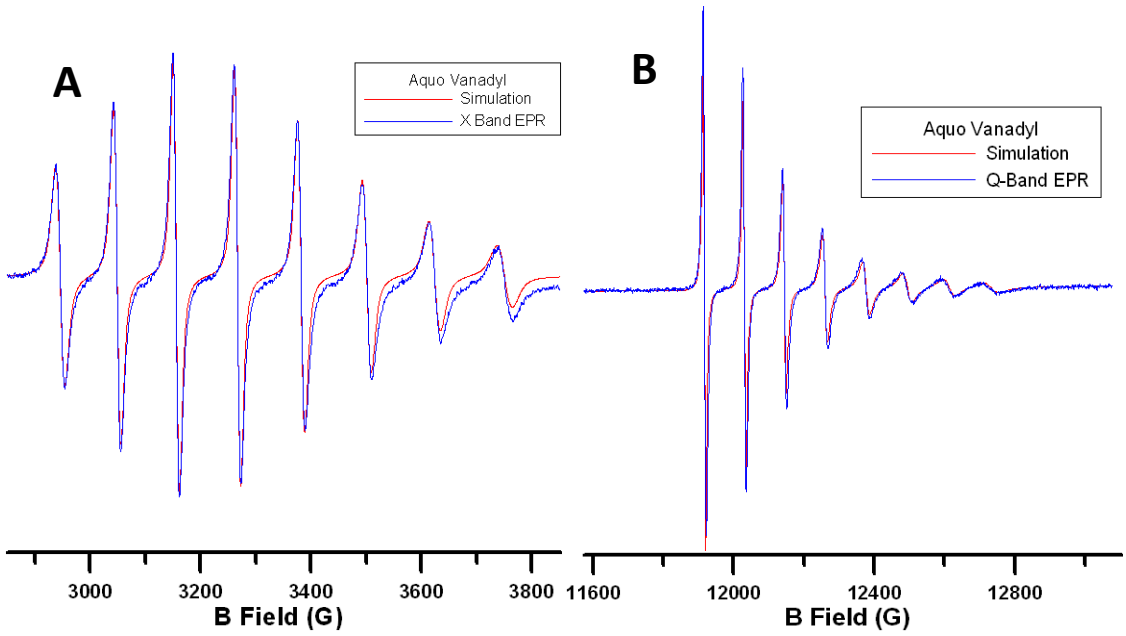

Figure 9.23. Comparison of X- and Q-band CW spectrum of 2 mM aquo-vanadyl in toluene. (A) X-band CW spectrum collected with 2.0 G modulation amplitude, 100 KHz modulation frequency, 5 mW power, and 1000 G sweep width. (B) Q-band spectrum collected at a frequency of 1.5218 GHz, 30 dB, 80 G sweep width, and a sweep time of 120 s.

Figure 9.24 is the comparison between X- and L-band for $Cu(dtc)_2$. For $Cu(dtc)_2$, coupling to the I = 3/2 copper nucleus gives 4 lines. The most conspicuous differences in spectra between L-band and X-band are the changes in linewidths that result from incomplete motional averaging of g- and A- anisotropies. The impact of g-anisotropy increases with increasing magnetic field, but the impact of A-anisotropy is field independent.

For the X-band spectrum, the fourth line was the sharpest and most defined, and the separate features for the ^{63}Cu and ^{65}Cu were well resolved. The four different hyperfine lines have different widths due to incomplete motional averaging of g- and A-

anitotropy. The X-band spectrum was simulated using both the EasySpin shareware as well as Asym to determine the tumbling correlation time (16 ps/rad).

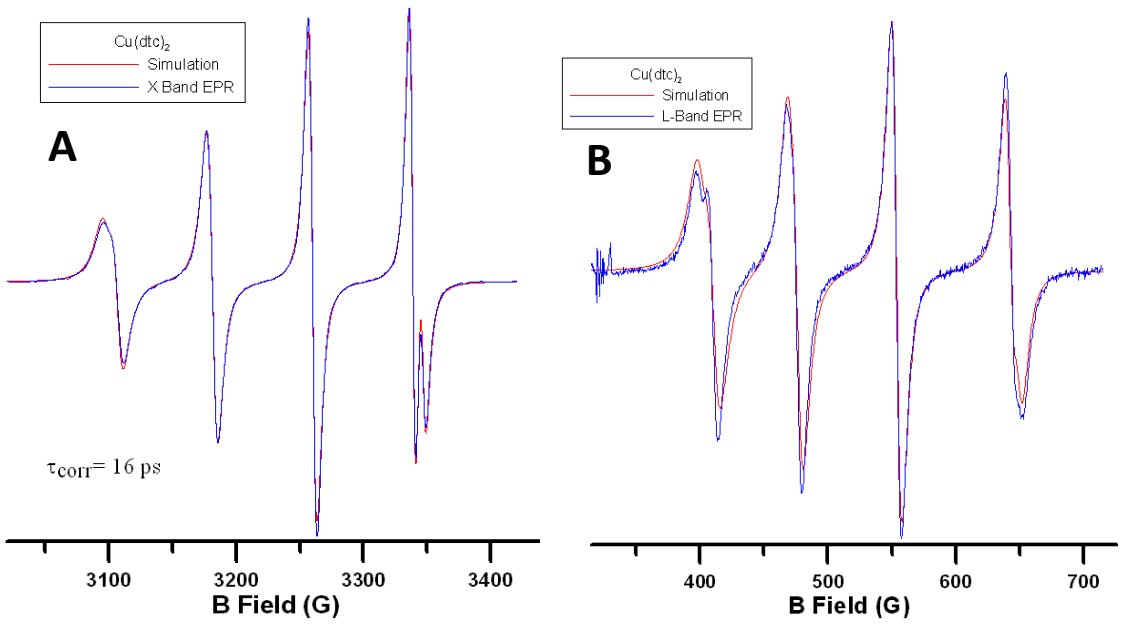

Figure 9.24. Comparison of X- and Q-band CW spectrum of 2 mM $Cu(dtc)_2$ in toluene. (A) X-band CW spectrum collected with 2.0 G modulation amplitude, 100 KHz modulation frequency, 40 mW power, and 400 G sweep width. (B) Q-band spectrum collected at a frequency of 1.5288 GHz, 30 mW, 400 G sweep width, and a sweep time of 120 s.

Future Work. The study presented in this section could be extended to more microwave frequencies including vanadyl$(acac)_2$ at L-band and TEMPO at Q-band. CW spectra could also be collected at VHF (250 MHz). The selection of compounds and frequencies could be guided by simulations of the type used here.

Chapter 10: Conclusion and Future Work

Through this dissertation, the utility of X-band rapid-scan EPR was demonstrated. Rapid-scan EPR is a relatively straight-forward (in terms of application and analysis) EPR technique that will quickly become a more mainstream method along with CW and pulse EPR. Through studying various different samples such as ones with long longitudinal relaxation time T_1 (N_s^0 defects in diamond, $N@C_{60}$, and amorphous hydrogenated silicon), heterogeneous samples (crystalline 1:1 α,γ-bisdiphenylene-β-phenylallyl (BDPA) :benzene), lossy samples (aqueous nitroxyl radicals), and transient samples (5-tert-Butoxycarbonyl-5-methyl-1-pyrroline-N-oxide (BMPO)-superoxide adduct) the benefits of rapid-scan EPR were presented.

Experiments studying samples with long relaxation times can be further investigated with variable temperature rapid-scan EPR. We expect that the S/N enhancement with rapid-scan EPR relative to CW EPR will be much greater at lower temperatures.

Quantitative rapid-scan EPR is a field that needs to be studied further. Currently, we are able to do quantitative EPR in regimes where the signal is in the linear power response region (Quine et al., 2010). The theory to understand quantitative EPR under non-linear conditions needs to be expanded.

The S/N enhancement observed for many of the samples outlined in this dissertation is expected to be observed for other classes of compounds. Radiation induced defect (such as irradiated teeth dosimetry) compounds are another class of samples that would most likely benefit greatly from rapid-scan EPR because of long relaxation times but broad spectra (short T_2*). Rapid-scan EPR will decrease the limit of detection that is currently limiting EPR experiments for dosimetry.

The applications of rapid-scan to spin trapping experiments should be investigated thoroughly. This is a very large and important field. In this dissertation a first comparison between rapid-scan and CW for BMPO-OOH was shown. For this transient spin adduct, rapid-scan gave significantly better S/N. These experiments can be expanded to intercellular spin-trapping experiments.

Time-resolved experiments are also an exciting application of rapid-scan EPR. In the future, it may be possible to observe fast reactions in real time. Our estimation is that rapid-scan EPR will be able to measure reactions occurring on the millisecond time scale. If we can achieve a millisecond time scale, we hope to apply this method of observing reactions in real time to protein folding. Initially, we would measure the folding rate for a well characterized protein such as cytochrome *c* (folding time≈10 ms) (Bandi, et al., 2008). Because we are observing protein folding, we would observe changes in the shape of the EPR line rather than the integration. The shape of the line is dependent upon several factors, one being the ability of the spin label to have many conformations. As the motion of a spin label becomes more rigid (as the protein folds) the line broadens. Thus, we would be able to observe a protein folding in real time via rapid scan EPR.

Similarly, rapid changes in relative proportions of overlapping signals from multiple species can be studied with rapid-scan EPR.

While there are current limitations to rapid-scan EPR (scan width of 80 G), the hardware will continue to improve to give larger scan widths to study a larger variety of samples.

This work used triangular or sinusoidal magnetic field scans. Many other shapes could be used to exploit various relaxation properties. Rapid RF/microwave frequency scans could replace magnetic field scans in some measurements.

The Eaton lab has made significant progress developing X-band rapid-scan EPR and applying this technique to many samples where it is advantageous. Many of the x-band results will transfer directly to other EPR frequencies, such as in vivo imaging at low fields or small samples at high fields. There are still many more avenues that should be explored including variable temperature experiments, metal samples, quantitative rapid-scan EPR, and time-resolved rapid-scan experiments.

References

[1] J.R. Biller, V. Meyer, H. Elajaili, G.M. Rosen, J.P.Y. Kao, S.S. Eaton, G.R. Eaton, Relaxation times and line widths of isotopically-substituted nitroxides in aqueous solution at X-band, J Magn Reson, 212 (2011) 370-377.
[2] A. Siddiqua, Y. Luo, V. Meyer, M.A. Swanson, X. Yu, G.H. Wei, J. Zheng, G.R. Eaton, B.Y. Ma, R. Nussinov, S.S. Eaton, M. Margittai, Conformational Basis for Asymmetric Seeding Barrier in Filaments of Three- and Four-Repeat Tau, J Am Chem Soc, 134 (2012) 10271-10278.
[3] G.M. Rosen, Free radicals : biology and detection by spin trapping, Oxford University Press, New York ; Oxford, 1999.
[4] B.A. Jacobsohn, R.K. Wangsness, Shapes of Nuclear Induction Signals, Phys Rev, 73 (1948) 942-946.
[5] N. Bloembergen, E.M. Purcell, R.V. Pound, Relaxation Effects in Nuclear Magnetic Resonance Absorption, Phys Rev, 73 (1948) 679-712.
[6] R.A. Serway, J.W. Jewett, Physics for scientists and engineers, 6th ed., Brooks/Cole, Pacific Grove, Calif. London, 2003.
[7] P. Ariotti, Galileo on Isochrony of Pendulum Isis, 59 (1968) 414-426.
[8] M.R. Matthews, C.F. Gauld, A. Stinner, SpringerLink (Online service), The Pendulum Scientific, Historical, Philosophical and Educational Perspectives, in, Springer, Dordrecht, 2005.
[9] P.W. Atkins, J. De Paula, Atkins' Physical chemistry, 8th ed., Oxford University Press, Oxford ; New York, 2006.
[10] R.J. Cook, D.H. Whiffen, Electron Spin Resonance and its Applications, Phys. Med. Biol., 7 (1962) 277-&.
[11] G.R. Eaton, S.S. Eaton, D.P. Barr, R.T. Weber, Quantitative EPR, Springer, Wien ; New York, 2010.
[12] E. Zavoisky, The paramagnetic absorption of a solution in parallel fields, J. Phys.-USSR, 8 (1944) 377-380.
[13] E. Zavoisky, Paramagnetic Absorption in Some Salts in Perpendicular Magnetic Fields, Zhurnal Eksperimentalnoi Teor. Fiz., 16 (1946) 603-606.
[14] J.S. Hyde, R.A. Strangeway, T.G. Camenisch, J.J. Ratke, W. Froncisz, W-band frequency-swept EPR, J Magn Reson, 205 (2010) 93-101.
[15] J.A. Weil, J.R. Bolton, Electron paramagnetic resonance : elementary theory and practical applications, 2nd ed., Wiley-Interscience, Hoboken, N.J., 2007.
[16] L.J. Berliner, Spin labeling : theory and applications, Academic Press, New York ; London, 1976.
[17] A. Lund, M. Shiotani, S. Shimada, SpringerLink (Online service), Principles and applications of ESR spectroscopy, in, Springer, Dordrecht ; London, 2010, pg.13-16.
[18] C.P. Poole, H.A. Farach, Handbook of electron spin resonance : data sources, computer technology, relaxation, and ENDOR, American Institute of Physics, New York, 1994.
[19] A. Schweiger, G. Jeschke, Principles of pulse electron paramagnetic resonance, Oxford University Press, New York, 2001.

[20] G.R. Eaton, S.S. Eaton, L.J. Berliner, Biological Magnetic Resonance, Springer, 2000.
[21] W.B. Mims, Measurement of linear electric-field effect in EPR using spin-echo method, Rev Sci Instrum, 45 (1974) 1583-1591.
[22] A.F. Kip, C. Kittel, R.A. Levy, A.M. Portis, Electronic structure of f-centers-hyperfine interactions in electron spin resonance, Phys Rev, 91 (1953) 1066-1071.
[23] A.I. Popov, K. Hallenga, Modern NMR techniques and their application in chemisry, Marcel Dekker, New York, NY, 1991.
[24] A. Lund, E. Sagstuen, A. Sanderud, J. Maruani, Relaxation-Time Determination from Continuous-Microwave Saturation of EPR Spectra, Radiation Research, 172 (2009) 753-760.
[25] J.C. Macosko, C.H. Kim, Y.K. Shin, The membrane topology of the fusion peptide region of influenza hemagglutinin determined by spin-labeling EPR, J Mol Biol, 267 (1997) 1139-1148.
[26] M.H. Rakowsky, A. Zecevic, G.R. Eaton, S.S. Eaton, Determination of high-spin iron(III)-nitroxyl distances in spin-labeled porphyrins by time-domain EPR, J Magn Reson, 131 (1998) 97-110.
[27] J.S. Hyde, W. Froncisz, Loop gap resonators, in: A.J. Hoff (Ed.) Advanced EPR: Applications in Biology and Biochemistry, Elsevier, Amsterdam, 1989, pp. 277-306.
[28] R.W. Quine, D.G. Mitchell, G.R. Eaton, A General Purpose Q-Measuring Circuit Using Pulse Ring-Down, Concept Magn Reson B, 39B (2011) 43-46.
[29] J. Dadok, R.F. Sprecher, Correlation Nmr-Spectroscopy, J Magn Reson, 13 (1974) 243-248.
[30] M. Weger, Passage Effects in Paramagnetic Resonance Experiments, Bell Syst Tech J, 39 (1960) 1013-1112.
[31] R. Beeler, D. Roux, G. Bene, R. Extermann, Rapid-Passage Effects in Electron Spin Resonance, Phys Rev, 102 (1956) 295-295.
[32] A.M. Portis, Rapid Passage Effects in Electron Spin Resonance, Phys Rev, 100 (1955) 1219-1221.
[33] J.S. Hyde, Magnetic Resonance and Rapid Passage in Irradiated Lif, Phys Rev, 119 (1960) 1483-1492.
[34] F. Bloch, W.W. Hansen, M. Packard, The Nuclear Induction Experiment, Phys Rev, 70 (1946) 474-485.
[35] J.C. McGurk, T.G. Schmalz, W.H. Flygare, Fast passage in rotational spectroscoy-Theory and Experiment, J Chem Phys, 60 (1974) 4181-4188.
[36] G. Duxbury, N. Langford, M.T. McCulloch, S. Wright, Rapid passage induced population transfer and coherences in the 8 micron spectrum of nitrous oxide, Mol Phys, 105 (2007) 741-754.
[37] S. Subramanian, J.W. Koscielniak, N. Devasahayam, R.H. Pursley, T.J. Pohida, M.C. Krishna, A new strategy for fast radiofrequency CW EPR imaging: Direct detection with rapid scan and rotating gradients, J Magn Reson, 186 (2007) 212-219.
[38] J.W. Stoner, D. Szymanski, S.S. Eaton, R.W. Quine, G.A. Rinard, G.R. Eaton, Direct-detected rapid-scan EPR at 250 MHz, J Magn Reson, 170 (2004) 127-135.

[39] J.P. Joshi, J.R. Ballard, G.A. Rinard, R.W. Quine, S.S. Eaton, G.R. Eaton, Rapid-scan EPR with triangular scans and fourier deconvolution to recover the slow-scan spectrum, J Magn Reson, 175 (2005) 44-51.
[40] M. Tseitlin, A. Dhami, R.W. Quine, G.A. Rinard, S.S. Eaton, G.R. Eaton, Electron spin T_2 of a nitroxyl radical at 250 MHz measured by rapid-scan EPR, Appl Magn Reson, 30 (2006) 651-656.
[41] R.W. Quine, G.A. Rinard, S.S. Eaton, G.R. Eaton, Quantitative rapid scan EPR spectroscopy at 258 MHz, J Magn Reson, 205 (2010) 23-27.
[42] J.P. Joshi, G.R. Eaton, S.S. Eaton, Impact of resonator on direct-detected rapid-scan EPR at 9.8 GHz, Appl Magn Reson, 28 (2005) 239-249.
[43] M. Tseitlin, G.A. Rinard, R.W. Quine, S.S. Eaton, G.R. Eaton, Deconvolution of sinusoidal rapid EPR scans, J Magn Reson, 208 (2011) 279-283.
[44] W.R. Hagen, Biomolecular EPR spectroscopy, CRC Press, Boca Raton, 2009.
[45] J.R. Harbridge, G.A. Rinard, R.W. Quine, S.S. Eaton, G.R. Eaton, Enhanced signal intensities obtained by out-of-phase rapid-passage EPR for samples with long electron spin relaxation times, J Magn Reson, 156 (2002) 41-51.
[46] M. Tseitlin, S.S. Eaton, G.R. Eaton, Uncertainty analysis for absorption and first-derivative electron paramagnetic resonance spectra, Concepts in Magnetic Resonance Part A, 40A (2012) 295-305.
[47] J.S. Hyde, W. Froncisz, A. Kusumi, Dispersion Electron-Spin Resonance with the Loop-Gap Resonator, Rev Sci Instrum, 53 (1982) 1934-1937.
[48] R.W. Quine, D.G. Mitchell, M. Tseitlin, S.S. Eaton, G.R. Eaton, A resonated coil driver for rapid scan EPR, Concept Magn Reson B, 41B (2012) 95-110.
[49] G.A. Rinard, S.S. Eaton, G.R. Eaton, Sensitivity in: C.P. Poole, H.A. Farach (Eds.) Handbook of Electron Spin Resonance American Institue of Phyics, New York,, 1994, pp. 1-23.
[50] E.L. Gintzon, Microwave Measurements, McGraw-Hill, 1957.
[51] D.G. Mitchell, R.W. Quine, M. Tseitlin, R.T. Weber, V. Meyer, A. Avery, S.S. Eaton, G.R. Eaton, Electron Spin Relaxation and Heterogeneity of the 1:1 alpha,gamma-Bisdiphenylene-beta-phenylallyl (BDPA)/Benzene Complex, J Phys Chem B, 115 (2011) 7986-7990.
[52] H.J. Halpern, M. Peric, T.D. Nguyen, D.P. Spencer, B.A. Teicher, Y.J. Lin, M.K. Bowman, Selective Isotopic Labeling of a Nitroxide Spin Label to Enhance Sensitivity for T2 Oxymetry, J Magn Reson, 90 (1990) 40-51.
[53] M. Tseitlin, D. Mitchell, S.S. Eaton, G.R. Eaton, Corrections for sinusoidal baackground and non-orthognoality of signal channels in sinusoidal rapid magnetic field scans, J Magn Reson, 223 (2012) 80-84.
[54] P. Tsai, K. Ichikawa, C. Mailer, S. Pou, H.J. Halpern, B.H. Robinson, R. Nielsen, G.M. Rosen, Esters of 5-carboxyl-5-methyl-1-pyrroline N-oxide: A family of spin traps for superoxide, J Org Chem, 68 (2003) 7811-7817.
[55] P.W. Anderson, P.R. Weiss, Exchange Narrowing in Paramagnetic Resonance, Rev Mod Phys, 25 (1953) 269-276.
[56] A. Carrington, A.D. McLachlan, Introduction to magnetic resonance with applications to chemistry and chemical physics, Harper & Row, New York,, 1967.

[57] P. Turek, J.J. Andre, A. Giraudeau, J. Simon, Preparation and Study of a Lithium Phthalocyanine Radical - Optical and Magnetic-Properties, Chem Phys Lett, 134 (1987) 471-476.
[58] K.J. Liu, P. Gast, M. Moussavi, S.W. Norby, N. Vahidi, T. Walczak, M. Wu, H.M. Swartz, Lithium Phthalocyanine - a Probe for Electron-Paramagnetic-Resonance Oximetry in Viable Biological-Systems, Proceedings of the National Academy of Sciences of the United States of America, 90 (1993) 5438-5442.
[59] C.F. Koelsch, Syntheses with Triarylvinylmagnesium Bromides - Alpha,Gamma-Bisdiphenylene-Beta-Phenylallyl, a Stable Free Radical, J Am Chem Soc, 79 (1957) 4439-4441.
[60] M. Bennati, C.T. Farrar, J.A. Bryant, S.J. Inati, V. Weis, G.J. Gerfen, P. Riggs-Gelasco, J. Stubbe, R.G. Griffin, Pulsed electron-nuclear double resonance (ENDOR) at 140 GHz, J Magn Reson, 138 (1999) 232-243.
[61] D. Goldfarb, Y. Lipkin, A. Potapov, Y. Gorodetsky, B. Epel, A.M. Raitsimring, M. Radoul, I. Kaminker, HYSCORE and DEER with an upgraded 95 GHz pulse EPR spectrometer, J Magn Reson, 194 (2008) 8-15.
[62] C. Durkan, M.E. Welland, Electronic spin detection in molecules using scanning-tunneling-microscopy-assisted electron-spin resonance, Appl Phys Lett, 80 (2002) 458-460.
[63] Y.A. Koksharov, I.V. Bykov, A.P. Malakho, S.N. Polyakov, G.B. Khomutov, J. Bohr, Radicals as EPR probes of magnetization of gadolinium stearate Langmuir-Blodgett film, Mat Sci Eng C-Bio S, 22 (2002) 201-207.
[64] E.L. Dane, T.M. Swager, Synthesis of a Water-Soluble 1,3-Bis(diphenylene)2-phenylallyl Radical, J Org Chem, 75 (2010) 3533-3536.
[65] L. Frydman, P. Giraudeau, Y. Shrot, Multiple Ultrafast, Broadband 2D NMR Spectra of Hyperpolarized Natural Products, J Am Chem Soc, 131 (2009) 13902-13903.
[66] J. Yamauchi, K.P. Adachi, Y. Deguchi, Heat-Capacity Anomaly in Crystalline Organic Free-Radical, P-Cl-Bdpa, Chem Lett, (1972) 733-735.
[67] J.S. Hyde, A. Jesmanowicz, J.J. Ratke, W.E. Antholine, Pseudomodulation - a Computer-Based Strategy for Resolution Enhancement, J Magn Reson, 96 (1992) 1-13.
[68] S. Stoll, A. Schweiger, EasySpin, a comprehensive software package for spectral simulation and analysis in EPR, J Magn Reson, 178 (2006) 42-55.
[69] G. Ilangovan, J.L. Zweier, P. Kuppusamy, Electrochemical preparation and EPR studies of lithium phthalocyanine. Part 2: Particle-size-dependent line broadening by molecular oxygen and its implications as an oximetry probe, J Phys Chem B, 104 (2000) 9404-9410.
[70] J.J. Lothe, G. Eia, Diphenyl-Picrylhydrazyl as a Standard in Electron Spin Resonance, Acta Chem Scand, 12 (1958) 1535-1537.
[71] L.S. Singer, C. Kikuchi, Paramagnetic Resonance Absorption in Single Crystals of Diphenylpicrylhydrazyl at Low Temperatures, J Chem Phys, 23 (1955) 1738-1739.
[72] D.G. Mitchell, M. Tseitlin, R.W. Quine, V. Meyer, M. Newton, A. Schnegg, B. George, G.R. Eaton, S.S. Eaton, X-band Rapid-scan EPR of Samples with Long Electron Spin relaxation, (2013) *Molecular Physics, 111*, DOI:10.1008/00268976.00262013. 0079295.

[73] D.G. Mitchell, R.W. Quine, M. Tseitlin, V. Meyer, S.S. Eaton, G.R. Eaton, Comparison of continuous wave, spin echo, and rapid scan EPR of irradiated fused quartz, Radiation Measurements, 46 (2011) 993-996.
[74] E. Janzen, N.T. Son, B. Magnusson, A. Ellison, Intrinsic defects in high-purity SiC, Microelectronic Engineering, 83 (2006) 130-134.
[75] M. Fehr, P. Simon, T. Sontheimer, C. Leendertz, B. Gorka, A. Schnegg, B. Rech, K. Lips, Influence of deep defects on device performance of thin-film polycrystalline silicon solar cells, Appl Phys Lett, 101 (2012).
[76] P.B. Feng, Y. Wang, X. Rong, J.H. Su, C.Y. Ju, J.F. Du, Characterization of the electronic structure of E-2 ' defect in quartz by pulsed EPR spectroscopy, Physics Letters A, 376 (2012) 2195-2199.
[77] W. Harneit, Fullerene-based electron-spin quantum computer, Phys Rev A, 65 (2002).
[78] A. Blank, E. Suhovoy, R. Halevy, L. Shtirberg, W. Harneit, ESR imaging in solid phase down to sub-micron resolution: methodology and applications, Phys Chem Chem Phys, 11 (2009) 6689-6699.
[79] A.M. Edmonds, U.F.S. D'Haenens-Johansson, R.J. Cruddace, M.E. Newton, K.M.C. Fu, C. Santori, R.G. Beausoleil, D.J. Twitchen, M.L. Markham, Production of oriented nitrogen-vacancy color centers in synthetic diamond, Phys. Rev. B, 86 (2012), 035201.
[80] M. Fehr, J. Behrends, S. Haas, B. Rech, K. Lips, A. Schnegg, Electrical detection of electron-spin-echo envelope modulations in thin-film silicon solar cells, Phys. Rev. B, 84 (2011) 193202.
[81] E. Suhovoy, A. Blank, High-Resolution ESR Imaging of N@C-60 Radicals on a Surface, Israel Journal of Chemistry, 48 (2008) 45-51.
[82] A. Cox, M.E. Newton, J.M. Baker, C-13, N-14 AND N-15 ENDOR Measurements on the Single Substitutional Nitrogen Center (P1) in Diamond, Journal of Physics-Condensed Matter, 6 (1994) 551-563.
[83] R.W. Quine, G.R. Eaton, S.S. Eaton, Pulsed EPR Spectrometer, Rev Sci Instrum, 58 (1987) 1709-1723.
[84] B. Rech, H. Wagner, Potential of amorphous silicon for solar cells, Applied Physics a-Materials Science & Processing, 69 (1999) 155-167.
[85] Y. Talmon, L. Shtirberg, W. Harneit, O.Y. Rogozhnikova, V. Tormyshev, A. Blank, Molecular diffusion in porous media by PGSE ESR, Phys Chem Chem Phys, 12 (2010) 5998-6007.
[86] S.S. Eaton, G.R. Eaton, Irradiated Fused-Quartz Standard Sample for Time-Domain Epr, J Magn Reson Ser A, 102 (1993) 354-356.
[87] G.R. Eaton, S.S. Eaton, R.W. Quine, D. Mitchell, V. Kathirvelu, R.T. Weber, A signal-to-noise standard for pulsed EPR, J Magn Reson, 205 (2010) 109-113.
[88] M. Newton, EPR, ENDOR and EPR Imaging of Defecs in Diamond, in: B.C. Gilbert (Ed.) Electron Paramagnetic Resonance, The Royal Society of Chemistry 2007, pp. 131-156.
[89] A. Tallaire, A.T. Collins, D. Charles, J. Achard, R. Sussmann, A. Gicquel, M.E. Newton, A.M. Edmonds, R.J. Cruddace, Characterisation of high-quality thick single-crystal diamond grown by CVD with a low nitrogen addition, Diamond and Related Materials, 15 (2006) 1700-1707.

[90] J.A. vanWyk, E.C. Reynhardt, G.L. High, I. Kiflawi, The dependences of ESR line widths and spin-spin relaxation times of single nitrogen defects on the concentration of nitrogen defects in diamond, Journal of Physics D-Applied Physics, 30 (1997) 1790-1793.
[91] A.W. Kittell, T.G. Camenisch, J.J. Ratke, J.W. Sidabras, J.S. Hyde, Detection of undistorted continuous wave (CW) electron paramagnetic resonance (EPR) spectra with non-adiabatic rapid sweep (NARS) of the magnetic field, J Magn Reson, 211 (2011) 228-233.
[92] A.W. Kittell, E.J. Hustedt, J.S. Hyde, Inter-spin distance determination using L-band (1-2 GHz) non-adiabatic rapid sweep electron paramagnetic resonance (NARS EPR), J Magn Reson, 221 (2012) 51-56.
[93] R.R. Ernst, Sensitivity enhancement in magnetic resonance. I. Analysis of method of time averaging., Rev Sci Instrum, 36 (1965) 1689-1692.
[94] M. Tseitlin, R.W. Quine, G.A. Rinard, S.S. Eaton, G.R. Eaton, Combining absorption and dispersion signals to improve signal-to-noise for rapid-scan EPR imaging, J Magn Reson, 203 (2010) 305-310.
[95] S.S. Eaton, R.W. Quine, M. Tseitlin, D.M. Mitchell, G.A. Rinard, G.R. Eaton, Rapid-scan EPR, in: S.K. Misra (Ed.) Handbook of High Frequency EPR Wiley, 2014.
[96] R.W. Quine, T. Czechowski, G.R. Eaton, A Linear Magnetic Field Scan Driver, Concept Magn Reson B, 35B (2009) 44-58.
[97] A. Schnegg, J. Behrends, M. Fehr, K. Lips, Pulsed electrically detected magnetic resonance for thin film silicon and organic solar cells, Phys Chem Chem Phys, 14 (2012) 14418-14438.
[98] D. Griller, K.U. Ingold, Persistent Carbon-Centered Radicals, Accounts Chem Res, 9 (1976) 13-19.
[99] H.J. Halpern, M. Peric, C. Yu, E.D. Barth, G.V.R. Chandramouli, M.W. Makinen, G.M. Rosen, In vivo spin-label murine pharmacodynamics using low-frequency electron paramagnetic resonance imaging, Biophys J, 71 (1996) 403-409.
[100] E.G. Janzen, Blackbur.Bj, Detection and identification of short-lived free radicals by and electron spin resonance trapping technique, J Am Chem Soc, 90 (1968) 5909-5910.
[101] D.G. Mitchell, R.W. Quine, M. Tseitlin, S.S. Eaton, G.R. Eaton, X-band rapid-scan EPR of nitroxyl radicals, J Magn Reson, 214 (2012) 221-226.
[102] L. Tan, Digital Signal Processing: Fundamentals and Applications, Elsevier, Burlington, 2007.
[103] K. Hensley, K.A. Robinson, S.P. Gabbita, S. Salsman, R.A. Floyd, Reactive oxygen species, cell signaling, and cell injury, Free Radical Biology and Medicine, 28 (2000) 1456-1462.
[104] J.V. Rodrigues, C.M. Gomes, Mechanism of superoxide and hydrogen peroxide generation by human electron-transfer flavoprotein and pathological varients, Free Radical Biology and Medicine, 54 (2012) 12-19.
[105] T.M. Buetler, A. Krauskopf, U.T. Ruegg, Role of superoxide as a signaling molecule, News in Physiological Sciences, 19 (2004) 120-123.

[106] L. Baillie, S. Hibbs, P. Tsai, G.L. Cao, G.M. Rosen, Role of superoxide in the germination of Bacillus anthracis endospores, Fems Microbiology Letters, 245 (2005) 33-38.
[107] K.W. Raines, T.J. Kang, S. Hibbs, G.L. Cao, J. Weaver, P. Tsai, L. Baillie, A.S. Cross, G.M. Rosen, Importance of nitric oxide synthase in the control of infection by Bacillus anthracis, Infection and Immunity, 74 (2006) 2268-2276.
[108] D.G. Mitchell, G.M. Rosen, M. Tseitlin, B. Symmes, S.S. Eaton, G.R. Eaton, Use of Rapid-scan EPR to Improve Detection Sensitivity for Spin-Trapped Radicals, . *Biophysical Journal*, 105(2), DOI: 10.1016/j.bpj.2013.06.005. (2013).
[109] G.R. Chalfont, M.J. Perkins, Horsfiel.A, A Probe for Homolytic Reactions in Solution. 2. Polymerization of Styrene, J Am Chem Soc, 90 (1968) 7141-&.
[110] J.R. Harbour, J.R. Bolton, Superoxide Formation in Spinach-Chloroplasts- Electron Spin Resonance Detection by Spin Trapping, Biochemical and Biophysical Research Communications, 64 (1975) 803-807.
[111] E. Finkelstein, G.M. Rosen, E.J. Rauckman, Spin trapping-Kinetics of the reaction of superoxide and hydroxyl radicals with nitrones., J Am Chem Soc, 102 (1980) 4994-4999.
[112] S. Pou, L. Keaton, W. Suricharmorn, G.M. Rosen, Mechanism of superoxide generation by nueronal nitric oxide synthase, Journal of Biological Chemistry, 274 (1999) 9573-9580.
[113] S. Pou, W.S. Pou, D.S. Bredt, S.H. Snyder, G.M. Rosen, Generation of superoxide by purified brain nitric-oxide synthase, Journal of Biological Chemistry, 267 (1992) 24173-24176.
[114] Y. Xia, L.J. Roman, B.S.S. Masters, J.L. Zweier, Inducible nitric-oxide synthase generates superoxide from the reductase domain, Journal of Biological Chemistry, 273 (1998) 22635-22639.
[115] J. Vasquez-Vivar, B. Kalyanaraman, P. Martasek, N. Hogg, B.S.S. Masters, H. Karoui, P. Tordo, K.A. Pritchard, Superoxide generation by endothelial nitric oxide synthase: The influence of cofactors, Proceedings of the National Academy of Sciences of the United States of America, 95 (1998) 9220-9225.
[116] C. Frejaville, H. Karoui, B. Tuccio, F. Lemoigne, M. Culcasi, S. Pietri, R. Lauricella, P. Tordo, 5-diethoxyphosphoryl-5-methyl-1-pyrroline-N-oxide (DEPMPO) - A new phosphorylated nitrone for the efficient in-vitro and in-vivo spin-trapping of oxygen-centered radicals., J Chem Soc Chem Comm, (1994) 1793-1794.
[117] H. Zhang, J. Joseph, J. Vasquez-Vivar, H. Karoui, C. Nsanzumuhire, P. Martasek, P. Tordo, B. Kalyanaraman, Detection of superoxide anion using an isotopically labeled nitrone spin trap: potential biological applications, Febs Letters, 473 (2000) 58-62.
[118] K. Stolze, N. Udilova, T. Rosenau, A. Hofinger, H. Nohl, Synthesis and characterization of EMPO-derived 5,5-disubstituted 1-pyrroline N-oxides as spin traps forming exceptionally stable superoxide spin adducts, Biological Chemistry, 384 (2003) 493-500.
[119] M.M. Huycke, W. Joyce, M.F. Wack, Augmented production of extracellular superoxide by blood isolates of Enterococcus faecalis, J Infect Dis, 173 (1996) 743-746.
[120] H. Kuthan, V. Ullrich, R.W. Estabrook, A quantitative test for superoxide radicals produced in biological systems, Biochemical Journal, 203 (1982) 551-558.

[121] I. Fridovich, Xanthine Oxidase, in: R.A. Greenwald (Ed.) CRC Handbook of Methods for Oxygen Radical Research, CRC Press, Boca Raton, 1985, pp. 51-53.
[122] P. Tsai, K. Ichikawa, C. Mailer, S. Pou, H.J. Halpern, B.H. Robinson, R.D. Nielsen, G.M. Rosen, Esters of 5-carboxyl-5-methyl-1-pyrroline N-oxide: a family of spin traps for superoxide, J. Org. Chem., 68 (2003) 7811-7817.
[123] D.R. Moore, Y. Kotake, M.M. Huycke, Effects of iron and phytic acid on production of extracellular radicals by Enterococcus faecalis, Exp Biol Med, 229 (2004) 1186-1195.
[124] M.M. Huycke, D. Moore, W. Joyce, P. Wise, L. Shepard, Y. Kotake, M.S. Gilmore, Extracellular superoxide production by Enterococcus faecalis requires demethylmenaquinone and is attenuated by functional terminal quinol oxidases, Mol Microbiol, 42 (2001) 729-740.
[125] D.G. Mitchell, R.W. Quine, M. Tseitlin, S.S. Eaton, G.R. Eaton, X-band Rapid-Scan EPR of Nitroxyl Radicals, J. Magn. Reson. , 214 (2012) 221-226
[126] D.G. Mitchell, M. Tseitlin, R.W. Quine, V. Meyer, M.E. Newton, A. Shnegg, B. George, S.S. Eaton, G.R. Eaton, X-Band Rapid-scan EPR of Samples with Long Electron Relaxation Times: A Comparison of Continuous Wave, Pulse, and Rapid-scan EPR, Mol. Phys., 111 (2013) DOI:10.1008/00268976.00262013.00792959
[127] R.W. Quine, D. Mitchell, G.R. Eaton, A General Purpose Q-Measuring Circuit Using Pulse Ring-Down, Conc. Magn. Reson. B (Magn. Reson. Engin.), 39B (2011) 43-46.
[128] M. Tseitlin, T. Czechowski, R.W. Quine, S.S. Eaton, G.R. Eaton, Background removal procedure for rapid scan EPR, J Magn Reson, 196 (2009) 48-53.
[129] S.R. Plimpton, M. Golkowski, D.G. Mitchell, C. Austin, S.S. Eaton, G.R. Eaton, C. Golkowski, M. Voskuil, Remote delivery of hyroxyl radicals via secondary chemistry of a nonthermal plasma effluent., Biotechnology and Bioengineering, 110 (2013) 1936-1944.
[130] G. Fridman, A.D. Brooks, M. Balasubramanian, A. Fridman, A. Gutsol, V.N. Vasilets, H. Ayan, G. Friedman, Comparison of direct and indirect effects of non-thermal atmospheric-pressure plasma on bacteria, Plasma Processes and Polymers, 4 (2007) 370-375.
[131] M. Laroussi, Low temperature plasma-based sterilization: Overview and state-of-the-art, Plasma Processes and Polymers, 2 (2005) 391-400.
[132] M. Moreau, N. Orange, M.G.J. Feuilloley, Non-thermal plasma technologies: New tools for bio-decontamination, Biotechnology Advances, 26 (2008) 610-617.
[133] G. Fridman, M. Peddinghaus, H. Ayan, A. Fridman, M. Balasubramanian, A. Gutsol, A. Brooks, G. Friedman, Blood coagulation and living tissue sterilization by floating-electrode dielectric barrier discharge in air, Plasma Chemistry and Plasma Processing, 26 (2006) 425-442.
[134] D. Dobrynin, G. Fridman, G. Friedman, A. Fridman, Physical and biological mechanisms of direct plasma interaction with living tissue, New Journal of Physics, 11 (2009).
[135] M. Golkowski, C. Golkowski, J. Leszczynski, S.R. Plimpton, P. Maslowski, A. Foltynowicz, J. Ye, B. McCollister, Hydrogen-Peroxide-Enhanced Nonthermal Plasma

Effluent for Biomedical Applications, Ieee Transactions on Plasma Science, 40 (2012) 1984-1991.
[136] S.G. Joshi, M. Cooper, A. Yost, M. Paff, U.K. Ercan, G. Fridman, G. Friedman, A. Fridman, A.D. Brooks, Nonthermal Dielectric-Barrier Discharge Plasma-Induced Inactivation Involves Oxidative DNA Damage and Membrane Lipid Peroxidation in Escherichia coli, Antimicrobial Agents and Chemotherapy, 55 (2011) 1053-1062.
[137] Y. Ma, G.J. Zhang, X.M. Shi, G.M. Xu, Y. Yang, Chemical mechanisms of bacterial inactivation using dielectric barrier discharge plasma in atmospheric air, Ieee Transactions on Plasma Science, 36 (2008) 1615-1620.
[138] S. Ikawa, K. Kitano, S. Hamaguchi, Effects of pH on Bacterial Inactivation in Aqueous Solutions due to Low-Temperature Atmospheric Pressure Plasma Application, Plasma Processes and Polymers, 7 (2010) 33-42.
[139] S. Perni, G. Shama, J.L. Hobman, P.A. Lund, C.J. Kershaw, G.A. Hidalgo-Arroyo, C.W. Penn, X.T. Deng, J.L. Walsh, M.G. Kong, Probing bactericidal mechanisms induced by cold atmospheric plasmas with Escherichia coli mutants, Appl Phys Lett, 90 (2007).
[140] R.A. Venezia, M. Orrico, E. Houston, S.M. Yin, Y.Y. Naumova, Lethal activity of nonthermal plasma sterilization against microorganisms, Infection Control and Hospital Epidemiology, 29 (2008) 430-436.
[141] S. Samukawa, M. Hori, S. Rauf, K. Tachibana, P. Bruggeman, G. Kroesen, J.C. Whitehead, A.B. Murphy, A.F. Gutsol, S. Starikovskaia, U. Kortshagen, J.P. Boeuf, T.J. Sommerer, M.J. Kushner, U. Czarnetzki, N. Mason, The 2012 Plasma Roadmap, Journal of Physics D-Applied Physics, 45 (2012).
[142] S. Kuhn, N. Bibinov, R. Gesche, P. Awakowicz, Non-thermal atmospheric pressure HF plasma source: generation of nitric oxide and ozone for bio-medical applications, Plasma Sources Science & Technology, 19 (2010).
[143] M.J. Thorpe, J. Ye, Cavity-enhanced direct frequency comb spectroscopy, Applied Physics B-Lasers and Optics, 91 (2008) 397-414.
[144] M. Tseitlin, G.A. Rinard, R.W. Quine, S.S. Eaton, G.R. Eaton, Rapid frequency scan EPR, J Magn Reson, 211 (2011) 156-161.
[145] P. Bruggeman, C. Leys, Non-thermal plasmas in and in contact with liquids, Journal of Physics D-Applied Physics, 42 (2009) 012003.
[146] M. Sato, T. Ohgiyama, J.S. Clements, Formation of chemical species and their effects on microorganisms using a pulsed high-voltage discharge in water, Ieee T Ind Appl, 32 (1996) 106-112.
[147] H. Kabashima, H. Einaga, S. Futamura, Hydrogen generation from water, methane, and methanol with nonthermal plasma, Ieee T Ind Appl, 39 (2003) 340-345.
[148] N.J. Stokes, B.J. Tabner, C.N. Hewitt, The Determination of Hydroxyl Radical Concentrations in Environmental Chambers Using Electron-Spin-Resonance, Chemosphere, 28 (1994) 999-1008.
[149] P. Drzewicz, G. Nalecz-Jawecki, M. Gryz, J. Sawicki, A. Bojanowska-Czajka, W. Gluszewski, K. Kulisa, S. Wolkowicz, M. Trojanowicz, Monitoring of toxicity during degradation of selected pesticides using ionizing radiation, Chemosphere, 57 (2004) 135-145.

[150] P. Drzewicz, M. Trojanowicz, R. Zona, S. Solar, P. Gehringer, Decomposition of 2,4-dichlorophenoxyacetic acid by ozonation, ionizing radiation as well as ozonation combined with ionizing radiation, Radiation Physics and Chemistry, 69 (2004) 281-287.
[151] K. Sehested, J. Holcman, E. Bjergbakke, E.J. Hart, Use of Pulse-Radiolysis for the Study of the Chemistry of Aqueous Ozone and Ozonide Solutions, J Radioan Nucl Ch Ar, 101 (1986) 239-250.
[152] G. Merenyi, J. Lind, S. Naumov, C. von Sonntag, Reaction of Ozone with Hydrogen Peroxide (Peroxone Process): A Revision of Current Mechanistic Concepts Based on Thermokinetic and Quantum-Chemical Considerations, Environmental Science & Technology, 44 (2010) 3505-3507.
[153] G. Merenyi, J. Lind, S. Naumov, C. von Sonntag, The Reaction of Ozone with the Hydroxide Ion: Mechanistic Considerations Based on Thermokinetic and Quantum Chemical Calculations and the Role of HO4- in Superoxide Dismutation, Chemistry-a European Journal, 16 (2010) 1372-1377.
[154] G.R. Eaton, S.S. Eaton, Quality Assurance in EPR, in: I.S.o.M. Resonance (Ed.) Bulletin of Magnetic Resonance, 1992, pp. 83-89.
[155] B. Cage, A. Weekley, L.C. Brunel, N.S. Dalal, K3CrO8 in K2NbO8 as a proposed standard for g-factor, spin concentration, and field calibration in high-field EPR spectroscopy, Analytical Chemistry, 71 (1999) 1951-1957.
[156] N.S. Dalal, J.M. Millar, M.S. Jagadeesh, M.S. Seehra, Paramagnetic-Resonance, Magnetic-susceptibility, and anti-ferromagnetic exchange in a CR-5+ paramagnet-ptassium perchromate (K3CRO8), J Chem Phys, 74 (1981) 1916-1923.
[157] W.G. Faix, V. Krivan, Determination of Chromium, Iron, and Cobalt in high-purity niobium by radiochemical neutron-activation analysis., Fresenius Zeitschrift Fur Analytische Chemie, 302 (1980) 269-274.
[158] W.G. Faix, V. Krivan, K. Schulze, Ultratrace analysis- Determination of Cr, Fe, and Co in the PPB and PPT range for checking the preparation of high-purity niobium, Angewandte Chemie-International Edition in English, 19 (1980) 197-198.
[159] R.A. Rowe, M.M. Jones, Preparation from Vanadium(V) oxide through prior reduction to oxovanadium (IV) ion, Inorganic Syntheses, 5 (1957) 114-114.
[160] M.J. Weeks, J.P. Fackler, Single-crystal Electron Paramagnetic Resonance Studies of Copper Diethyldithiocarbamamate, Inorganic Chemistry, 7 (1968) 2548-2553.
[161] D. Kivelson, Theory of ESR linewidths of free radicals, J Chem Phys, 33 (1960) 1094-1106.